

THE UNIVERSITY OF MANITOBA

**Relaxation Dynamics in Some
Reentrant Disordered Magnetic Systems:
FeNiCr, FeNiMn, CrFe**

BY

DAWEI LI

A THESIS SUBMITTED TO
THE FACULTY OF GRADUATE STUDIES OF
THE UNIVERSITY OF MANITOBA
IN PARTIAL FULFILLMENT OF THE REQUIRMENTS OF
THE DEGREE OF DOCTOR OF PHILOSOPHY

DEPARTMENT OF PHYSICS
WINNIPEG, MANITOBA
MAY, 1997



**National Library
of Canada**

**Acquisitions and
Bibliographic Services**

**395 Wellington Street
Ottawa ON K1A 0N4
Canada**

**Bibliothèque nationale
du Canada**

**Acquisitions et
services bibliographiques**

**395, rue Wellington
Ottawa ON K1A 0N4
Canada**

Your file Votre référence

Our file Notre référence

The author has granted a non-exclusive licence allowing the National Library of Canada to reproduce, loan, distribute or sell copies of this thesis in microform, paper or electronic formats.

The author retains ownership of the copyright in this thesis. Neither the thesis nor substantial extracts from it may be printed or otherwise reproduced without the author's permission.

L'auteur a accordé une licence non exclusive permettant à la Bibliothèque nationale du Canada de reproduire, prêter, distribuer ou vendre des copies de cette thèse sous la forme de microfiche/film, de reproduction sur papier ou sur format électronique.

L'auteur conserve la propriété du droit d'auteur qui protège cette thèse. Ni la thèse ni des extraits substantiels de celle-ci ne doivent être imprimés ou autrement reproduits sans son autorisation.

0-612-23627-7

**THE UNIVERSITY OF MANITOBA
FACULTY OF GRADUATE STUDIES
COPYRIGHT PERMISSION**

**RELAXATION DYNAMICS IN SOME REENTRANT DISORDERED
MAGNETIC SYSTEMS: FeNiCr, FeNiMn, CrFe**

by

DAWEI LI

**A Thesis submitted to the Faculty of Graduate Studies of the University of Manitoba
in partial fulfillment of the requirements of the degree of**

DOCTOR OF PHILOSOPHY

DAWEI LI © 1997

**Permission has been granted to the LIBRARY OF THE UNIVERSITY OF MANITOBA
to lend or sell copies of this thesis, to the NATIONAL LIBRARY OF CANADA to microfilm this
thesis and to lend or sell copies of the film, and to UNIVERSITY MICROFILMS to publish an
abstract of this thesis.**

**This reproduction or copy of this thesis has been made available by authority of the copyright
owner solely for the purpose of private study and research, and may only be reproduced and
copied as permitted by copyright laws or with express written authorization from the copyright
owner.**

Abstract

The relaxation response of three reentrant disordered ferromagnetic systems $\text{Fe}_{0.65}\text{Ni}_{0.35-x}\text{Cr}_x$ ($x = 0.11, 0.12$), $\text{Cr}_{1-x}\text{Fe}_x$ ($x = 0.21$), and $(\text{Fe}_{0.65}\text{Ni}_{0.35})_{1-x}\text{Mn}_x$ ($x = 0.118$), have been investigated over a range of temperatures both below and above their glass temperatures.

The measurements were performed with a home-made variable temperature, variable frequency SQUID dc-susceptometer with a temperature range from 4.2 K to 250 K and a dc-field range up to 100 Oe.

The relaxation response was measured using a variety of experimental procedures. In the simplest procedure, the sample was field cooled from a reference temperature in the paramagnetic regime to the measurement temperature, held at fixed temperature for a waiting time t_w , after which the field was removed and the response was measured over an observation time $2s \leq t \leq 10^4s$. In more complicated procedures, the temperature was cycled or shifted during the waiting time t_w or subjected to a field change of varying amplitude.

All samples investigated here were characterized by two thermally distinct relaxation regimes, a high temperature regime of equilibrium, power law dynamics which coincided with the ferromagnetic regime, and a low temperature regime of nonequilibrium, age-dependent dynamics which coincided with the reentrant glass phase. The relaxation isotherms in both regimes were fitted to specific functional forms predicted by various models of slow relaxation in disordered systems including Fisher and Huse's droplet scaling theory of domain growth, hierarchically constrained dynamics, Bouchaud's theory of random traps, an Elementary Decay Model based on a stochastic distribution of activation energies, and a percolation theory for relaxation of dispersive excitations within finite domains. The fitting parameters extracted from these fits provided detailed information on the organization of metastable states in the configuration space of a structurally disordered

system, on their evolution with temperature, and on their fragility with response to field and temperature fluctuations, and allow us to compare the various theoretical approaches to slow relaxation, establish possible correlations and expose inconsistencies.

Acknowledgement

I deeply appreciate and thank Dr. R. M. Roshko, my supervisor, for his guidance and help through my Ph.D program. I would like to thank all my committee members, Dr. G. Williams, Dr. P. Zetner, Dr. D. Hall, and Dr. E. Lahderanta for their suggestions and comments. I would also like to thank Dr. H.P. Kunkel, Mr. G. Roy, Mr. G. Yang, and Ms. P. Mitchler for their help in the sample preparation and experiments.

Contents

1	Introduction	1
1.1	Basic Concepts and Phenomena in Disordered Magnets .	1
1.2	Spin Glass Systems	8
1.2.1	RKKY Spin Glasses	8
1.2.2	Insulating and Semiconducting Spin Glasses . . .	12
1.3	Relaxation and Aging in Disordered Magnetic Systems .	13
1.4	Relaxation and Aging Behavior in Other Complex Systems	17
2	Theory	27
2.1	Basic Concepts	27
2.2	The EA Model and The Replica Symmetric Solution . .	31
2.3	The SK Model and Parisi's Replica Symmetry Breaking Solution	36
2.4	Pure States, Metastable States, and Dynamic Behaviour	46
2.5	The Droplet Scaling Model	52
2.6	The Model of Random Traps	58
2.7	The Elementary Decay Model (EDM)	69

2.8	A Percolation Model for Magnon Relaxation	78
2.9	Comments on These Relaxation Models	83
3	Sample Preparation and Measurement Techniques	88
3.1	Magnetic Properties and Sample Preparation	88
3.1.1	The FeNiCr System	89
3.1.2	The CrFe System	96
3.1.3	The FeNiMn System	101
3.2	Apparatus and Measurement Techniques	107
3.2.1	The ⁴ He Cryostat	107
3.2.2	The Magnetization Measurement System	112
3.2.3	Calibration of The SQUID Magnetometer	115
4	Data Analysis and Discussion	118
4.1	Temperature Dependence of The Static Magnetization .	119
4.2	Experimental Relaxation Procedures	124
4.3	Relaxation Dynamics: A Stretched Exponential and A Power Law Analysis	128
4.4	Relaxation Dynamics: A Random Trap Analysis and Scaling of The Relaxation Isotherms	144
4.5	Relaxation Dynamics: An Elementary Decay Model (EDM) Analysis	163
4.6	Relaxation Dynamics: A Percolation Analysis	178

4.7	Relaxation Dynamics: Temperature Fluctuation Effects .	188
4.8	Relaxation Dynamics: Field Effects	202
5	Summary and Conclusions	214
6	References	225
7	Appendix A	233
8	Appendix B	243
9	Appendix C	257
10	Appendix D	275

Chapter 1

Introduction

1.1 Basic Concepts and Phenomena in Disordered Magnets

In 1972, Cannella and Mydosh (1972) noticed a cusp in the a.c. susceptibility of a dilute AuFe alloy. Since then a fascinating new topic—spin glasses—emerged in condensed matter physics. The mid-1970's to mid-1980's, was a very fruitful period for spin glass research, both in theory and experiment. Hundreds of papers per year were written on spin glasses, and the most important models and theoretical concepts were constructed. The experimental phenomena were explained reasonably well. After that, the tempo slowed down and a tranquility appeared, with more sophisticated theories, subtle new experiments and the identification of 'ideal' spin glass materials. "Spin glasses" are still an active, frontier topic in physics. The theory is evolving towards a more complete description, with newer ideas. Experimentation is continuing with investigations of novel forms of spin glasses and even more subtle effects. Spin glass theory has had a rather large and unexpected impact on some problems far from spin glasses themselves. It turns out that a number of problems in fields outside physics share some of the essential features – randomness and frustration – that characterize spin glasses. This

is especially true of the particularly novel concepts of mean field theory: broken ergodicity is a fundamental concept and broken replica symmetry may be a basic tool for analysing complex systems. There is a richness of analogies with many other areas extending from astrophysics to molecular evolution to zoology (Stein 1992; Mezard and Parisi 1985, 1986; Orland 1985).

Now, the spin glass has become a fundamental and general form of magnetism; in its frequency of occurrence as a 'magnetic ordering' phenomenon, it occupies the third place, after ferromagnetism and antiferromagnetism. Randomness, frustration, glassiness and amorphousness represent very important phenomena in contemporary physics.

What is a spin glass, and what are the necessary ingredients to form a spin glass state? The simplest answer is that a spin glass is a collection of spins (i.e. magnetic moments) whose low-temperature state is a frozen disordered one without the kind of long range uniform or periodic pattern observed in conventional ferro- and antiferromagnets. To create a disordered magnetic system which exhibits spin glass characteristics, two ingredients are necessary: randomness of interactions between the magnetic moments and competition among the different interactions. It follows that no single configuration of the spins is uniquely favoured by all the interactions, and this is commonly called 'frustration'.

As an example, Figure 1.1 shows two magnetic clusters. In both (a) and (b) interactions are random between the randomly distributed magnetic moments. The exchange interaction constant J may be either positive or negative between moments as shown in the figure. In (a), the configuration has no competition or in other words, it is unfrustrated, all the bond energies are satisfied and there will only be a two-fold degenerate ground state. This latter arbitrariness is caused by the initial choice of the first spin direction. But in (b), only one is negative, and in this case all the bond energies cannot simultaneously be satisfied. One spin

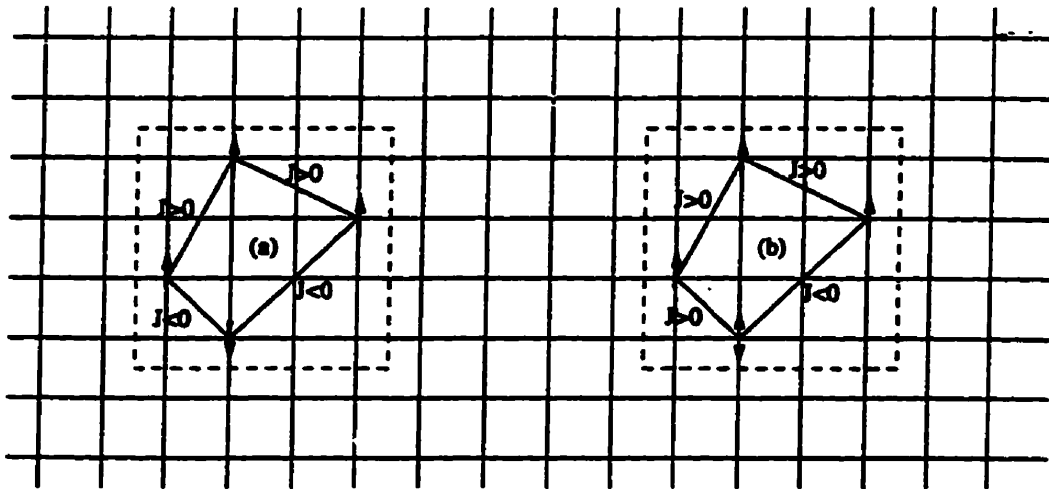


Figure 1.1: Two spin clusters on a lattice with mixed interactions: $j > 0$ means ferro- and $j < 0$ means antiferromagnetic interaction. (a) unfrustrated, which is two-fold degenerate and (b) frustrated, which is 8-fold degenerate energy state.

remains frustrated, or one bond is broken, no matter what we do. Now the cluster has an 8-fold degenerate state (any spin could be the one with frustration). So the frustration will cause more possible configurations with the same energy.

To create randomness, we can randomly distribute the magnetic species substitutionally on a non-magnetic host lattice. Fortunately, nature already provided us with this kind of magnetic alloy even before the name spin glass was coined. They are composed of magnetic impurities bearing a moment or localized spin and randomly occupying lattice sites in a non-magnetic host metal. Spin glasses were accidentally discovered by studying such binary alloys. Here we want to control the concentration x of these impurities so that they can interact with each other in a random way. The host can be just about any non-magnetic metal that dissolves the 'good moment' elements such as Mn, Fe, Gd, Eu, etc. The archetypal specimens of the metallic site-random spin glasses are $\underline{\text{Cu}}_{1-x}\text{Mn}_x$ and $\underline{\text{Au}}_{1-x}\text{Fe}_x$ (the underlined metal is the host). These noble-metal alloys are also called canonical spin glasses.

For a spin glass system, when the temperature goes from a high temperature to a low temperature, it will undergo a glassy phase transition at a freezing temperature T_f . For above this temperature, the system is an ordinary paramagnet, and it is simply a collection of paramagnetic spins, i.e., independent and rapidly rotating arrows in the 'chaos' caused by the high temperature. When the temperature is lowered from $T \gg T_f$, many of these randomly positioned and freely rotating spins build themselves into locally correlated units or clusters, even domains, which can then rotate as a whole. As the temperature disorder is further removed, the various spin components begin to interact with each other over a longer range. The system seeks its ground state configuration for the particular distribution of spins and exchange interactions. This means a favourable set of random alignment axes, generated by the local anisotropy, into which the spins or clusters can lock. However, the frustration plays its role and a multi-degenerate

array of ground states presents itself for the system to choose from. For such disordered systems there are many metastable configurations which are possible, and which may “trap” the system.

To study freezing or phase transitions, the best quantity to measure is the frequency-dependent susceptibility. Usually the ac susceptibility is measured in a very small biasing dc-field (< 1 Oe). But by using highly sensitive SQUID techniques we can also measure the static magnetization in a very small applied field. As $H \rightarrow 0$, there must be a similarity between the dc susceptibility $\chi_{dc} = M/H$ and the ac susceptibility $\chi_{ac} = dM/dH$. There are two distinct ways to measure the susceptibility with a dc field: field cooling (FC) and zero-field cooling (ZFC). In FC measurements, we apply the field above T_f and cool the sample in this field to $T \ll T_f$, and record the magnetization (or heat the sample from $T \ll T_f$ to $T \gg T_f$, and record the magnetization). The FC curve is reversible. In ZFC measurements, we cool the sample in zero field from $T \gg T_f$ to $T \ll T_f$, and apply the field at this low temperature, then we heat the sample and measure $M(t)$ to $T \gg T_f$ in this constant field. When we measure the ZFC curve, χ_{ZFC} is unstable and always drifts upwards towards χ_{FC} . Figure 1.2 shows the FC and ZFC curves for $\chi(t)$ for two different concentrations of CuMn. At temperatures below the peak, the FC curve is reversible, while the ZFC curve is irreversible. The peak in χ_{ZFC} and the plateau in χ_{FC} reveal the onset of the glassy transition at $T = T_f$.

At small fields $H < 100$ Gauss, this peak in χ_{ZFC} is well defined. When the applied field is increased, the ZFC curve relaxes to the FC curve very fast. It seems that the field removes the criticality of the phase transition, yet it does not fully prevent the formation of the frozen state. In order to avoid all the complications with relaxation and irreversibility, a good experiment to perform is the FC measurement. For certain canonical spin glasses, a small peak and then a

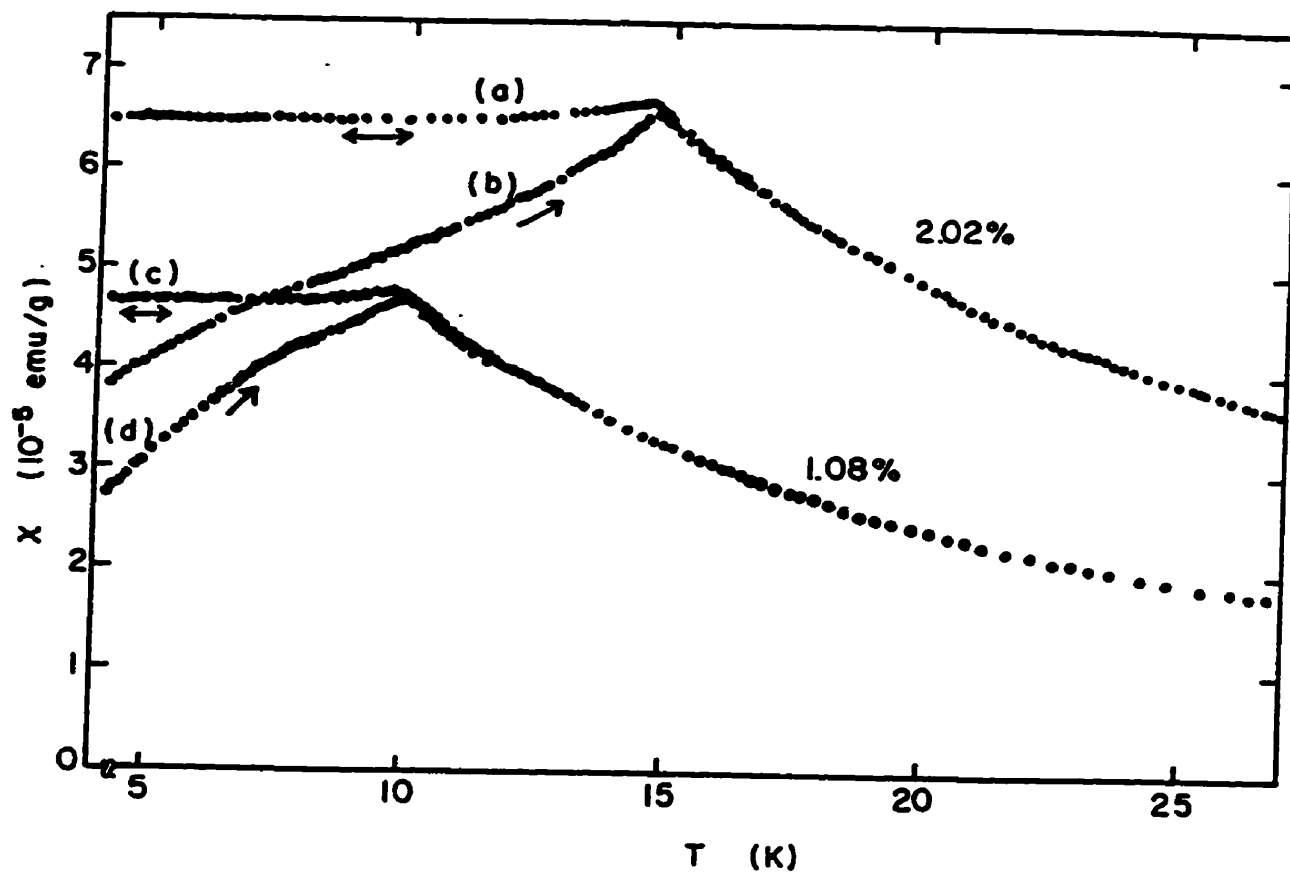


Figure 1.2: Field cooled [(a),(c)] and zero-field cooled [(b),(d)] magnetizations ($\chi \equiv M/H$, $H = 5.9$ gauss) for CuMn (1.08 and 2.02 at%Mn) as a function of temperature. Initial susceptibility of (b) and (d) were measured with increasing temperature in the field. From Nagata et al. (1979).

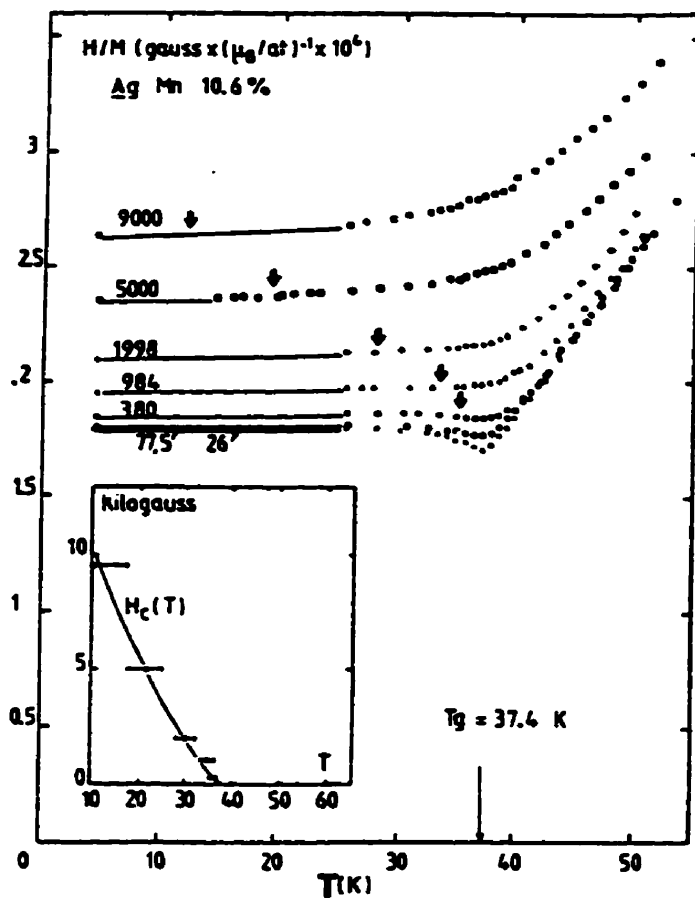


Figure 1.3: Inverse of the FC-susceptibility (H/M) for AgMn (10.6 at%) as a function of temperature for various magnetic fields (indicated on each curve in gauss). Data were obtained by slow cooling in a constant field. The onset of the 'plateau' (marked by arrows) is taken arbitrarily as the point of the $M(T)$ curve departing by 3% from its low-temperature value thereby defining T_f . The resulting boundary of the spin-glass phase $H_c(T)$ is shown in the inset. T_g is the zero field value of T_f . From Monod and Bouchiat (1982).

plateau develops at T_f . Figure 1.3 is a plot of the inverse magnetization divided by the cooling field (H/M) versus the temperature. At small fields, the inverted cusp denotes T_f . However, the peak rapidly disappears with increasing field. Now we must use the onset of the plateau to establish T_f , as shown by the arrows. These points not only shift downward in T with increasing H , but become much more diffuse. An estimate of T_f is given in the inset of the figure where an $H - T$ phase diagram is attempted, albeit with large error bars. At large fields T_f is simply not well defined.

1.2 Spin Glass Systems

So, a spin glass is a random, mixed–interaction magnetic system characterized by a temperature T_f below which a highly irreversible, metastable frozen state occurs without the usual long-range magnetic order. The random-interactions could be achieved by the **random-site** occupancy of the alloys, as mentioned above, in which the magnetic impurities are randomly distributed in a non-magnetic metal host, or by creating **random-bond** types of systems. The latter was found to exist only recently in real materials, e.g. the compounds $\text{Rb}_2\text{Cu}_{1-x}\text{Co}_x\text{F}_4$ and $\text{Fe}_{1-x}\text{Mn}_x\text{TiO}_3$ were discovered to give reasonable approximations of $\pm J$ couplings (Mydosh, 1993). Suffice it to say, there must be disorder in the constitution of a spin glass: either **site randomness** with a distribution of distances between the magnetic spins, or **bond randomness** where the nearest-neighbour interaction varies between parallel coupling $+J$ and antiparallel coupling $-J$.

1.2.1 RKKY Spin Glasses

If a magnetic alloy shows spin glass behavior, usually the concentration of the impurities is very low and the spins cannot interact with each other directly.

The mechanism of the interaction is **indirect** and induced by the conduction electrons, which is the now famous Ruderman, Kittel, Kasuya, Yosida (RKKY) interaction whose Hamiltonian is $\mathcal{H} = J(r) \mathbf{S}_i \cdot \mathbf{S}_j$. A local moment with spin \mathbf{S}_i polarizes the host's conduction electrons in its neighborhood, which will cause a damped oscillation in the response of the conduction electrons. These oscillations will influence the orientation of the second magnetic moment \mathbf{S}_j , and thereby cause a coupling between spins \mathbf{S}_i and \mathbf{S}_j with coupling constant:

$$J(r) = 6\pi Z J_0^2 N(E_F) \left[\frac{\sin(2k_F r)}{(2k_F r)^4} - \frac{\cos(2k_F r)}{(2k_F r)^3} \right] \quad (1.1)$$

where Z is the number of conduction electrons per atom, J_0 is the s-d exchange constant, $N(E_F)$ is the host density of states at the Fermi level, k_F is the Fermi momentum and r is the distance between two impurities. This reduces to

$$J(r) = \frac{J_0 \cos(2k_F r + \phi)}{(2k_F r)^3} \quad (1.2)$$

at large distances. A phase factor ϕ is included to account for the charge difference between impurity and host and the former's angular momentum. Such oscillatory behavior of $J(r)$, or really the Pauli susceptibility, which in the free-electron model has spherical symmetry, is illustrated by the two coupling schemes in Figure 1.4.

Notice that the $(1/r)^3$ fall-off is sufficiently long-ranged so that it can effectively reach a number of near-neighbour sites. Now if a second magnetic impurity with spin \mathbf{S}_j is put at one of the neighbouring sites, it will produce its own RKKY polarization. The two conduction-electron-mediated polarizations will overlap in such a way as to establish a parallel or an antiparallel alignment of the two spins. Figure 1.4 plots the Pauli susceptibility of the conduction electrons to show these situations. Note that the sign ($+ = \uparrow\uparrow$ and $- = \uparrow\downarrow$) of the impurity coupling varies with distance. If we combine this property with site disorder (various separations between the spins), we have generated a random distribution of coupling strengths

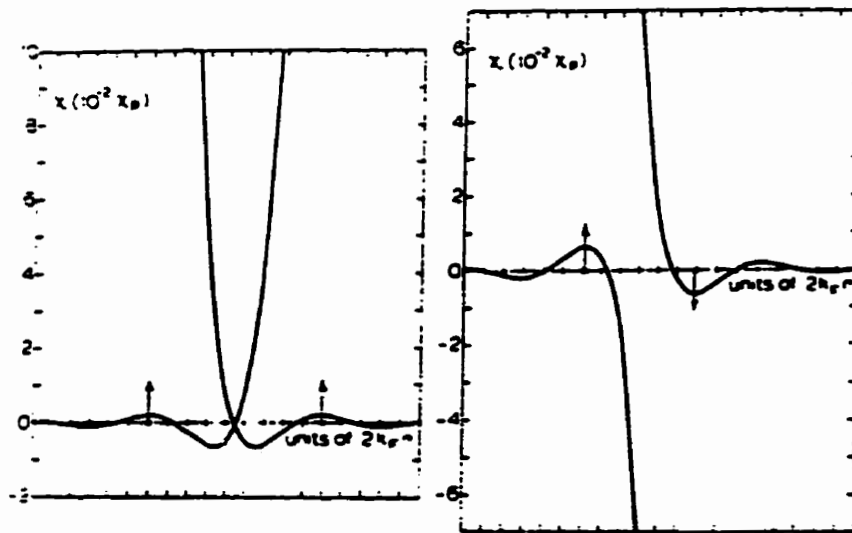


Figure 1.4: RKKY interaction between two impurities in terms of the Pauli susceptibility χ_p . From Mydosh (1993).

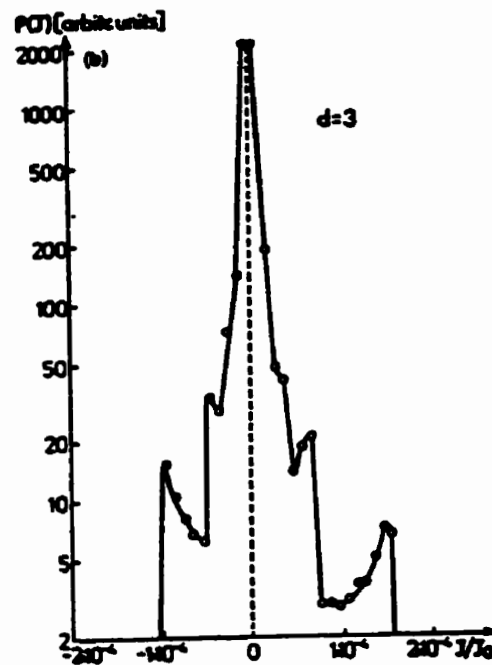


Figure 1.5: Computer simulation of probability distribution of coupling strengths for about 10^3 spins resulting from an RKKY interaction in a 3-dimensional dilute magnetic alloy. From Binder and Schröder (1976).

and directions. Figure 1.5 shows the probability function $P(J_{ij})$ from a computer simulation for some bonds J_{ij} coupling a random-site magnetic alloy. The number of + and - bonds is nearly symmetric. Here the required feature of 'competition' among ferro and antiferromagnetic exchange bonds is obtained in a natural way, namely via the oscillating RKKY interaction. This is why the whole spin-glass problem started with magnetic alloys. We must once again emphasize that it is the combination of site disorder and the + and - RKKY interactions that causes a mixture of competitive bonds that will eventually lead to frustration in some of these bonds.

RKKY spin glasses are alloys which usually consist of noble metal hosts with transition metal impurities, like CuMn , AuFe etc, and transition metal/transition metal combinations like PdFe etc, which has the strongest coupling. Many, many hundreds of these kinds of combinations can be fabricated in the laboratory. RKKY alloys can also be fabricated from magnetic rare-earth elements by diluting them into a non-magnetic host metal and letting the RKKY interaction perform its coupling. This kind of alloy does not have a Kondo effect, that is a localized antiferromagnetic interaction of an isolated or single-impurity spin with the surrounding conduction electrons (Mydosh 1993), and usually has a limited solubility.

An amorphous compound without crystallographic order (that is, so-called natural site randomness) can also be an RKKY spin glass. There are many combinations of these systems with a single magnetic species of a transition metal. These compounds are formed by melt-quenching or splat-cooling and sputtering techniques. As they are non-crystalline, it is possible to make any desired amounts of ferro- and antiferromagnetic exchange in any ratio and absolute magnitude. But amorphous spin glasses, with their higher resistivity, will dampen the range of the RKKY interaction.

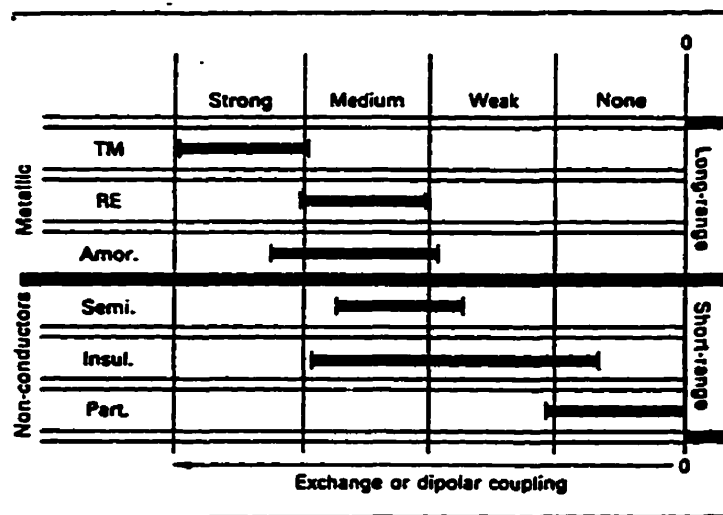
1.2.2 Insulating and Semiconducting Spin Glasses

Besides the RKKY magnetic interaction in disordered magnetic systems, a superexchange interaction also exists which can yield a spin glass state. In insulating or semiconducting materials, since there are no conduction electrons, a sort of covalent mixing of p and d (or f) wave functions occurs. Some lead to parallel spins, like $p-d$, $d-f$ and $p-f$. Some lead to antiparallel configurations, like $p-p$, $d-d$ and $f-f$. So, if randomly spaced, the parallel or antiparallel orientations between the magnetic spins will result in the competing interactions which will form the spin glass state.

In addition to the above two interactions, **dipolar** and **magnetic anisotropy** in small particle materials can also be present in a spin glass but they are the weakest interactions. (Vincent et al. 1996). Table 1.1 is a list of the different interactions and their strengths.

Table 1.1: Strengths of differently coupled random magnetic systems.

From Mydosh (1993).



Exchange or dipolar coupling

TM = CuMn, AuFe, PtMn, etc.
 RE = LaGd, (YGd)Al₂, (CeGd)Ru₂, etc.
 Amor. = α-(FePd)₁₀₀, Fe₂, α-FeSn etc.
 Semi. = (EuSr)S, CdMnTe etc.
 Insul. = (MgFe)Cl₂, ZnFeF₂, α-CoO·Al₂O₃·SiO₂ etc.
 Part. = CoO, α-(Ho₂O₃)(B₂O₃), etc.

1.3 Relaxation and Aging in Disordered Magnetic Systems

Relaxation and aging effects in disordered magnets were first observed by Lundgren et al.(1983), and were then studied extensively. The aging experiments can be performed in two ways: one is to quench the sample from a reference temperature $T_R > T_c$ (the critical temperature, the same as T_f for a spin glass) in a magnetic field h to $T_m < T_c$, wait a certain length of time t_w at constant T_m and h , and then remove the field h and measure the decay of the magnetization $M(t)$ versus the measuring time t . Another way is to quench the sample from $T_R > T_c$ in zero magnetic field $h = 0$ to $T_m < T_c$, wait a certain length of time t_w , and then apply the magnetic field $h \neq 0$ and measure the magnetization $M(t)$ versus t . In both cases, the magnetization has an inflection point around $t = t_w$ which is a direct manifestation of the nonequilibrium nature of the state in which the system found itself at the end of the wait time t_w . The inflection time is just equal to the “aging” or wait time t_w (Lundgren et al., 1983). This is why this is known as an aging effect.

Figure 1.6 shows relaxation measurements for three different wait times $t_w = 300$ s, 1000 s, and 3000 s, on an amorphous sample of $(\text{Fe}_{0.15}\text{Ni}_{0.85})_{75}\text{P}_{16}\text{B}_6\text{Al}_3$. The effect of aging is seen as an inflection point on a $\log t$ scale at $t \approx t_w$, in figure (a), and in figure (b) which shows the relaxation rate $S_{ZFC}(t_w, t) = \partial M_{ZFC} / \partial \log t$, there is a corresponding maximum at $t \approx t_w$.

The aging effect is very field dependent. If we apply a different field, or perform a field step change during the aging period, the aging effect is different or the memory of the aging process may be partially destroyed or completely eliminated. Figure 1.7 is a plot of $S_{ZFC}(t_w, t)$ vs. $\log t$ for different magnetic fields h , at $T = 16.3$ K and $t_w = 300$ s, for the same sample as in Figure 1.6. We can see

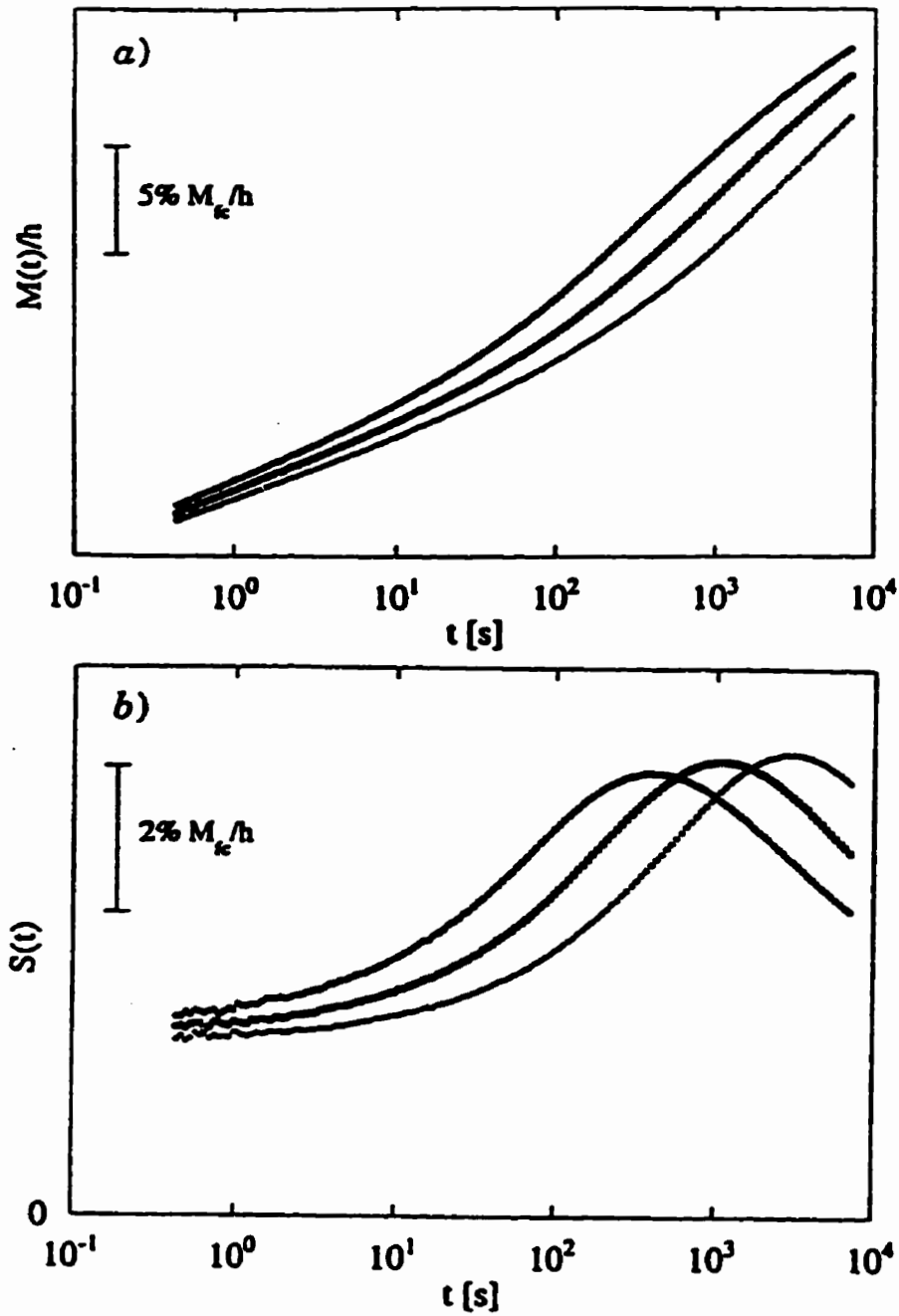


Figure 1.6: Relaxation of the zero-field-cooled magnetization at $T = 16.3$ K and different wait times t_w : from top to bottom $\circ t_w = 300$ s, $\square t_w = 1000$ s, $\diamond t_w = 3000$ s. a) M_{ZFC}/h vs. $\log t$. b) Relaxation rate $S = 1/h (dM_{ZFC}/d\log t)$ vs. $\log t$. $h = 0.1$ Oe. From Djurberg (1995).

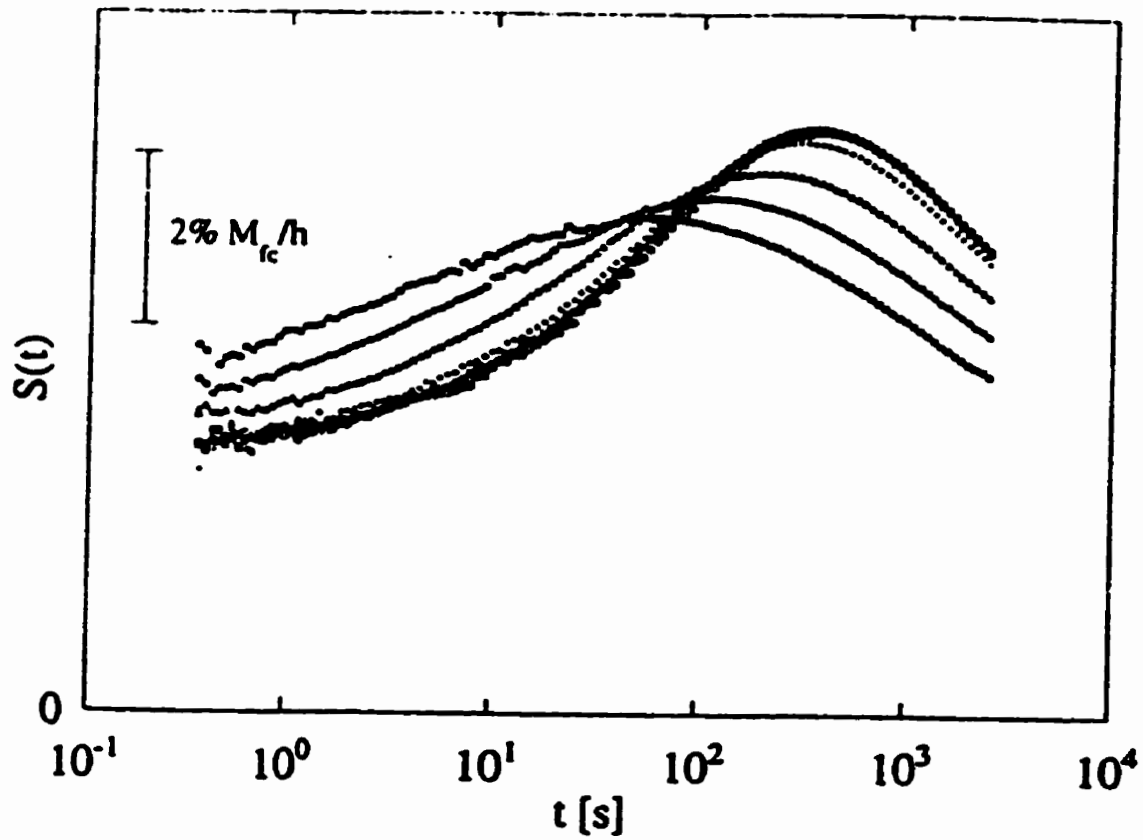


Figure 1.7: Relaxation rate $S_{ZFC} = (1/h)dM_{ZFC}/d\log t$ vs. $\log t$ at different fields h (Oe): from bottom to top (l.h.s) \circ 0.3, \square 0.5, \diamond 0.8, \times 1.0, $+$ 2.0, \triangle 4.0, \bullet 6.0, \blacksquare 8.0. $T = 16.3$ K, $t_w = 300$ s. From Djurberg et al. (1995).

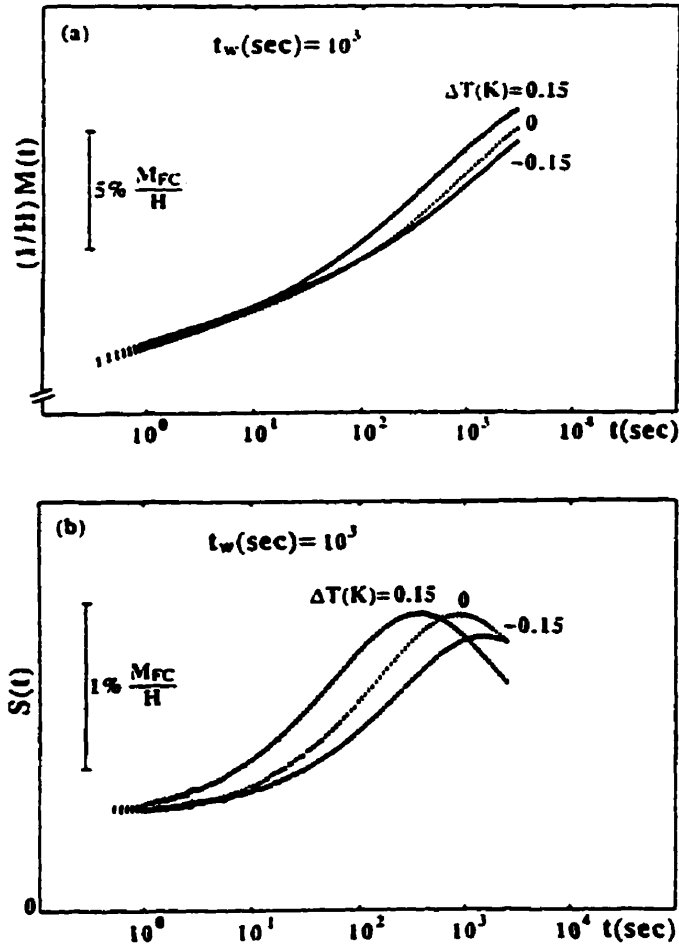


Figure 1.8: Zero-field-cooled susceptibility $(1/H)M(t)$ and the corresponding relaxation rate $S(t) = (1/H)\partial M/\partial \ln(t)$ at $t_w = 10^3$ sec, plotted vs. $\log_{10}(t)$. The sample has been aged below ($\Delta T = 0.15$ K) and above ($\Delta T = -0.15$ K) the measurement temperature. Also plotted is a conventional ($\Delta T = 0$ K) ZFC curve. $T_m/T_g = 0.91$, $H = 0.8$ G. (a) $(1/H)M(t)$, 5% of $(1/H)M_{FC}$ indicated. (b) $S(t)$, 1% of $(1/H)M_{FC}$ indicated. From Granberg et al. (1988).

that at low fields, $h < 1$ Oe, the response does not depend on field: for larger fields the curves become field dependent, and deviate from the linear low-field response. The relaxation rate then typically increases at short times and the maximum, originally at $t \approx t_w$, is shifted towards shorter observation times.

Another interesting experiment involves a temperature fluctuation before the measurement, performed near the measurement temperature T_m . Temperature shifting ($T_R \rightarrow T_m - \Delta T < T_f$, age for t_w , $T_m - \Delta T \rightarrow T_m$) and temperature cycling ($T_R \rightarrow T_m < T_f$, age for t_w , $T_m \rightarrow T_m + \Delta T \rightarrow T_m$) will also influence the aging process. Figure 1.8 shows temperature shifting results on a sample of Cu-10 at %Mn: a positive temperature shift ($\Delta T = 0.15$ K) yields a relaxation curve characterized by an apparent wait time $t_{w_{app}} < t_w$ and a negative temperature shift ($\Delta T = -0.15$ K) yields a relaxation curve characterized by an apparent wait time which is longer than t_w , $t_{w_{app}} > t_w$ (Granberg et al. 1988).

The aging effects which are observed under various circumstances and the corresponding theories proposed to explain them are most interesting topics which will be the principal focus of this thesis.

1.4 Relaxation and Aging Behavior in Other Complex Systems

Anomalous relaxation behavior and aging effects are common features in all complex systems (Struik 1978; Jäckle 1986). A collection of conference papers in RELAXATIONS IN COMPLEX SYSTEMS (edited by Ngai and Wright, 1991.) gives a detailed study of the relaxations in a variety of materials. Here I will give two typical examples, polymers and window glass, to show the similar behaviour to that observed in disordered magnetic systems.

Figure 1.9 is a volume-temperature relation between the crystal, liquid and

glass states in a super cooled liquid. On cooling a liquid from the initial state A, the volume will decrease steadily along AB. If the rate of cooling is slow, and nuclei are present, crystallization will take place at the freezing temperature T_f . The volume will decrease sharply from B to C, and thereafter, the solid will contract with falling temperature along CD. If the rate of cooling is sufficiently rapid, crystallization does not take place at T_f , and the volume of the supercooled liquid decreases along BE, which is a smooth continuation of AB. At a certain temperature T_g , the volume-temperature graph undergoes a significant change in slope and continues almost parallel to the contraction graph CD of the crystalline form. T_g is called the glass transformation or glass transition temperature. Only below T_g is the material a glass. The location of E, the point corresponding to T_g , varies with the rate of cooling, and thus it is appropriate to call it a transformation *range* rather than a fixed point. At T_g the viscosity of the material is very high, about 10^{13} poise.

If the temperature of the glass is held constant at a little below T_g , the volume G will continue to decrease slowly. Eventually it reaches the level G' on the dotted line, which is a smooth continuation of the contraction graph BE of the supercooled liquid. If we perform relaxation experiments on physical and mechanical properties, for example torsional stress, the resulting slow relaxation in the glass phase does not have a simple exponential form.

Figure 1.10(a) is the relaxation function $\Phi(t)$ for torsional stress relaxation in a soda-lime-silica glass at different temperatures below T_g . The relaxation function $\Phi(t)$ has a *stretched exponential* form

$$\Phi(t) \propto \exp[-(t/\tau_0)^\beta], \quad 0 < \beta < 1 \quad (1.3)$$

This function can be applied rather universally to a very broad class of materials (Ngai and Wright, 1991). By using the time-temperature scaling principle (Ferry, 1980), the relaxation curves at different temperatures fall on a single “master

curve", which is shown in Figure 1.10(b).

The aging effect in polymers is another example. Figure 1.11 is the experimental procedure to study the aging effects on the small-strain creep properties of a polymer. The tested sample was usually first annealed to reduce any internal stresses generated by earlier compression molding or extrusion operations. The sample to be examined is placed in the creep tester, and subjected to the thermal treatment. First, the sample is heated to a temperature T_0 , 10-15 °C above the glass temperature T_g . A period of 10-20 minutes at T_0 suffices for the establishment of thermodynamic equilibrium. Next, the sample is quenched to a temperature T_1 below T_g , and kept at this temperature. The quench takes a few minutes. When a certain time t_e has elapsed after the quench, a creep test is started. The sample is subjected to a constant stress σ_0 ; the resulting strain ϵ is measured as a function of time t , with $t = 0$ defined at the moment of loading.

Figure 1.12 shows the aging effects in this test of a PVC (polyvinylchloride) sample of about $1 \times 10 \times 20$ mm³ at small strains. The most important features of the results are: (i) Aging produces nearly horizontal shifts of the creep curves, without large changes in shape. Thus, aging primarily affects the rate of creep. (ii) In certain temperature ranges below T_g , the creep rate increases by a factor of about 10 per tenfold increase in aging time.

Both the relaxation behavior in soda-lime-silica glass and the aging effects in polymers can be explained by the Williams, Landel and Ferry (WLF) (1955) free volume picture, in which the rate change is not primarily due to thermal activation but rather to *thermal expansion* (Kovacs, 1963). The characteristic time τ of the expansion of the free volume v_f is very dependent on T . As long as T is high, the free volume is large and τ is small, thus the thermal contraction of v_f can follow the cooling process. At T_g , the relaxation time becomes so long that the changes in v_f can no longer keep up with the cooling process. To a first

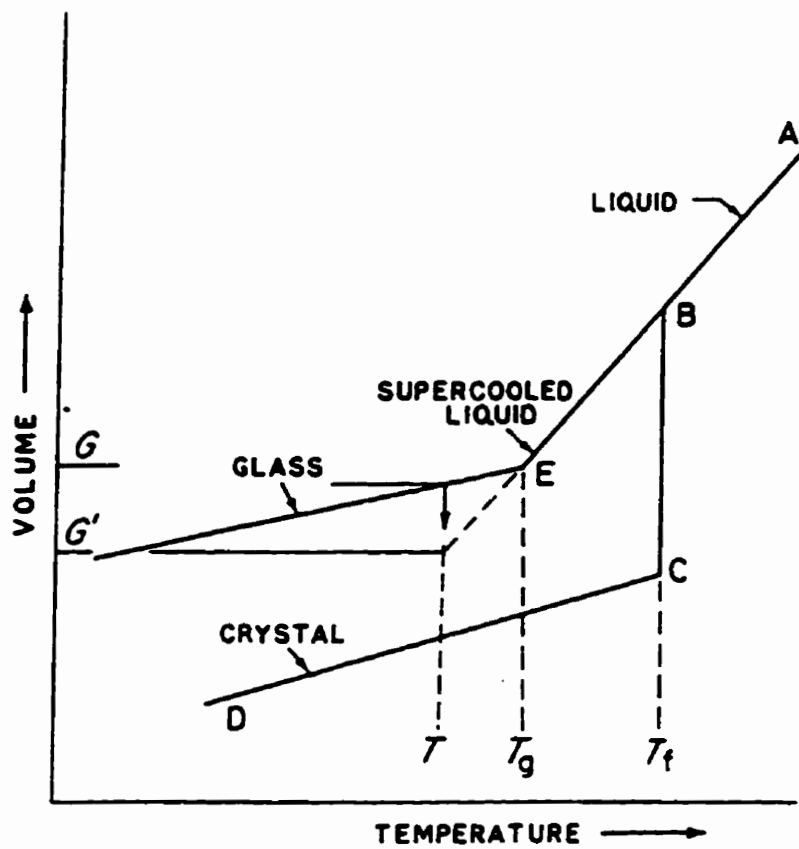


Figure 1.9: Relationship between the glassy, liquid and solid states. From Paul (1982).

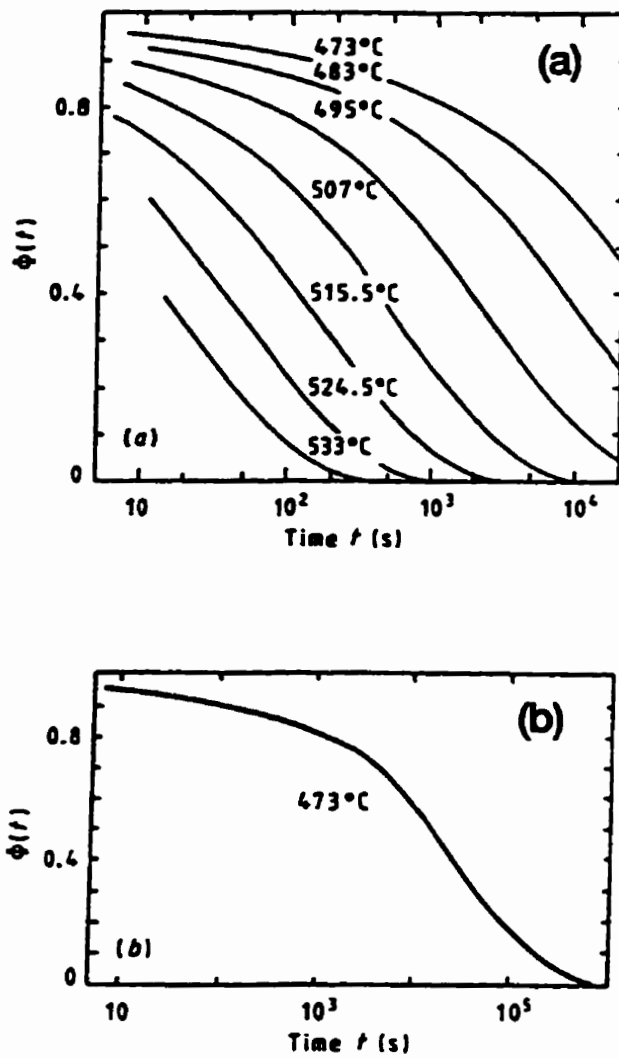


Figure 1.10: (a) Relaxation function $\Phi(t)$ for torsional relaxation in a soda-lime-silica glass at different temperatures. (b) Master curve $\Phi(t)$ at 473 °C produced by time-temperature scaling. From Jäckle (1986).

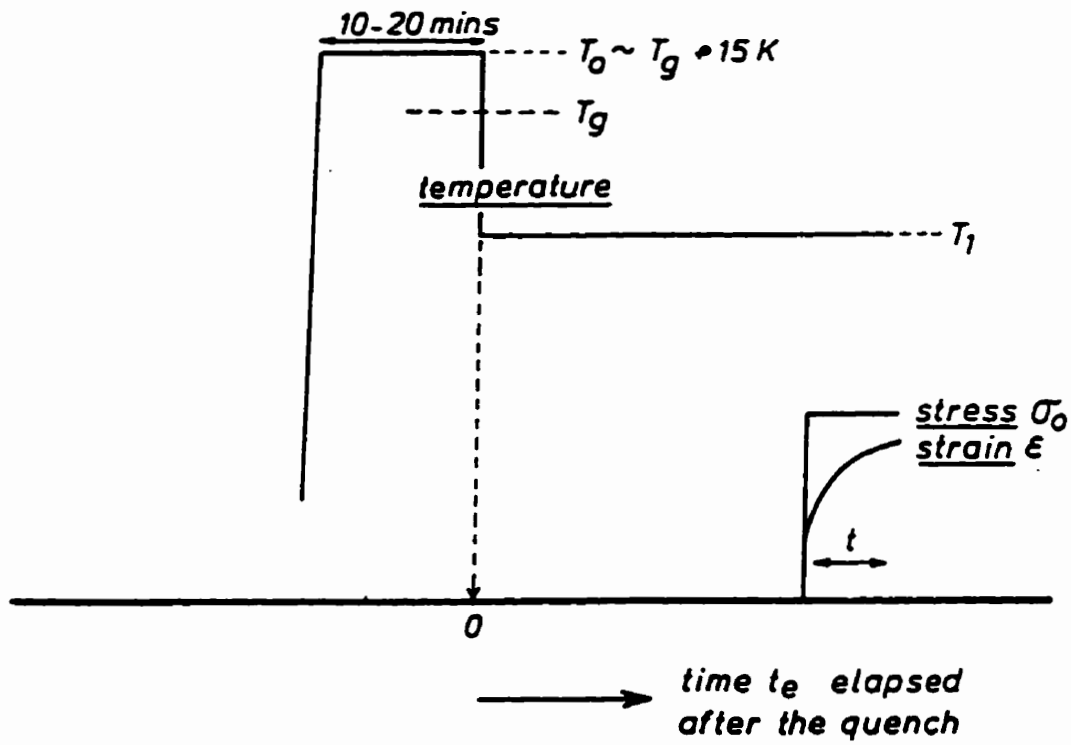


Figure 1.11: Outline of the procedure for measuring aging effects. From Struik (1978)

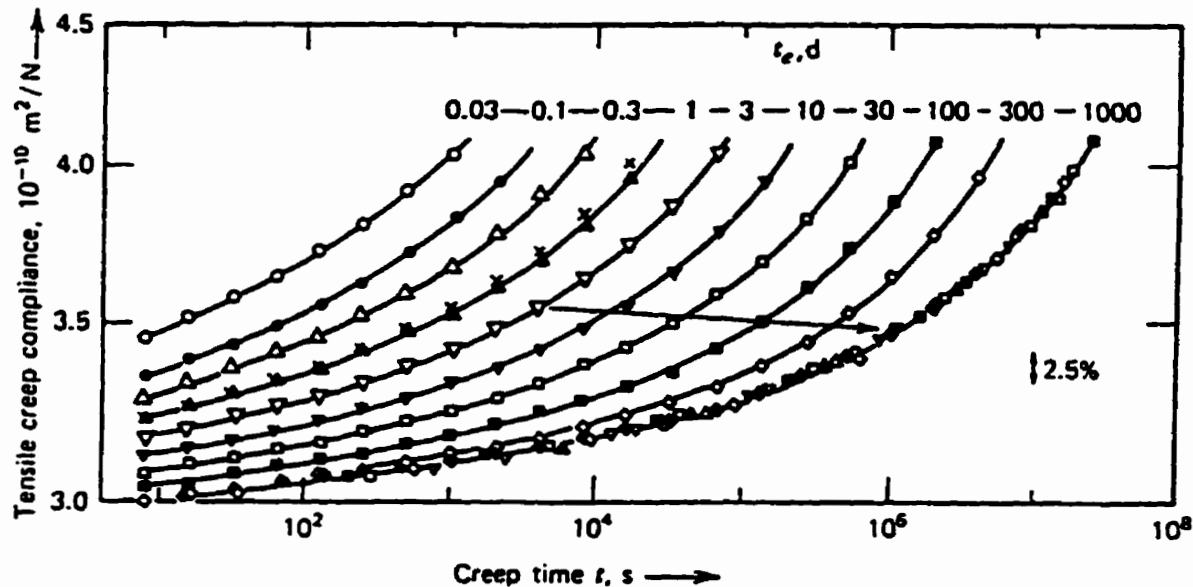


Figure 1.12: Small-strain tensile creep curves of a rigid PVC quenched from 90 °C (i.e. 10 °C above T_g) to 20 °C and kept at 20 ± 0.1 °C for a period of 4 years. The different curves were measured for various values of the time, t_e , in days, elapsed after the quench. The master curve at $t_e = 1000$ days gives the results of a superposition by shifts which were almost horizontal; the shifting direction is indicated by the arrow. The crosses on the $t_e = 1$ day curve were found when, after 1000 days of aging, the sample was reheated to 90 °C, requenched to 20 °C, and remeasured for a t_e of 1 day; they show that the aging is thermoreversible as it should be (on reheating to above T_g the material reaches the equilibrium state, i.e. all history is forgotten). From Struik (1991).

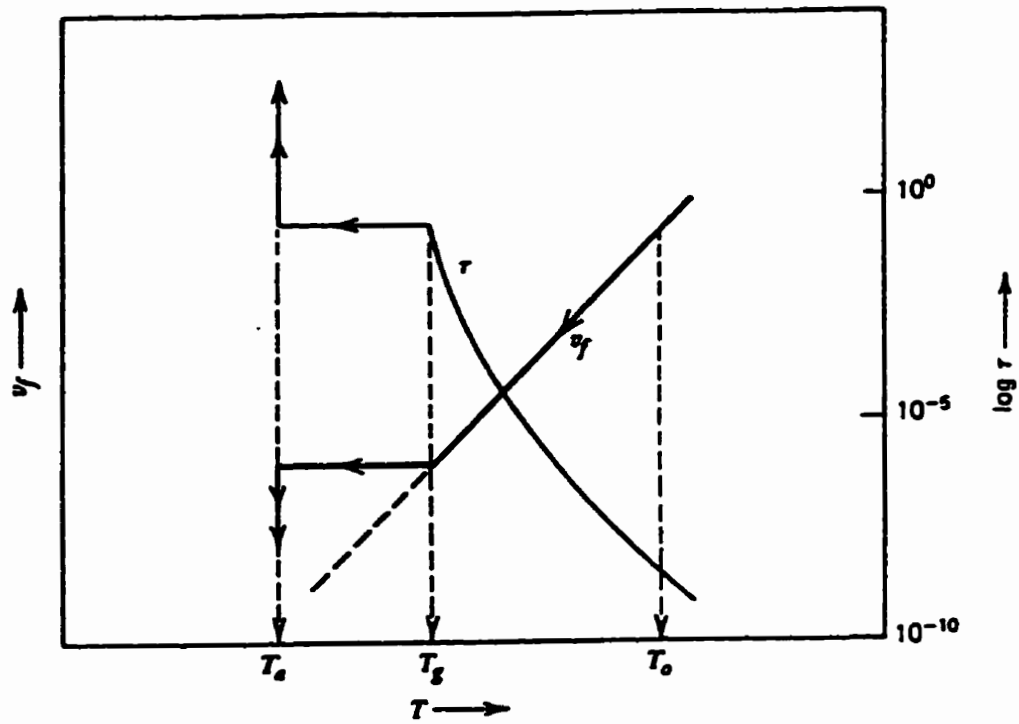


Figure 1.13: Change in free volume v_f and relaxation time τ during rapid cooling from $T_0 > T_g$ to $T_a < T_g$ and subsequent isothermal aging at T_a . The time units on the τ -scale are arbitrary; the heavy dashed line is the supposed equilibrium for v_f below T_g . From Struik (1991).

approximation the volume v_f at T_g is frozen-in and v_f no longer decreases during further cooling from T_g to T_a (Figure 1.13). If the WLF ideas can be applied to the range below T_g , we can expect a similar change in τ during cooling above T_g and a constant value of τ during further cooling from T_g to T_a . This ignores the small changes of v_f during cooling from T_g to T_a .

After the cooling, if the material is kept at a constant temperature T_a below T_g , the free volume is higher than it should be and the relaxation time τ is not large enough, and consequently v_f will slowly decrease towards the equilibrium line. Now we apply the free-volume picture to the non-equilibrium state below T_g . It then immediately follows that the volume contraction will be accompanied by a change in τ . In other words, the slow decrease in v_f will be accompanied by a gradual increase in τ . This implies that the 'stiffening' process seen during cooling through the T_g -range simply continues. All properties which depend on τ and strongly change around T_g will continue to change during the isothermal stay at T_a . This process is named *physical aging*.

In spin-glasses and reentrant ferromagnets, the situation is much more complicated. The relaxation curves at the different temperatures and different wait times can not be scaled by simply shifting the time scale. Many theories and experiments have been proposed to explore these phenomena. In the next chapter I will focus on the theories of spin glasses and their dynamics, with an emphasis on the physical explanations.

Significance of my research: The systems described above all exhibit anomalous relaxation dynamics, that is, not a simple Debye form $e^{-t/\tau}$, and an understanding of the physical mechanisms underlying these dynamics has important implications for the general problem of relaxation in complex systems, like glasses and polymers. In fact, the dielectric, mechanical, and magnetic properties of ordinary glasses, amorphous polymers, random magnets, ferroelectrics, super-

cooled liquids, and high- T_c superconductors all exhibit non-Debye response to a step-function excitation, as well as non-equilibrium aging effects.

Chapter 2

Theory

In this chapter I will introduce the fundamental theories of spin glasses and some of the current dynamic theories for relaxation and aging.

2.1 Basic Concepts

Averaging in disordered systems:

In ordinary statistical mechanics, if we want to calculate some observable quantity of a system, we usually use ensemble theory, for example the canonical ensemble, to calculate the partition function Z and then calculate the variable. The free energy of the system (Binder and Young, 1986; Fisher and Hertz, 1991) is given by

$$F = -k_B T \ln[Z\{x\}]_{av} \quad (2.1)$$

$$Z\{x\} = Tr_{\{S_i\}} \exp[-\mathcal{H}\{x, S_i\}/k_B T] \quad (2.2)$$

where $\{S_i\}$ are the statistical spin variables and $\{x\}$ are the randomness variables and $[\]_{av}$ means that we average over the different configurations of the random variable x . In this case, the random variables $\{x\}$ come to thermal equilibrium

and the average over x and S are treated on an equal footing. This averaging process is called an *annealed average*. Experimentally, this process requires that the measuring time t_{exp} satisfies $t_{exp} \gg t_{dis}$, where t_{dis} is the corresponding fluctuation time for the random variable among its various microscopic configurations.

In a spin glass, if the system is quenched from above the phase transition (or freezing) temperature T_f to a temperature below T_f , it can be trapped in any one of a large number of metastable states due to the randomness and frustration. The hopping times (or fluctuation times) among these metastable states occupy a very wide time scale, and for some, $t_{dis} \gg t_{exp}$. In this case, we cannot calculate $[Z]_{av}$ and then calculate the variables of the system as in equation 2.1, but we must average the free energy over the various configurations:

$$F = [F\{x\}]_{av} = -k_B T [\ln Z\{x\}]_{av} = -k_B T \int dx P\{x\} \ln Z\{x\} \quad (2.3)$$

instead. This is called a *quenched average*. If we deal with the spin glass problem, we must perform a quenched average.

Broken ergodicity:

When a system undergoes a phase-transition from a disordered state to an ordered state, the symmetry of the system (for example, the translation symmetry) is lowered; this is called *broken symmetry*. Broken symmetry leads to *broken ergodicity*, which means that the ergodic hypothesis that, in equilibrium, the system should be found with the Gibbs-Boltzmann probability $\propto e^{-\beta E}$ in each of its possible configurations, is violated. A ferromagnet with its net magnetization up will never be found in a state with its net magnetization down, in the limit as the number of spins $N \rightarrow \infty$. Its motion is restricted to the part of its configuration space with positive magnetization $M > 0$ only. This is an example where the ergodic hypothesis is satisfied. A spin glass is a state with broken ergodicity (Palmer, 1982).

Spin-glass systems exhibit a “freezing transition” to a state with a new kind of “order” in which the spins are locked in random orientations. The ordered phase is characterized by an order parameter. In ferromagnetic systems, the order parameter is the spontaneous magnetization per site $\mathbf{M} = \frac{1}{N} \sum_i \langle \mathbf{S}_i \rangle_T$. What is the order parameter for a spin glass? To describe the “order” in a spin glass, several order parameters have been defined:

(a) **Edwards and Anderson order parameter** q_{EA} (Edwards and Anderson, 1975):

Since there is no long-range order, order parameters based on spatial correlations are useless, and Edwards and Anderson focused on time correlations. At one observation time t_0 , a particular spin is $\mathbf{S}_i(t_0)$. If it is studied again long time later at $t + t_0$, there is a nonvanishing probability that $\mathbf{S}_i(t + t_0)$ will point in the same direction. Then a time autocorrelation function is defined:

$$q_{EA} = \lim_{t \rightarrow \infty} \langle \langle \mathbf{S}_i(t_0) \cdot \mathbf{S}_i(t + t_0) \rangle_T \rangle_C \quad (2.4)$$

where the inner angular brackets represents a thermal averaging and the outer a configurational C averaging over all spins. When $T = 0$, $q_{EA} = 1$ and when $T \rightarrow T_f$, $q_{EA} = 0$. The parameter then plays the role of the mean field in the Curie-Weiss theory of ferromagnetism. For ergodic systems the local time correlation is identical to

$$q_{EA} = q = \langle \langle \mathbf{S}_i \rangle_T^2 \rangle_C \quad (2.5)$$

So, q_{EA} measures the mean square local spontaneous magnetization, averaged over all configurations.

(b) **Parisi’s overlap order parameter** $q_{\alpha\beta}$ (Parisi, 1983; Mezard et al., 1984):

A disadvantage of q_{EA} is that it is nonzero for a normal unfrustrated ferromagnetic or antiferromagnetic material, as well as for a spin-glass. As we will

see shortly, spin glasses are characterized by a multitude of nearly degenerate pure states, and Parisi defined a new order parameter which is the overlap of the magnetization between two different pure or thermodynamic states:

$$q_{\alpha\beta} = \frac{1}{N} \sum_{i=1}^N \mathbf{m}_i^\alpha \cdot \mathbf{m}_i^\beta \quad (2.6)$$

where, \mathbf{m}_i^α is the thermal average of the magnetization at site i in state α , \mathbf{m}_i^β is the thermal average of the magnetization at site i in state β , and N is the total number of spins. The self-overlap $q_{\alpha\alpha}$ is the Edwards-Anderson order parameter q_{EA} . The two parameters are related by

$$-1 \leq -q_{EA}(T) \leq q_{\alpha\beta} \leq q_{EA}(T) \leq 1. \quad (2.7)$$

Parisi also introduced another parameter $x(q)$

$$x(q) = \int_{-1}^q dq P(q) \quad (2.8)$$

$$P(q) = \sum_{\alpha\beta} P_\alpha P_\beta \delta(q - q_{\alpha\beta}) \quad (2.9)$$

where $P(q)$ is the probability distribution of the $q_{\alpha\beta}$. P_α and P_β are the probabilities that the system is in pure state α and β respectively. So, $x(q)$ is the probability of that two pure states chosen at random have an overlap smaller than q . $x(q)$ is a monotonic and an inverse function, which is obviously defined in the interval 0 to 1. $q(x)$ is a multivalued order parameter for the infinite-range SK spin glass, which I will discuss later.

(c) **Hamming distance** $d_{\alpha\beta}$ (Rammal, 1986):

The Hamming distance is originally a mathematical concept for describing the difference between two binary numbers. It was borrowed to describe the spin

glass problem. It is defined as the fraction of spins that must reorient to convert one pure state to another:

$$d_{\alpha\beta} = \frac{1}{N} \sum_{i=1}^N (\mathbf{S}_i^\alpha - \mathbf{S}_i^\beta)^2. \quad (2.10)$$

So,

$$d_{\alpha\beta} = \frac{1}{N} \sum_{i=1}^N (\mathbf{S}_i^{\alpha 2} + \mathbf{S}_i^{\beta 2} - 2\mathbf{S}_i^\alpha \cdot \mathbf{S}_i^\beta) \quad (2.11)$$

$$= \frac{1}{2}(q_{EA} - q_{\alpha\beta}) \quad (2.12)$$

2.2 The EA Model and The Replica Symmetric Solution

To describe the sudden random freezing of a spin glass at a transition temperature, Edwards and Anderson (EA) (1975) proposed a random bond distribution picture, and a time autocorrelation order parameter q_{EA} .

The Hamiltonian in a 3-dimension random-bond system can still be written in the form:

$$\mathcal{H} = - \sum_{ij} J_{ij} \mathbf{S}_i \cdot \mathbf{S}_j - \sum_i \mathbf{H}_i \cdot \mathbf{S}_i, \quad (2.13)$$

where \mathbf{S}_i and \mathbf{S}_j are the classical spins on sites i and j . J_{ij} is the exchange interaction between the two spins. Edwards and Anderson assumed the distribution of J_{ij} to be a Gaussian function

$$P(J_{ij}) = \frac{1}{(2\pi\Delta^2)^{\frac{1}{2}}} \exp\left(-\frac{J_{ij}^2}{2\Delta^2}\right) \quad (2.14)$$

where Δ is the variance.

Following the procedure discussed above, we first determine the free energy for a fixed configuration of bonds, which is given in terms of the partition function Z by

$$F = -k_B T \ln Z = -k_B T \text{Tr} \left(\exp\left(-\frac{\mathcal{H}}{k_B T}\right) \right). \quad (2.15)$$

We are dealing with a system which has *quenched disorder* as I mentioned in the last section. So, we must average $\ln Z$ over the distribution $P(J_{ij})$, i.e., $\langle \ln Z_i \rangle_C$. Evaluating $\langle \ln Z_i \rangle_C$ is not easy, and EA employed the so-called replica method for the first time to make this possible. Using the relation, $Z^n = \exp(n \ln Z) \approx 1 + n \ln Z$ as $n \rightarrow 0$, we have

$$\ln Z = \lim_{n \rightarrow 0} \left[\frac{1}{n} (Z^n - 1) \right]. \quad (2.16)$$

The average over $\ln Z$ is then

$$[\ln Z \{x\}]_{av} = \lim_{n \rightarrow 0} \frac{1}{n} ([Z^n \{x\}]_{av} - 1) = \lim_{n \rightarrow 0} \frac{\partial}{\partial n} [Z^n \{x\}]_{av} \quad (2.17)$$

The problem left is to average Z^n , which is easier. For positive n , we can express $Z^n \{x\}$, where $\{x\}$ represents the set of bonds describing the disorder, in terms of n identical replicas of the system

$$Z^n \{x\} = \prod_{\alpha=1}^n Z_{\alpha}(x) \quad (2.18)$$

$$= \prod_{\alpha=1}^n \text{Tr} \exp [-\mathcal{H}\{x, S_i^{\alpha}\}/k_B T] \quad (2.19)$$

$$= \text{Tr}_{\{S_i^{\alpha}\} \text{ all } i, \text{ all } \alpha} \exp \left[- \sum_{\alpha=1}^n \mathcal{H}\{x, S_i^{\alpha}\}/k_B T \right] \quad (2.20)$$

where Z_α is the partition function of the α th replica, and the trace is over all spins in all replicas.

The configurational average of $Z^n\{x\} \equiv \langle Z^n \rangle_C$ over the disorder is computed by evaluating the trace

$$\langle Z^n \rangle_C = \text{Tr}_{\{S_i^\alpha\}\{x\}} \exp \left[- \sum_{\alpha=1}^n \mathcal{H}\{x, S_i^\alpha\} / k_B T \right] \quad (2.21)$$

Substituting the Hamiltonian (with $\mathbf{H}_i = 0$ for simplicity) into (2.21) leads to

$$\langle Z^n \rangle_C = \text{Tr}_{\{S_i^\alpha\}\{x\}} \prod_{\langle i,j \rangle} \exp \left[\frac{J_{ij}}{k_B T} \sum_{\alpha=1}^n S_i^\alpha S_j^\alpha \right] dJ_{ij} P(J_{ij}) \quad (2.22)$$

$$\langle Z^n \rangle_C = \sum_{\{S_i^\alpha\}} \int_{-\infty}^{+\infty} \left[\prod_{\langle i,j \rangle} dJ_{ij} P(J_{ij}) \exp \left[\frac{1}{k_B T} \sum_{\langle i,j \rangle} J_{ij} \sum_{\alpha=1}^n S_i^\alpha S_j^\alpha \right] \right] \quad (2.23)$$

The integration is usually performed using a Gaussian form for $P(J_{ij})$. In the mean field approximation, it is assumed that $\langle \langle S_i^\alpha S_j^\beta \rangle_T \rangle_C = 0$, and defining $q = \langle \langle S_i \rangle_T^2 \rangle_C$ the free energy $F(q)$ is calculated, where $q = q_{EA}$ is the Edwards and Anderson order parameter. Using the condition $\partial F / \partial q = 0$, in the limits $T \rightarrow 0$ and $T \rightarrow T_f$, the results (Edwards and Anderson, 1975; Mydosh, 1993) are

$$q(T \rightarrow 0) = 1 - \left(\frac{2}{3\pi} \right)^{\frac{1}{2}} \frac{T}{T_f} \quad (2.24)$$

and

$$q(T \rightarrow T_f) = -\frac{1}{2} \left[1 - \left(\frac{T_f}{T} \right)^2 \right]. \quad (2.25)$$

The susceptibility can be written using the fluctuation–dissipation theorem as

$$\chi(T, H = 0) = \frac{(g\mu_B)^2}{3k_B T} \sum_{i,j} [\langle\langle S_i^2 \rangle_T \rangle_C - \langle\langle S_i \rangle_T^2 \rangle_C] \quad (2.26)$$

Since $\langle\langle S_i^2 \rangle_T \rangle_C = 1$ and $\langle\langle S_i \rangle_T^2 \rangle_C = q$, we get

$$\chi(T, H = 0) = \frac{(g\mu_B)^2}{3k_B T} (1 - q(T)) \approx \chi_{ac}(T). \quad (2.27)$$

Using the limiting results for $q(T)$, we have

$$\chi_{ac}(T \leq T_f) = \frac{(g\mu_B)^2}{3k_B T_f} - O(T_f - T)^2 \quad (2.28)$$

and

$$\chi_{ac}(T \rightarrow 0) = \frac{(g\mu_B)^2}{3k_B T} \left(\frac{2}{3\pi}\right)^{\frac{1}{2}} \frac{T}{T_f} = \text{const} \quad (2.29)$$

which means χ approaches a constant value when $T \rightarrow 0$, and at T_f an asymmetric peak occurs.

So, the EA model elegantly replaces the site disorder and RKKY interactions by a Gaussian exchange bond distribution, and predicts a phase transition at a temperature T_f . Fisher's results (Fisher, 1975) for a quantum spin ($S = \frac{1}{2}$) version of the EA model predict sharp peaks both in the susceptibility and the specific heat, as shown in Figure 2.1. The susceptibility nicely resembles experiment. But the specific heat also has a sharp cusp at T_f , and this is a puzzle compared with the experimental result, which has a very broad peak, and no obvious transition temperature (Brodale et al., 1983)). So, a true mean-field theory for spin glasses is still incomplete.

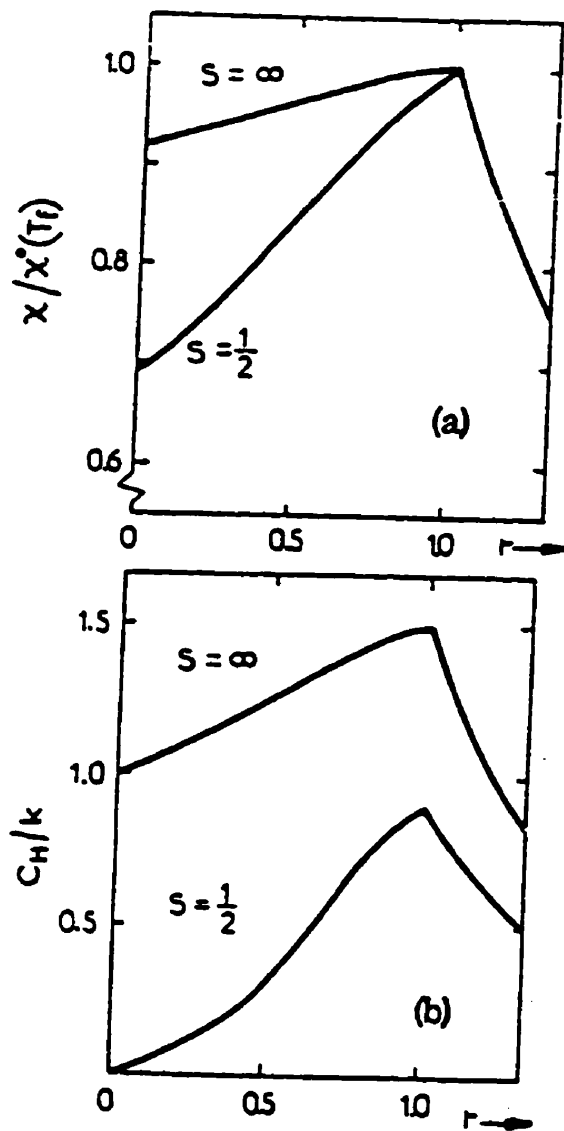


Figure 2.1: (a) Susceptibility and (b) specific heat versus reduced temperature calculated from the EA model for two spin values. From Fisher (1975).

2.3 The SK Model and Parisi's Replica Symmetry Breaking Solution

Sherrington and Kirkpatrick (SK) in 1975 proposed that the proper mean-field theory (MFT) of spin glasses should be the exact solution of an infinite-range EA model. The spins couple equally with each other with the same distribution $P(J_{ij})$ no matter where they are located. The probability distribution of the interactions J_{ij} between each pair ij of spins is taken to be Gaussian

$$P(J_{ij}) = \frac{1}{(2\pi\Delta'^2)^{\frac{1}{2}}} \exp\left[-\frac{(J_{ij} - J'_0)^2}{2\Delta'^2}\right] \quad (2.30)$$

where J'_0 is the mean, and includes the possibility of ferromagnetism, and Δ' is the variance. This assumption might be unphysical, but it is a reasonable description of a long-range disordered system, with RKKY long-range interactions as in these systems. Scaling of Δ' and J'_0 is introduced in order that the thermodynamic quantities be finite in the large N limit, i.e., $\Delta' = \Delta/N^{\frac{1}{2}}$ and $J'_0 = J_0/N$, so the new Δ and J_0 are both intensive. Thus,

$$P(J_{ij}) = \left(\frac{N}{2\pi\Delta^2}\right)^{\frac{1}{2}} \exp\left[-N\frac{(J_{ij} - J_0/N)^2}{2\Delta^2}\right] \quad (2.31)$$

Repeating the 'replica trick', i.e., calculating $\langle Z^n \rangle_C$ instead of $\langle \ln Z \rangle_C$, the free energy is given by

$$F = -k_B T \langle \ln Z \rangle_C = -k_B T \lim_{n \rightarrow 0} \frac{1}{n} (\langle Z^n \rangle_C - 1) \quad (2.32)$$

and, after many calculations (Sherrington and Kirkpatrick, 1975), the final expression is

$$F = -k_B T \lim_{n \rightarrow 0} \frac{1}{n} \left\{ \exp\left[\frac{\Delta^2 N n}{4(k_B T)^2}\right] \int \int_{-\infty}^{\infty} \left[\prod_{(\alpha\beta)} \left(\frac{N}{2\pi}\right)^{\frac{1}{2}} dy^{(\alpha\beta)} \right] \right\}$$

$$\times \left[\prod_{\alpha} \left(\frac{N}{2\pi} \right)^{\frac{1}{2}} dx^{\alpha} \right] \times \exp \left[-N \sum_{(\alpha\beta)} \frac{1}{2} (y^{(\alpha\beta)})^2 - N \sum_{\alpha} \frac{1}{2} (x^{\alpha})^2 \right. \\ \left. + N \ln Tr_S \exp \left(\frac{\Delta}{k_B T} \sum_{(\alpha\beta)} y^{(\alpha\beta)} S^{(\alpha)} S^{(\beta)} + \left(\frac{J_0}{k_B T} \right)^{\frac{1}{2}} \sum_{\alpha} x^{\alpha} S^{\alpha} \right) \right] - 1 \Big\} \quad (2.33)$$

where the trace is now over n replicas at a single site. $y^{(\alpha\beta)}$ and x^{α} are dummy variables of integration, and $(\alpha\beta)$ label the distinct pairs of replicas. SK assumed that the thermodynamic limit $N \rightarrow \infty$, and the replica limit $n \rightarrow 0$ can be interchanged in order to perform the integration more easily, (by the method of steepest descent). They considered the replicas to be indistinguishable, which is called the *replica-symmetric* solution, meaning that $q_{\alpha\beta} = q = \text{constant}$ for all pairs of replicas $(\alpha\beta)$.

Substituting $y \rightarrow q \cdot \left(\frac{\Delta}{k_B T} \right)$ and $x \rightarrow m \cdot \left(\frac{J_0}{k_B T} \right)^{\frac{1}{2}}$, and removing the terms linear in n as $n \rightarrow 0$ yields

$$F = N k_B T \left\{ \frac{-J_0^2 (1-q)^2}{(2k_B T)^2} + \frac{\Delta m^2}{2k_B T} - \frac{1}{(2\pi)^{1/2}} \times \right. \\ \left. \int dz \exp\left(\frac{-z^2}{2}\right) \ln \left[2 \cosh \left(\frac{J_0 q^{1/2} z}{2k_B T} + \frac{\Delta m}{k_B T} \right) \right] \right\}, \quad (2.34)$$

where z is a variable related to q and m in the effective field, $\tilde{H}(z) = Jq^{1/2}z + J_0m + H$ (Binder and Young, 1986). Differentiating with respect to q and m to determine the self-consistent simultaneous equations for q and m , the results are

$$q = 1 - \frac{1}{\sqrt{2\pi}} \int \exp\left(\frac{-z^2}{2}\right) \text{sech}^2 \left[\frac{\Delta q^{\frac{1}{2}}}{k_B T} z + \frac{J_0 m}{k_B T} \right] dz \quad (2.35)$$

$$m = \frac{1}{\sqrt{2\pi}} \int \exp\left(\frac{-z^2}{2}\right) \tanh \left[\frac{\Delta q^{\frac{1}{2}}}{k_B T} z + \frac{J_0 m}{k_B T} \right] dz. \quad (2.36)$$

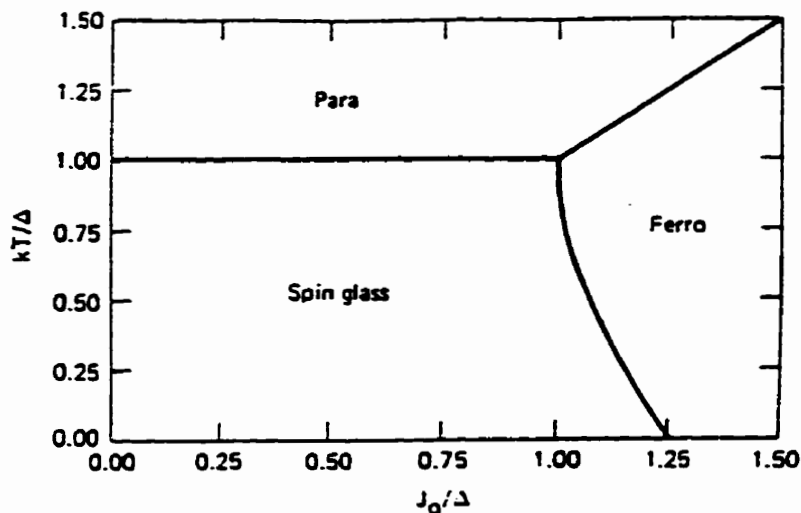


Figure 2.2: Magnetic phase diagram predicted by SK model. From Sherrington and Kirkpatrick (1975).

Here there are two order parameters q and m . q is related to finite-ranged interactions and m is related to infinite-ranged interactions:

$$q \equiv \langle \langle S_i \rangle^2 \rangle_C \quad (2.37)$$

and

$$m \equiv \langle \langle S_i \rangle \rangle_C . \quad (2.38)$$

A nonzero q indicates magnetic order, while nonzero m (in addition to q) indicates that the order is ferromagnetic. When $m = 0$ but $q \neq 0$, the order is a "spin-glass" state. For given ratios of J_0/Δ , $q(T)$ and $m(T)$ can be calculated and a magnetic phase diagram is thereby established. Figure 2.2 is the $\frac{k_B T}{\Delta}$ versus J_0/Δ plot for Ising spin interactions. The possibility of the following phase transitions is predicted : (i) paramagnetic \rightarrow spin glass; (ii) paramagnetic \rightarrow ferromagnetic; and (iii) double (or re-entrant) transitions paramagnetic \rightarrow ferromagnetic \rightarrow spin

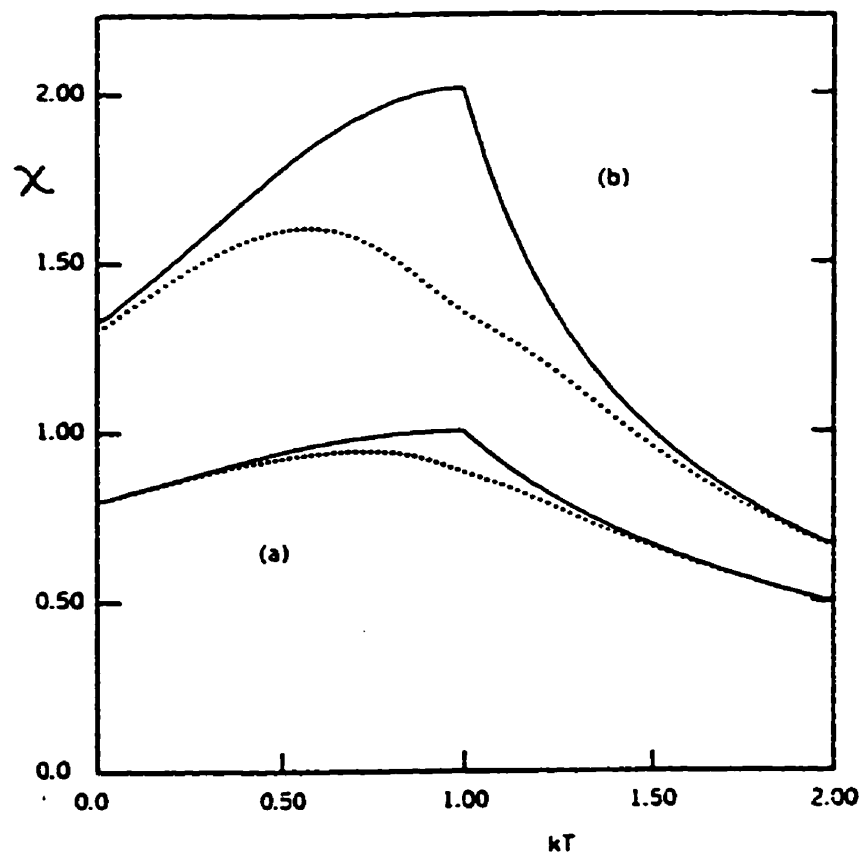


Figure 2.3: Differential susceptibility without external field (solid lines) and with a field $H = 0.1\Delta$ (dotted lines) for $J_0/\Delta = 0$, curves (a), and $J_0/\Delta = 0.5$, curves (b). From Sherrington and Kirkpatrick (1975).

glass.

The differential (or ac-) susceptibility may be obtained from the $q(T)$ function by adding an external field term and then taking the zero field limit:

$$\chi(T) = \frac{[1 - q(T)]}{k_B T - J_0[1 - q(T)]} = \frac{\chi^{(0)}}{1 - J_0 \chi^{(0)}} \quad (2.39)$$

where $\chi^{(0)}$ is the value for $J_0 = 0$. Above the ordering temperature, where $q = 0$, this is just a Curie-Weiss law. In the spin-glass state, the fluctuations decrease χ , while J_0 increases it. Two examples are plotted in Figure 2.3 for $J_0/\Delta = 0$ and 0.5, and fields $H = 0$ and 0.1Δ . Once again a cusp in the susceptibility exists at a specific critical temperature, which is rounded and shifted downward in a dc field.

But when the specific heat is calculated (SK, 1978), there is also a cusp in the predicted $C_m(T)$ at T_f . For $T < T_f$, the leading term of $C_m(T) \propto T$. For $T > T_f$, $C_m = Nk_B \Delta^2 / (2(k_B T)^2)$, hence a tail in $C_m \propto 1/T^2$ persists to higher temperatures, which is in contrast to the usual mean-field-theory result where $C_m = 0$ for $T > T_f$. The entropy S equals $Nk_B [\ln 2 - \Delta^2 / (2k_B T)^2]$ above the transition temperature T_f , but goes to a negative limit $-k_B/2\pi$ at $T = 0$. This is an unacceptable unphysical feature of the model.

de Almeida and Thouless (1978) performed a detailed analysis of the SK solution and showed that both the paramagnetic and ferromagnetic phases were unstable at low temperatures, and traced the instability line as a function of field. In the presence of an applied field $H \neq 0$ the instability line of the SK-solution is plotted in Figure 2.4. The $H - T$ plot yields the AT line which gives the stability limits of the SK solution. The functional form is

$$\frac{T_f - T_{AT}(H)}{\Delta} = \left(\frac{3}{4}\right)^{\frac{1}{3}} \left(\frac{H}{\Delta}\right)^{\frac{2}{3}}. \quad (2.40)$$

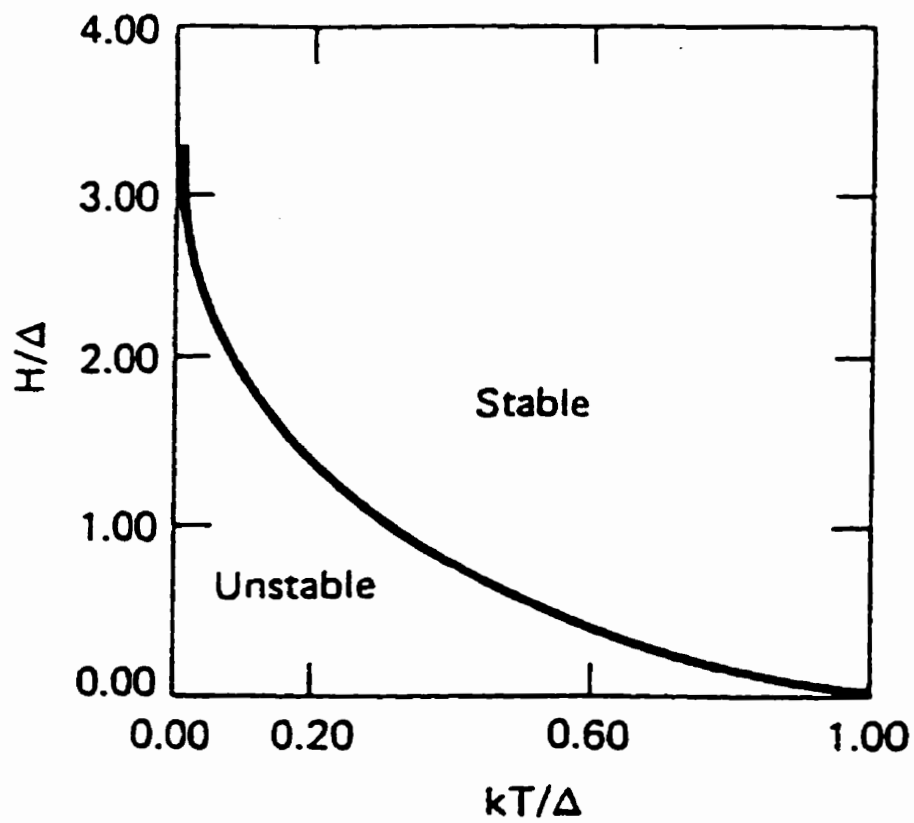


Figure 2.4: $H - T$ phase diagram (or AT line) illustrating the stability limits of the SK solution for the case of $J_0 = 0$. From de Almeida and Thouless (1978).

So, treating all the replicas as indistinguishable, that is, assuming $q_{\alpha\beta} = q$ for all $(\alpha\beta)$, makes the SK solution unstable. We must search for a way to overcome the replica symmetric instability problem.

Parisi(1979) proposed an ansatz to break replica symmetry. His procedure was as follows. First start with an $n \times n$ replica symmetric matrix with all elements equal to q_0 (identical parameters). As an example, we take $n = 8$ (Mydosh, 1993). In the first step, we divide the $(n \times n)$ matrix into sub-matrices $(n/m_1) \times (n/m_1)$ with sizes $m_1 \times m_1$ ($m_1 = 4$ here). We leave the off-diagonal blocks unchanged with elements q_0 , and assign the diagonal blocks elements q_1 as shown in Figure 2.5. We repeat this step on the diagonal blocks and get the sub-sub-matrices along the diagonal blocks $(m_1/m_2) \times (m_1/m_2)$ with sizes $m_2 \times m_2$ ($m_2 = 2$ here). In this step, we create order parameter q_2 as the new diagonal block elements. Then iterate the process R times until we get the smallest diagonal block of sizes $m_R \times m_R$. Throughout this construction, the successive sizes of the blocks are

$$n \geq m_1 \geq m_2 \cdots \geq m_R \geq 1 \quad (2.41)$$

But, all of these numbers are positive integers. For calculating the free energy in the limit $n \rightarrow 0$, we must reverse the above procedure, and the m_i become arbitrary real numbers between 0 and 1 (Parisi, 1980),

$$0 \leq m_1 \leq m_2 \cdots \leq m_R \leq 1 \quad (2.42)$$

If R is very large, the m_i are *continuous*, and for the k th step in the sequence:

$$m_k/m_{k+1} \rightarrow 1 - dx/x \quad \text{and} \quad q_k \rightarrow q(x) \quad (2.43)$$

where x is defined in the interval $0 \leq x \leq 1$ as in section 2.1. We now have an infinite number of order parameters $q(x)$, which is the most important result to be obtained from the Replica Symmetry Breaking (RSB) solution, as well as a distribution function $P(q) \equiv dx/dq$ which gives the probability of replica

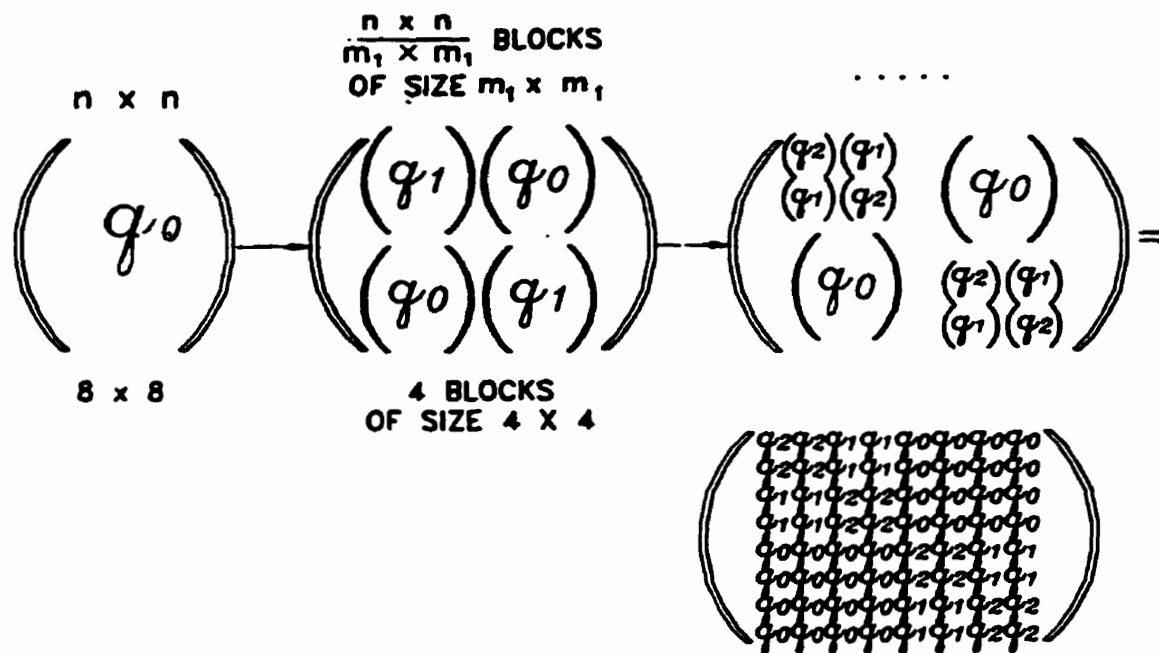


Figure 2.5: Replica symmetry breaking (RSB) scheme for $q_{\alpha\beta}$ with two levels of breaking ($n = 8$, $m_1 = 4$; $m_2 = 2$). From Mydosh, (1993).

overlap q . Lastly, we would like to mention that the SK replica symmetric solution corresponds to the $k=0$ step or the original q_0 matrix, which means that $q(x) = q_0$, which is independent of x .

There is another way to visualize the Parisi's RSB scheme. Figure 2.6 is a tree which represents the order parameter (or overlap) matrix $q_{\alpha\beta}$ of Figure 2.5. The uppermost level represents the individual replicas with self-overlap q_{max} , which is the largest possible value of q . Each level groups together replicas with a certain overlap $q_{\alpha\beta}$. The lowest level q_0 is the minimum value of q , that is the smallest possible overlap, so at this level, all replicas are identical. To find the overlap value $q_{\alpha\beta}$ for a particular pair of replicas $(\alpha\beta)$, we trace back along the branches of the tree from α and from β until they join. For example, $q_{12} = q_2$, $q_{14} = q_1$ and $q_{18} = q_0$.

Based on the RSB model, the susceptibility and the internal energy are given respectively by (Binder and Young, 1986)

$$\chi = \frac{1}{k_B T} \int_0^1 [1 - q(x)] dx \quad (2.44)$$

and

$$U = -\frac{J^2}{2k_B T} \int_0^1 [1 - q^2(x)] dx - HM \quad (2.45)$$

where M is the magnetization per spin. We see that linear-response theory, where $\chi = C/T(1 - q)$, breaks down. Further calculations indicated that (Binder and Young, 1986) $\chi(RSB)$ is a constant for all $T < T_f$, which corresponds to the field-cooled susceptibility χ_{FC} , and that the entropy S vanishes at $T = 0$, (remember that S is negative in the SK solution). So, by RSB, the unphysical negative entropy is removed.

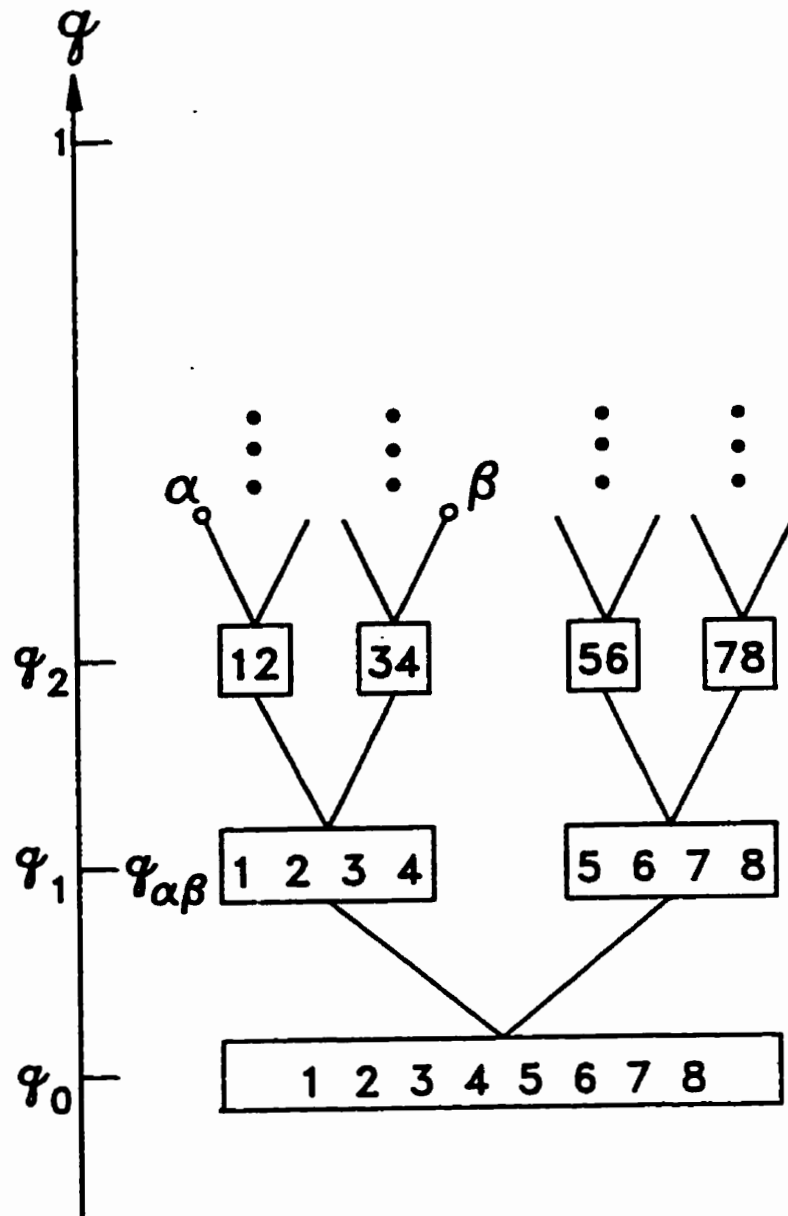


Figure 2.6: Tree representation of Parisi's RSB scheme. To find $q_{\alpha\beta}$ ($\alpha = 1$ and $\beta = 4$ here) trace back along the branches of the tree from α and β until they join: $q_{\alpha\beta} = q_1$ is the value of q at this point. From Mydosh, (1993).

2.4 Pure States, Metastable States, and Dynamic Behaviour

In this section, I will draw a series of phenomenological pictures about the formation of the metastable states and their dynamic behaviour in spin glasses, to get a feeling for the processes which can occur in the ordered spin glass phase.

To understand the coexistence of many phases in a system, let us first look at the analogies that exist between fluids and ferromagnets. Figure 2.7 compares their coexistence diagrams below the critical temperature T_c . In a ferromagnet, the magnetic field H and magnetization M correspond to the pressure P (or chemical potential μ) and the density ρ in a fluid. At a low temperature $T < T_c$, there is a coexistence curve in both cases. Inside this curve the magnet breaks up into “up” and “down” domains, or each of which corresponds to a “pure” state of the system. The term “pure” state means a set of microscopic configurations in thermal equilibrium with each other. This is analogous to gas-liquid coexistence in fluids. At a constant temperature $T < T_c$, the phase transition, “up” \leftrightarrow “down” domains in ferromagnets, and “gas” \leftrightarrow “liquid” in fluids, is a first order phase transition.

In each of the above cases, there are two different pure states of phases in the coexistence region. But in the spin glass state, due to randomness and frustration, the number of coexisting pure phases is “infinite”, with some kind of distribution. These configurations have the lowest free energy. There are also very many other configurations with higher free energies which correspond to metastable states. By contrast, in a ferromagnet at $T < T_c$ and $H = 0$ (Figure 2.8(a)), only two degenerate stable phases coexist. If we apply a magnetic field to the system, one state in (a) is still stable and the other one becomes metastable (Figure 2.8(b)). The phase with $m = -m_0$ (the metastable one) will eventually flip over a energy barrier δ to the stable phase with $m = +m_0$. The flipping

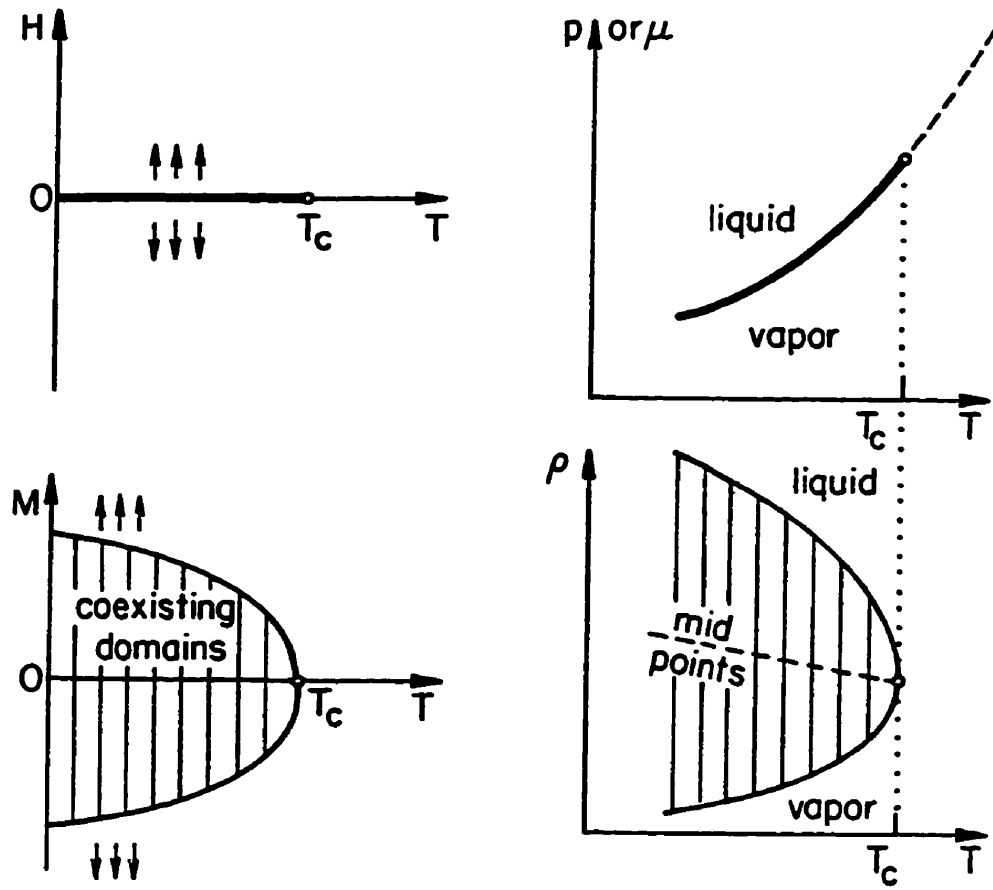


Figure 2.7: Phase and coexistence diagram illustrating the magnet-fluid analogy. Note magnetization M corresponds to density ρ and magnetic field H to pressure P or chemical potential μ . From M.E.Fisher (1983).

time is $\tau \propto e^{\delta/T}$. So, in a ferromagnet, only one stable and one metastable phase coexist at $T < T_c$, when $H \neq 0$, and there is only one flipping time τ . In a spin glass, the situation is much more complicated. A spin glass is a coexistence of many phases and many metastable states. For a thermodynamic system the “many” is “infinite”. Parisi’s RSB solution gives the the number of pure states (De Dominicis et al., 1985) with free energy f_i to be

$$P(f_i) \propto e^{x \frac{f_i - f_0}{T}} \quad (2.46)$$

where f_i is the free energy of a pure system, x is a temperature dependent parameter between 0 and 1, and f_0 is a characteristic energy. There are very few states with $f_i \ll f_0$. There are very many with $f_i \gg f_0$ but they all have negligible weight when built replaced by the Boltzmann factor $\exp(-f_i/T)$ since $x < 1$. Thus the states of interest have $f_i \cong f_0$. If we borrow the “valley/sub-valley” picture to describe this, the pure phases are separated by infinite barriers, forming mutually inaccessible valleys in configuration space. The time to flip from one pure phase to another is very long. Inside each valley, is a very rough landscape with a broad distribution of finite energy barriers separating sub-valleys, which represent the metastable states. The individual pure states may have very different magnetizations, as may the metastable states within each pure state.

To plot the energy landscape in configuration space, we imagine imposing local magnetizations $\{m_i\}$ on the system and calculate the free energy $G(\{m_i\})$, and plot it in an $(N + 1)$ -dimensional space, where N is the number of the magnetic moments, whose axes are labelled by the $\{m_i\}$ and G . All of the local minima of G which satisfy $\frac{\partial G}{\partial m_i} = 0$ and $\frac{\partial^2 G}{\partial m_i \partial m_j} > 0$ are states corresponding to locally stable magnetization configurations. Some of the barriers are infinite and separated configuration space into valleys – the lowest energy state in each valley is a pure state and the rest form metastable sub-valleys. Each valley has a net magnetization $\propto \sqrt{N}$ in zero field, where N is the number of the magnetic atoms.

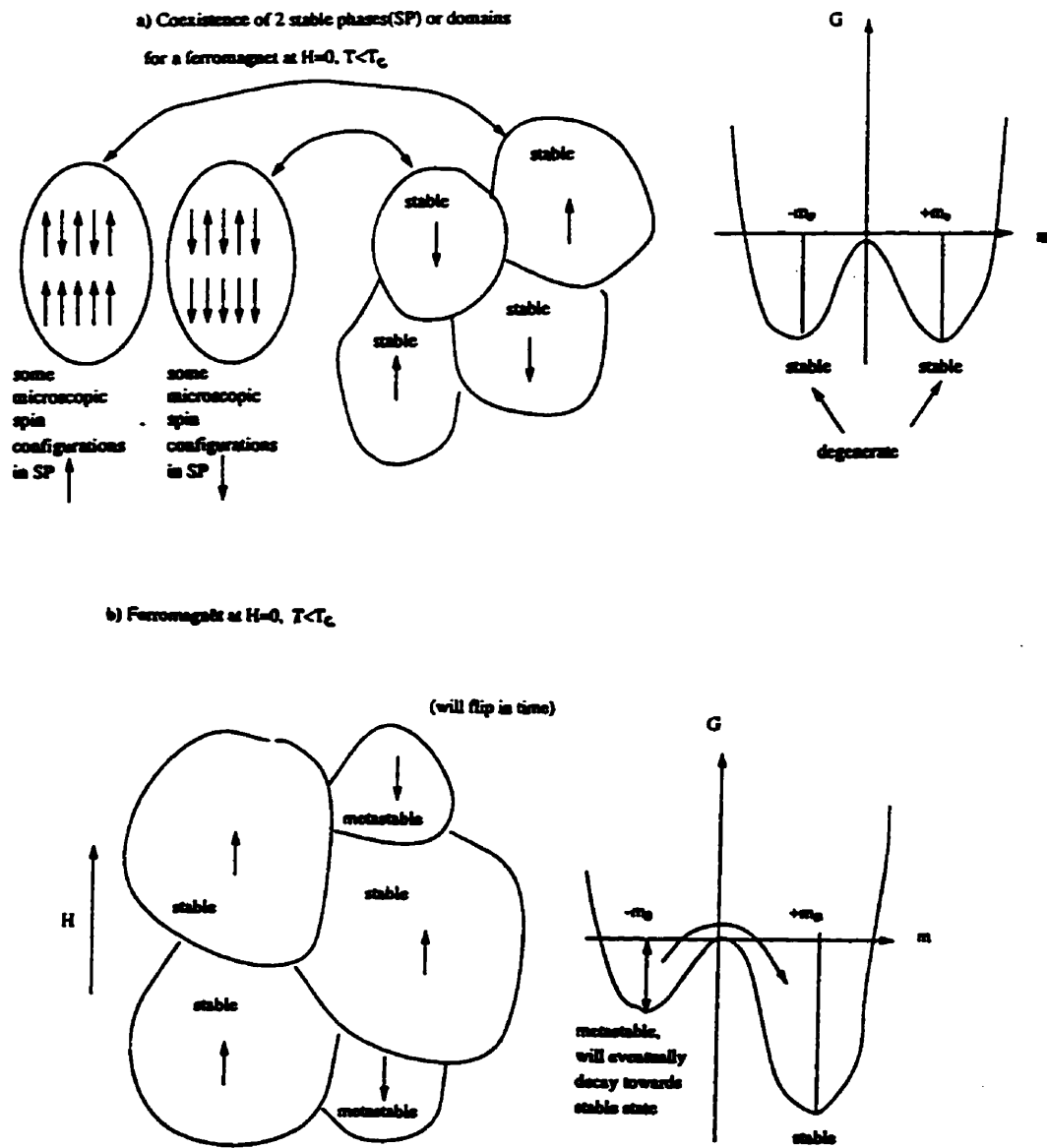


Figure 2.8: (a) Ferromagnet at $H = 0$ and $T < T_c$. Two kinds of states (domains) coexist with same energy. (b) Ferromagnet at $H \neq 0$ and $T < T_c$. One state is stable and the other one is metastable. The metastable one will flip over to the stable state.

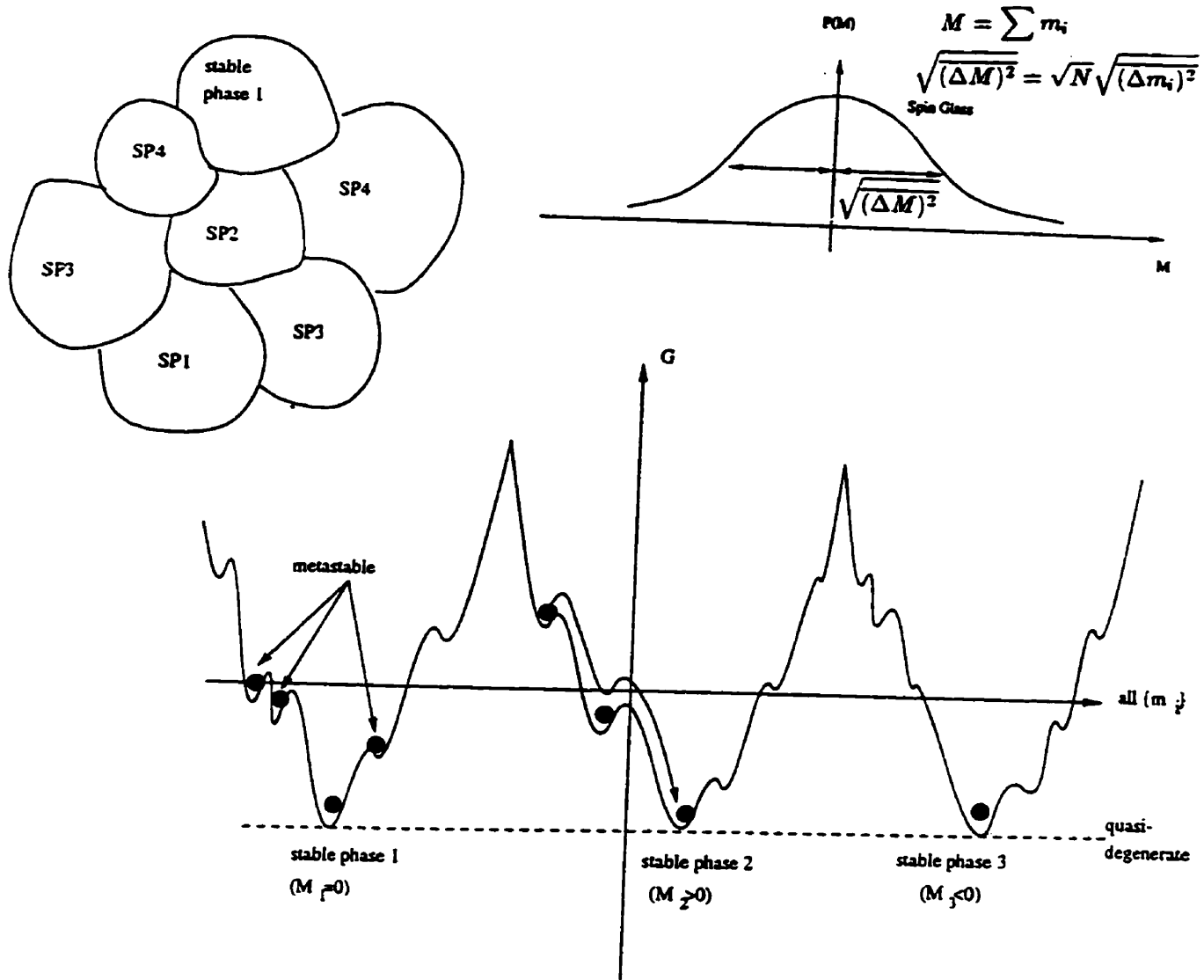


Figure 2.9: Spin glass state at $H = 0$ and $T < T_f$.

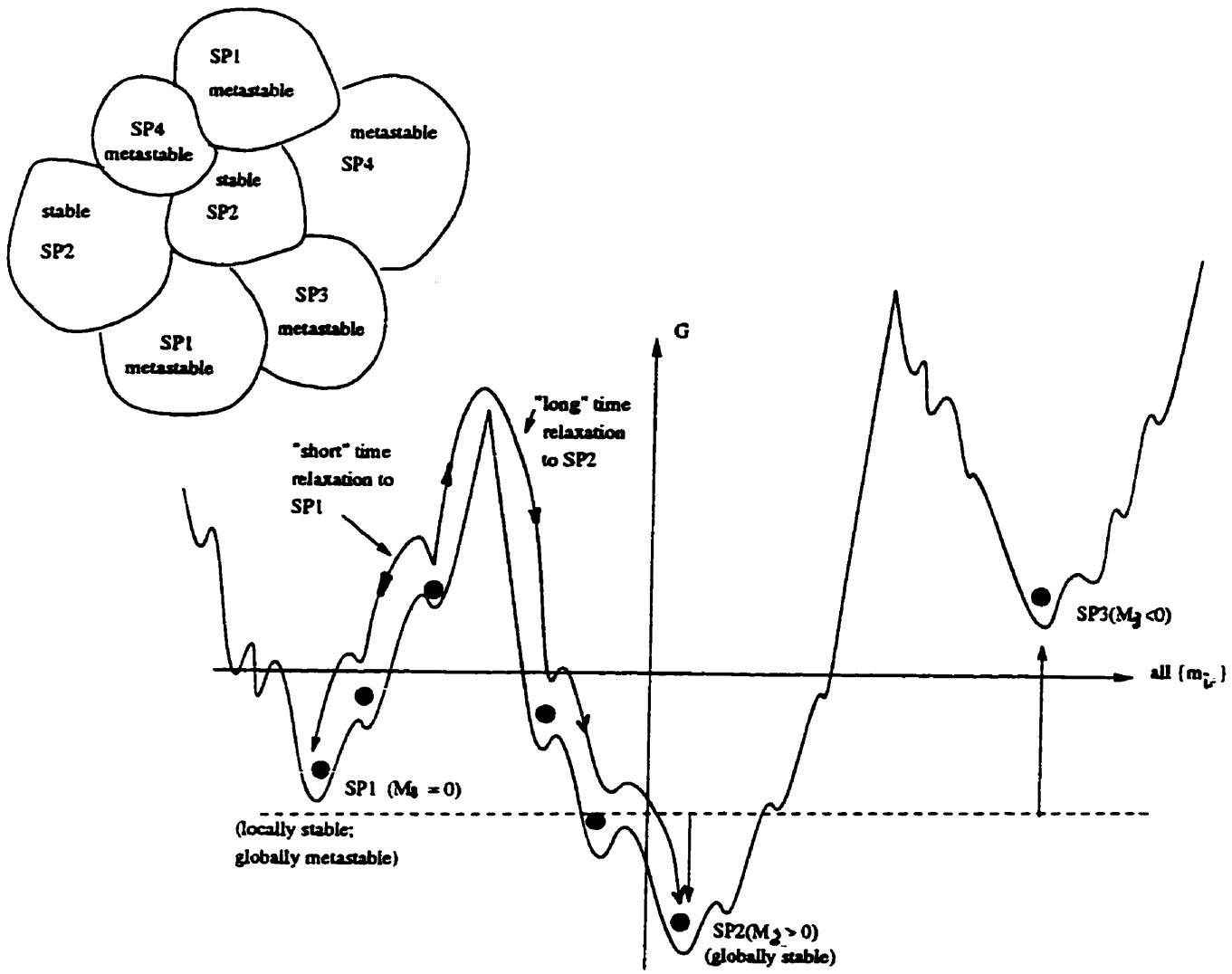


Figure 2.10: Spin glass state at $H \neq 0$ and $T < T_f$.

When a spin glass is quenched from $T > T_f$ to $T < T_f$ in zero field, it will nucleate all possible pure phases in various regions of the sample. If the system is trapped locally in a metastable state, it will gradually relax toward the nearest pure state, as shown in Figure 2.9. When $H \neq 0$ some of the formerly pure states will themselves become metastable as shown in Figure 2.10 and these regions of the sample will evolve toward a stable pure phase. Presumably there will be two types of relaxation process, very slow processes between valleys, and “faster” processes between metastable subvalleys. The latter will be responsible for the measured slow dynamics. When the field is reduced to zero, similar relaxation processes are expected to occur.

2.5 The Droplet Scaling Model

Fisher and Huse proposed a phenomenological theory (Fisher and Huse, 1986, 1988a, 1988b) for the low temperature behaviour of spin glasses. This approach is based on the concept of droplet excitations in a short-range Ising spin glass, and assumes that there are only two pure equilibrium states Γ and $\bar{\Gamma}$ below T_f , related by global spin-reversal symmetry. If the system is in ground state Γ , then the lowest-energy relaxation is a droplet of reversed spins $\bar{\Gamma}$ of length scale L .

For example, in Figure 2.11, Γ is the ground state, and $\bar{\Gamma}$, which is Γ 's global spin reversal, is a droplet surrounded by a domain wall. The low-lying droplet excitations on length scale L have a wide free energy distribution which grows with droplet sizes as $F_L \propto \Upsilon(T)L^\theta$, where θ is a exponent with a limit $\theta \leq \frac{d-1}{2}$ (d is the dimension of the system), and Υ is the stiffness constant. This scaling ansatz gives the following distribution $\rho_L(F_L)dF_L$ of droplet free energies

at length scale L :

$$\rho_L(F_L) \approx \frac{1}{\Upsilon L^\theta} \bar{\rho}\left(\frac{F_L}{\Upsilon L^\theta}\right). \quad (2.47)$$

Macroscopic phenomena result from the microscopic energy excitations. Most of the excitations involve only one or a few spins flipping over, and only contribute to the high frequency or short time scale phenomena. But, we are more interested in the long time, low-frequency phenomena, which are related to the large droplet excitations. Because of the randomness of the excitations, the surface of the droplet becomes very complicated, as shown in Figure 2.11. The surface area of the droplet scales as $A_L \sim L^{d_s}$, where d_s satisfies the relation $d - 1 < d_s < d$.

Droplets with free energy $F_L \sim L^\theta$ will have barriers to their creation and annihilation. The energy barriers will also grow as a power of L as $B \sim L^\psi$ where ψ is a new independent exponent which satisfies $\theta \leq \psi \leq d - 1$. Thus a droplet will last for a time τ_L :

$$\tau_L = \tau_0 \exp\left(\frac{B}{k_B T}\right) \quad (2.48)$$

where τ_0 is a microscopic time. Thus, in an observation time t , the droplet will have grown to a size L given by:

$$t \sim \tau_0 \exp\left(\frac{L^\psi}{k_B T}\right) \quad (2.49)$$

$$\text{or } L \sim \left[k_B T \ln\left(\frac{t}{\tau_0}\right)\right]^{1/\psi}. \quad (2.50)$$

The thermally active droplets with anomalously low free energies have long-time autocorrelations which decay as

$$\overline{C(t)} \sim q_{EA} \frac{T}{\Upsilon} \left[\frac{\Delta}{T \ln(t/\tau_0)} \right]^{\theta/\psi} \quad (2.51)$$

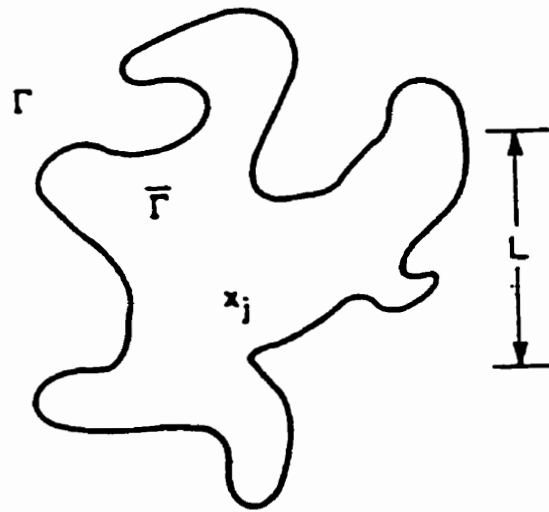


Figure 2.11: Schematic picture of the droplet of length scale L (containing site j). Outside the droplet the spins are aligned as in ground state Γ . While inside the droplet the spins are reversal, as in the ground state $\bar{\Gamma}$, which is just the global spin flip of Γ . The surface of the droplet is fractal. From Fisher and Huse (1988b).

which is a slow logarithmic decay, where q_{EA} is the Edwards and Anderson order parameter, and where Δ sets the overall free-energy scale of the barriers ($\Delta \sim J$ for $T \ll T_c$).

Now, we consider the non-equilibrium behaviour as the system approaches equilibrium after a quench from temperature $T \gg T_f$ to $T \ll T_f$. Because both Γ and $\bar{\Gamma}$ are nucleated after the quench, the system will try to lower its free energy by decreasing the amount of interface between Γ and $\bar{\Gamma}$, so both Γ and $\bar{\Gamma}$ grow larger and larger. This growth will be very slow because of the randomness-induced free-energy barriers, which must be surmounted in order to move sections of the wall between Γ and $\bar{\Gamma}$.

In a time t_a after the quench, the characteristic length R_{t_a} of a droplet will be

$$R_{t_a} \sim \left[\frac{T \ln(t_a/\tau_0)}{\Delta(T)} \right]^{\frac{1}{\psi}} \quad (2.52)$$

where t_a is the total age of the system, which equals the wait time t_w plus the measurement time t , and τ_0 is a microscopic time. This slow domain growth determines the non-equilibrium dynamics of the spin-glass below the freezing temperature. If a corresponding field quench is performed by turning off an infinite magnetic field, the magnetization $m(t)$ will decay, with the formation and growth of the “zero-magnetization-domains”, according to

$$m(t) \sim \frac{1}{R_t^\lambda} \sim \left[\frac{\Delta}{T \ln t} \right]^{\frac{\lambda}{\psi}} \quad (2.53)$$

where λ is a new dynamic exponent related to the non-equilibrium growth.

The droplet model may also be used to describe the aging effect, i.e., the response of the system if we wait for a time t_w after a thermal quench in a field, and then turn off the field. In this experiment, relaxation processes are probed

on a length scale L_t which starts growing as soon as the field is turned off:

$$L_t \sim \left[\frac{T \ln t}{\Delta(T)} \right]^{\frac{1}{\psi}}. \quad (2.54)$$

Let us consider two limiting cases: $\ln t \ll \ln t_w$ and $\ln t \gg \ln t_w$.

In the first case, the probing length scale is much smaller than the domain size:

$$L_t \sim \left[\frac{T \ln t}{\Delta(T)} \right]^{\frac{1}{\psi}} \ll R_{t_a} \sim R_{t_w} \sim \left[\frac{T \ln t_w}{\Delta(T)} \right]^{\frac{1}{\psi}} \quad (2.55)$$

where $t_a = t_w + t \approx t_w$. So, R_{t_a} will be constant in this ‘early epoch’ regime, which is probed on the scale L_t . In other words, the probing scale is so small that it does not “see” beyond the domain walls, but only samples the dynamics within the pure states Γ and $\bar{\Gamma}$. So, this is quasi-equilibrium behavior, i.e., the relaxation of the magnetization approximates the characteristics of equilibrium, and the magnetization decays as

$$m(t) \sim \frac{H}{(\ln t)^{\theta/\psi}} \quad (2.56)$$

where both θ and ψ are equilibrium exponents.

Second, if $\ln t \gg \ln t_w$, $t_a = t + t_w \approx t$, which is the “late epoch”, the experiments now clearly sense the non-equilibrium dynamic behaviour due to domain growth. The decay of the magnetization is now

$$m(t) \sim H \left[\frac{\ln t_w}{\ln t} \right]^{\frac{\lambda}{\psi}} \quad (2.57)$$

where a non-equilibrium exponent λ defines the magnetization decay.

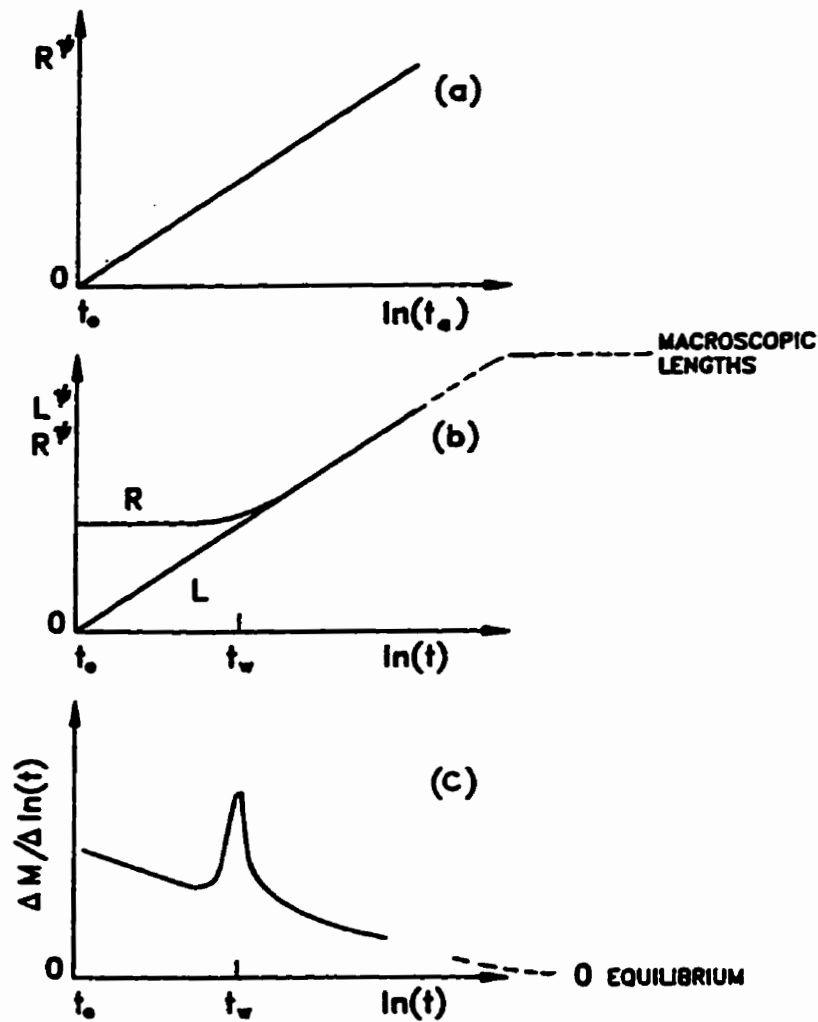


Figure 2.12: Growth with time of domain size R , experimental-probing-length scale L , and relaxation rate: (a) R^ψ vs. $\ln t_a$, $t_a = t + t_w$ the total age of the system; (b) R^ψ and L^ψ vs. $\ln t$. t is the time of measurement, t_w , the waiting time, and t_0 , a microscopic time; and (c) relaxation rate $\partial M / \partial \ln t$ vs. $\ln t$. ψ is a barrier exponent. From Lundgren (1988).

The system will thus experience a crossover from quasi-equilibrium to non-equilibrium dynamics, at $\ln t = \ln t_w$. Figure 2.12 shows R^ψ vs. $\ln t_a$, L^ψ and R^ψ vs. $\ln t$, and $\frac{\Delta m}{\Delta \ln(t)}$ vs. $\ln(t)$. At the crossover t_w , the magnetization decay rate changes rapidly. This is why aging yields a characteristic anomaly at the aging time t_w . As $t \rightarrow \infty$, L and R have the same macroscopic length scales, so the number of domains and their walls become insignificant. True equilibrium will finally be reached, and the magnetization and its decay rate will both go to zero. This process is confirmed experimentally both in the literature and in our results (see Chapter 4).

2.6 The Model of Random Traps

Bouchaud proposed a phenomenological model for relaxation and aging in disordered systems (Bouchaud, 1992; 1994). I will discuss this model here, and our improvements for a real disordered system, in detail. The basic principles are as follows.

For a finite disordered system, the energy landscape is expected to be extremely rough, with many local minima corresponding to metastable states, as shown in Figure 2.13. These states are surrounded by energy barriers, which makes them trap-like, and they have a distribution of energies f given by (De Dominicis et al., 1985):

$$P(f) = \frac{x}{T} \exp\left[-\frac{x(f - f_0)}{T}\right], \quad 0 \leq x \leq 1 \quad (2.58)$$

where f_0 is the minimal energy required to “hop” between any two states, and x is a temperature dependent parameter. This result is based on the assumption that Parisi’s Replica Symmetry Breaking (RSB) solution of the SK model (Mezard et al., 1985) for the pure states applies to the metastable states within each pure

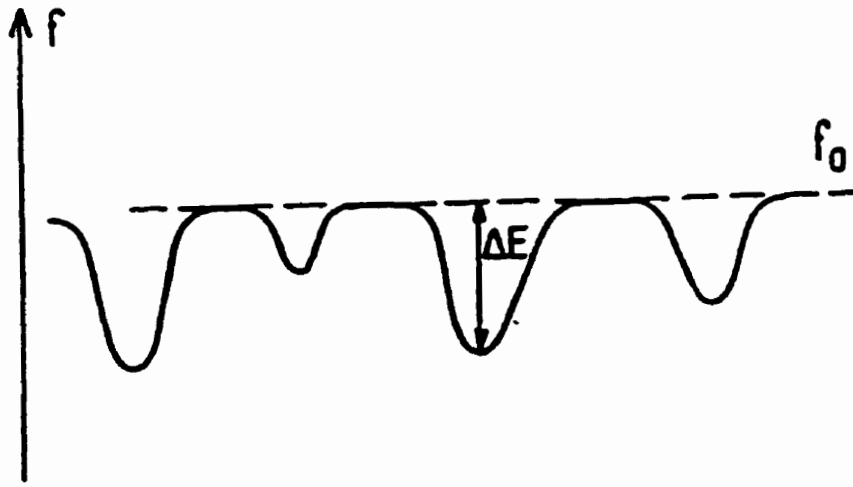


Figure 2.13: Schematic view of the energy landscape: holes are drilled below the reference energy f_0 which is the minimal energy needed to go from one metastable state to another. Note that this drawing is one dimensional: in reality mountains of height $\gg f_0$ also exist between different states. From Bouchaud (1992).

state as well.

Each trap has a corresponding trapping time τ , and there is a distribution of these trapping times. If we define the trap depth by

$$\Delta E = f_0 - f \quad (2.59)$$

then, the trapping time τ is

$$\tau = \tau_0 e^{\Delta E/T}, \quad \text{where} \quad \tau_0 \sim 10^{-12} \text{s} \quad (2.60)$$

and the distribution of trapping times τ is given by:

$$\psi(\tau)d\tau = P(f)df. \quad (2.61)$$

Transforming from f to τ :

$$f = f_0 - \Delta E = f_0 - T \ln\left(\frac{\tau}{\tau_0}\right) \quad (2.62)$$

We can write

$$\frac{df}{d\tau} = -\frac{T}{\tau} \quad (2.63)$$

and have

$$\psi(\tau)d\tau = P(f)\left|\frac{df}{d\tau}\right|d\tau \quad (2.64)$$

$$= \frac{x}{T} \exp\left[\frac{x}{T}(-T \ln(\frac{\tau}{\tau_0}))\right] \cdot \left|-\frac{T}{\tau}\right|d\tau \quad (2.65)$$

$$= \frac{x}{T} e^{\ln(\frac{\tau}{\tau_0})^{-x}} \left|-\frac{T}{\tau}\right|d\tau \quad (2.66)$$

$$= x\left(\frac{\tau}{\tau_0}\right)^{-x} \frac{1}{\tau} d\tau \quad (2.67)$$

$$= \frac{x\tau_0^x}{\tau^{1+x}} d\tau. \quad (2.68)$$

Checking the normalization:

$$\int_{\tau_0}^{\infty} \psi(\tau)d\tau = x\tau_0^x \int_{\tau_0}^{\infty} \frac{d\tau}{\tau^{x+1}} \quad (2.69)$$

$$= x\tau_0^x \left[\frac{\tau^{-x}}{-x}\right]_{\tau_0}^{\infty} \quad (2.70)$$

$$= -\tau_0^x \left[\frac{1}{\tau^x}\right]_{\tau_0}^{\infty} \quad (2.71)$$

$$= 1 \quad (2.72)$$

which is independent of x ($x > 0$). However, it is crucial to notice that for such a distribution, the average exploration time $\langle \tau \rangle$ diverges, i.e. $\int_{\tau_0}^{\infty} \psi(\tau) \cdot \tau \cdot d\tau = \infty$, for $0 < x < 1$. This is ultimately the origin of aging.

A real spin glass is a *collection of many finite independent spin glass subsystems*. Any given subsystem has a finite number S of traps. There will be a

distribution of sizes of the subsystems $P(S)dS$, with $0 < S < \infty$, but all subsystems are characterized by the same trapping distribution $\psi(\tau)$.

If a subsystem is initially in some particular trap, it will perform a random walk and explore deeper and deeper traps, which are more and more stable. The total time elapsed after taking S steps is $t_e = \sum_{i=1}^S \tau_i$, where τ_i is an independent random variable chosen from the distribution $\psi(\tau)$, with $\tau_0 < \tau < \infty$. For a finite number S of steps, there will be a largest (or most probable) term t_c in this series. The probability that the maximum value of $\tau = t_c$ is encountered only once in S steps is:

$$\int_{t_c}^{\infty} \psi(\tau) d\tau = \frac{1}{S} \quad (2.73)$$

and substituting for $\psi(\tau)$ from (2.68) yields:

$$x\tau_0^x \int_{t_c}^{\infty} \frac{d\tau}{\tau^{x+1}} = x\tau_0^x \left[\frac{\tau^{-x}}{-x} \right]_{t_c}^{\infty} = \frac{1}{S} \quad (2.74)$$

which defines the ergodic or equilibrium time $t_{erg}(S)$ for subsystem S :

$$t_c = \tau_0 S^{1/x} \equiv \text{Ergodic Time } t_{erg}(S). \quad (2.75)$$

Now, suppose we wait for a time $t_w \ll t_{erg}(S)$ so that the subsystem visits $N(t_w) < S$ states. What is the deepest trap τ_{max} actually encountered during t_w ? Following the same argument as above, the probability of encountering τ_{max} once in N steps is $\int_{\tau_{max}}^{\infty} \psi(\tau) d\tau = \frac{1}{N}$, and this yields

$$\tau_{max} = \tau_0 N^{1/x}. \quad (2.76)$$

Now

$$t_w = \sum_{i=1}^{N(t_w)} t_i \cong \langle \tau \rangle N(t_w) \quad (2.77)$$

$$= N(t_w) \int_{\tau_0}^{\tau_{max}} \tau \psi(\tau) d\tau \quad (2.78)$$

$$= N(t_w) x \tau_0^x \int_{\tau_0}^{\tau_{max}} \frac{d\tau}{\tau^x} \quad (2.79)$$

$$= N(t_w) x \tau_0^x \left[\frac{\tau^{-x+1}}{1-x} \right]_{\tau_0}^{\tau_{max}}. \quad (2.80)$$

If $x < 1$

$$t_w = N(t_w) x \tau_0^x [\tau_{max}^{1-x} - \tau_0^{1-x}] \frac{1}{1-x} \quad (2.81)$$

$$\approx N(t_w) x \tau_0^x \tau_{max}^{1-x} \frac{1}{1-x} \quad (2.82)$$

$$= N(t_w) \tau_0^x \frac{x}{1-x} [\tau_0 N^{1/x}]^{1-x} \quad (2.83)$$

$$= \frac{x}{1-x} \tau_0 N^{1/x} \cong \tau_{max}. \quad (2.84)$$

Thus for $x < 1$, the deepest trap τ_{max} that is probed is limited only by the wait time t_w . The longer the wait time, the more of phase space is probed. This is the origin of AGING. Equilibrium is attained only if $t_w \geq t_{erg}(S)$.

If $x > 1$

$$t_w = N(t_w) \frac{x}{1-x} \tau_0^x \left[\frac{1}{\tau_{max}^{x-1}} - \frac{1}{\tau_0^{x-1}} \right] \quad (2.85)$$

$$\cong \frac{x}{x-1} N \tau_0 \cong N \tau_0 \quad (2.86)$$

So,

$$\tau_{max} = \tau_0 N^{1/x} = \tau_0 \left(\frac{t_w}{\tau_0} \right)^{1/x} \quad (2.87)$$

$$= \tau_0^{1-\frac{1}{x}} t_w^{\frac{1}{x}} \ll t_w. \quad (2.88)$$

Thus, if $x > 1$, the deepest trap encountered is no longer limited by t_w .

To calculate the decay in the extreme nonequilibrium limit $t_w \ll t_{erg}(S)$ and for $x < 1$, we can essentially assume that $t_{erg} \cong \infty$. We define $P(\tau, t_w) = \text{Br}(\frac{\tau}{t_w})\tau\psi(\tau)$ as the probability of finding a subsystem in the trap τ , where B is a normalization factor, and $r(\frac{\tau}{t_w})$ is the probability that a specific trap occurs. B is determined by the normalization condition:

$$\int_0^{t_{erg} \cong \infty} P(\tau, t_w) d\tau = 1 \quad (2.89)$$

$$Bx\tau_0^x \int_0^\infty r(\frac{\tau}{t_w}) \frac{1}{\tau^x} d\tau = 1 \quad (2.90)$$

or, defining $u \equiv \frac{\tau}{t_w}$:

$$Bx\tau_0^x \int_0^\infty r(u) \frac{1}{u^x t_w^x} t_w du = 1 \quad (2.91)$$

$$Bx\tau_0^x t_w^{1-x} \int_0^\infty \frac{r(u) du}{u^x} = 1. \quad (2.92)$$

If we take $r(u)$ to be a step function for simplicity:

$$r(u) = \begin{cases} 1 & \text{for } u \leq 1 \\ 0 & \text{for } u > 1 \end{cases} \quad (2.93)$$

then

$$A \equiv \int_0^1 \frac{du}{u^x} = \frac{1}{1-x}, \quad (2.94)$$

so,

$$B = \frac{1}{x\tau_0^x t_w^{1-x} A}, \quad (2.95)$$

and have

$$P(\tau, t_w) = \frac{1}{x\tau_0^x t_w^{1-x} A} \cdot \tau \left(\frac{\tau}{t_w}\right) \cdot \tau \cdot \psi(\tau) \quad (2.96)$$

$$= \frac{1}{A} \cdot \tau \left(\frac{\tau}{t_w}\right) \cdot t_w^{x-1} / \tau^x. \quad (2.97)$$

This is the probability of finding the subsystem in a trap τ before the field is cut off.

After the field is cut off, the distribution becomes:

$$G(\tau, t) = P(\tau, t + t_w) \times g(\tau) \quad (2.98)$$

where the $t + t_w$ allows for the possibility of continued aging when $H = 0$, and where $g(\tau)$ is a factor which describes how the traps empty after the field is cut off, which is approximately a step function:

$$g(\tau) = \begin{cases} 0 & \text{for } \tau \leq t \\ 1 & \text{for } \tau > t \end{cases}. \quad (2.99)$$

Now the decay is determined from

$$\frac{dm}{dt} = -\frac{m}{\tau} \quad (2.100)$$

$$\frac{dm}{m} = -\frac{dt}{\tau} = -\langle \frac{1}{\tau} \rangle dt \quad (2.101)$$

$$= -dt \frac{\int_t^{t+t_w} \text{(from } \tau) d\tau \cdot \frac{1}{\tau} \cdot G(\tau, t)}{\int_t^{t+t_w} d\tau \cdot G(\tau, t)} \quad (2.102)$$

$$= -dt \frac{\int_t^{t+t_w} d\tau \cdot \frac{1}{A} \cdot \frac{(t+t_w)^{x-1}}{\tau^{x+1}}}{\int_t^{t+t_w} d\tau \cdot \frac{1}{A} \cdot \frac{(t+t_w)^{x-1}}{\tau^x}} \quad (2.103)$$

$$= -dt \frac{\int_t^{t+t_w} \frac{d\tau}{\tau^{x+1}}}{\int_t^{t+t_w} \frac{d\tau}{\tau^x}} \quad (2.104)$$

$$= -dt \frac{\left[\frac{t^{-x}}{1-x} \right]^{t+t_w}}{\left[\frac{t^{-x+1}}{1-x} \right]^{t+t_w}} \quad (2.105)$$

$$= -dt \left(-\frac{1-x}{x} \right) \frac{\left[\frac{1}{(t+t_w)^x} - \frac{1}{t^x} \right]}{\left[(t+t_w)^{1-x} - t^{1-x} \right]} \quad (2.106)$$

$$= -dt \left(\frac{1-x}{x} \right) \frac{\frac{1}{t^x} \left[1 - \left(\frac{t}{t+t_w} \right)^x \right]}{(t+t_w)^{1-x} \left[1 - \left(\frac{t}{t+t_w} \right)^{1-x} \right]} \quad (2.107)$$

$$= -dt \cdot t^{-x} \cdot (t+t_w)^{x-1} \cdot \underbrace{\left(\frac{1-x}{x} \right) \cdot \frac{\left[1 - \left(\frac{t}{t+t_w} \right)^x \right]}{\left[1 - \left(\frac{t}{t+t_w} \right)^{1-x} \right]}}_{\equiv U\left(\frac{t}{t+t_w}\right) \text{ slowly varies}} \quad (2.108)$$

Note, that (2.108) is a universal function of $\frac{t}{t_w}$ only. If we approximate $U\left(\frac{t}{t+t_w}\right)$ as a constant γ , then we have

$$m(t) = m_0 \exp\left[-\gamma \int_0^t t^{-x} (t+t_w)^{x-1} dt\right]. \quad (2.109)$$

Our assumption of “artificial” step functions in (2.93) and (2.99) means that the limits of integration in the calculation of $\langle 1/\tau \rangle$ are controlled by the rectangular “pulse” shown in Figure 2.14.

As we mentioned previously, a real system is composed of many subsystems. Each subsystem has its own ergodic time t_{erg} and if $t+t_w > t_{erg}$, $t+t_w$ should be replaced by t_{erg} in function (2.109). For simplicity, we compare t_w and t_{erg} in order to choose the appropriate functional form for the decay, which is either

$$m(t) = \begin{cases} m_0 \exp\left[-\gamma \int_0^t t^{-x} (t+t_w)^{x-1} dt\right], & t_w < t_{erg} \\ m_0 \exp\left[-\gamma' \int_0^t t^{-x} (t+t_{erg})^{x-1} dt\right], & t_w > t_{erg} \end{cases} \quad (2.110)$$

Since a real system has a distribution of sizes and of ergodic times $P(t_{erg})$,

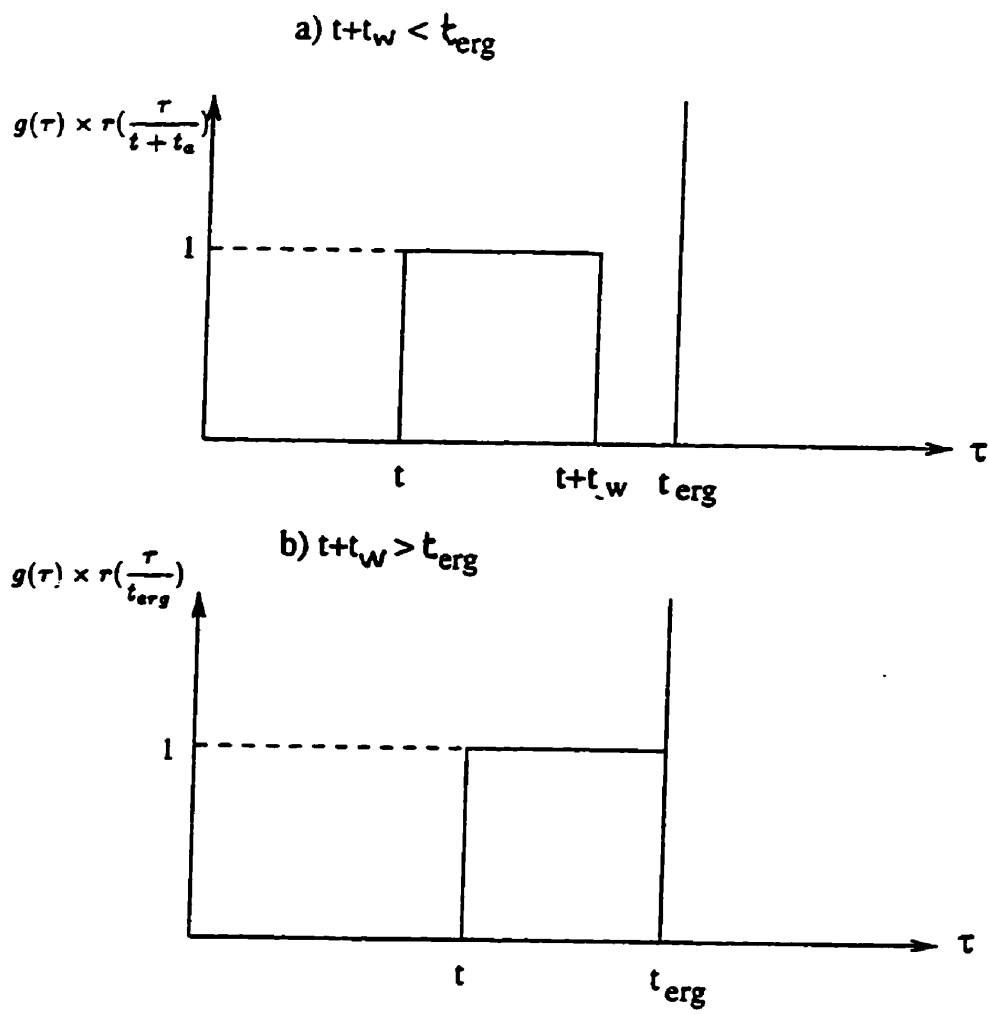


Figure 2.14: The "pulse" which defines the calculation of $\langle 1/\tau \rangle$. a) $t+t_w < t_{erg}(S)$, b) $t+t_w > t_{erg}(S)$.

the total magnetization is the superposition of that in each subsystem:

$$M(t) = M_0 \left\{ \int_0^{t_w} dt_{erg} P(t_{erg}) \exp[-\gamma \int_0^t t^{-x}(t+t_{erg})^{x-1} dt] \right. \\ \left. + \int_{t_w}^{\infty} dt_{erg} P(t_{erg}) \exp[-\gamma \int_0^t t^{-x}(t+t_w)^{x-1} dt] \right\}. \quad (2.111)$$

By factoring out the purely nonergodic t_w -dependent exponent, this equation can be recast as the product of a universal function $f(t/t_w)$ and a non-universal correction factor $1 - F$ which describes the deviation from the $\frac{t}{t_w}$ -scaling:

$$M(t) = M_0 \underbrace{\exp[-\gamma \int_0^t t^{-x}(t+t_w)^{x-1} dt]}_{f(t/t_w)} \cdot \left\{ 1 - \right. \\ \left. \underbrace{\int_0^{t_w} dt_{erg} P(t_{erg}) \left[1 - \exp \left(-\gamma \int_0^t t^{-x}(t+t_{erg})^{x-1} dt + \gamma \int_0^t t^{-x}(t+t_w)^{x-1} dt \right) \right]}_F \right\} \quad (2.112)$$

Thus, a plot of $M(t)/(M_0(1 - F))$ versus t/t_w should restore universality.

In practice, we choose a log-normal distribution of ergodic times:

$$P(\log_{10} t_{erg}) = \frac{1}{\sqrt{2\pi\sigma_{erg}^2}} \exp \left[-\frac{(\log_{10} t_{erg} - \overline{\log_{10} t_{erg}})^2}{2\sigma_{erg}^2} \right] \quad (2.113)$$

where $\sigma = \sigma_{erg}$ is the half-width of the distribution (see Figure 2.15). To calculate the correction factor numerically, we divide the integration range into 32 intervals, each of width $\sigma/4$, and take 32 discrete points. We define

$$X \equiv \log_{10} t_{erg} \quad (2.114)$$

$$X_0 \equiv \overline{\log_{10} t_{erg}} \quad (2.115)$$

$$X_n = X_0 + (n - \frac{32}{2}) \frac{\sigma}{4} \quad (2.116)$$

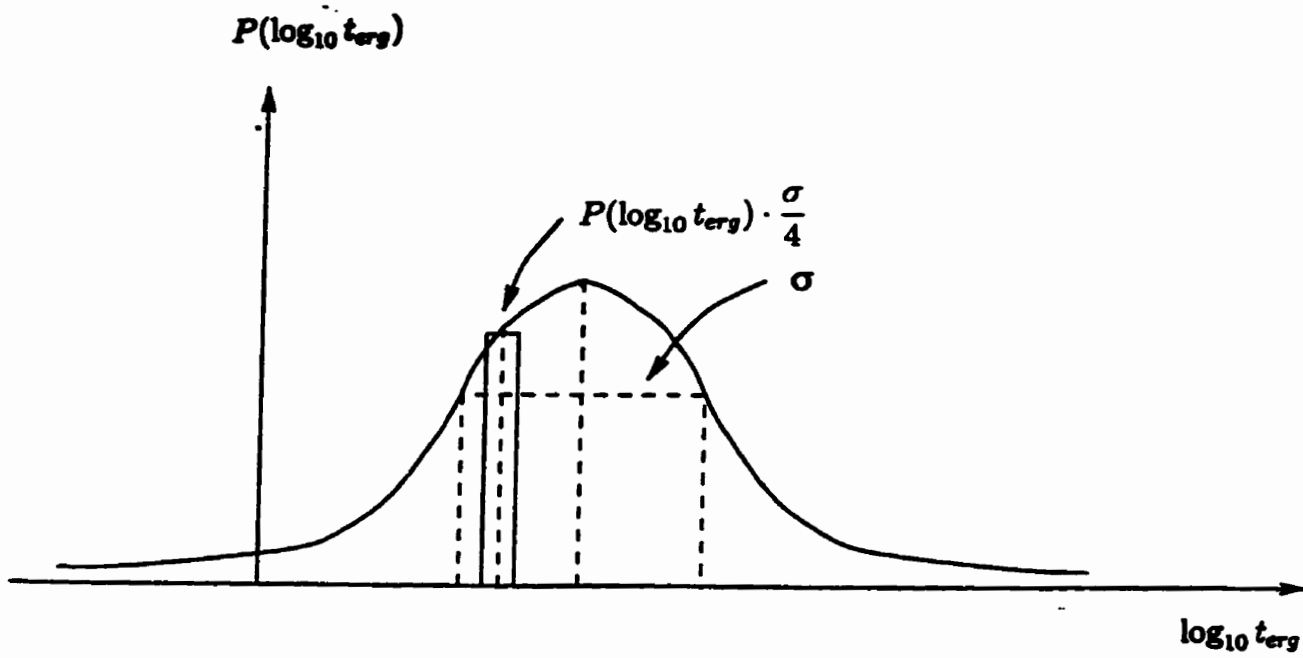


Figure 2.15: A distribution $P(\log_{10} t_{erg})$ vs. $\log_{10} t_{erg}$.

and convert the integration over t_{erg} into a sum over the 32 intervals, so that the correction factor F is computed from:

$$F = \sum_{n=1}^{32} P(\log_{10} t_{erg}) \cdot \frac{\sigma}{4} \cdot \left[1 - \exp \left(-\gamma \int_0^t t^{-x} (t + t_{erg})^{x-1} dt + \gamma \int_0^t t^{-x} (t + t_w)^{x-1} dt \right) \right] \quad (2.117)$$

2.7 The Elementary Decay Model (EDM)

Recently, Erhart et al. (1994a; 1994b) presented an elementary decay model for relaxation in disordered systems based on the simple assumption that the initial activation energy barrier distribution in a disordered system has a Poissonian form,

$$f_0(E) = \frac{1}{\bar{E}} e^{-E/\bar{E}} \quad (2.118)$$

where \bar{E} is the average energy. This is actually consistent with Parisi's RSB solution of the SK model (Mezard et al., 1985). Each energy fraction decays independently with an Arrhenius rate,

$$r = r_0 e^{-E/T}, \quad (2.119)$$

so that, following a step function change in field, a physical observable $X_E(t)$ changes as:

$$\frac{dX_E(t)}{dt} = -r(E)X_E(t). \quad (2.120)$$

Integrating,

$$\int_1^{X_E} \frac{dX_E(t)}{X_E} = - \int_0^t r(E) dt \quad (2.121)$$

yields

$$X_E(t) = X_{0E}e^{-rt} = X_{0E}e^{-(r_0e^{-E/T})t}. \quad (2.122)$$

For a disordered system, $X(t)$ will be a superposition of decays for all E , so,

$$X(t) = X_0 \int_0^\infty f_0(E) \exp[-r_0t \exp(-E/T)] dE \quad (2.123)$$

$$= X_0 \int_0^\infty \frac{1}{\bar{E}} \exp(-E/\bar{E}) \exp[-r_0t \exp(-E/T)] dE \quad (2.124)$$

If we make the following variable changes:

$$\tau \equiv r_0t \quad (2.125)$$

$$s \equiv r_0t \exp(-E/T) = \tau \exp(-E/T) \quad (2.126)$$

$$b \equiv \frac{T}{\bar{E}} \quad (2.127)$$

then,

$$X(t) = X_0 \int_\tau^0 \frac{1}{\bar{E}} e^{\frac{T}{\bar{E}} \ln(\frac{\tau}{s})} e^{-s} \left(-\frac{T}{s}\right) ds \quad (2.128)$$

$$= X_0 b \tau^{-b} \int_0^\tau s^{b-1} e^{-s} ds \quad (2.129)$$

so,

$$X_0(t)/X_0 = b \tau^{-b} \int_0^\tau s^{b-1} e^{-s} ds = b \tau^{-b} \gamma(b, \tau) \quad (2.130)$$

$$= g(b, \tau) = g_b(\tau), \quad (2.131)$$

where $\gamma(b, \tau) = \int_0^\tau s^{b-1} e^{-s} ds$ is known as the *incomplete gamma function*.

The single parameter $b = T/\bar{E}$ determines the shape of the curve and hence the type of the decay: nearly logarithmic for $b \ll 1$, but with the correct values

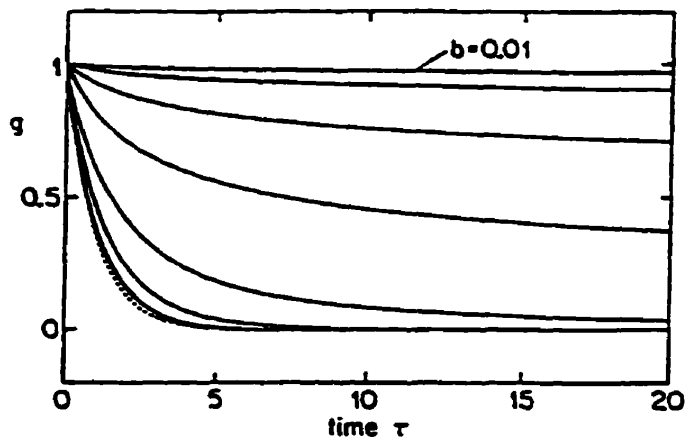


Figure 2.16: Normalized decay function $g(b, \tau) = X(\tau)/X_0$ against normalized time $\tau = r_0 t$ with global rate r_0 , displayed for the values $b = kT/\bar{E}$ (from top) 0.01, 0.03, 0.1, 0.3, 1, 3, 10. The broken curve corresponds to $\exp(-\tau)$. From Erhart et al. (1994a)

of one and zero for $t = 0$ and $t \rightarrow \infty$, respectively, a power law for intermediate values of $b \sim 1$, but starting at one, and approximately exponential behaviour for $b \gg 1$. Figure 2.16 illustrates these functions in a linear plot in order to show both the initial and limiting behaviour, and Figures 2.17 and 2.18 plot the function in various ways in order to show the similarities to simpler functions.

These simple functional forms show “memory” effects if we plot them versus a delayed time t_d defined by $t = t_d + t_w$, as shown in Figure 2.19. The derivative of a logarithmic decay will then show an inflection point around $t_d \cong t_w$, and the derivative of a power law decay will exhibit a peak at $t_d = t_w/b$. The latter is very similar to the aging peak observed in real spin glass systems.

In the EDM, the aging process is attributed to changes in the activation energy distribution itself during the wait time t_w . In order to make a connection between the physical process and its mathematical representation, we can write the total time after the quench as the sum of two parts $t = t_w + t_d$, where t_d is the

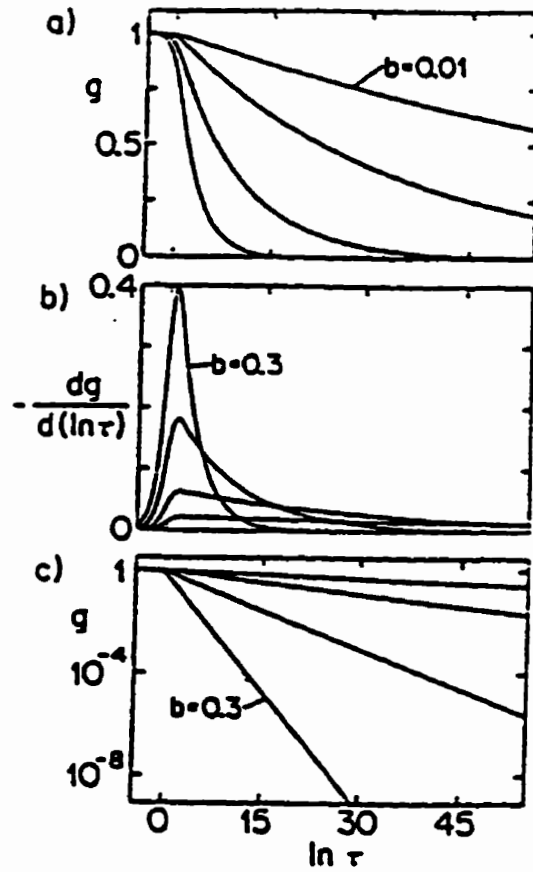


Figure 2.17: Decay function $g(b, \tau)$ for $b = 0.01, 0.03, 0.1, 0.3$. (a) $g(b, \tau)$ against $\ln \tau$; (b) derivative $-dg/d(\ln \tau)$ against $\ln \tau$; (c) regions close the power law $g \propto \tau^{-b}$ are shown in a ln-ln plot: $\ln g(b, \tau)$ against $\ln \tau$. From Erhart et al. (1994a)

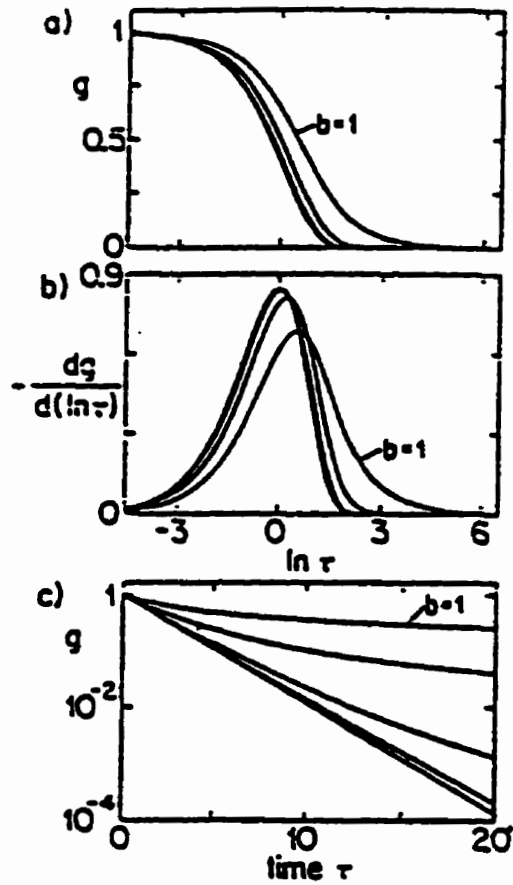


Figure 2.18: Similar to figure 2.17, but for b values (a), (b) $b = 1, 3, 10$ and (broken curves) $\exp(-\tau)$; except (c) regions close to exponential $\exp(-\tau)$ are shown in a ln-linear plot $\ln g(b, \tau)$ against τ for $b = 1, 3, 10, 30$, and (broken curve) $\exp(-\tau)$. From Erhart et al. (1994a)

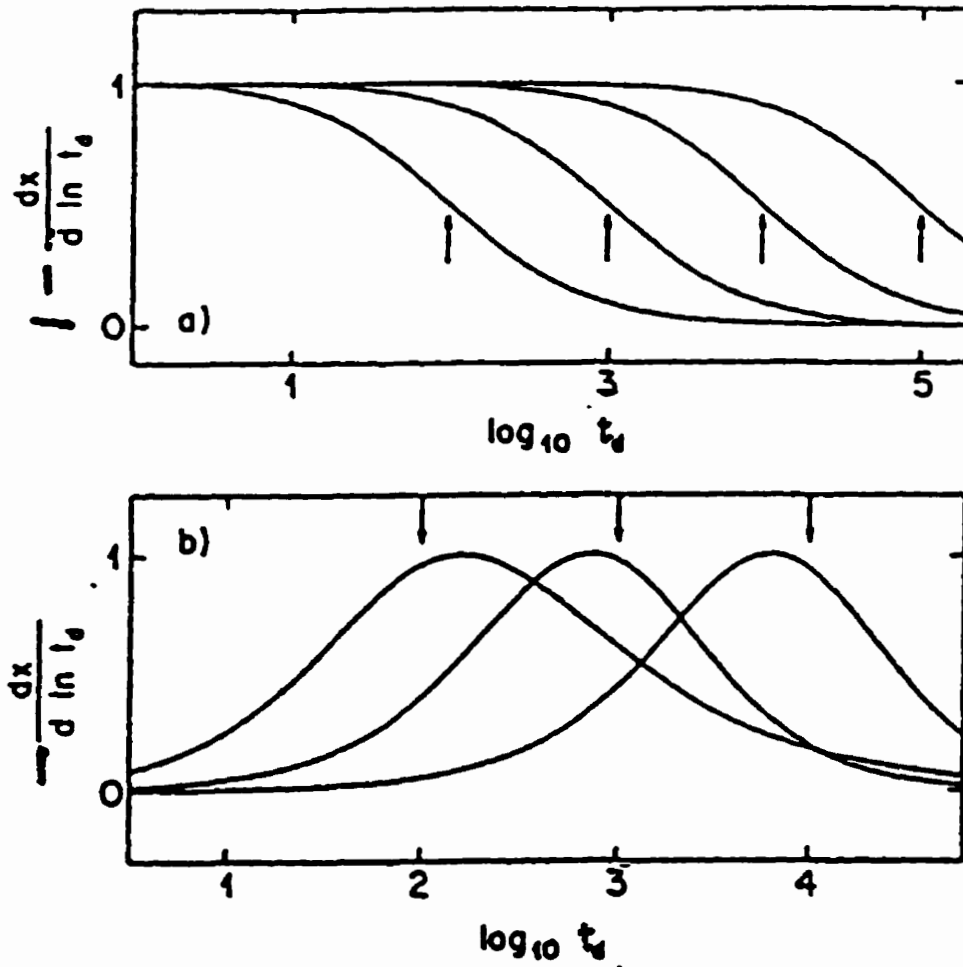


Figure 2.19: 'Memory' effect without a second step when the derivative $-dx/d(\ln t_d)$ of non-exponential functions $x(t)$ are plotted as a function of the *logarithm* of a *delayed* time t_d with $t = t_d + t_w$. (a) Derivative $-dx/d(\ln t_d)$ of a logarithmic decay $x(t) = 1 - \ln t$ against $\log_{10} t_d$ for $t_w = 10^q$ with $q = 2, 3, 4, 5$ (arrows). Note the inflection points at $t_d = t_w$. (b) Derivative $-dx/d(\ln t_d)$ of the power law $x(t) = t^{-b}$ against $\log_{10} t_d$ for $t_w = 100, 1000, 10000$ (arrows) and $b = 0.6, 1.3, 1.5$, respectively. Note the extrema at $t_d = t_w/b$. From Erhart et al. (1994b)

delayed time, or the observation time starting at the moment of the step function field change. Equation (2.123) then becomes:

$$X'_{t_w}(t_d) = X'_0 \int_0^\infty f'_0(E, t_w) \exp[-t_d r_0 \exp(E/T)] dE \quad (2.132)$$

where X'_0 is the initial value of $X'_{t_w}(t_d)$ at $t_d = 0$, and f'_0 is the renormalized wait time (t_w) dependent distribution,

$$f'_0(E, t_w) = \frac{f_0(E) \exp[-t_w r_0 \exp(-E/T)]}{\int_0^\infty f_0(E) \exp[-t_w r_0 \exp(-E/T)] dE}. \quad (2.133)$$

If we make variable changes in function (2.132) as before, the age-dependent decay then becomes:

$$\frac{X'_{\tau_w}(\tau_d)}{X'_0} \equiv g'_{b, \tau_w}(\tau) = \frac{g_b(\tau = \tau_w + \tau_d)}{g_b(\tau = \tau_w)}. \quad (2.134)$$

When $b \sim 1$, the derivative of this function has a peak at $\tau_d = \tau_w/b$, as shown in Figure 2.20.

In fitting real spin glass data, we must superpose two components: one with aging and with a t_w built-in, and one with no aging, as follows:

$$g_{aging} = (1 - c)g'_1(b_1, \tau_{in1}; \tau_d + \tau_w) + cg'_2(b_2, \tau_{in2}; \tau_d) \quad (2.135)$$

so,

$$M(t, t_w) = M_0 \left\{ (1 - c) \frac{g_1(b_1, \tau = r_0(t + t_w + t_{in1}))}{g_1(b_1, \tau = r_0(t_w + t_{in1}))} + c \frac{g_2(b_2, \tau = r_0(t + t_{in2}))}{g_2(b_2, \tau = r_0 t_{in2})} \right\}. \quad (2.136)$$

There are 7 parameters in this function. They represent respectively:

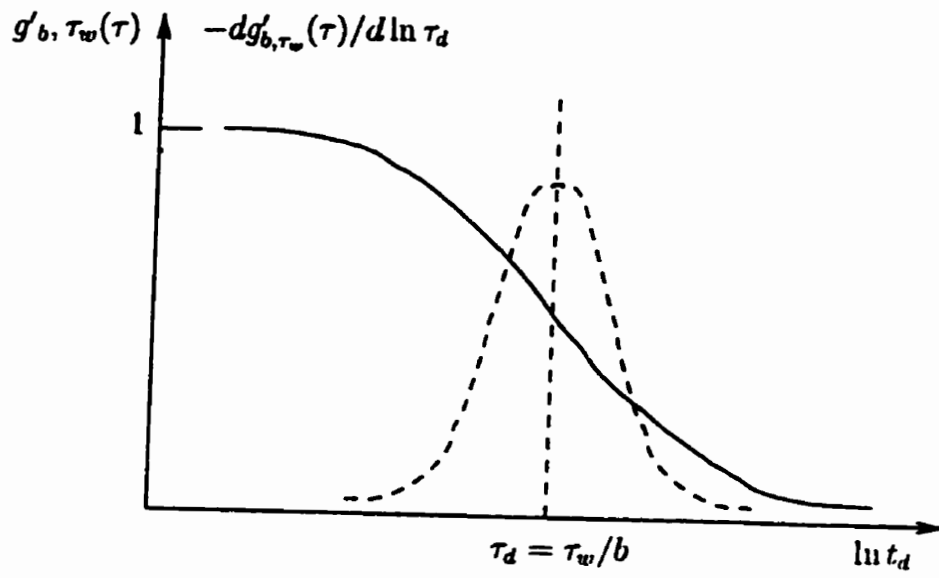


Figure 2.20: $g'_{b, \tau_w}(\tau)$ and $-dg'_{b, \tau_w}(\tau)/d \ln \tau_d$ versus $\ln \tau_d$

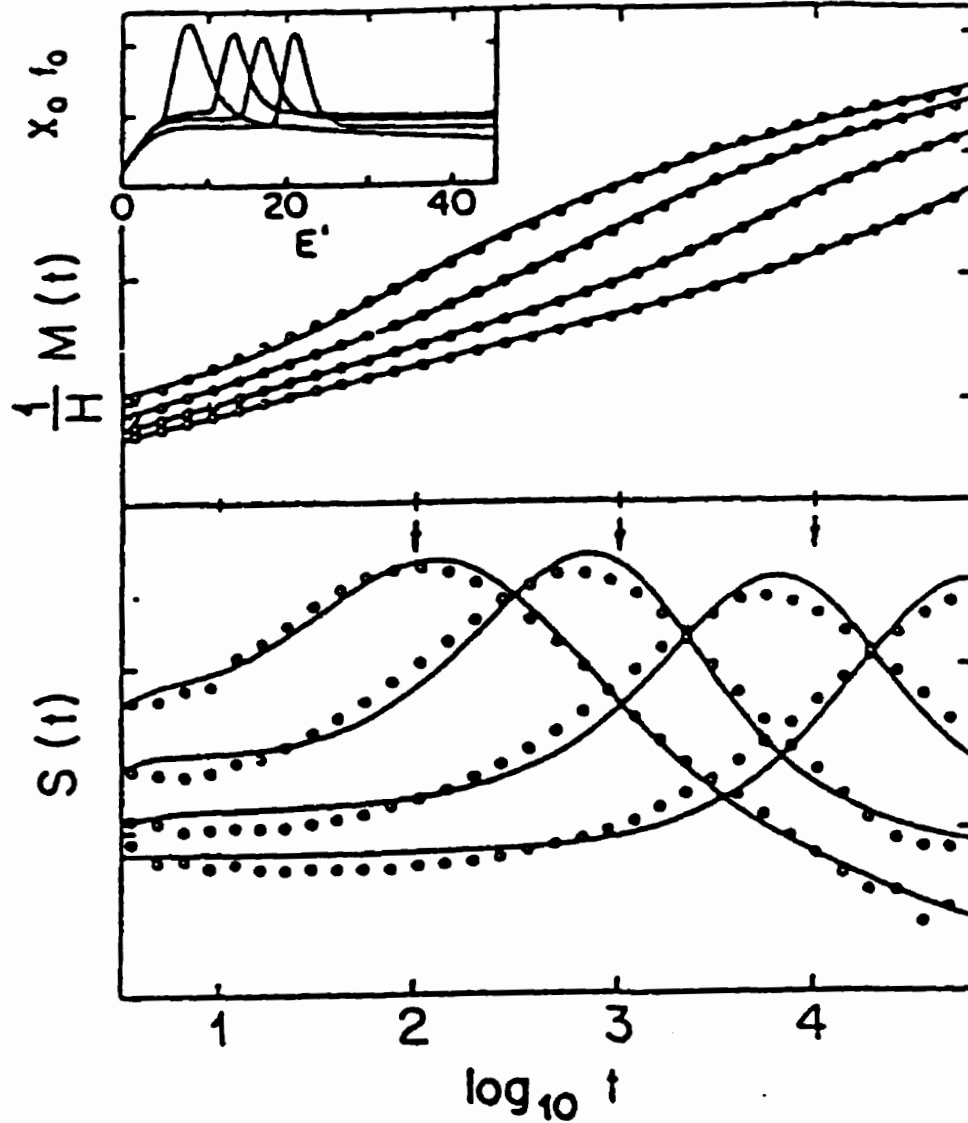


Figure 2.21: 'Aging' effect in the amorphous metallic spin glass $(\text{Fe}_x\text{Ni}_{1-x})_{75}\text{B}_{16}\text{P}_6\text{Al}_3$. Points: zero field cooled susceptibility $[(1/H)M(t)]$ and corresponding relaxation rate $[S(t) = (1/H)dM/d \ln t]$ at different waiting times $t_w = 10^2, 10^3, 10^4$, and 10^5 sec) plotted against $\log_{10} t$ where $t = t_d$ starts at the field step to $H = 0.1$ G. Curves: fits with function (2.136) of the EDM with the above t_w , and $b_1 = 0.6, 1.3, 1.5, 2.7$; $b_2 = 0.02, 0.02, 0.01, 0.01$; $r_{0,1,2} = 0.7, 0.7, 0.9, 1.4$; $t_{in,1} = 4, 8, 3, 5$ s; $t_{in,2} = 1.5, 1.5, 0.8, 2.1$ s; $c = 0.976, 0.977, 0.949, 0.932$; $X_0 = 1.1, 1.0, 0.4, 0.3$; respectively. Inset: distribution function $X_0 f_0(E')|_{t_d=0}$ of activation energies $E' = E/T$ evaluated with the above EDM parameters. From Erhart (1994b).

- M_0 - the initial value of the magnetization at $t_d = 0$
- c - the proportion of aging and non-aging components
($c = 1$ corresponds to no aging)
- b_1 - the type of decay for the aging component (generally $b_1 \sim 1$)
- b_2 - the type of decay for the non-aging component (generally $b_2 \ll 1$)
- t_{in1} - a correction to the aging time, which might be due to the influence of a finite cooling time
- t_{in2} - a similar correction for the non-aging component
- r_0 - a normalizing factor, which is very insensitive and is usually fixed at 1

The most crucial parameters are c , b_1 and b_2 . These determine essentially all the decay characteristics.

As an example, Figure 2.21 shows the fitting results for an amorphous metallic sample $(\text{Fe}_x\text{Ni}_{1-x})_{75}\text{B}_{16}\text{P}_6\text{Al}_3$, using the function $M(t, t_w) = M_0(1 - g_{aging})$, which is an increasing function rather than a decay function in Eq.(2.136).

2.8 A Percolation Model for Magnon Relaxation

Chamberlin and Haines (1990) proposed another model for glassy dynamics, which is based on the activated relaxation of dispersive excitations in a percolation distribution of finite-sized domains or clusters. This model gives good fits to the magnetic relaxation of spin-glass and ferromagnetic systems, and also to stress relaxation in a structural glass (Chamberlin et al., 1991a; 1991b), over a broad range of measurement times from 10^{-4} to 10^4 seconds.

The model defines a dynamically correlated domain (DCD) as a local region where excitations relax with a single uniform relaxation rate, and considers this to be the primary relaxation response. Secondary response like domain growth, domain rotation, and domain wall motion are ignored. Assuming a distribution of domain sizes n_s , size-dependent relaxation rates w_s , and a size-dependent initial response P_s , where s is the number of spins in one domain, the net relaxation is

the weighted sum over all sizes:

$$M(t) = \sum_{s=0}^{\infty} (P_s n_s) \times e^{-w_s t}. \quad (2.137)$$

The equilibrium response is proportioned to the number of responding particles $P_s = P_0 s$, so

$$M(t) = P_0 \sum_{s=0}^{\infty} s n_s e^{-w_s t}. \quad (2.138)$$

If a given spin is assumed to be correlated with at least one of its neighbors with probability p , percolation theory provides specific predictions for the distribution of finite domains. For $p > p_c$ where p_c is the critical probability for bond percolation in three dimensions (Lubensky et al., 1981),

$$(s n_s) \propto s^{10/9} \exp[-(C's)^{2/3}] \quad (2.139)$$

where $C' \propto |p - p_c|^{1/\sigma}$ and $\sigma = 0.45$. For activated relaxation of quantized systems at temperature T , $w_s \propto e^{-\delta E/k_B T}$. All dispersive excitations in finite systems have an average energy-level spacing δE which is inversely proportional to the number of particles in the system. This is simply a statement that since s discrete levels fill a fixed bandwidth Δ , $\delta E = \Delta/s$, where Δ depends only on the average interaction between spins, independent of domain size. (see Figure 2.22). Using $x = C's$, the net relaxation becomes

$$M(t) = M_i \int_0^{\infty} x^{10/9} \exp(-x^{2/3}) \exp(-t w_{\infty} e^{-C/x}) dx \quad (2.140)$$

where the adjustable parameters are $C = C'\Delta/k_B T$, which is called the correlation coefficient, the initial response $[3\Gamma(\frac{19}{6})/2]M_i = 3.518M_i$, and w_{∞} the relaxation rate for the infinite domain. Although the average-sized domains $[\bar{x} = (\frac{19}{6})^{3/2}]$ produce the dominant behaviour, for $C \gg 1$ the spectrum is extremely broad.

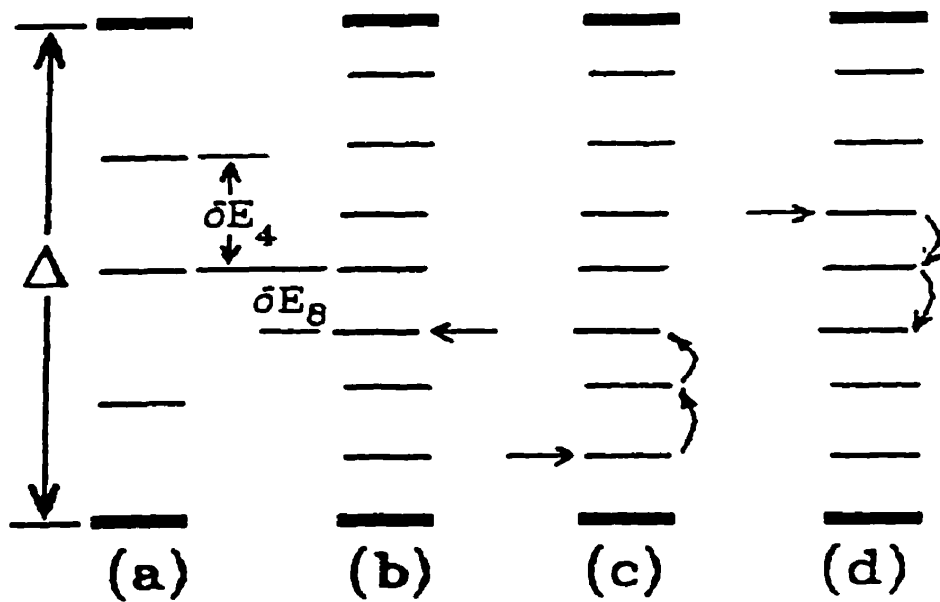


Figure 2.22: Schematic representation of excitation levels in a finite cluster. The bandwidth, Δ , is fixed by the average interaction between particles. (a) and (b) The average energy-level spacing, δE , varies in inverse proportion to the number of particles in the cluster. (b) At equilibrium, all cluster have the same average internal energy. (c) for 'aligned' clusters, the energy of which was reduced by an external perturbation, the internal increases toward equilibrium. (d) The internal energy of 'antialigned' clusters decreases when the external perturbation is removed. From Chamberlin (1991b).

A ferromagnetic sample cooled from the paramagnetic regime in zero external field contains domains oriented in all possible directions, resulting in no net magnetization. At finite temperatures, the magnetic moment of each domain is reduced from saturation by magnon excitations. The average magnon density is uniform for all zero-field-cooled domains, but the level of excitation in field-cooled domains depends on their orientation. "Aligned" domains have a reduced density of magnons, so that their net internal energy *increases* after H is removed. In this case $\delta E > 0$ and larger energy level spacings hinder the relaxation process, so smaller domains relax more slowly, and $w_{al} = w_- \exp(-C_-/x)$ with $C_- > 0$, where w_- is the relaxation rate of the largest domain. Aligned domains have $C > 0$; they need not be aligned with H but in general will be oriented with the local field. Similarly "antialigned" domains have their ground state magnetic moment opposite in direction to H and have an initially higher level of excitation, which *decreases* during relaxation. In this case $\delta E < 0$, and a larger energy level spacing expedites the relaxation process, so smaller domains relax faster and $w_{anti} = w_+ \exp(+C_+/x)$ with $C_+ > 0$. Thus, two separate equations can be used to describe the relaxation of aligned and antialigned domains:

$$M(t) = M_i \int_0^\infty x^{10/9} \exp(-x^{2/3} \exp(-tw_+ e^{C_+/x})) dx \quad (2.141)$$

$$M(t) = M_i \int_0^\infty x^{10/9} \exp(-x^{2/3} \exp(-tw_- e^{-C_-/x})) dx \quad (2.142)$$

where w_- is the fastest relaxation rate of the largest aligned domains, and w_+ is the slowest relaxation rate of the largest antialigned domains. As a test of this model, Chamberlin fitted the predicted decay to a sample of Au 11.9%at:Fe. Figure 2.23 shows that Eq.(2.141) fits the measured relaxation curves above the transition temperature very well, which means this relaxation may be due to domains with

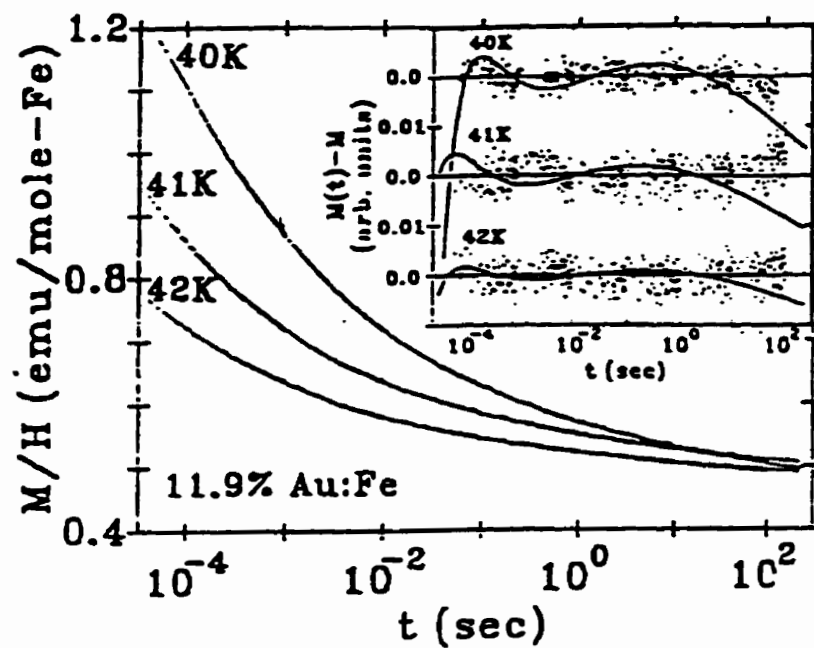


Figure 2.23: Magnetic relaxation of sample 11.9%at Au:Fe at 3 temperatures above the transition $T_m = 39$ K. The solid curves are the best fits using Eq.(2.141) over the range $10^{-4} - 10$ sec. Extrapolation to shorter and longer times reveals no systematic deviation. Inset: Difference between Eq(2.141) and the data. The best fits by a simple power law (solid curves) are shown for comparison. From Chamberlin (1990).

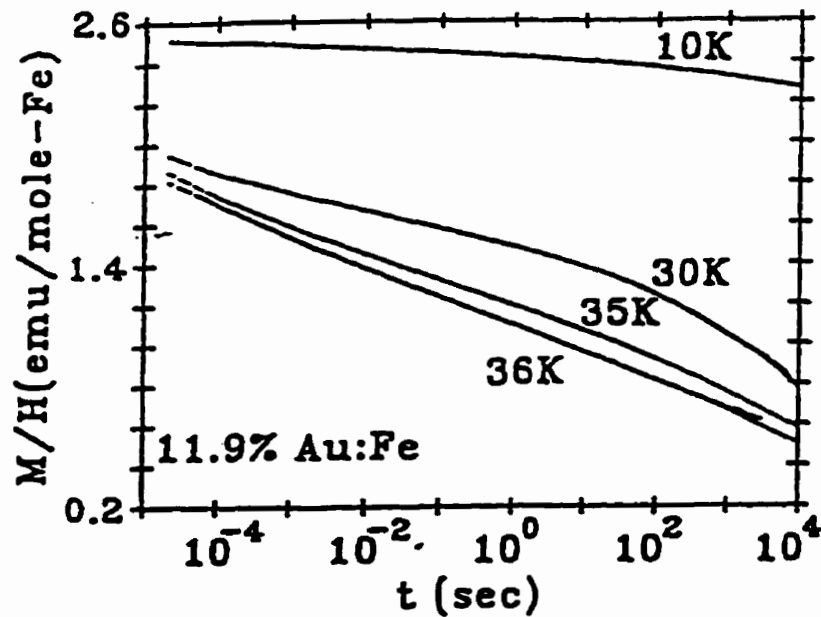


Figure 2.24: Magnetic relaxation of 11.9% Au:Fe at 4 temperatures below $T_m = 39$ K. The solid curves are the best fits using Eq.(2.141) + Eq.(2.142) over the range $10^{-1} - 10^2$ sec. From Chamberlin (1990).

pure ferromagnetic order, or domains whose ground state magnetic moment was aligned with H .

However, below the transition temperature, both functions (2.141) and (2.142) are needed to fit the relaxation curves, as shown in Figure 2.24.

2.9 Comments on These Relaxation Models

If the energy of a system in some particular state can be characterized by a single value E_i , for example a ferromagnet described by its site average magnetic moment and with energy $-\mathbf{m}_i \cdot \mathbf{H}$ in a magnetic field \mathbf{H} , then when this state changes to another state characterized by equilibrium energy E_j the system will

relax to the new state by a conventional Debye function

$$q(t) = q_0 \exp(-t/\tau) \quad (2.143)$$

where τ is a characteristic time related to the energy barrier between the two states. But in a disordered system, usually there is a complex structure of metastable states, each with a corresponding metastable energy and a corresponding relaxation time τ_i connecting it to the new state. So, the whole system is some superposition of the behaviour of each metastable state. Any superposition of simple Debye functions will result in a non-Debye form for the anomalous relaxation,

$$q(t) = \int_0^{\infty} P(\tau) \exp(-t/\tau) d\tau \quad (2.144)$$

where $P(\tau)$ is the characteristic time distribution of a real system. This is the common feature of all disordered systems. For example, Aharoni (1985) suggested a gamma-distribution function for $P(\tau)$

$$P(\tau) = \frac{1}{\tau_0 \Gamma(p)} \left(\frac{\tau}{\tau_0}\right)^{p-1} e^{-\tau/\tau_0} \quad (2.145)$$

for a disordered system, where p and τ_0 are adjustable parameters, which yields the following relaxation function for the magnetization:

$$\sigma(t) = \sigma(0) \frac{2}{\Gamma(p)} \left(\frac{t}{\tau_0}\right)^{p/2} K_p \left[2\left(\frac{t}{\tau_0}\right)^{1/2}\right] \quad (2.146)$$

where K_p is the modified Bessel function of the third kind (Watson, 1962). This function fits experiment reasonably well (Aharoni et al., 1985; 1992).

But a good theory should not only be able to give a quantitative description, but must also give the physical reasons underlying the choice of distribution: For example, a stretched exponential form

$$q(t) = q_0 \exp\left[-\left(\frac{t}{\tau}\right)^{1-n}\right], \quad 0 < n < 1 \quad (2.147)$$

is widely used to describe the anomalous relaxation in various materials (Ngai, 1980; Chamberlin, 1984; Ngai et al., 1991; Ruan, 1993). The fitting results are always quite good. This function was shown by Palmer et al. (1984) to be a consequence of *hierarchically constrained dynamics*, and by De Dominicis et al. (1985) to be a characteristic of relaxation with a distribution of independent *random free energy levels*. Both parameters τ and n have very complicated forms and they are the combinations of many micro-parameters. So, from the results for τ and n , it is difficult to understand the physical process. However, the stretched exponential form is still the most powerful and the simplest description of much anomalous relaxation behaviour. The other models discussed in this chapter are more physical and provide a better understanding of the physics behind the dynamics, especially the aging effects.

Fisher and Huse's **droplet scaling model** is based on the assumption that a spin glass has only two ground states, which contradicts the long-range SK model. It explains the aging effect and why, at $t = t_w$ the relaxation rate $dM/d \ln t$ has a peak. This model represents pioneering work in the study of relaxation dynamics, and gives a physically appealing explanation for the dynamic response, but does not yield complete relaxation functions valid for all observation times t which can be used to fit experimental data.

Bouchaud's **random trap model** and Erhart et al's **EDM** both give relaxation functions which can quantitatively describe the relaxation curves very well (Bouchaud, 1992;1994; Erhart, 1994a, 1994b; also see next chapter). An important feature of these two models is that they have a simple aging mechanism built in, and do not require the addition of a constant baseline to the relaxation function, which is necessary in both the stretched exponential and Chamberlin's percolation model descriptions, and which is hard to justify physically.

Both models have parameters which are related to the distribution of

metastable state energies: x in the random trap model, and b in the EDM model. The rate of aging as a function of temperature (that is the fact that aging is more effective at higher measurement temperatures) is also a feature of these two models: in the random trap model, we introduced a distribution of ergodic times to describe the difference in the aging rate at different temperatures. At different temperatures the fraction of active (or non-ergodic) subsystems with aging, and equilibrium (or ergodic) subsystems without aging, are different. In the EDM, a similar parameter c , also controls the proportion of the aging and non-aging components in the system.

These two models also have stretched exponential and simple power law features. In the random trap model, if we expand function (2.109)

$$m = m_0 e^{-\gamma \int_0^t t^{-x} (t+t_w)^{x-1} dt} \quad (2.148)$$

for $t \ll t_w$, we get

$$m \propto e^{-\frac{\gamma}{1-x} (\frac{t}{t_w})^{1-x}} \quad (2.149)$$

which is a stretched exponential function, while for $t \gg t_w$

$$m \propto (\frac{t}{t_w})^{-\gamma} \quad (2.150)$$

which is a power law. In the EDM model, if $b \gg 1$, the EDM function is a stretched exponential, while if $b \sim 1$, it is a power law (Erhart, 1994a).

Chamberlin's percolation model gives a reasonable fit to the relaxation curves, but it is necessary to add a constant baseline. Furthermore, this model has no explicit aging time t_w built in, so it is difficult to appreciate the relationship between the model parameters and aging. However, this model also shows stretched exponential and simple power law behaviour in some limits: for $Cw_-t \gg 1$, Eq(2.141) becomes a simple power law $m(t) \sim t^{-\alpha}$; for $Cw_+t \leq 1$

Eq(2.142) is a stretched exponential $m(t) \sim \exp(-t^\beta)$. (Chamberlin and Haines, 1990).

Chapter 3

Sample Preparation and Measurement Techniques

3.1 Magnetic Properties and Sample Preparation

As stated in section 1.2, the conduction-electron-mediated RKKY interaction between the transition-metal impurities yields the strongest impurity-impurity coupling. These kinds of materials exhibit the archetypal properties of disordered magnetic systems, like anomalously slow relaxation, aging, and so on. They are ideal systems for the purpose of our experiments. We have chosen one binary system, CrFe, and two ternary (pseudo-binary) systems, FeNiCr and FeNiMn, for our investigations. In this section I will first discuss their magnetic properties, then their phase diagrams, finally the sample preparation procedure for each system.

3.1.1 The FeNiCr System

i) Magnetic properties and phase diagram

FeNiCr alloys in the γ -range are widely used as commercial Elinvar and even more importantly as austenitic stainless steels. Therefore, the magnetic properties of this system have been extensively studied (Majumdar et al., (1984); Deryabin et al., (1984, 1985, 1987); Acet et al. (1987, 1988); Takei et al. (1984, 1986, 1987)). Figure 3.1 shows the magnetic phase diagram. Along the rim of the FM-range, FeNiCr alloys show reentrant spin glass(RSG) behaviour at low temperatures (hatched area) with a pure spin glass(SG) region adjacent to it (dotted area).

Figure 3.2 shows the differential magnetic susceptibility $\chi = dm/dh$ of alloys in the series $\text{Fe}_{65}\text{Ni}_{35-x}\text{Cr}_x$, for $x = 0, 5, 10, 15$. The results show that for $x = 0$, which is the classical Invar alloy, the ordering is purely ferromagnetic, and there is no spin-glass state. The alloys with $x = 5$ and 10 are ferromagnetic at high temperatures, and have a reentrant spin glass state at low temperatures. The peaks at the higher temperatures for $x = 5$ and 10 correspond to the critical peaks from the ferromagnetic phase transition. For $x = 15$, where a pure spin glass with $T_{SG} \simeq 15$ K. The Curie temperatures for each concentration x of Cr are shown in Figure 3.3.

Figure 3.4 is the magnetic phase diagram of another series of alloys $\text{Fe}_{30-x}\text{Ni}_x\text{Cr}_{20}$. We can see from the diagram that for $x = 19$ and 21 , the system is a spin glass at low temperatures because the concentration of Ni is too low to support long-range ferromagnetism. For larger values of x , like $x = 23$ and 26 , the system evolves from a long-ranged ferromagnetic state to a mixed (FM + SG) state as the temperature is lowered.

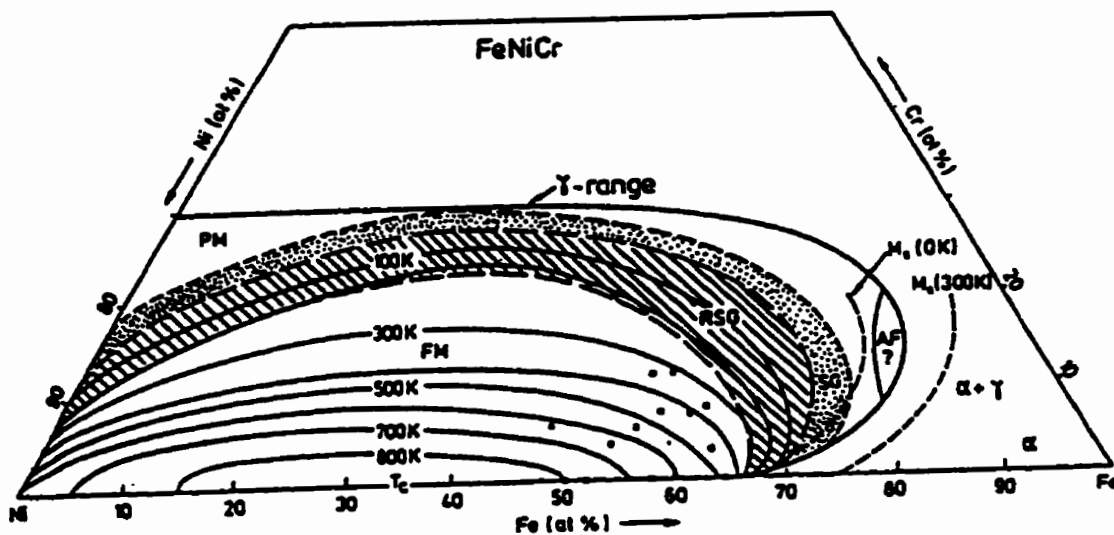


Figure 3.1: Ternary magnetic phase diagram of FeNiCr in the γ -range. The full lines show contours of constant Curie-temperature projected into the zero Kelvin plane. RSG-area is shown hatched, the pure SG- area dotted. Crosses in the FM region mark commercial Invar and Elinvar compositions. From Wassermann (1980).

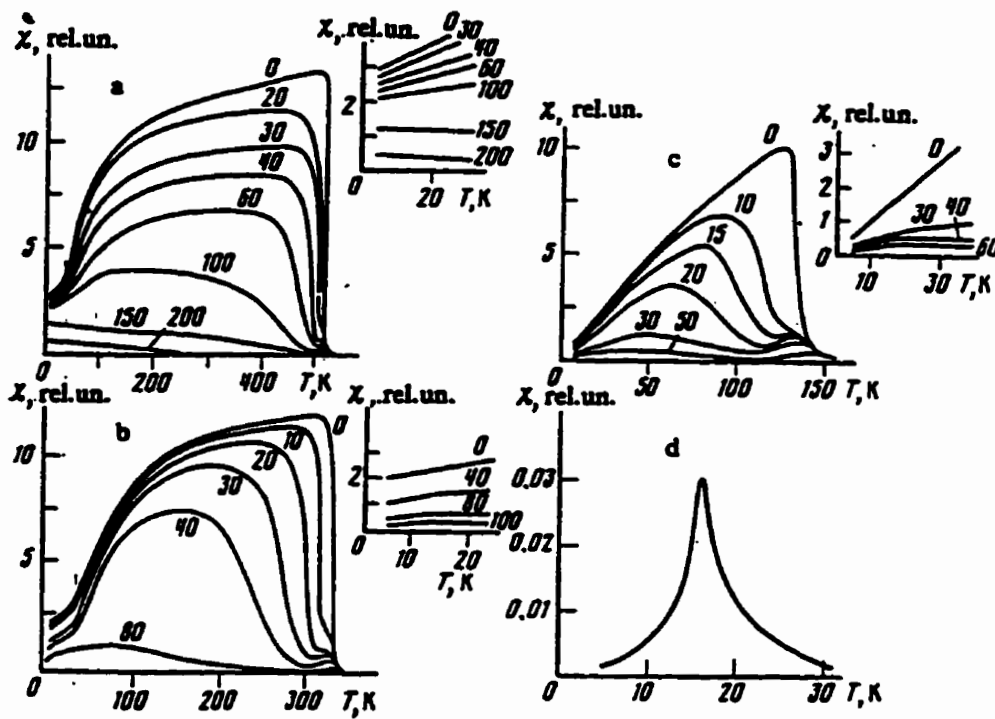


Figure 3.2: Temperature dependence of the differential magnetic susceptibility of $\text{Fe}_{65}\text{Ni}_{35-x}\text{Cr}_x$ alloys with $x = 0$ (a), 5 (b), 10 (c) and 15 (d). The numbers on the curves indicate the value of the external constant field in Oe. From Deryabin et al. (1984).

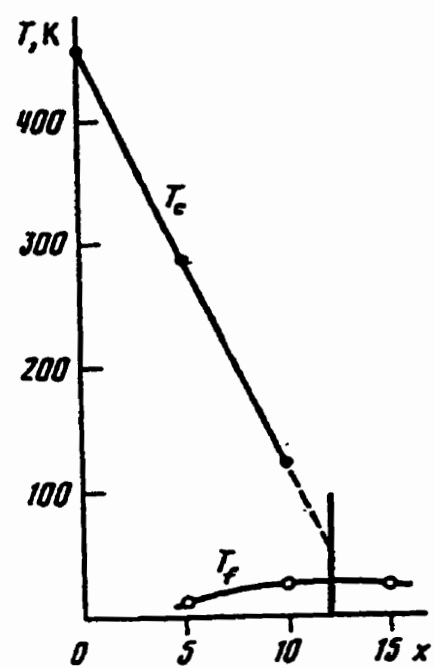


Figure 3.3: Magnetic phase diagram of the system $\text{Fe}_{65}\text{Ni}_{35-x}\text{Cr}_x$. From Deryabin et al. (1984).

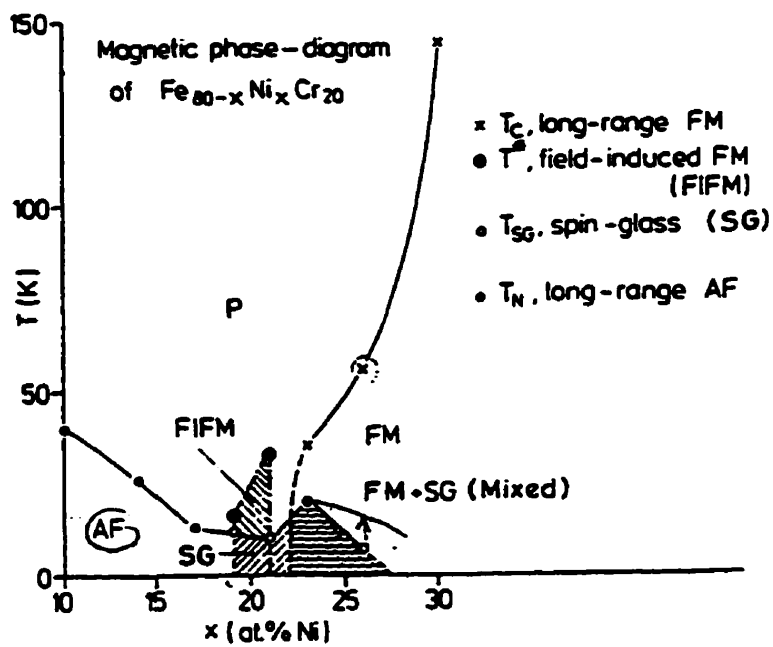


Figure 3.4: Temperature (T) vs Ni concentration (x in units of at.%) magnetic phase diagram of $\text{Fe}_{80-x}\text{Ni}_x\text{Cr}_{20}$ alloys ($10 \leq x \leq 30$). From Majumdar et al. (1984).

ii) Sample preparation

A total of eight different concentrations of FeNiCr alloys were prepared from the two series $\text{Fe}_{0.65}\text{Ni}_{0.35-x}\text{Cr}_x$ with $x = 0.10, 0.11, 0.12, 0.13, 0.15$, and $\text{Fe}_{0.80-x}\text{Ni}_x\text{Cr}_{0.20}$ with $x = 0.21, 0.24, 0.26$, by melting the appropriate amounts of 99.99% pure Fe foil, 99.995% pure Ni foil, and 99.99% pure Cr chunks, all supplied by Aldrich Chemical Company Inc., on the water cooled copper hearth of an argon arc furnace, using a tungsten electrode and a titanium getter.

Pre-melting of each pure metal showed that they are all stable with negligible losses during the melting. The melting and boiling points of each metal are shown in Table 3.1. An etching reagent was used to clean surface contamination from the metals and the alloys after each melt, and was also used to reduce the amounts of the pure metals to get the precise amount needed for the alloys. The ingots were inverted and remelted ~ 5 to 6 times to ensure homogeneity, then cold rolled into a thin sheet from which the samples were spark cut. Sand-paper was used to smooth the surface of the samples or to make them even thinner.

The samples were put into small vycor tubes. The tubes were vacuumized and sealed under a partial argon atmosphere (160 Torr) and placed into a furnace at a temperature of $T_{ann} = 1000^\circ\text{C}$, annealed (t_{ann}) for 4 days, and then quenched rapidly (t_q) (in ~ 1 second) into cold water by breaking the tube. The sample parameters are listed in Tables 3.2 and 3.3.

Table 3.1: Physical and chemical properties of Fe, Ni, Cr, Mn and their alloys.

	Melting point (°C)	Boiling point (°C)	Etching reagent
Fe	1535	2750	aqua regia: HCl:HNO ₃ :H ₂ O = 3:1:2 + a few drops of H ₂ O ₂
Ni	1453	2732	pure HNO ₃
Cr	1857	2672	pure HCl (37%)
Mn	1244	1962	HNO ₃ :H ₂ O = 1:5
FeNiCr alloys	-	-	HCl:HNO ₃ :H ₂ O:glycerol = 2:1:3 + a few drops of H ₂ O ₂
CrFe alloys	-	-	HCl:HNO ₃ :glycerol = 2:1:3 + a few drops of H ₂ O ₂
FeNiMn alloys	-	-	HNO ₃ :H ₂ O = 1:5

Table 3.2: Fe_{0.65}Ni_{0.35-x}Cr_x samples. (Typical dimensions are 8×0.4×0.3 mm³ if they are not listed).

<i>x</i>	dimensions a×b×c (mm ³)	m (mg)	T _{ann} (°C)	t _{ann} (days)	t _q (s)
10		5.6	950	4	1
		6.5	950	4	1
		7.1	950	4	1
11	needle, a=8.2	1.6	1040	4	1
	needle, a=8.1	2.1	1040	4	1
	needle, a=9.2	2.7	1040	4	1
12		4.9	1000	4	1
		5.2	1000	4	1
		5.6	1000	4	1
13		4.0	1000	4	1
		5.0	1000	4	1
		6.0	1000	4	1
15		7.4	1000	4	1
		8.9	1000	4	1
		9.0	1000	4	1

Table 3.3: $\text{Fe}_{0.80-x}\text{Ni}_x\text{Cr}_{0.20}$ samples. (Typical dimensions are $8 \times 0.4 \times 0.3 \text{ mm}^3$ if they are not listed).

x	dimensions $a \times b \times c \text{ (mm}^3\text{)}$	m (mg)	T_{ann} ($^{\circ}\text{C}$)	t_{ann} (days)	t_g (s)
21		9.3	1000	4	1
		10.7	1000	4	1
24		5.1	1000	4	1
		6.1	1000	4	1
		6.6	1000	4	1
26		6.1	1000	4	1
		7.9	1000	4	1
		8.2	1000	4	1

3.1.2 The CrFe System

i) Magnetic properties and phase diagram

The magnetic properties of the $\text{Cr}_{1-x}\text{Fe}_x$ system have been well studied (Burke and Rainford, 1983; Burke et al., 1983; Fukusaka, 1986) and the magnetic phase diagram is reasonably well established (Burke et al., 1983) as shown in Figure 3.5. Its principal features are as follows: for Fe concentrations $x < 0.16$ the system is an itinerant antiferromagnet, with a crossover from incommensurate to commensurate spin density wave order above $x \simeq 0.023$, a spin glass in the narrow range between $0.16 < x < 0.19$, and a ferromagnet for $x \leq 0.19$, with a reentrant sequence between $0.19 \leq x \leq 0.25$.

Figure 3.6 shows the susceptibility of samples of Cr-17.5 at% Fe and Cr-19.5 at% Fe. The two curves are remarkably similar, both showing a sharp asymmetric peak at 30 K. Closer examination of the 19.5 at% Fe data reveals a slight shoulder between 40 and 60 K which is absent in the 17.5 at% Fe data. This shoulder gives a weak maximum in $d\chi/dT$ at 44 K (Burke et al., 1983). It is suggested that this point corresponds to a ferromagnetic phase transition. This

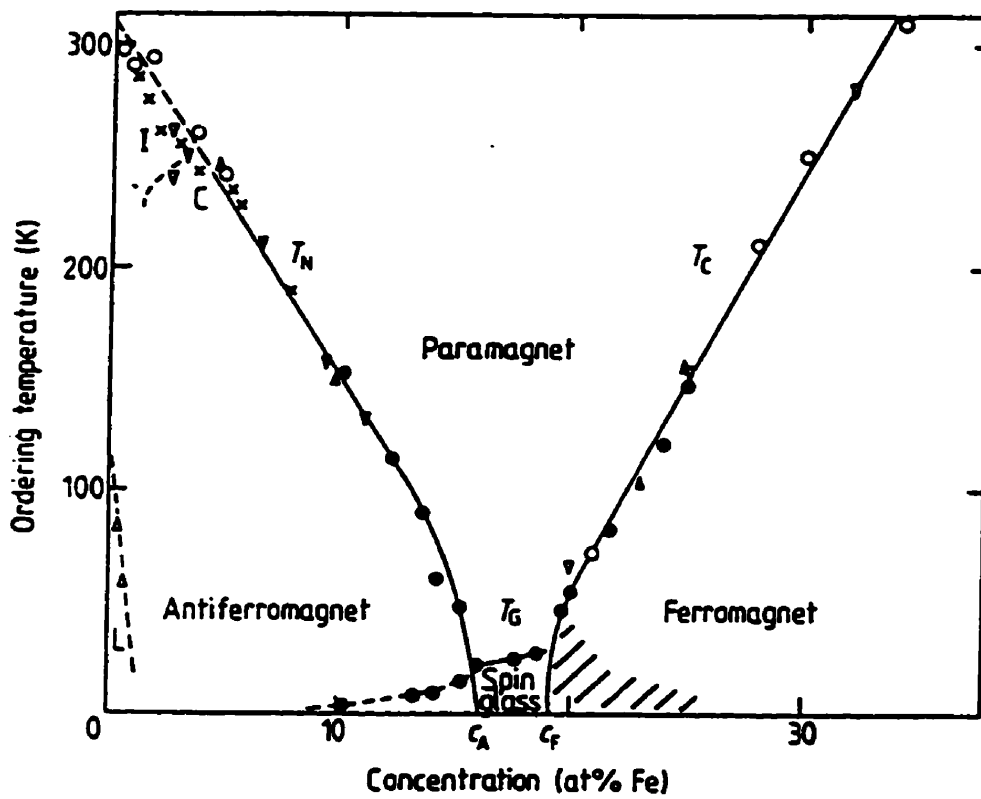


Figure 3.5: Magnetic phase diagram for $\text{Cr}_{1-x}\text{Fe}_x$ alloys. Complex magnetic properties are observed in the hatched region. From Burke et al. (1983).

is supported by neutron small-angle scattering (Fig.3.6). So the sample Cr-19.5 at% Fe is a re-entrant ferromagnet with a Curie temperature $T_C \cong 44$ K and a reentrant glass temperature $T_{SG} \simeq 30$ K. The absence of a shoulder in Cr-17.5 at% Fe suggests that it is a pure spin glass with $T_{SG} \simeq 30$ K.

Figure 3.7 shows several more concentrated samples. They are all typical reentrant ferromagnets. The arrows indicate the Curie temperatures determined by neutron small-angle scattering.

ii) Sample preparation

The $\text{Cr}_{1-x}\text{Fe}_x$ samples were prepared by using a similar procedure to that in section 3.1.2.. 99.99% pure Fe wire and 99.99% pure Cr chunks were obtained from Aldrich Chemical Company Inc.. A master alloy containing $x = 0.24$ was prepared first and given an homogenizing anneal at $T_h = 1160$ °C for $t_{ann} = 4$ days and cooled slowly to room temperature. After the anneal, the ingot was spark-cut into small pieces, which were used to make the remaining alloys by dilution with pure Cr. Melting losses were negligible(0.001 out of 4) at all times. After cleaning with a solution(see Table 3.1), the samples were spark cut from the individual ingots. Finally, these samples were sealed in vycor tubes under a partial argon atmosphere (160 Torr) and placed inside a furnace at $T_{ann} = 1160$ °C for 4 days, then quenched rapidly by breaking the tube in cold water. The parameters of the samples are shown in Table 3.4.

Table 3.4: $\text{Cr}_{1-x}\text{Fe}_x$ samples.

x (at%)	dimensions $a \times b \times c$ (mm ³)	m (mg)	T_{ann} (°C)	t_{ann} (days)	t_q (s)
21.0	7.26×0.44×0.27	6.5	1130	4	1
22.0	8.37×0.42×0.41	11.4	1160	4	1

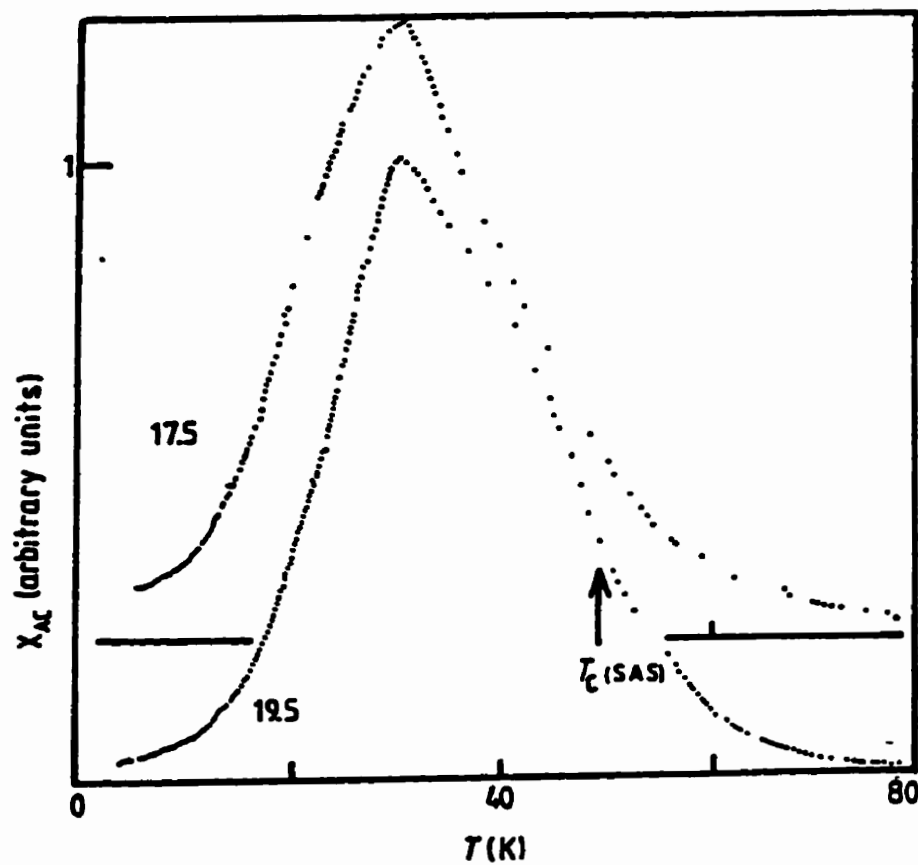


Figure 3.6: AC susceptibility of Cr-17.5 at% Fe and ferromagnetic Cr-19.5 at% Fe as a function of temperature. The two curves have been displaced for clarity. The Curie temperature determined by neutron small-angle scattering (SAS) for the 19.5 at% alloy is shown by an arrow. Alloy concentrations (at% Fe) are indicated. From Burke et al. (1983).

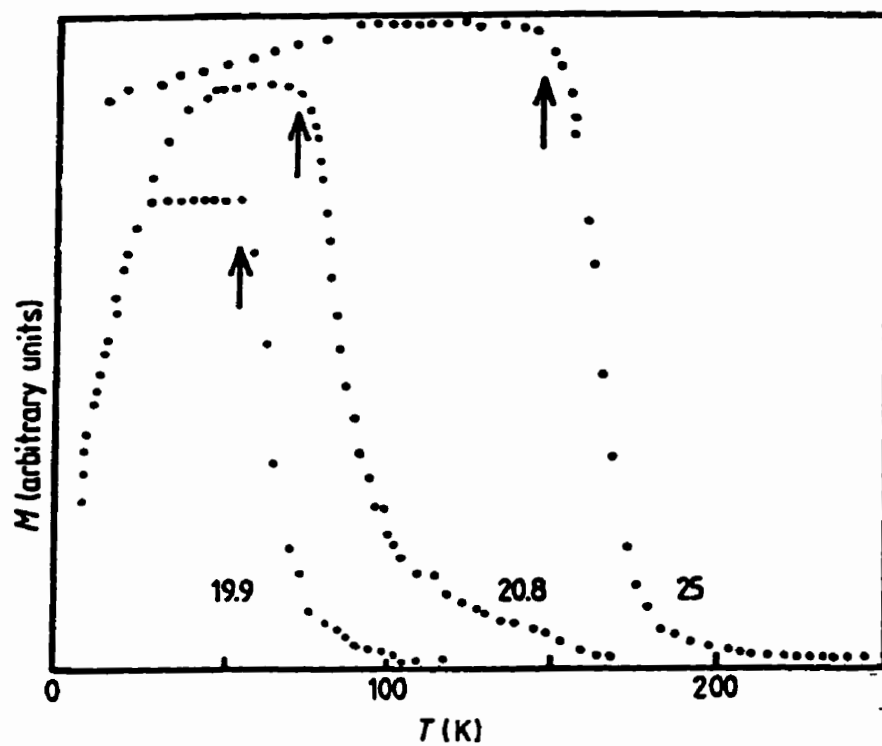


Figure 3.7: Low-field magnetization of ferromagnetic Cr-19.9 at% Fe, Cr-20.8 at% Fe and Cr-25 at% Fe alloys. Magnetization in an applied field of 10 Oe is shown as a function of temperature. The Curie temperatures determined by neutron small-angle scattering (SAS) are indicated by arrows. Alloy concentrations (at% Fe) are indicated. From Burke et al. (1983).

3.1.3 The FeNiMn System

i) Magnetic properties and phase diagram

Figure 3.8 shows the magnetic phase diagram of the FeNiMn ternary system. The system exhibits a wide range of fcc γ -stability, with exceptions at the corners of Fe (α Fe and low temperature ϵ -martensite), Mn (α Mn) and around the ordered phase of NiMn.

Very recently Wulfes (1992) investigated the magnetic phase diagram of the system $(\text{Fe}_{0.65}\text{Ni}_{0.35})_{1-x}\text{Mn}_x$ ($0 \leq x \leq 0.30$) in detail. The results are shown in Figure 3.9. For low Mn concentrations ($x < 0.02$) the system behaves like a normal ferromagnet. At high temperatures there is a paramagnetic-ferromagnetic transition, characterized by a Curie temperature T_C below which the system is purely ferromagnetic. With increasing Mn concentration, the value of T_C decreases rapidly. Between the Mn concentrations $0.02 \leq x \leq 0.06$, a second phase transition with a characteristic temperature T_m (≤ 20 K) is observed below T_C , and this phase can be interpreted as a mixed ferromagnetic and spin glass phase. In the Mn concentration range $0.06 \leq x \leq 0.14$, a third characteristic temperature $T_{im} < T_m$ is observed. On cooling from high temperatures the system exhibits the following transitions: paramagnet \leftrightarrow ferromagnet \leftrightarrow mixed ferromagnet and spin glass \leftrightarrow spin glass. At a Mn concentration $x \approx 0.14$, the Curie temperature T_C and T_{im} reach the same value, and the ferromagnetic phase vanishes. This is a first triple point in the phase diagram. In the range of $0.14 \leq x < 0.20$ the system behaves as a pure spin glass. There is a transition from paramagnetism to a spin glass at about $T_m \approx T_{im} \approx 50$ K. There is a second triple point in the magnetic phase diagram at $x \approx 0.20$. For higher Mn concentrations $x \geq 0.20$ a new characteristic temperature is observed. The system shows reentrant antiferromagnetic behaviour: there is an antiferromagnetic phase, probably mixed with spin glass components, and a spin glass phase at low temperatures.

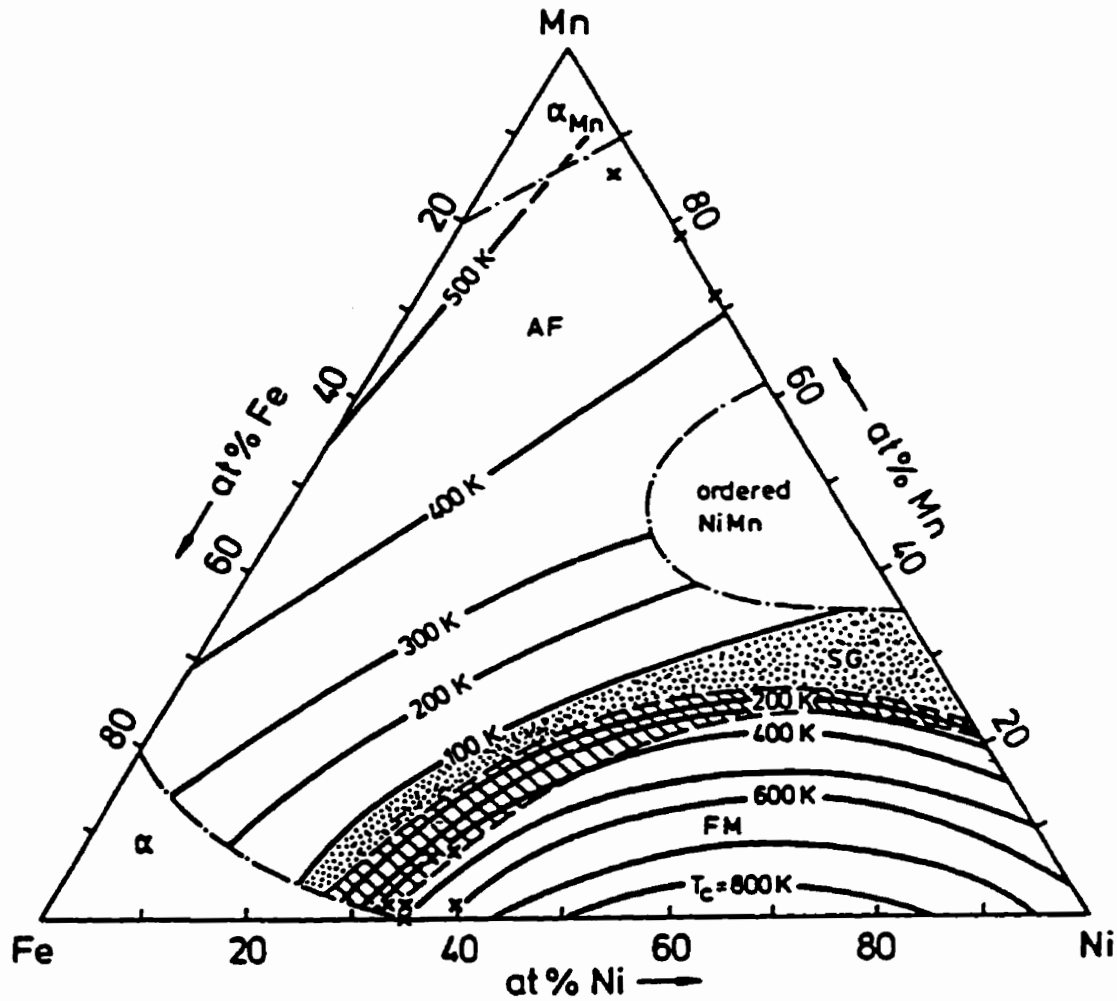


Figure 3.8: Magnetic phase diagram of the ternary system FeNiMn in the fcc γ -phase. Contour lines for constant Néel-temperatures T_N in the antiferromagnetic AF-phase and Curie-temperature T_c in the ferromagnetic FM-phase are shown. The dotted region marks a pure spin-glass SG-phase separating the AF- and FM-regions. The hatched region gives the area of a reentrant-spin-glass RSG-phase, which occurs below the FM ordering. Crosses mark commercial Invar and Elinvar compositions. From Wassermann (1980).

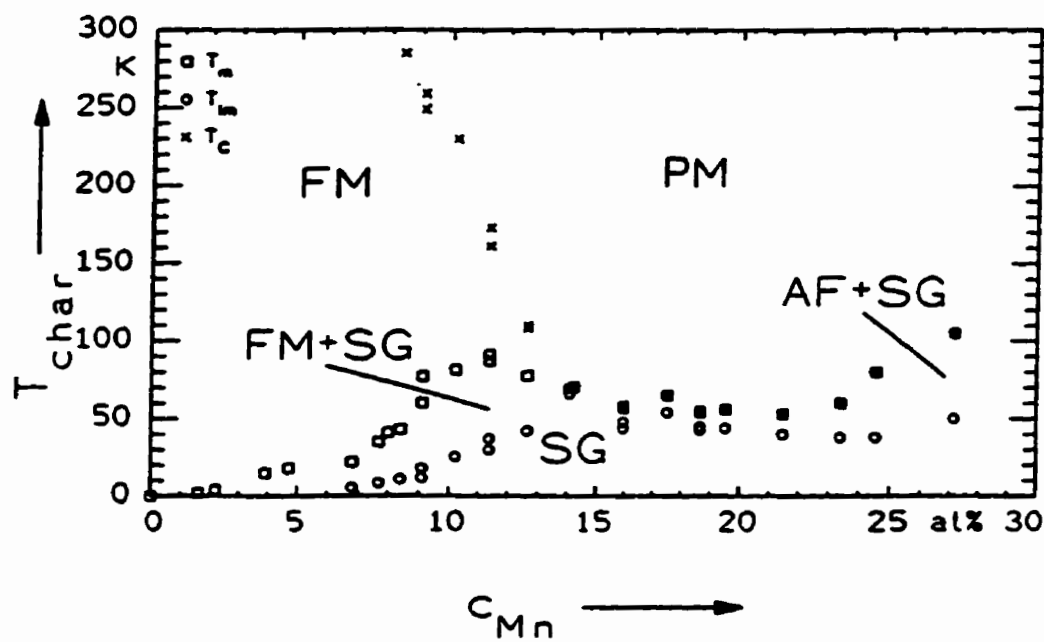


Figure 3.9: Magnetic phase diagram for the alloy system $(\text{Fe}_{0.65}\text{Ni}_{0.35})_{1-x}\text{Mn}_x$ extrapolated to $B_{\text{ext}} = 0$ (T) showing the dependence of the characteristic temperature (T_m , T_{im} , T_C) versus Mn concentration. From Wulfes et al. (1992)

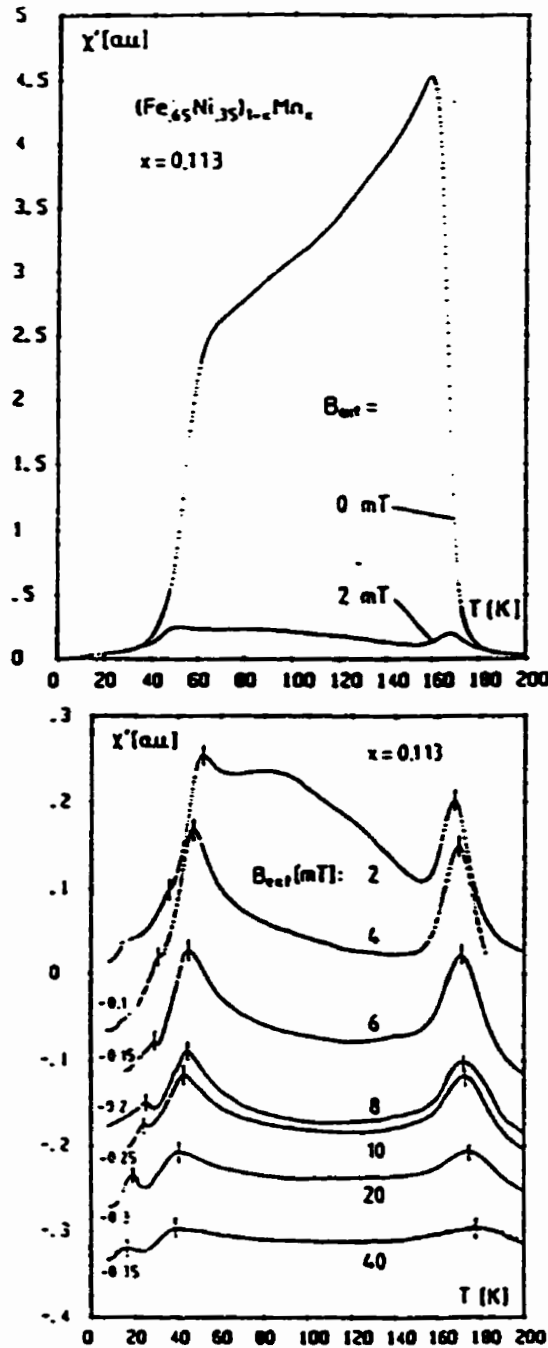


Figure 3.10: (a) AC susceptibility vs. temperature ($\nu = 137$ Hz, $H_{0,ac} = 5.5$ A/m) for $(\text{Fe}_{0.65}\text{Ni}_{0.35})_{0.887}\text{Mn}_{0.113}$. The measurement without an external dc field shows a ferromagnetic-like Hopkinson maximum just below T_C and an anomalous break down below 60 K. Note the large influence of the small external dc field on the amplitude of the χ' -signal. (b) AC susceptibility vs. temperature in external dc fields. At 2 mT there are two well defined peaks at $T_{R,i}$ and T_C . With increasing external field the low temperature peak is split into two peaks indicating a different field dependence of T_i and T_R . From Huck et al.(1988).

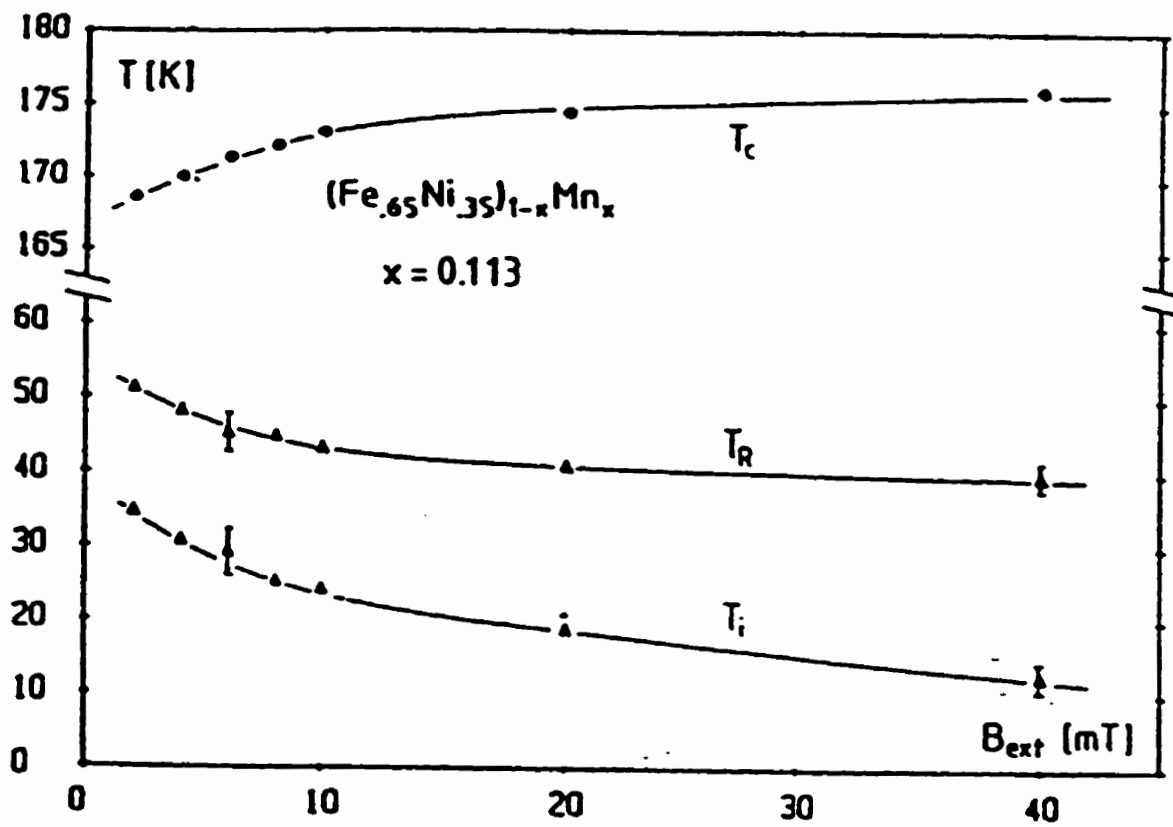


Figure 3.11: Field dependence of the three characteristic temperatures T_c , T_R and T_i . The extrapolations $T_R(B \rightarrow 0)$ and $T_i(B \rightarrow 0)$ deliver different zero field values indicating an intrinsic anisotropy of the spin system. From Huck et al. (1988).

The characteristic temperatures T_C , T_m and T_{im} are identified by structure of the temperature dependence of the magnetization or susceptibility. The structure is very dependent on the concentration of Mn and the external D.C. biasing field. An example is shown in Figure 3.10, for the A.C. susceptibility of a reentrant $(\text{Fe}_{0.65}\text{Ni}_{0.35})_{0.987}\text{Mn}_{0.113}$ ferromagnet in various D.C. biasing fields. The characteristic temperatures $T_C > T_m$ (T_R in the diagram) $> T_{im}$ (T_i in the diagram) are defined by the locations of the three peaks in susceptibility, extrapolated to zero field, as shown in Figure 3.11.

ii) Sample preparation

The $(\text{Fe}_{0.65}\text{Ni}_{0.35-x})_{1-x}\text{Mn}_x$ alloys were prepared by using a similar procedure to that in section 3.1.2.. The pure elements 99.99% pure Fe wire, 99.997% pure Ni foil, and 99.99% pure Mn flakes were supplied by Aldrich Chemical Company Inc.. First, an alloy of $\text{Fe}_{0.65}\text{Ni}_{0.35}$ called INVAR was prepared. Then, by adding the appropriate amount of Mn into the INVAR, we fabricated a master alloy with Mn containing $x = 0.187$. The master alloy was then given an homogenizing anneal at $T_h = 1100$ °C for 3 days and cooled slowly to room temperature. After the annealing, a 1:5 solution of $\text{HNO}_3/\text{H}_2\text{O}$ was used to remove the surface contamination from the ingot. The final concentration of Mn in the master alloy was calculated after considering the high stability of INVAR, and attributing the melting, etching and annealing losses primarily to Mn, which vapourized relatively easily (Mn has a low boiling point as shown in table 3.1). Other concentrations of Mn were prepared by diluting the master alloy with pure Mn.

The ingots were cold rolled into sheets, from which the samples were spark-cut. Finally, these samples were sealed in vycor tubes under a partial argon atmosphere (160 Torr) and placed into a furnace at $T_{ann} = 900$ °C for 4 days, then quenched rapidly by breaking the tube into cold water. The parameters of

the samples are shown in Table 3.5.

Table 3.5: $(\text{Fe}_{0.65}\text{Ni}_{0.35})_{1-x}\text{Mn}_x$ samples.

x (at%)	dimensions $a \times b \times c$ (mm ³)	m (mg)	T_{ann} (°C)	t_{ann} (days)	t_q (s)
18.7	5.33×0.89×0.81	30.0	900	4	1
11.8	8.14×0.36×0.24(A)	5.8	920	4	1
	7.18×0.54×0.21(B)	6.9	920	4	1

3.2 Apparatus and Measurement Techniques

Magnetic phase transitions in disordered magnetic systems often occur well below room temperature, and the magnetic signals are weak. So we need a cryogenic environment and a high resolution, high sensitivity SQUID (Superconducting QUantum Interference Device) probe to perform the measurements. In this section I will introduce the apparatus of the SQUID Magnetometer which I used in my experiments.

3.2.1 The ⁴He Cryostat

The measuring core of the apparatus is immersed in a liquid helium dewar, and connected to the vacuum system, measurement electronics and the temperature control unit. Figure 3.12 shows the configuration of the ⁴He cryostat. At the bottom, a wooden box filled with sand rests on four rubber feet ($\sim 4''$ high and $\sim 8''$ in diameter). This base reduces the mechanical vibrations. The aluminum frame rests in the sand box and supports the nitrogen dewar by four aluminum rods, and also supports the helium dewar which is fixed to the top of the frame. The sample chamber, the SQUID sensor, remote terminal board and pick-up coils, and the D.C. solenoid coils are inserted together as a unit through the top of the

helium dewar. The helium dewar is vacuum sealed at its upper flange.

Two mechanical pumps, MP1 (Sargent Welch Model 1402) and MP2 (Alcatel Model 2033), and an oil vapour diffusion pump are used to produce a vacuum in the sample chamber in the helium dewar and in the vacuum space of the helium dewar. Figure 3.13 shows the flow diagram of the pumping system. Before the system is cooled, the helium dewar is flushed and pumped with N_2 gas 5 to 6 times using MP2, to reduce the partial pressure of air, and then filled with N_2 gas to slightly over one atmosphere. The vacuum space of the helium dewar is flushed and pumped with air 5 to 6 times using MP1, and then sealed under a partial vacuum (7-8 mTorr). This partial pressure is helpful in cooling the inside of the helium dewar when transferring the liquid nitrogen in the beginning, and the small quantity of air freezes very quickly after the temperature is lowered to produce a good vacuum between the walls of the helium dewar. The sample chamber is also flushed with N_2 gas 5 to 6 times using MP1 and pumped until 100 K after the liquid nitrogen transferred. The pressure of the helium dewar is measured with a thermocouple gauge TC3. The pressure of the sample chamber is measured with a thermocouple gauge TC1 and an ionization gauge I (Model 270 Gauge Controller, Granille Phillips). TC2 measures the pressure in the vacuum space of the helium dewar.

After the sample rod is inserted into the sample chamber, and the sample chamber is flushed with N_2 gas, both MP1 and the diffusion pump are used to reduce the pressure in the sample chamber.

Next the liquid nitrogen is transferred into the nitrogen dewar and the sample begins to cool. The sample chamber is pumped continuously until the temperature of the sample reaches 250 K (this requires about 2 hours), where the outgassing of the sample, due to mostly the G.E. varnish and Ag paint used to glue the sample to the sample rod, becomes insignificant. Then ~ 200 mTorr

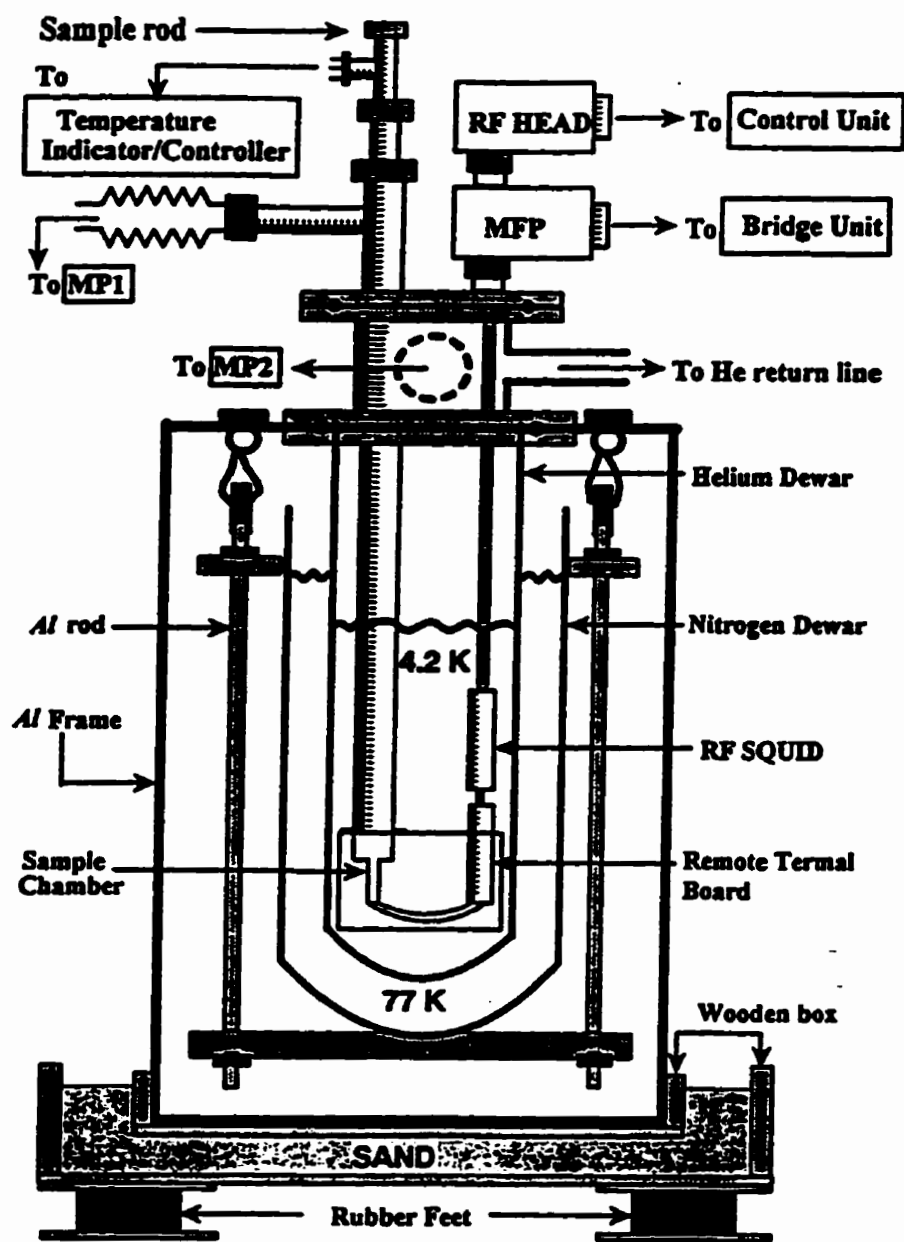


Figure 3.12: ^1He Cryostat. From W. Ruau (1993).

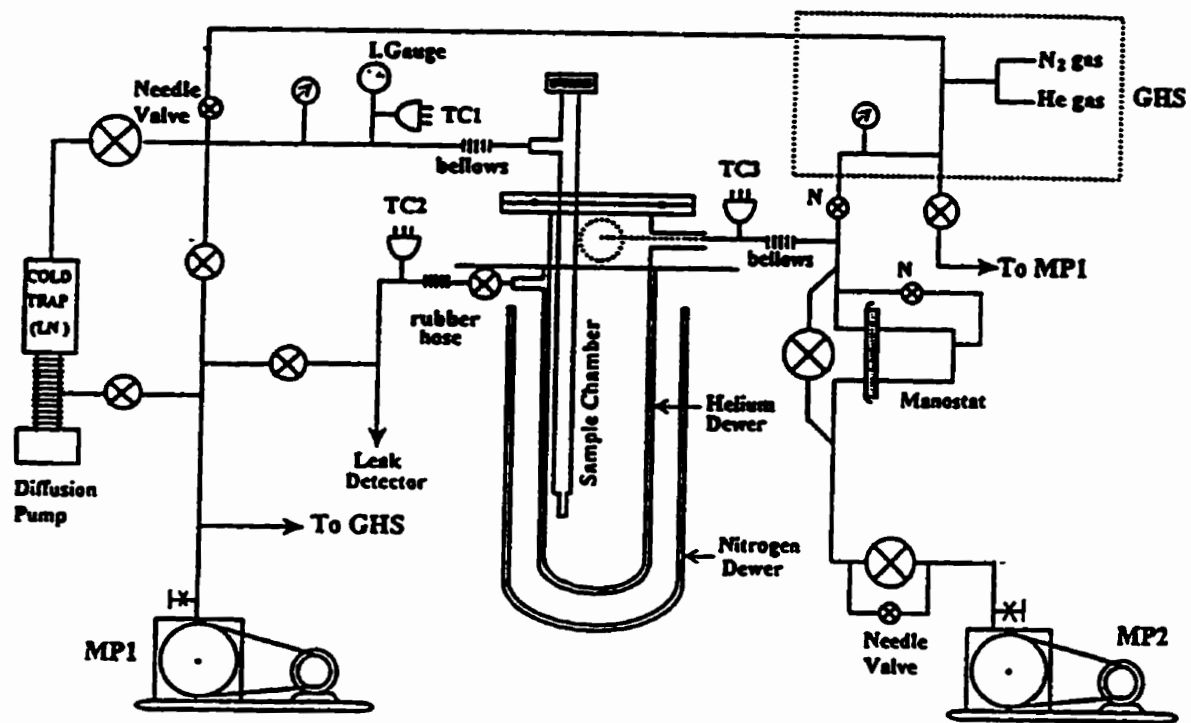


Figure 3.13: Flow diagram of pumping lines. From W. Ruan (1993).

of N_2 exchange gas is leaked into the sample chamber to speed up the cooling process. It is important to cool the system slowly towards 77 K, since most of the significant contraction of materials occur between 300 K and 77 K. Cooling from 250 K to 100 K requires about another 2 hours. As the system cools, the pressure inside the helium dewar drops below one atmosphere, and more N_2 exchange gas must be added to the dewar to maintain a pressure of one atmosphere. When the temperature of the sample reaches about 100 K, the N_2 exchange gas in both the sample chamber and the helium dewar are removed and both spaces are pumped and flushed 5 to 6 times with 4He exchange gas via MP1 and MP2 respectively. The N_2 and 4He gas are supplied through the gas handling system (GHS) labeled in Figure 3.13. Liquid helium can then be transferred into the helium dewar in order to cool the sample to 4.2 K.

By pumping with both MP1 and the diffusion pump, the sample chamber can be evacuated to $\sim 2 \times 10^{-5}$ Torr and the sample can be heated. The temperature of the sample can be varied between 4.2 K and 250 K, and controlled with a long term stability of ± 5 mK between 15 and 250 K. In this regime, the temperature of the sample is stabilized by a balance between the cooling power from the 4.2 K helium bath outside the sample chamber and the heater power from the heater. It is quite tricky to control the temperature between 4.2 K and 15 K, since this requires just the right amount of the 4He exchange gas to counteract the heat leak along the sample rod from room temperature. It is also possible to reach temperatures below 4.2 K by pumping the 4He bath with MP2 and controlling the pressure with a manostat, since the boiling point of the helium bath decreases with a reduction in its vapour pressure.

In the magnetic relaxation experiments, which in theory require an instantaneous “temperature quench”, an appropriate amount (~ 50 m Torr) of 4He exchange gas is leaked into the sample chamber at the paramagnetic reference temperature in order to initiate the cooling process and then *gradually pumped*

out as the desired temperature is approached in order to minimize overshooting. The final pressure is determined by the specific measurement temperature T_m .

Figure 3.14 shows the details of the insert of the ^4He cryostat. A thin walled aluminum can covered with lead sheet provides shielding from stray magnetic noise, and encloses the SQUID remote terminal board, sample chamber and the pick-up coils. Two copper radiation shields are soldered onto the supporting rods to reduce liquid helium boiling caused by radiation. Figure 3.15 shows the configuration of the pick-up coils, A.C. coil, D.C. solenoid and the Ag sample block. The sample chamber was machined from a solid rod of Emerson and Cumming 1266 Stycast epoxy, and glued with 1266 Stycast epoxy to one end of a one meter long, $\frac{3}{4}$ "-outer diameter stainless steel tube of thickness 0.020". The sample rod essentially consists of $\frac{1}{4}$ "-outer diameter, low thermal conductivity stainless steel tube approximately 1 meter long and of wall thickness 0.010", with a silver sample block attached to one end. The sample is glued with G.E. varnish which provides mechanical strength, and high-purity silver paint which provides good thermal contact (from SPI Supplies, West Chester PA) to the end of the pin on the silver block (0.060" diameter). A 25 Ω heater is anchored with G.E. varnish to the silver block. The temperature of the silver block and hence the sample is measured with a calibrated silicon diode (Model DT-470-SD-13 Lake Shore Cryotronics) which is glued with G.E. varnish near the end of the cylinder, and as close as possible to the sample. The temperature is controlled with a Model 520 Cryogenic Temperature Indicator/Controller (Lake Shore Cryotronics).

3.2.2 The Magnetization Measurement System

The pick-up coil and the D.C. field solenoid are all wound on a Stycast 1266 epoxy former and designed to fit concentrically about the bottom of the sample chamber. The two pick-up coils are counterwound, which reduces stray

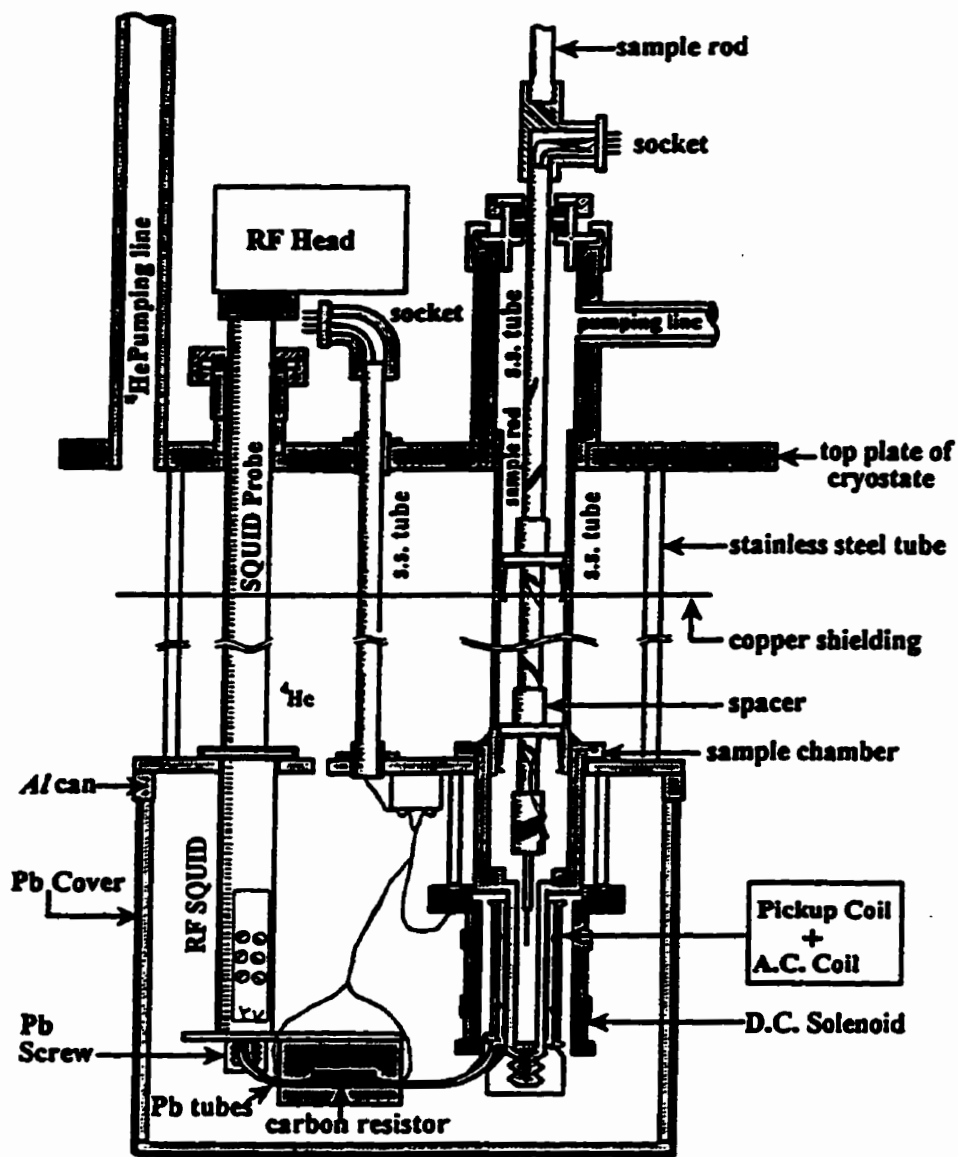


Figure 3.14: Insert of ^1He cryostat. From W. Ruan (1993).

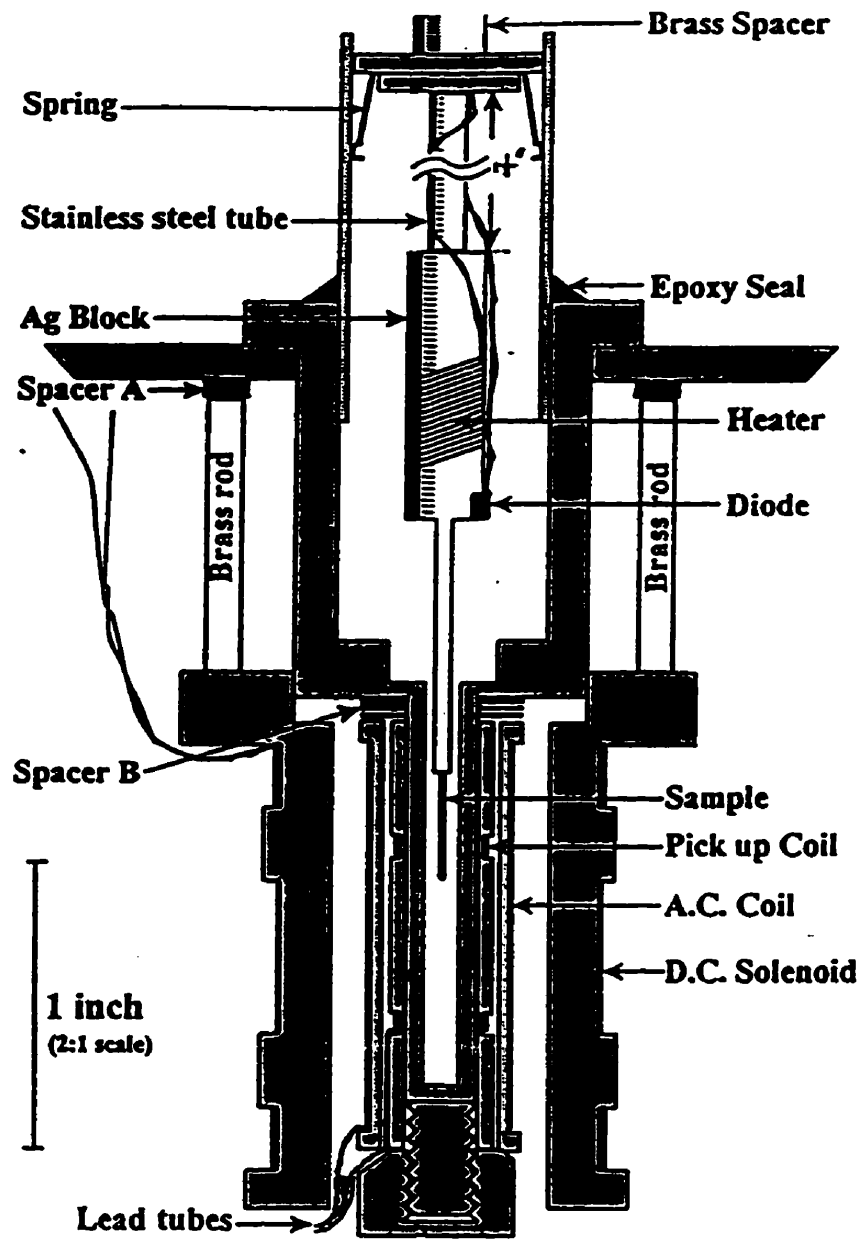


Figure 3.15: Configuration of the pick up coil, A.C. coil, D.C. solenoid and the Ag sample block. From W. Ruan (1993).

interference, and the sample is situated in only one coil of the pair. The solenoid is specially designed to produce a uniform magnetic field over the volume of the sample and the astatic pair of pick-up coils. It produced a magnetic field of 46 Oe/A.

Figure 3.16 is the electronic block diagram of the measurement system. In magnetization measurements, the magnetic flux in the pair of pick-up coils is coupled into the signal coil in the SQUID probe. The voltage output of the Model 30 Control Unit is proportional to the change of magnetic flux in the pick-up coils induced by a change in either the temperature or the magnetic field, and thus is proportional to the magnetic moment M of the sample. The voltage is measured with a RACAL-DANA Model 5003 digital voltmeter (DVM). In magnetic relaxation experiments, the decay of the sample magnetization (in volts) is collected from the DVM by IBM PC (Datatrain -286) via an IEEE interface bus, and the magnetization M versus $\log_{10}t$ is displayed on the screen at the same time.

3.2.3 Calibration of The SQUID Magnetometer

When measuring the magnetization of the sample with the SQUID we get an output signal in volts. If we want the magnetic moment of the sample, we need to convert volts to the electromagnetic unit (emu) of moment. We use a paramagnetic oxide Gd_2O_3 to calibrate the system. A cylindrical sample holder was machined out of aluminum, with dimensions of 0.56 mm interior diameter, and 1 mm outer diameter, and 8 mm long. The holder was filled with 4.8 mg of Gd_2O_3 powder (Aldrich Chemical Co., Wisconsin), and was sealed with an aluminum cap using Stycast 1266 epoxy. The magnetization was measured at several fixed temperatures $T = 4.2, 20, 30, 40$ K, in a static field $H_a = 10$ Oe. The magnetic moment of Gd_2O_3 for a given field H and temperature T can be

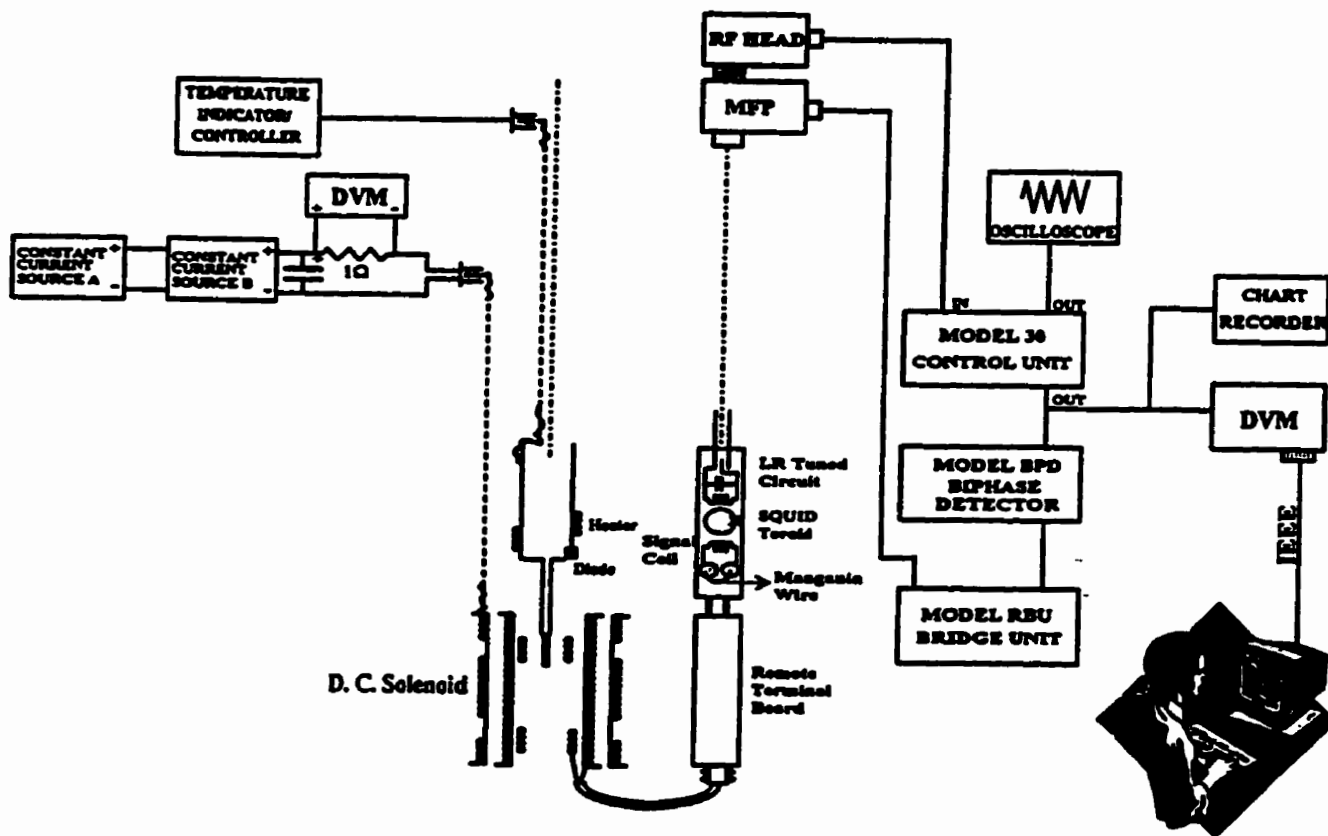


Figure 3.16: Electronic block diagram of the SQUID AC Susceptometer/Magnetometer. From W. Ruan (1993).

calculated from the following formula

$$M = \frac{N\mu_{eff}^2 H}{3k_B(T - \theta)} \quad (3.1)$$

where $N = 3.32 \times 10^{21}$ atoms/g is the number of Gd atoms per gram, $\mu_{eff} = (7.70 \pm 0.04)\mu_B$ is the effective magnetic moment of Gd, $k_B = 1.38 \times 10^{-16}$ erg/K is the Boltzmann constant, and $\theta = -13$ K is the Curie-Weiss temperature. Comparison with the measured moment in volts gives the calibration factor:

$$1\text{Volt} \approx 1.5 \times 10^{-5} \text{emu} \quad (3.2)$$

Chapter 4

Data Analysis and Discussion

In this chapter I will focus on our measurements of the relaxation of the thermoremanent magnetization (TRM) in some disordered magnetic systems, and the analysis of the experimental data in the context of the models developed in Chapter 2, and I will try to make connections between the experiments and the physical principles. The samples I have measured included:

(a) $\text{Fe}_{0.65}\text{Ni}_{0.35-x}\text{Cr}_x$ system, with $x = 0.11$ and $x = 0.12$

(b) $\text{Cr}_{1-x}\text{Fe}_x$ system, with $x = 0.21$

(c) $(\text{Fe}_{0.65}\text{Ni}_{0.35})_{1-x}\text{Mn}_x$ system, with $x = 0.118$

The dimensions and masses of the samples are listed in Chapter 3. All of them are reentrant ferromagnets, which means that there is sufficiently strong exchange bond disorder to cause the ferromagnetic ordering to collapse at low temperatures.

4.1 Temperature Dependence of The Static Magnetization

Measuring the profile of the static magnetization M in a small field H versus the temperature, which gives the dc-susceptibility $\chi_{dc}(T) = M/H$, is one of the ways to study phase transitions, and to define the transition temperatures. So, we first measured both the field-cooled(FC) and zero-field-cooled(ZFC) magnetizations, in a static applied field H_a .

Figure 4.1(a) shows the FC and ZFC magnetizations for $\text{Fe}_{0.65}\text{Ni}_{0.24}\text{Cr}_{0.11}$, measured in an applied field $H_a = 0.6$ Oe. The FC magnetization was obtained by applying H_a at a reference temperature $T_{ref} = 160$ K within the paramagnetic phase, cooling in this field to 4.2 K, and then warming. The ZFC magnetization was measured by cooling to 4.2 K in zero field(the earth field is compensated), applying H_a , and then warming. The ZFC magnetization rises rapidly with decreasing temperature, passes through an inflection point around 120 K then a peak around 100 K, then drops off slowly before decreasing suddenly below 30 K. The FC magnetization is identical to the ZFC magnetization above 120 K. Below this, $M_{FC} > M_{ZFC}$ and M_{FC} exhibits less well-defined structure. The diagram suggests that a paramagnetic-ferromagnetic transition takes place near $T_c \cong 120$ K(the Curie temperature), and the possibility of a ferromagnetic collapse below about $T_R \cong 22$ K (vertical arrows in Figure 4.1(a)), which is consistent with the measurements of Deryabin et al. (1984). Above T_c , the magnetization curve falls off very slowly with temperature, which is a indication that this alloy has more than one phase and perhaps some phases with a higher Curie temperature than 120 K. But the phase with $T_c \cong 120$ K dominates the alloy. Fig.4.1(b) shows the ac susceptibility(Deryabin et. al., 1984) of $\text{Fe}_{0.65}\text{Ni}_{0.25}\text{Cr}_{0.10}$, which shows a set of ferromagnetic critical peaks suggesting a Curie temperature of $T_c \cong 130$ K and a set of low temperature peaks(see inset) which suggest a reentrant temperature

$T_R \cong 20$ K.

Figure 4.2(a) shows the FC and ZFC curves for $(\text{Fe}_{0.65}\text{Ni}_{0.35})_{0.882}\text{Mn}_{0.118}$. It indicates that $T_c \cong 150$ K and $T_R \cong 70$ K (vertical arrows in Figure 4.2(a)), which is consistent with the work of Wulfes et al. (1983). Fig. 4.2(b) shows the triple peaked structure which typically characterizes the ac susceptibility in this reentrant system (Huck et al. 1988). The highest temperature set of peaks are ferromagnetic critical peaks.

Figure 4.3(a) shows the FC curve for the same FeNiCr system, but for a different concentration, corresponding to $\text{Fe}_{0.65}\text{Ni}_{0.23}\text{Cr}_{0.12}$. It indicates that $T_c \cong 60$ K and $T_R \cong 25$ K (vertical arrows in Figure 4.3(a)), which is also consistent with the work of Deryabin et al. (1984). Comparing with $\text{Fe}_{0.65}\text{Ni}_{0.24}\text{Cr}_{0.11}$, we find that increasing the concentration of Cr only changes the Curie temperature of the alloy but does not influence the glass temperature very much. T_c and T_R come closer as the concentration of Cr increases. Figure 4.3(b) shows the FC and ZFC curves for $\text{Cr}_{0.79}\text{Fe}_{0.21}$. It indicates that $T_c \cong 70$ K and $T_R \cong 25$ K (vertical arrows in Figure 4.3(b)), which is consistent with the measurements of Burke et al. (1983).

So, in all these systems the magnetic response function $\chi_{dc}(T)$ and $\chi_{ac}(T)$ shows the abrupt decline at low temperatures customarily identified with the onset of the 'reentrant' phase. Of course, the structures observed in the static magnetization as a function of temperature and described above are really thermal blocking effects, and are thus only suggestive of phase transitions and do not constitute proof. In order to confirm the existence of a critical transition, it is necessary to measure the ac susceptibility as a function of temperature in the presence of a static biasing field. At a paramagnetic-ferromagnetic transition, the ac susceptibility will exhibit a peak as a function of temperature (Deryabin et al. 1984; Huck et al. 1988). The temperature of this peak varies with as $|T_p - T_c| \sim$

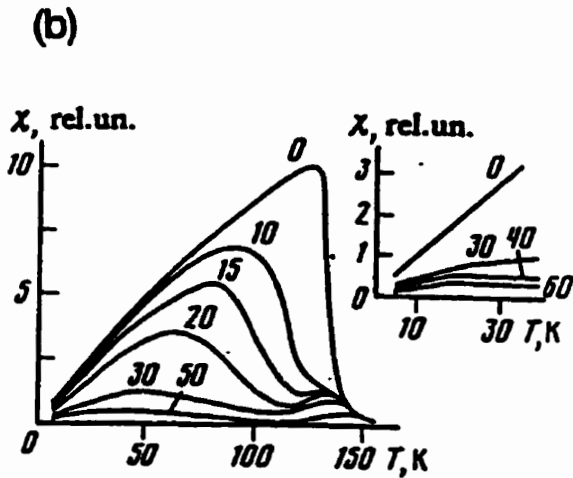
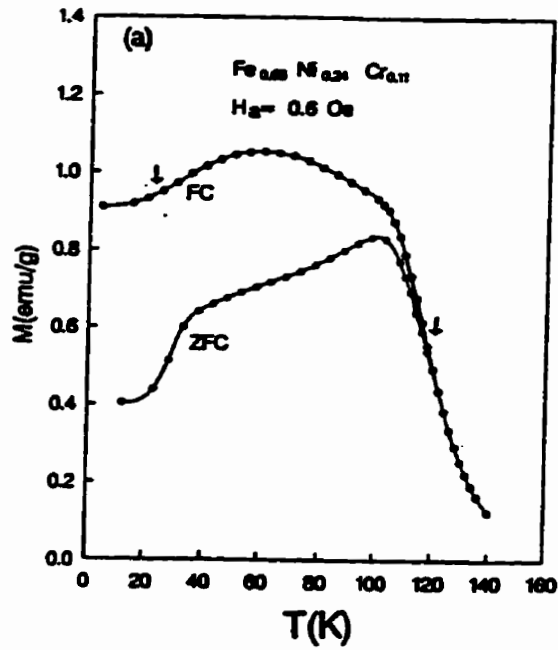


Figure 4.1: (a) The temperature dependence of the static magnetization of $\text{Fe}_{0.65}\text{Ni}_{0.24}\text{Cr}_{0.11}$ measured under both FC and ZFC conditions in a field $H_n \approx 0.6$ Oe. The arrows indicate the Curie temperature T_c and the reentrant temperature T_R . (b) AC susceptibility of $\text{Fe}_{0.65}\text{Ni}_{0.25}\text{Cr}_{0.10}$. From Deryabin et al. (1984).

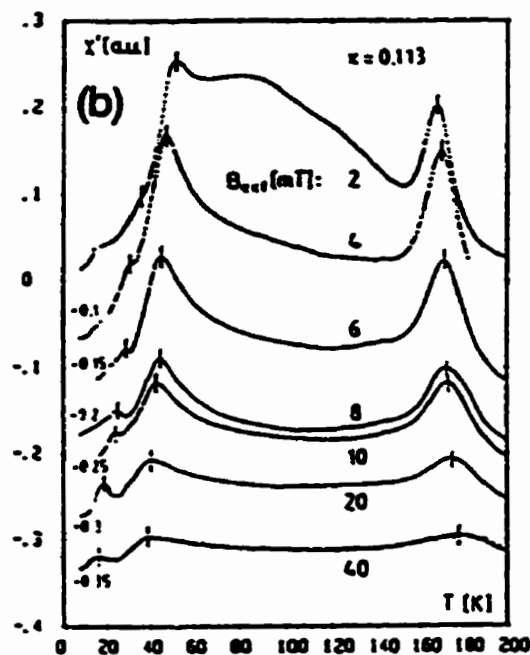
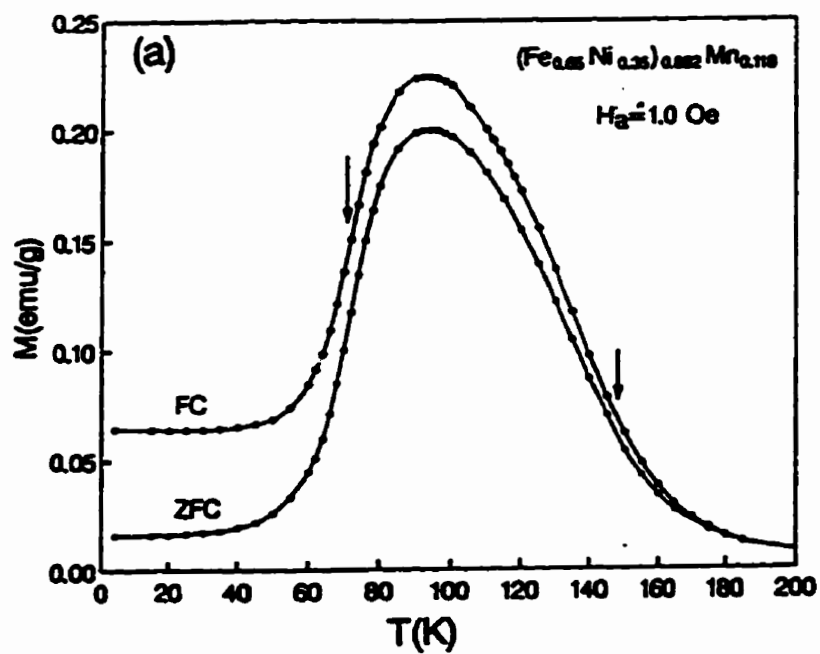


Figure 4.2: (a) The temperature dependence of the static magnetization of $(\text{Fe}_{0.65}\text{Ni}_{0.35})_{0.882}\text{Mn}_{0.118}$ measured under both FC and ZFC conditions in an applied field $H_a = 1.0$ Oe. The arrows indicate the Curie temperature $T_c \approx 150\text{K}$ and the reentrant temperature $T_R \approx 70\text{K}$. (b) AC susceptibility of sample $(\text{Fe}_{0.65}\text{Ni}_{0.35})_{0.887}\text{Mn}_{0.113}$. From Huck et al.(1988).

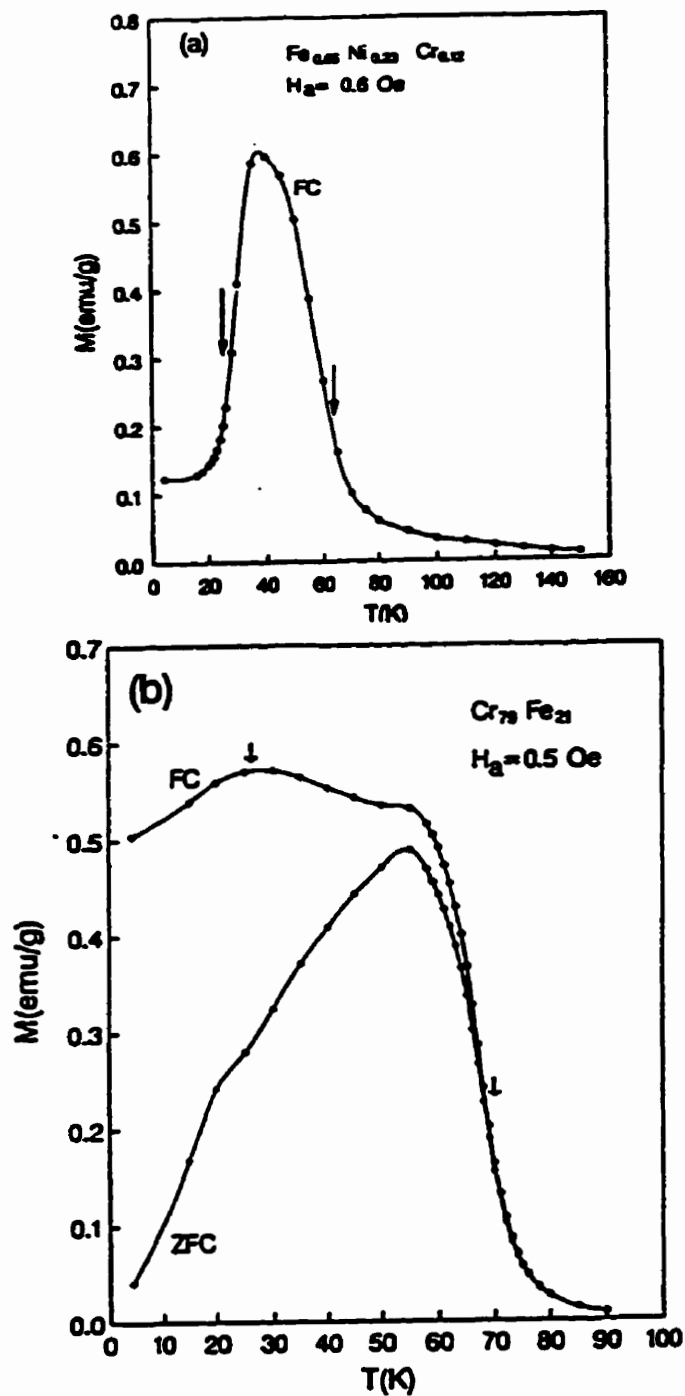


Figure 4.3: (a) The temperature dependence of the static magnetization of $\text{Fe}_{0.65}\text{Ni}_{0.23}\text{Cr}_{0.12}$ measured under FC conditions only in a field $H_a \approx 0.6$ Oe. The arrows indicate the Curie temperature T_c and the reentrant temperature T_R . (b) The temperature dependence of the static magnetization of $\text{Cr}_{0.79}\text{Fe}_{0.21}$ measured under both FC and ZFC conditions in an applied field $H_a = 0.5$ Oe. The arrows indicate the Curie temperature $T_c \approx 70$ K and the reentrant temperature $T_R \approx 25$ K.

$H^{1/(\gamma+\beta)}$ and the amplitude of the peak varies with field as $\chi(T_p) \sim H^{(1/\delta)-1}$, where γ , β , and δ are critical exponents. Peaks like these have been observed in both the FeNiCr and the FeNiMn systems as shown in Figures 4.1(b) and 4.2(b), and are a symptom of long-ranged ferromagnetism.

The ferromagnetic-spin glass reentrant boundary is much more difficult to identify. The ac susceptibility shows peaks as well, as shown in Figures 4.1(b) and 4.2(b), but these have never been identified as genuinely critical. Ideally, this reentrant transition should yield a “divergence” in the nonlinear components of the susceptibility (Deryabin et al. 1984; Huck et al. 1988), but this effect is often masked by domain wall dynamics from the ferromagnetic phase. Perhaps the best way to recognize the onset of the reentrant spin glass phase is through the aging effects in the relaxation response studied here.

4.2 Experimental Relaxation Procedures

The most interesting temperature range for us is around and below the reentrant temperature T_R , where anomalous relaxation behaviour occurs. Figure 4.4 shows the basic procedure for measuring the TRM relaxation: The sample is heated to a reference temperature T_{ref} in the paramagnetic phase above T_c , where a magnetic field H_a is applied and kept constant. Then, the sample is cooled “quickly” in the field to the measuring temperature T_m , below T_R or T_g . The typical cooling time in our experiments is about 10–15 minutes although it necessarily varies with $(T_{ref} - T_m)$. At T_m , we can perform four different types of relaxation experiments as illustrated in Figure 4.5:

a) After the sample has been cooled from the reference temperature T_{ref} through T_c to the measurement temperature T_m , we simply wait for a length of time t_w , then cut off the field, and measure the decay of the magnetization over

four decades of observation of time $1s < t \leq 10^4s$.

b) The sample is over-cooled from T_{ref} through T_c to a temperature $T_m - \Delta T$, where we wait for a length of time t_w , then raise the temperature to T_m , cut off the field, and measure the decay of the magnetization;

c) The sample is under-cooled from T_{ref} through T_c to a temperature $T_m + \Delta T$, where we wait for a length of time t_w , then lower the temperature to T_m , cut off the field, and measure the decay of the magnetization;

d) After the sample has been cooled from T_{ref} through T_c to the measurement temperature T_m , we wait a length of time t_w , then cycle the temperature from $T_m \rightarrow T_m + \Delta T \rightarrow T_m$, cut off the field, and measure the decay of the magnetization.

The measurement of the decay after the waiting period t_w spans the time window $1s$ to 10^4s . The total magnetization decay includes two parts: an instantaneous decay which is reversible, followed by a slow decay which is irreversible. The second part is the thermoremanent magnetization(TRM) relaxation which is of primary interest to us. In order to measure accurately the influence of aging on the relaxation, a small field step is necessary, so that the magnetic response is linear in field. Thus H_a should be typically a few Gauss. The precise criterion for this field may differ from system to system however(Chu et al., 1995; Djurberg et al., 1995; and section 4.8 in the chapter). If the field is outside the linear response range, then the field change will at least partially destroy the aged state, and alter the apparent age of the system and hence the true relaxation response. Such field effects will also be studied in this chapter.

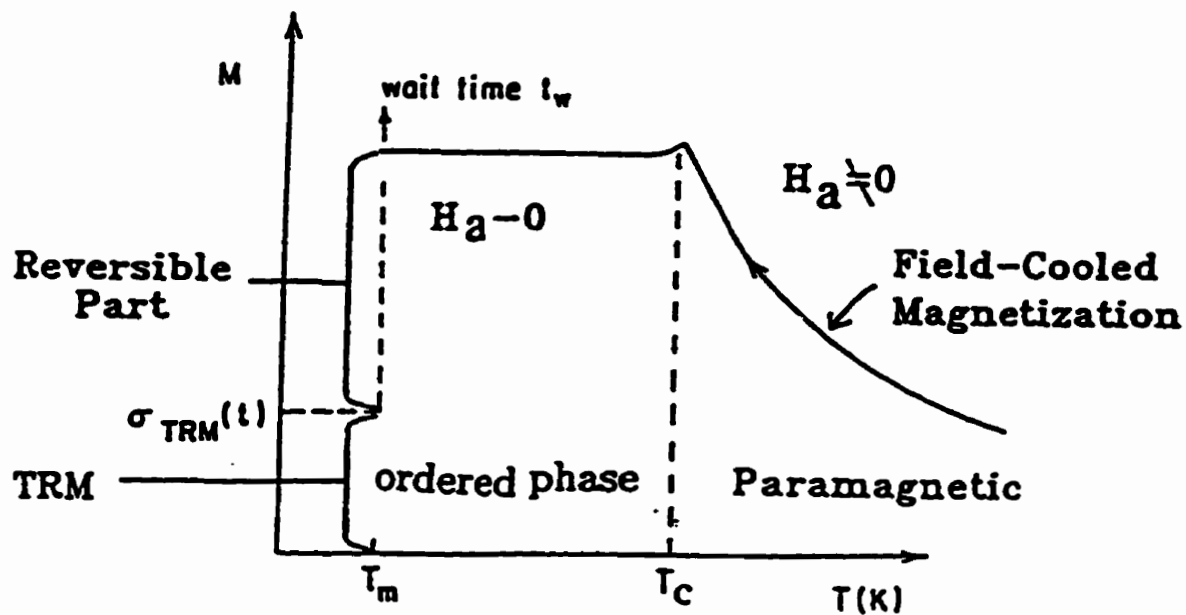


Figure 4.4: Procedure for the TRM decay measurement. The sample is cooled in a field H_a quickly from above T_c to T_m . In our measurements "ordered" phase means reentrant spin-glass. One waits a time t_w at T_m before reducing the field to zero (or to the trapped field). There is a rapid decay, followed by a slow decay of the irreversible part (TRM) of the magnetization. From Chu et al. (1995).

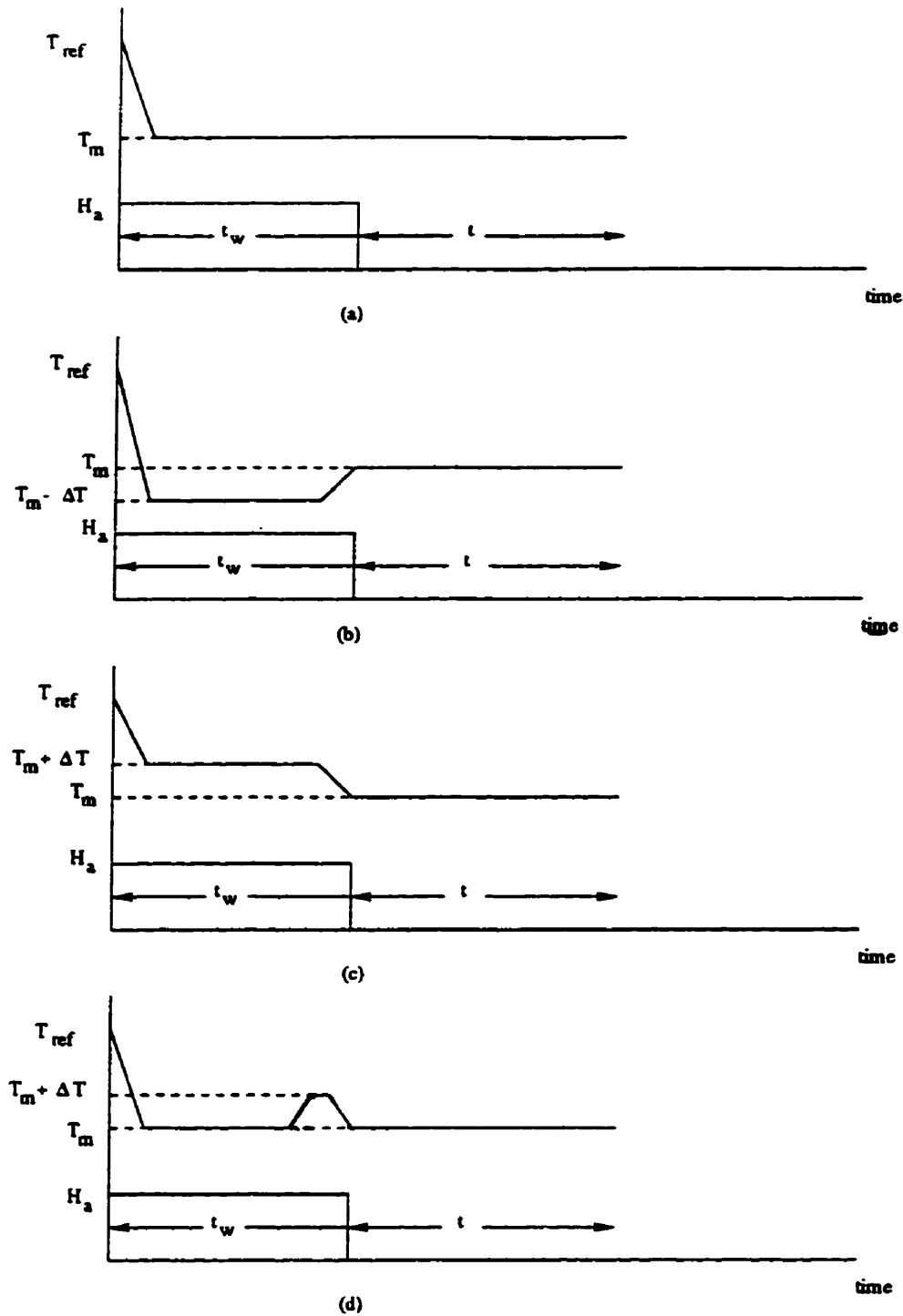


Figure 4.5: Types of relaxation experiments: a) Ordinary case: both aging and measurement at T_m ; b) Overcooling case: aging at $T_m - \Delta T$ and measurement at T_m ; c) Undercooling case: aging at $T_m + \Delta T$ and measurement at T_m ; d) Cycling case: aging at T_m , cycling $T_m \rightarrow T_m + \Delta T \rightarrow T_m$ and measurement at T_m ; Temperature shifting from $T_m \pm \Delta T \rightarrow T_m$ takes about 150 seconds. Temperature cycling takes about 300 seconds.

4.3 Relaxation Dynamics: A Stretched Exponential and A Power Law Analysis

Thermoremanent relaxation isotherms of type (a) in Fig.4.5 section are one of the important experiments to quantitatively describe the relaxation response of a spin glass. Theoretical analysis of the data, by fitting to the predictions of various models, can help us to understand the physical mechanisms which govern the approach to equilibrium and the response to a step function excitation in disordered magnetic systems.

Figures 4.6 - 4.8 illustrate typical TRM relaxation isotherms for $(\text{Fe}_{0.65}\text{Ni}_{0.35})_{0.882}\text{Mn}_{0.118}$. The dots are the data points and the solid curves are theoretical functions. These isotherms can be grouped into two thermally distinct regions with completely different relaxation characteristics:

a) For temperatures $T_m \leq T_g \simeq 70$ K in Figures 4.6 and 4.7, which corresponds closely to the reentrant phase, the relaxation isotherms all exhibit a profile which may be described qualitatively as some portion of an S-shaped curve with an inflection point (vertical arrows), and quantitatively by the superposition of a stretched exponential and a constant:

$$M_R(t) = M_0 + M_i \exp[-(t/\tau)^{1-n}]. \quad (4.1)$$

This empirical representation, which is frequently invoked in the analysis of pure spin-glass relaxation (Hoogerbeets et al., 1986), provides an excellent description of the experimental data over the entire observation window as shown by the solid curves in Figures 4.6 and 4.7. The best-fit values of the parameters n and τ listed in Table 4.1 are indeed typical of pure spin glasses (Hoogerbeets et al., 1986); in particular, the exponent n increases with increasing temperature and the trend towards unity indicates that the system is approaching its glass temperature.

The necessity to supplement the stretched exponential with a substantial baseline term M_0 , which at low temperatures accounts for approximately 90% of the entire remanent signal, is consistent with vector spin models of bond-disordered systems, which predict a longitudinal ferromagnetic spontaneous magnetization to coexist with transverse spin-glass freezing (Mitchler et al., 1993).

Furthermore, the relaxation response in this regime is *not unique*, but rather exhibits a dependence on system age t_w which indicates that the low-temperature phase is a *nonequilibrium* phase. This is illustrated in Figure 4.7 for $(\text{Fe}_{0.65}\text{Ni}_{0.35})_{0.882}\text{Mn}_{0.118}$ for temperature $T_m = 57$ K and for a sequence of wait times in the range $60\text{s} \leq t_w \leq 10800\text{s}$; the effect is clearly visible in the relaxation rate $S(t) \equiv -\partial M_R(t)/\partial \ln t$, shown in Figure 4.7(b), as a propagation of the maximum, corresponding to the inflection point in $M_R(t)$, towards longer observation times with increasing system age. The solid curves in Figure 4.7(a) are best fits to Eq. (4.1). An inspection of the corresponding parameters in Table 4.1 confirms that the aging process primarily affects the location of the inflection point (τ), without significantly altering the overall shape (n), at least for wait times $t_w \leq 10^4\text{s}$.

(b) Over the temperature range $T_g \leq T_m \leq T_c$, which is essentially coincident with the ferromagnetic phase, the curvature of the relaxation isotherms is uniformly positive (Fig.4.8), and all are accurately described by an empirical function consisting of the superposition of a simple power law and a constant (solid curves);

$$M_R(t) = M_0 + M_i t^{-m}, \quad (4.2)$$

with best-fit parameters for $(\text{Fe}_{0.65}\text{Ni}_{0.35})_{0.882}\text{Mn}_{0.118}$ listed in Table 4.2. The functional form of the decay and the values of the exponent m are both typical of glassy relaxation dynamics in the extreme equilibrium limit of infinite age (Lundgren et al., 1986). In fact, in contrast to the reentrant phase, the isotherms in this regime

exhibit *no* measurable dependence on system age, for wait times $t_w \leq 10^4$ s, indicating that, within the slow-cooling constraints of the current investigation, equilibrium is established far more rapidly in the high-temperature phase. This behavior is also consistent with that observed in “good” random ferromagnets, like $\text{Pd}_{0.986}\text{Fe}_{0.014}$ (Mitchler et al., 1993), which is not reentrant and has “ideal” Heisenberg critical exponents, and with the droplet fluctuation model of Huse and Fisher, which predicts (Huse and Fisher, 1987) a power-law decay of the average temporal autocorrelation function in Ising ferromagnets with quenched bond disorder.

A power law decay of thermoremanent magnetization of ferromagnets has been predicted theoretically. For example, in the droplet theory of Ising ferromagnets (Huse and Fisher, 1987), Huse and Fisher argued that the long-time equilibrium dynamics of long-range ordered Ising ferromagnets are dominated by the creation and annihilation of long-lived droplet fluctuations. Two types of disordered ferromagnets are considered: *random-exchange disorder* and *random field disorder*. One important dynamic quantity which they computed is the spatial average of the temporal autocorrelation function $\overline{C(t)}$

$$\overline{C(t)} \equiv \langle C_i(t) \rangle_c = \langle \langle S_i(0)S_i(t) \rangle_t - \langle S_i^2 \rangle_t \rangle_c \quad (4.3)$$

where $\langle \dots \rangle_t$ denotes the infinite time average, and $\langle \dots \rangle_c$ is the configuration (spatial) average. The time dependence of $\overline{C(t)}$ depends on the dynamics of the droplet fluctuations.

According to Huse and Fisher (1987), the free energy F_D of a droplet fluctuation consists of the free energy of the domain wall plus the free energy cost of flipping the interior spins of the domain when the system is subject to a random or uniform field. In order to create or annihilate a droplet, a free energy barrier B_D has to be surmounted, and the lifetime of the droplet fluctuation τ_D

is activated according to

$$\tau_D \sim \exp(B_D/T) \quad (4.4)$$

For long times t , only those long-lived droplets with $\tau_D \geq t$ contribute significantly to $C_i(t)$ and the long time dynamics are dominated by these so-called *rare* droplets.

For simplicity Huse and Fisher (1987) considered a roughly circular or spherical droplet of radius r , which has an average free energy F_D given by

$$F_D = A_d \sigma r^{d-1} \quad (4.5)$$

where σ is the average surface tension and A_d is the surface of a unit circle or sphere in d dimensions. Huse and Fisher suggested that the activation barrier B_D is proportional to r^{d-1} ,

$$B_D \cong b(f)r^{d-1} \quad (4.6)$$

with f to be defined as a ratio of the actual free energy to the average free energy of a droplet. Thus the lifetime for a droplet is given by

$$\tau_D \sim \exp(b(f)r^{d-1}/T), \quad (f < 1). \quad (4.7)$$

For a given f , the radius of the long-lived droplets can be obtained using $\tau_D \approx t$, and is given by:

$$r^{d-1} \approx \frac{T \ln(t/t_0)}{b(f)} \quad (4.8)$$

where t_0 is a microscopic time. Eq.(4.7) and Eq.(4.8) indicate that the lifetimes of the droplets which dominate the long time dynamics of $\overline{C}(t)$ are exponentially rare in $\ln t$, and the spatially averaged autocorrelation function becomes

$$\overline{C}(t) \sim t^{-z(T)} \quad (4.9)$$

that is, a power-law decay of the autocorrelation at long times for a *random-exchange system*. The exponent $\overline{x(T)}$ will depend on the temperature T , and on nonuniversal details of the system.

For random-field systems, an extra term due to the random fields acting over the entire interior of the droplet has to be added in Eq.(4.5), while Eq.(4.6) and Eq.(4.7) still keep the same form, viz, the radius of the long-lived droplets varies as a function of $\ln t$. The spatially averaged temporal correlation function is

$$\overline{C(t)} \sim \exp(-k(\ln t)^y) \quad (4.10)$$

where $y = (d - 2)/(d - 1)$ and k depends on the details of the distribution of the random-field free energy, and on the temperature. The decay described in Eq.(4.10) is slower than that in Eq.(4.9). Notice that Eq.(4.9) can be included in Eq.(4.10) by setting $y = 1$. This is not surprising since in both cases, the relaxation times of the long-lived droplets are exponentially rare in $\ln t$. The exponent y simply reflects the nature of the randomness.

A stretched exponential relaxation function has also been predicted theoretically. One such theory by De Dominicis, Orland and Laine (1985) is based on the mean field theory of Sherrington and Kirkpatrick. According to Parisi's solution of the infinite-range Sherrington-Kirkpatrick model, the spin glass is characterized by a large number of quasi-degenerate states, and the free energies F_a of these degenerate states are independent random variables. The equilibrium probability for the state occupation is

$$P_a^{eq} = \exp(-\beta F_a)/Z \quad (4.11)$$

where $Z = \sum_a \exp(-\beta F_a)$ and $F_a \equiv F_0 + f_a$ (f_a is a small fluctuation). Since it is assumed that all the F_a are quasidegenerate, the probability law for the random

variable F_a , or the small fluctuation f_a , is an exponential or can be linearized into an exponential around its frozen value.

De Dominicis et al. used a master equation which governs the relaxation to equilibrium of the state occupation $P_a(t)$, and employed detailed balance and a simple assumption for the transition probability, to show that the probability $x(q_M)$, where q_M is the Edwards-Anderson self overlap, decays as

$$x(t) = 1 - \overline{\sum_a (P_a(t))^2} \quad (4.12)$$

or

$$x(t) \simeq x + 2\left(\frac{1-x}{x}\right) e^{-v_0 \Gamma(1-x)(t/\tau_0)^x} [v_0 \Gamma(1-x)(t/\tau_0)^x]^{-1} \quad (4.13)$$

where v_0 is a finite non-universal constant. While the stretched exponential behaviour is promising, it is not clear that the parameter x is directly related to the thermoremanent magnetization, which is measured experimentally.

Another model which predicts stretched exponential behaviour is a model of hierarchically constrained dynamics by Palmer, Stein, Abrahams and Anderson (1984). The simplest way to obtain a relaxation response different from the conventional Debye relaxation, $q(t) = q_0 \exp(-t/\tau)$, is to postulate a statistical distribution of relaxation times with a weight function $w(\tau)$

$$q(t) = \int_0^\infty w(\tau) \exp(-t/\tau) d\tau \quad (4.14)$$

This approach tends to be microscopically arbitrary, and also assumes parallel relaxation, where each degree of freedom x_i relaxes independently with a characteristic time τ_i . Palmer et al. proposed a series approach involving many sequential correlated activation steps. The theory assumes that strongly interacting systems are characterized by constraints which, for example, prevent atom or cluster A

from moving until atom or cluster B first moves out of the way. The theory also involves a heirarchy of degrees of freedom, with faster degrees of freedom successively constraining slower ones, so that some atoms or groups of atoms are only able to move appreciably when several of the faster ones happen to move in just the right way, leaving a hole or a weakened bond. In particular, Palmer et al. consider a discrete series of levels $n = 0, 1, 2, \dots$ with level n represented by N_n Ising spins S_i . Each spin in level $n + 1$ is only free to change its state if μ_n spins in level n attain one particular state of their 2^{μ_n} possible states. The relaxation function is computed from

$$q(t) = \sum_{n=0}^{\infty} w_n \exp(-t/\tau_n) \quad (4.15)$$

where $w_n = N_n/N$, $N = \sum_{n=0}^{\infty} N_n$ and

$$\tau_n = \tau_0 \exp\left(\sum_{k=0}^{n-1} \tilde{\mu}_k\right)$$

where $\tilde{\mu}_k = \mu_k \ln 2$.

The theory contains two unspecified functions μ_n and w_n (or N_n). If it is assumed that

$$\left\{ \begin{array}{l} \mu_n = \mu_0 n^{-p} \quad (p \geq 1) \\ \text{and } N_{n+1} = N_n/\lambda \end{array} \right\}$$

then Eq.(4.15) yields, when replaced by an integral:

$$q(t) \sim w_0 \exp\left[-\left(\frac{t}{\tau}\right)\beta\right] \quad (4.16)$$

where $\beta = 1/(1 + \tilde{\mu}_0)$ and

$$\tau = \tau_0 \exp\left(\tilde{\mu}_0 \left(\frac{\ln \lambda}{\mu_0}\right)^{-\tilde{\mu}_0} (1 + \tilde{\mu}_0)^{-\beta}\right)$$

While the two stretched exponential theories described above place the Kohlraush stretched exponential on a more firm theoretical foundation, neither contains any mechanism for the aging process, which we regard as perhaps one of the most crucial constitutive features of a spin glass. Consequently we have not pursued this analysis any further here.

The relaxation isotherms for the remaining samples have similar features to those for $(\text{Fe}_{0.65}\text{Ni}_{0.35})_{0.882}\text{Mn}_{0.118}$ and are shown in Figures A.1–A.10, Appendix A, along with the best-fits to the stretched exponential and power law functions. The best-fit parameters are listed in Tables 4.3 through 4.8. If we inspect the parameters in these tables, we find that all systems exhibit similar systematics: a) the baseline M_0 decreases with increasing temperature T and wait-time t_w ; b) M_i shows the opposite behaviour to M_0 ; c) n increases from about 0.6 at a temperatures far below T_g to around 0.9 at temperatures close to T_g , but appears to be independent of wait time t_w ; d) τ always corresponds to the inflection point in the relaxation isotherms. τ decreases with increasing temperature, and increases with increasing wait time t_w . The sensitivity of τ to t_w becomes noticeably weaker at higher temperatures.

The errorbars in the parameter tables are the standard deviations of the parameter estimates by a standard least-square fitting procedure (Press, 1992). The same procedure was used for all of the model fits in this thesis.

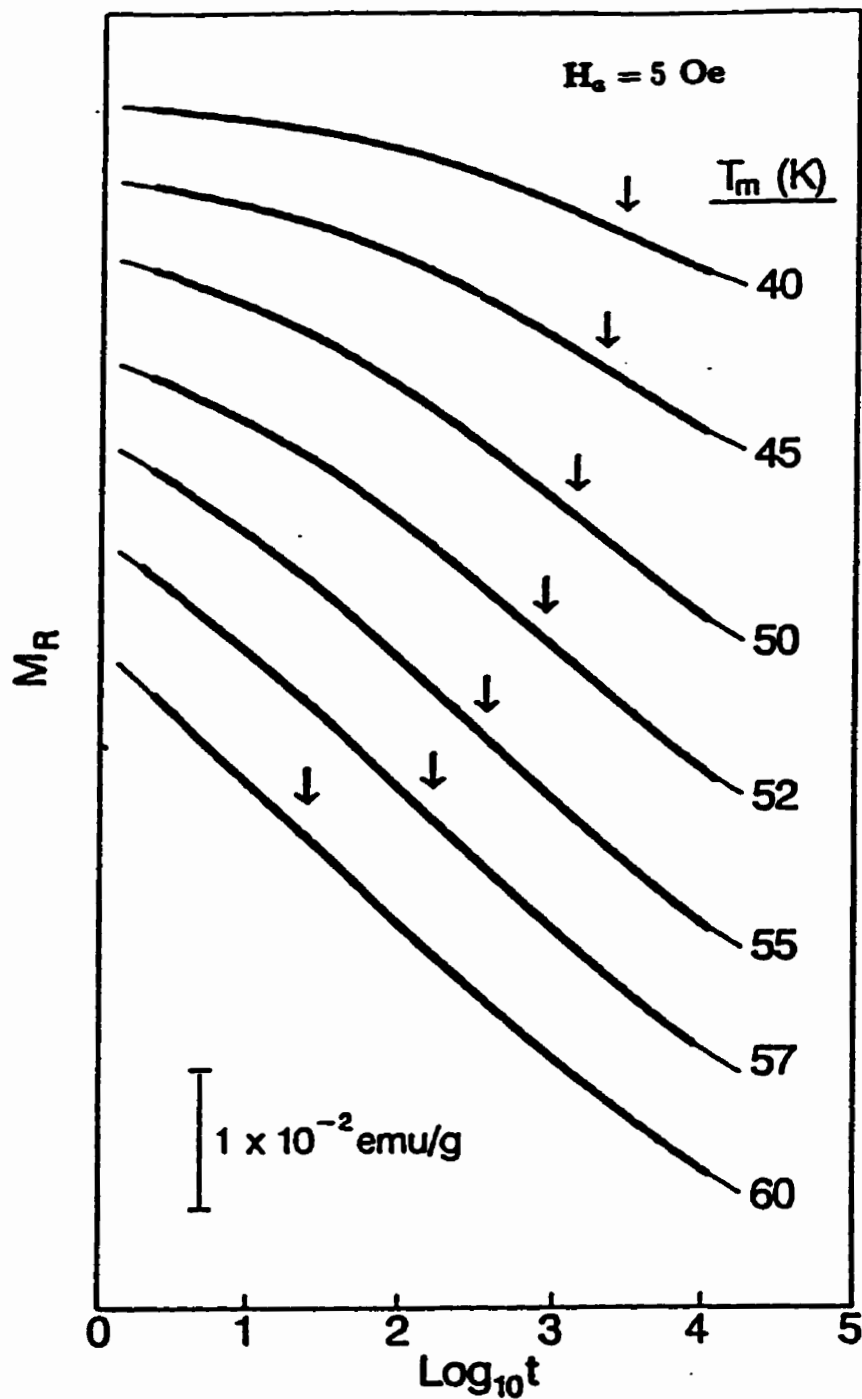


Figure 4.6: Thermoremanent relaxation isotherms of $(\text{Fe}_{0.65}\text{Ni}_{0.35})_{0.882}\text{Mn}_{0.118}$ for a sequence of temperatures $T_m \leq 60 \text{ K}$ ($T_R \approx 70\text{K}$) and for a common wait time $t_w = 60\text{s}$. The solid curves are fits to Eq.(4.1) and vertical arrows mark the characteristic times (inflection points) τ .

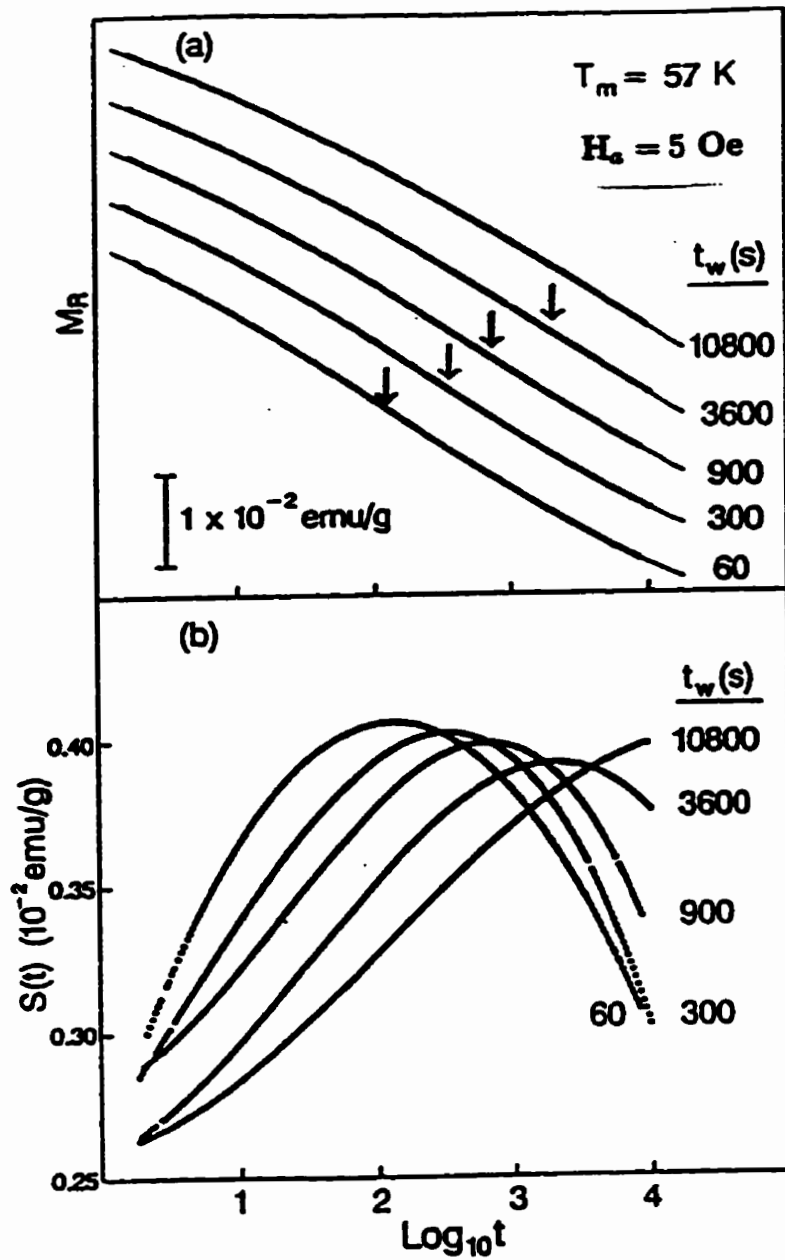


Figure 4.7: (a) Wait-time dependence of the thermoremanent relaxation of $(\text{Fe}_{0.65}\text{Ni}_{0.35})_{0.882}\text{Mn}_{0.118}$ at $T_m = 57 \text{ K}$. The solid curves are fits to Eq.(4.1) and vertical arrows mark the characteristic times (inflection points) τ . (b) The relaxation rates $S(t)$ for the isotherms in (a).

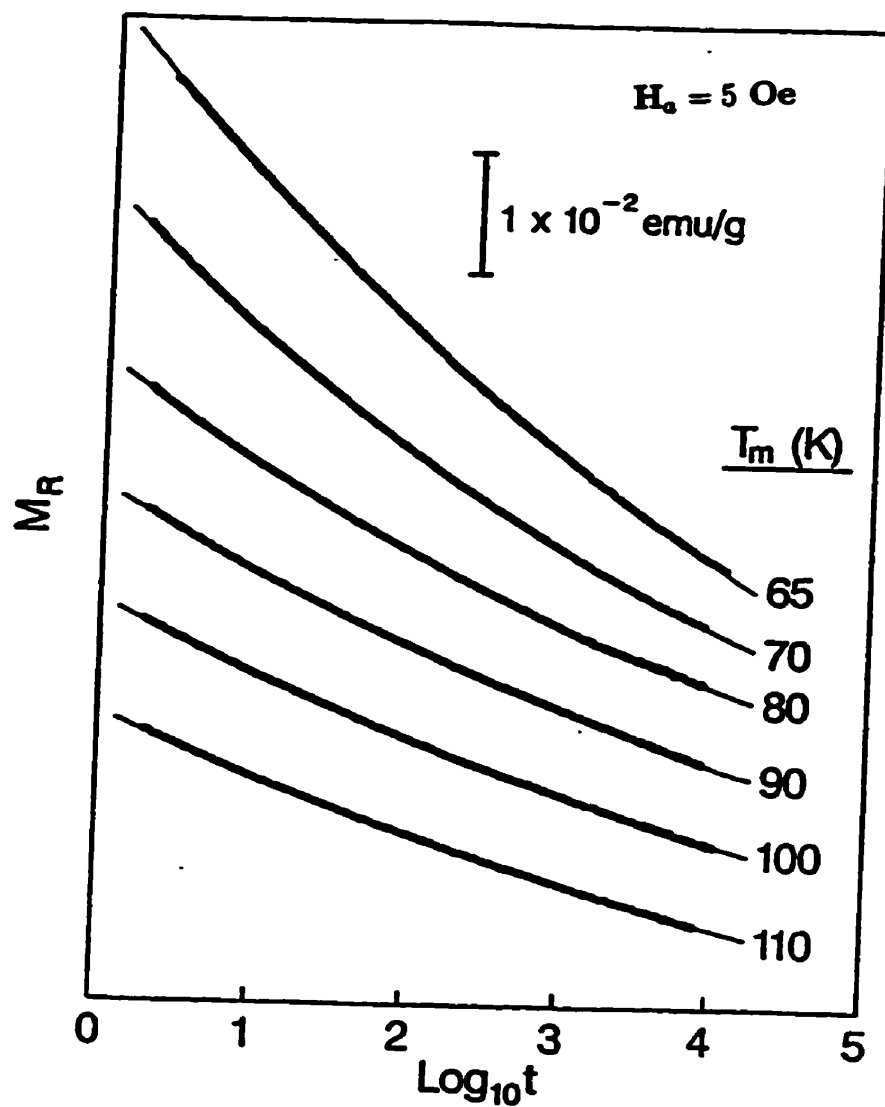


Figure 4.8: Thermoremanent relaxation isotherms of $(\text{Fe}_{0.65}\text{Ni}_{0.35})_{0.882}\text{Mn}_{0.118}$ for a sequence of temperatures $T_m \geq 65 \text{ K}$ ($T_c \approx 150\text{K}$) and for a common wait time $t_w = 60\text{s}$. The solid curves are fits to Eq.(4.2).

Table 4.1: Best-fit parameters of $(\text{Fe}_{0.65}\text{Ni}_{0.35})_{0.882}\text{Mn}_{0.118}$ to the stretched exponential in Eq.(4.1).

T (K)	t_w (sec)	M_0 (10^{-3}emu/g)	M_i (10^{-3}emu/g)	n	τ (sec)
40	60	117.90 ± 0.05	15.10 ± 0.06	0.650 ± 0.005	2830 ± 50
45	60	110.70 ± 0.08	22.90 ± 0.10	0.680 ± 0.005	2120 ± 40
50	60	101.90 ± 0.11	34.50 ± 0.16	0.730 ± 0.003	1370 ± 20
52	60	97.30 ± 0.09	39.30 ± 0.16	0.740 ± 0.005	856 ± 9
55	60	87.80 ± 2.71	51.00 ± 0.28	0.790 ± 0.005	357 ± 3
57	60	85.30 ± 0.15	60.90 ± 0.43	0.820 ± 0.005	162 ± 2
57	300	86.00 ± 0.16	58.00 ± 0.36	0.810 ± 0.005	313 ± 4
57	900	82.40 ± 0.18	62.30 ± 0.33	0.830 ± 0.005	642 ± 10
57	3600	73.80 ± 0.35	72.60 ± 0.53	0.850 ± 0.005	3090 ± 130
57	10800	58.00 ± 2.00	89.50 ± 2.59	0.880 ± 0.005	28900 ± 7000
60	60	81.80 ± 0.08	84.80 ± 0.42	0.870 ± 0.005	23.4 ± 0.5

Table 4.2: Best-fit parameters of $(\text{Fe}_{0.65}\text{Ni}_{0.35})_{0.882}\text{Mn}_{0.118}$ to the power law in Eq.(4.2).

T (K)	t_w (sec)	M_0 (10^{-3}emu/g)	M_i (10^{-3}emu/g)	m
65	60	55.40 ± 0.30	63.80 ± 0.28	0.072 ± 0.001
70	60	73.40 ± 0.10	43.80 ± 0.10	0.088 ± 0.001
80	60	85.90 ± 0.19	34.10 ± 0.18	0.082 ± 0.001
90	60	95.00 ± 0.14	33.60 ± 0.13	0.066 ± 0.001
100	60	97.70 ± 0.12	29.80 ± 0.12	0.064 ± 0.001
110	60	90.90 ± 0.15	27.70 ± 0.14	0.060 ± 0.001

Table 4.3: Best-fit parameters of $\text{Fe}_{0.65}\text{Ni}_{0.24}\text{Cr}_{0.11}$ to the stretched exponential in Eq.(4.1).

T (K)	t_w (sec)	M_0 (emu/g)	M_i (emu/g)	n	τ (sec)
8	60	3.424 ± 0.001	0.029 ± 0.001	0.745 ± 0.004	6850 ± 890
10	60	3.301 ± 0.001	0.055 ± 0.001	0.677 ± 0.002	3660 ± 160
12	60	3.280 ± 0.001	0.103 ± 0.001	0.650 ± 0.001	3395 ± 68
14	60	3.209 ± 0.001	0.164 ± 0.001	0.640 ± 0.001	2092 ± 29
15	60	3.131 ± 0.001	0.209 ± 0.001	0.657 ± 0.001	1869 ± 22
16	60	3.106 ± 0.001	0.259 ± 0.001	0.669 ± 0.001	1726 ± 17
17	60	3.042 ± 0.001	0.322 ± 0.001	0.704 ± 0.001	1191 ± 14
17	900	3.020 ± 0.001	0.311 ± 0.001	0.681 ± 0.001	2189 ± 33
17	1800	2.991 ± 0.002	0.321 ± 0.002	0.687 ± 0.001	3385 ± 86
17	3600	2.983 ± 0.004	0.361 ± 0.004	0.707 ± 0.002	8715 ± 476
17	7200	2.820 ± 0.015	0.527 ± 0.016	0.748 ± 0.002	87000 ± 14000
18	60	2.950 ± 0.001	0.411 ± 0.002	0.746 ± 0.001	742 ± 11
19	60	2.871 ± 0.001	0.576 ± 0.003	0.810 ± 0.001	390 ± 4
19	300	2.877 ± 0.002	0.513 ± 0.003	0.782 ± 0.001	633 ± 12
19	900	2.902 ± 0.001	0.479 ± 0.002	0.763 ± 0.001	810 ± 9
19	1800	2.893 ± 0.001	0.483 ± 0.002	0.765 ± 0.001	1174 ± 11
19	3600	2.869 ± 0.001	0.474 ± 0.001	0.762 ± 0.001	1510 ± 10
19	7200	2.853 ± 0.001	0.494 ± 0.001	0.769 ± 0.001	2508 ± 29
20	60	2.773 ± 0.002	0.632 ± 0.004	0.820 ± 0.001	243 ± 2
21	60	2.680 ± 0.002	0.849 ± 0.007	0.868 ± 0.001	69 ± 1
21	600	2.682 ± 0.002	0.837 ± 0.004	0.866 ± 0.001	103 ± 1
21	1800	2.693 ± 0.002	0.773 ± 0.004	0.855 ± 0.001	179 ± 1
21	7200	2.683 ± 0.002	0.767 ± 0.004	0.856 ± 0.001	298 ± 3
22	60	2.596 ± 0.002	1.004 ± 0.010	0.892 ± 0.001	16 ± 1

Table 4.4: Best-fit parameters of $\text{Fe}_{0.65}\text{Ni}_{0.24}\text{Cr}_{0.11}$ to the power law in Eq.(4.2).

T (K)	t_w (sec)	M_0 (emu/g)	M_i (emu/g)	m
24	60	2.058 ± 0.003	0.908 ± 0.002	0.0435 ± 0.0001
25	60	2.057 ± 0.002	0.806 ± 0.002	0.0443 ± 0.0001
26	60	1.918 ± 0.007	0.915 ± 0.007	0.0334 ± 0.0003
28	60	1.861 ± 0.020	0.936 ± 0.021	0.0288 ± 0.0007
30	60	1.632 ± 0.064	1.118 ± 0.064	0.0230 ± 0.0015
33	60	1.464 ± 0.082	1.284 ± 0.082	0.0221 ± 0.0016
35	60	0.814 ± 0.030	1.910 ± 0.030	0.0151 ± 0.0003
40	60	1.297 ± 0.016	1.324 ± 0.016	0.0217 ± 0.0001
45	60	1.698 ± 0.004	0.879 ± 0.004	0.0299 ± 0.0001
50	60	1.727 ± 0.018	0.808 ± 0.018	0.0283 ± 0.0007
60	60	1.631 ± 0.037	0.769 ± 0.037	0.0245 ± 0.0013
70	60	1.441 ± 0.011	0.759 ± 0.010	0.0244 ± 0.0004

Table 4.5: Best-fit parameters of $\text{Fe}_{0.65}\text{Ni}_{0.23}\text{Cr}_{0.12}$ to the stretched exponential in Eq.(4.1).

T (K)	t_w (sec)	M_0 ($\times 10^{-1}\text{emu/g}$)	M_i ($\times 10^{-1}\text{emu/g}$)	n	τ (sec)
16	300	3.482 ± 0.002	0.574 ± 0.002	0.589 ± 0.001	2025 ± 23
18	300	3.382 ± 0.002	0.741 ± 0.003	0.602 ± 0.002	1225 ± 17
20	300	3.225 ± 0.002	1.106 ± 0.003	0.637 ± 0.001	1155 ± 10
20	900	3.242 ± 0.005	1.099 ± 0.006	0.632 ± 0.002	2215 ± 47
20	1800	3.065 ± 0.013	1.197 ± 0.014	0.653 ± 0.003	4583 ± 230
20	3600	2.839 ± 0.030	1.379 ± 0.032	0.674 ± 0.003	14615 ± 1500
20	7200	2.387 ± 0.097	1.752 ± 0.099	0.704 ± 0.004	80943 ± 2134
21	300	3.136 ± 0.002	1.281 ± 0.003	0.664 ± 0.009	803 ± 6
21	900	3.043 ± 0.004	1.206 ± 0.005	0.660 ± 0.001	1236 ± 17
21	1800	3.052 ± 0.004	1.252 ± 0.004	0.654 ± 0.001	2284 ± 30
21	3600	2.854 ± 0.020	1.421 ± 0.022	0.690 ± 0.003	6143 ± 444
21	7200	2.717 ± 0.040	1.540 ± 0.043	0.699 ± 0.004	14034 ± 1864
22	300	2.860 ± 0.004	1.647 ± 0.006	0.712 ± 0.001	760 ± 9
22	900	3.037 ± 0.002	1.525 ± 0.003	0.690 ± 0.006	1145 ± 8
22	1800	2.938 ± 0.003	1.529 ± 0.004	0.691 ± 0.008	1702 ± 19
22	3600	2.824 ± 0.011	1.663 ± 0.013	0.714 ± 0.002	3675 ± 13
22	7200	2.661 ± 0.020	1.759 ± 0.022	0.729 ± 0.002	8008 ± 513
23	300	2.512 ± 0.003	2.004 ± 0.009	0.747 ± 0.009	377 ± 3
24	300	2.636 ± 0.004	2.415 ± 0.011	0.783 ± 0.011	188 ± 1
24	900	2.683 ± 0.002	2.375 ± 0.006	0.782 ± 0.006	242 ± 1
24	1800	2.771 ± 0.002	2.260 ± 0.004	0.774 ± 0.005	349 ± 1
24	3600	2.587 ± 0.002	2.169 ± 0.003	0.771 ± 0.004	427 ± 1
24	7200	2.482 ± 0.003	2.389 ± 0.005	0.790 ± 0.004	913 ± 7
25	300	2.213 ± 0.007	5.221 ± 0.036	0.890 ± 0.001	14 ± 1

Table 4.6: Best-fit parameters of $\text{Fe}_{0.65}\text{Ni}_{0.23}\text{Cr}_{0.12}$ to the power law in Eq.(4.2).

T (K)	t_w (sec)	M_0 ($\times 10^{-1}\text{emu/g}$)	M_i ($\times 10^{-1}\text{emu/g}$)	m
26	300	0.566 ± 0.019	4.159 ± 0.018	0.068 ± 0.001
28	300	1.735 ± 0.003	2.847 ± 0.003	0.105 ± 0.001

Table 4.7: Best-fit parameters of $\text{Cr}_{0.79}\text{Fe}_{0.21}$ to the stretched exponential in Eq.(4.1).

T (K)	t_w (sec)	M_0 (10^{-3}emu/g)	M_i (10^{-3}emu/g)	n	τ (sec)
10	60	404.09 ± 0.15	39.49 ± 0.21	0.646 ± 0.002	1331 ± 22
12	60	384.45 ± 0.16	60.38 ± 0.24	0.652 ± 0.002	904 ± 10
14	60	348.49 ± 0.19	80.52 ± 0.34	0.699 ± 0.002	513 ± 5
14	300	343.73 ± 0.15	77.44 ± 0.23	0.679 ± 0.001	788 ± 6
14	900	352.81 ± 0.32	80.26 ± 0.40	0.683 ± 0.001	1959 ± 37
14	1800	352.60 ± 0.90	91.52 ± 1.04	0.709 ± 0.002	5058 ± 265
14	3600	293.23 ± 6.30	135.33 ± 6.54	0.754 ± 0.004	82000 ± 23000
16	60	329.81 ± 0.22	96.27 ± 0.48	0.748 ± 0.001	338 ± 3
18	60	324.74 ± 0.14	115.40 ± 0.44	0.817 ± 0.001	133 ± 1
20	60	378.96 ± 0.34	139.71 ± 1.10	0.874 ± 0.001	77.3 ± 1.3
22	60	289.37 ± 0.57	190.27 ± 2.42	0.914 ± 0.001	32.0 ± 1.1

Table 4.8: Best-fit parameters of $\text{Cr}_{0.79}\text{Fe}_{0.21}$ to the power law in Eq.(4.2).

T (K)	t_w (sec)	M_0 (10^{-3}emu/g)	M_i (10^{-3}emu/g)	m
26	60	366 ± 3	11 ± 3	0.01847 ± 0.00002
30	60	166.8 ± 0.4	124.1 ± 0.4	0.04397 ± 0.00001

4.4 Relaxation Dynamics: A Random Trap Analysis and Scaling of The Relaxation Isotherms

Bouchaud's random trap model is based on the concept of a very rough energy landscape with many local minima corresponding to metastable configurations, surrounded by high energy barriers, each of which can trap the system for a time τ . For a broad distribution $\psi(\tau)$, such as that associated with the random energy model (REM) (Derrida, 1981) or the standard mean field SK model (Sherrington and Kirkpatrick, 1975):

$$\psi(\tau) \sim \tau^{-(1+x)}, \quad \text{with} \quad 0 < x < 1, \quad (4.17)$$

$\langle \tau \rangle$ diverges, and ergodicity is broken, in the sense that the system is essentially never able to probe the deepest traps within the experimental observation window as it evolves towards equilibrium. In the extreme non-ergodic limit of 'short' wait times, the model predicts a decay of the form:

$$m(t) = m_0 \exp \left[-\gamma \int_0^t t^{-x} (t + t_w)^{x-1} dt \right] \quad (4.18)$$

with a crossover from stretched exponential behaviour for $t \ll t_w$, to a power law behaviour for $t \gg t_w$.

When $x > 1$, the distribution of lifetimes $\psi(\tau)$ in Eq.(4.17) decays rapidly enough for $\tau \cdot \psi(\tau)$ to become normalizable, $\langle \tau \rangle$ is finite, and the model predicts that the deepest trap encountered during the waiting time t_w is $\tau_{max} \ll t_w$, so that the system equilibrates essentially instantaneously after the quench. In fact, by following a procedure analogous to that described by Bouchaud for $x < 1$, we have been able to show that the relaxation dynamics in the $x > 1$ regime is determined by a microscopic cut-off time τ_0 (rather than by the macroscopic waiting time t_w),

and obey a simple power law:

$$m(t) = m_0 \left(\frac{\tau_0}{t} \right)^{x-1}, \quad x > 1 \quad (4.19)$$

Applying the extreme non-ergodic function (4.18) to the relaxation isotherms of $\text{Fe}_{0.65}\text{Ni}_{0.24}\text{Cr}_{0.11}$ we can obtain quite good fits without the need to add an “artificial” constant baseline. In fact, the additional of such a baseline degrades the quality of the fits. Isotherms for $T_m < T_g$ are all compatible with Eq.(4.18), and, as an illustration, the solid curves in Figures 4.9, 4.10 and 4.11 are the best fits of the data for $\text{Fe}_{0.65}\text{Ni}_{0.24}\text{Cr}_{0.11}$ to this expression, with the best fit parameters m_0, γ and x listed in Table 4.9, and with t_w assigned its *experimental* value. The shape of the theoretical curves (4.18) is parameterized exclusively by x , which is less than unity and increases monotonically as $T \rightarrow T_g$. Its physical significance will be discussed shortly. All three fitting parameters do vary with system age. Nevertheless, these fits lend considerable credibility to the proposed aging mechanism, which is manifested explicitly through a single, *experimentally-defined* parameter t_w . The systematic deviations apparent in some of the isotherms at long observation times, particularly in younger versions of the system ($t < 300s$) where the data tend to exhibit more curvature than the theoretical expression, are qualitatively similar to those encountered in pure spin glasses. This may be a consequence of some of the simplifying approximations (such as the assumption of constant $G(\tau/t_w)$ in equation (2.108), or perhaps the specific form of the cut-off function $\exp(-t/\tau)$ introduced in equation (2.102). or may have a physical origin related to a distribution of subsystem sizes and ergodic times which we will discuss later. Nevertheless, the essential features of the time dependence of the thermoremanent decay in the low-temperature glassy phase, including its variation with temperature and system age, are replicated remarkably well by a picture in which ergodicity is broken by a *divergent* mean trapping time, which prevents a system of *finite* experimental age t_w from exploring all of the available

configuration space.

For temperatures $T_m > T_g$, the relaxation isotherms are accurately described by the power law decay in equation(4.19), which however must be superposed on a constant baseline, $m(t) = m'_0 t^{-(x-1)} + c$, where the $x - 1$ is the m in equation (4.2). For the high temperature data, all of the m exponents are between $0 \leq m \leq 1$, so x is larger than unity in this regime. Thus, the relaxation response in the high-temperature phase, where the dynamics are observed to be *stationary* (that is, age-independent), is analytically consistent with the model prediction in the extreme equilibrium limit where the system ergodically probes a phase space for which the deepest traps of any significance are $\tau_{max} \ll t_w$, due to the form of the trapping distribution.

The preceding analysis offers new insight, from a dynamical perspective, into the phenomenon of sequential transitions in ferromagnets, as well as empirical support for a recent model of glassy dynamics based on a mechanism of anomalous diffusion in a disordered energy landscape.

The power law distribution function (4.17) for the lifetime of the metastable states follows directly from an exponential distribution of free energy wells, $P(f) = (x/T) \exp[x(f - f_0)/T]$, where f_0 is a reference level, which is a characteristic of both the standard SK model (Sherrington and Kirkpatrick, 1975) and the REM (Derrida, 1981). Thus the parameter $x(T)$ provides information on the structure of phase space. In the REM, $x = T/T_g$, the energy landscape is temperature independent, and configuration space consists of many completely uncorrelated, but perfectly frozen metastable valleys at T_g , while, in the standard SK model, x has a non-trivial temperature dependence and decreases towards zero as $T \rightarrow T_g$, meaning that only a relative few states out of the many available in Parisi's hierarchical replica symmetry breaking scheme (Mezard et al., 1986) *dominate* the properties of the system in this limit. In the fits to all the samples studied

here, x increases with temperature through the glassy phase, thus offering some preliminary support for the REM picture, although the temperature dependence is not linear, in agreement with the recent observations of Bouchaud(1992).

Above T_g , as we have said, the data are no longer compatible with the extreme non-ergodic expression in equation (4.18) and, more importantly, *aging ceases to be observable experimentally*. However, the random trap formalism is capable of replicating the time dependence of the decay in this regime as well, provided that x is allowed to *exceed* unity. Moreover, this is precisely the condition which reduces aging effects to negligible proportions in the model, and which guarantees an equilibrium relaxation response for any macroscopic wait time $t_w \gg \tau_0 \sim 10^{-12}$ s. We emphasize that this situation is physically quite distinct from the scenario of ‘interrupted aging’ for $x < 1$, according to which equilibrium is achieved only when the wait time is long enough to exceed an ergodic time $t_{erg} \sim \tau_0 S^{1/x}$, where S is the total number of metastable states (Bouchaud, 1992). Although the model offers little evidence concerning the types of frozen spin configurations which are expected to yield an energy landscape with $x > 1$, the current analysis, coupled with the observation of ‘stationary’ power law decay, with similar exponents, in the thermoremanence of ‘good’ (non-reentrant) random-exchange ferromagnets like $\text{Pd}_{0.986}\text{Fe}_{0.014}$ (Bouchaud et al., 1994), suggests that this may be a constitutive feature of a state with predominantly ferromagnetic order.

The same analysis based on Eq.(4.18) of the random trap model has been performed on all the other samples. The best-fit parameters are listed in Tables 4.10–4.12 and corresponding fits are shown in Figures B.1–B.5, Appendix B. This expression is only valid for temperatures T_m below the glass temperature T_g . So, when T_m is very close to T_g , the description of the TRM isotherms by Eq.(4.18) encounters obvious difficulties, for example at $T_m = 21$ K for $\text{Fe}_{0.65}\text{Ni}_{0.24}\text{Cr}_{0.11}$

($T_g \cong 22$ K), and at $T_m = 24$ K and 25 K for $\text{Fe}_{0.65}\text{Ni}_{0.23}\text{Cr}_{0.12}$ ($T_g \cong 25$ K). But, generally speaking if we allow m_0 , γ , and x to vary freely with temperature and wait time, we can fit all of the thermoremanent isotherms very well. An inspection of the parameters in tables 4.9-4.12 shows that γ increases with temperature and wait-time, and has a magnitude of around 10^{-2} for all of the systems. x also increases as the temperature increases, but depends only weakly on the wait-time t_w .

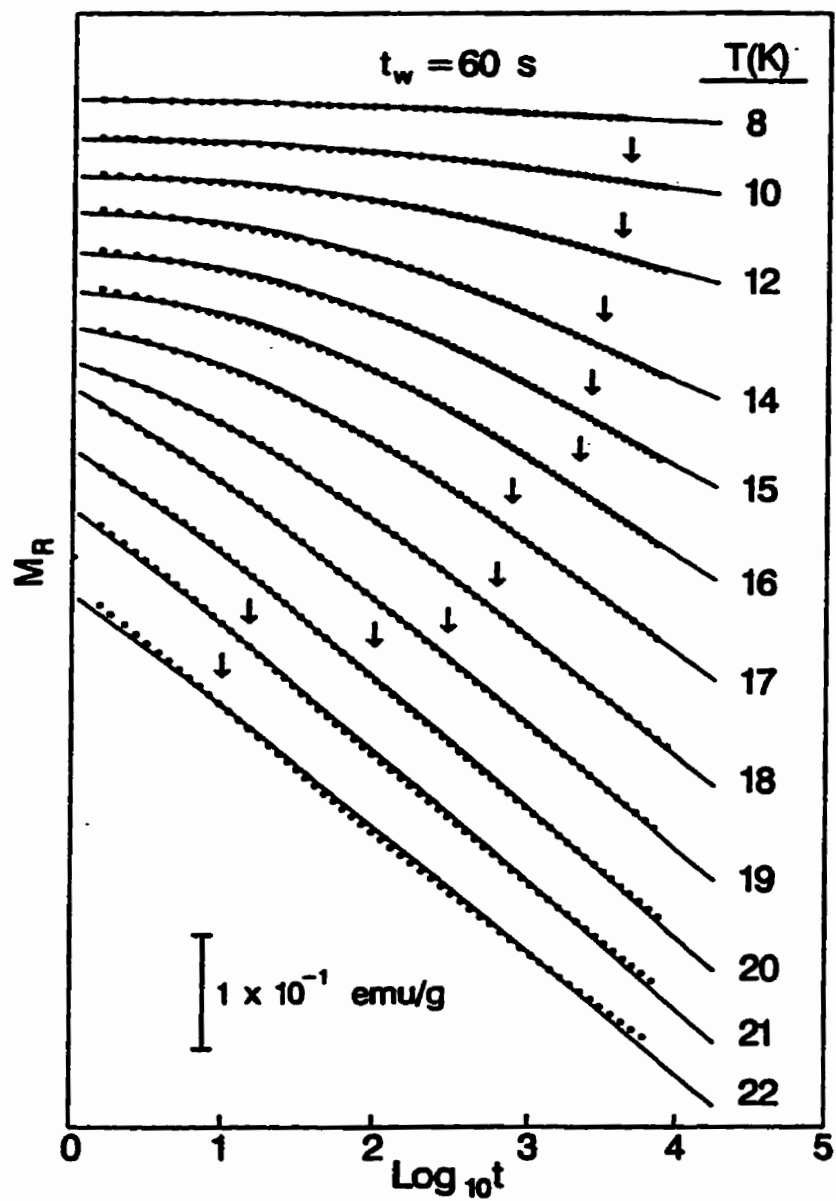


Figure 4.9: Random Trap Model fits of Eq.(4.18) (solid curves) to thermomagnetic relaxation isotherms of $\text{Fe}_{0.65}\text{Ni}_{0.24}\text{Cr}_{0.11}$ for a sequence of temperatures $T_m \leq 22 \text{ K}$ and for a common wait time $t_w = 60 \text{ s}$. The vertical arrows mark the characteristic times (inflection points) τ .

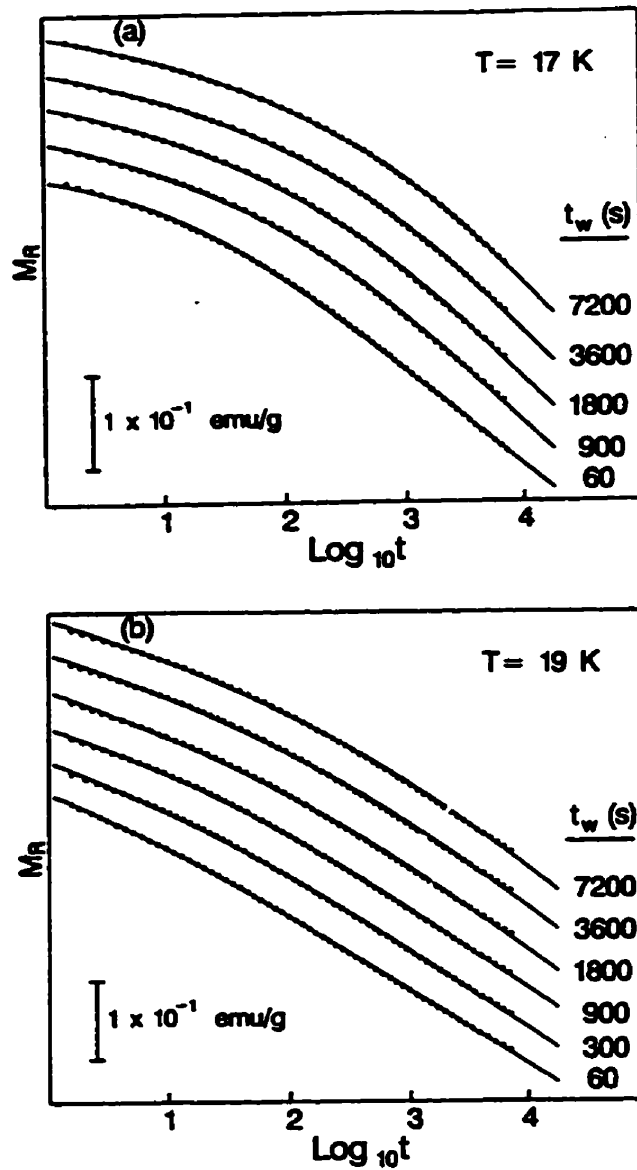


Figure 4.10: (a) Random Trap Model fits of Eq.(4.18)(solid curves) to the wait-time dependence of the thermoremanent relaxation of $\text{Fe}_{0.65}\text{Ni}_{0.21}\text{Cr}_{0.11}$ at $T_m = 17$ K. (b) Same sample and analysis as in (a) but for $T_m = 19$ K.

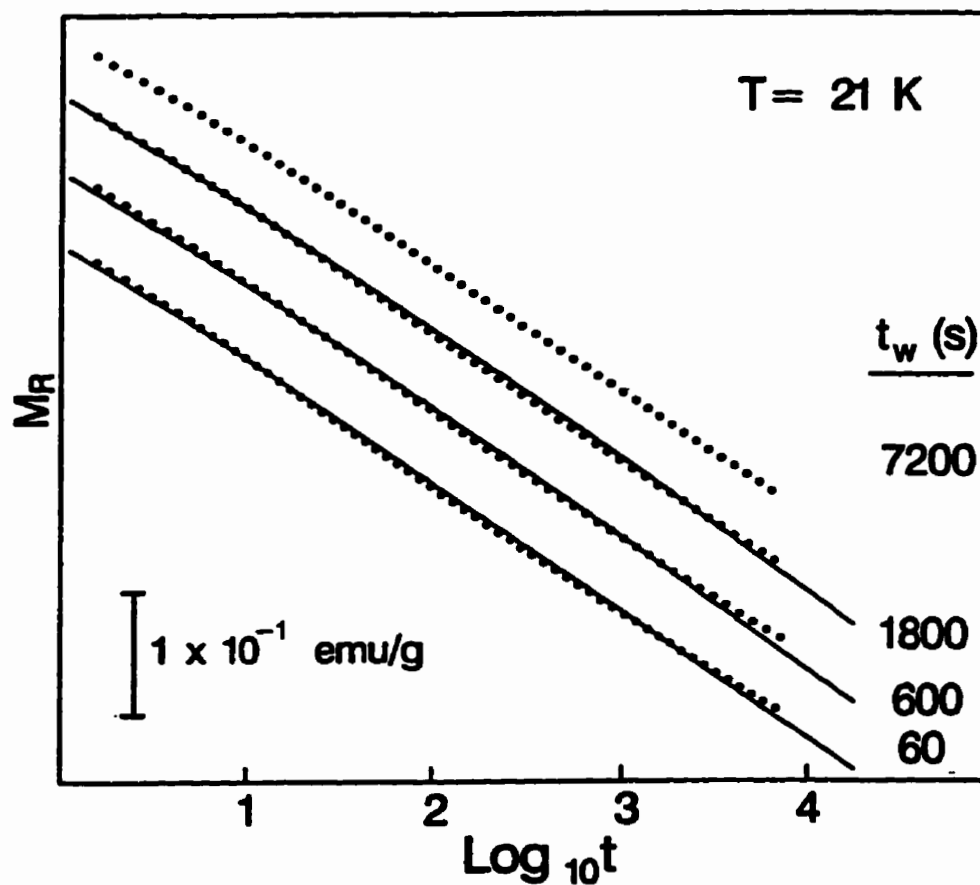


Figure 4.11: Random Trap Model fits of Eq.(4.18)(solid curves) to the wait-time dependence of the thermoremanent relaxation of $\text{Fe}_{0.65}\text{Ni}_{0.24}\text{Cr}_{0.11}$ at $T_m = 21$ K. The fitting quality is not as good as $T_m = 17$ K and 19 K. Function(4.18) would not work for the isotherm with $T_m = 21$ K and $t_w = 2$ h.

Table 4.9: Best-fit parameters of $\text{Fe}_{0.65}\text{Ni}_{0.24}\text{Cr}_{0.11}$ to the random trap model Eq.(4.18).

T (K)	t_w (sec)	M_0 ($\times 10^{-2}\text{emu/g}$)	γ ($\times 10^{-3}$)	x
8	60	345.06 ± 0.01	0.70 ± 0.01	0.562 ± 0.011
10	60	335.24 ± 0.01	1.82 ± 0.01	0.402 ± 0.005
12	60	337.66 ± 0.01	3.68 ± 0.01	0.288 ± 0.003
14	60	336.17 ± 0.01	6.33 ± 0.01	0.364 ± 0.002
15	60	332.57 ± 0.01	7.88 ± 0.01	0.436 ± 0.001
16	60	334.72 ± 0.01	9.49 ± 0.01	0.483 ± 0.001
17	60	334.43 ± 0.01	10.88 ± 0.01	0.626 ± 0.001
17	900	335.05 ± 0.02	12.86 ± 0.01	0.779 ± 0.001
17	1800	333.25 ± 0.02	13.64 ± 0.01	0.786 ± 0.001
17	3600	335.93 ± 0.01	14.32 ± 0.01	0.784 ± 0.001
17	7200	335.46 ± 0.01	15.30 ± 0.01	0.786 ± 0.001
18	60	335.29 ± 0.03	12.26 ± 0.01	0.760 ± 0.001
19	60	351.95 ± 0.09	13.02 ± 0.01	0.882 ± 0.001
19	300	351.93 ± 0.07	13.87 ± 0.01	0.892 ± 0.001
19	900	346.03 ± 0.05	14.03 ± 0.01	0.866 ± 0.001
19	1800	350.64 ± 0.05	15.23 ± 0.01	0.891 ± 0.001
19	3600	346.26 ± 0.04	16.12 ± 0.01	0.887 ± 0.001
19	7200	344.86 ± 0.04	17.06 ± 0.01	0.882 ± 0.001
20	60	351.37 ± 0.13	13.99 ± 0.01	0.899 ± 0.001
21	60	372.10 ± 0.31	14.08 ± 0.01	0.934 ± 0.001
21	600	395.28 ± 0.34	14.86 ± 0.01	0.951 ± 0.001
21	1800	405.10 ± 0.36	15.16 ± 0.01	0.955 ± 0.001
21	7200	-	-	-
22	60	365.32 ± 0.40	13.84 ± 0.01	0.939 ± 0.001

Table 4.10: Best-fit parameters of $\text{Fe}_{0.65}\text{Ni}_{0.23}\text{Cr}_{0.12}$ to the random trap model Eq.(4.18).

T (K)	t_w (sec)	M_0 ($\times 10^{-3}\text{emu/g}$)	γ ($\times 10^{-3}$)	x
16	300	405.03 \pm 0.02	24.20 \pm 0.02	0.578 \pm 0.001
18	300	413.51 \pm 0.03	31.18 \pm 0.02	0.656 \pm 0.001
20	300	434.84 \pm 0.04	42.81 \pm 0.02	0.686 \pm 0.001
20	900	437.02 \pm 0.03	45.55 \pm 0.02	0.702 \pm 0.001
20	1800	428.63 \pm 0.03	49.02 \pm 0.03	0.711 \pm 0.001
20	3600	422.92 \pm 0.03	51.51 \pm 0.04	0.711 \pm 0.001
20	7200	414.40 \pm 0.03	52.26 \pm 0.05	0.722 \pm 0.001
21	300	448.62 \pm 0.05	46.54 \pm 0.02	0.746 \pm 0.001
21	900	434.35 \pm 0.05	49.38 \pm 0.02	0.767 \pm 0.001
21	1800	437.09 \pm 0.04	54.10 \pm 0.03	0.748 \pm 0.001
21	3600	432.09 \pm 0.04	56.32 \pm 0.03	0.755 \pm 0.001
21	7200	429.07 \pm 0.03	60.65 \pm 0.04	0.751 \pm 0.001
22	300	460.71 \pm 0.08	53.30 \pm 0.02	0.784 \pm 0.001
22	900	469.85 \pm 0.06	54.74 \pm 0.02	0.791 \pm 0.001
22	1800	459.98 \pm 0.06	58.85 \pm 0.02	0.791 \pm 0.001
22	3600	458.71 \pm 0.05	61.15 \pm 0.03	0.792 \pm 0.001
22	7200	449.52 \pm 0.05	65.02 \pm 0.04	0.792 \pm 0.001
23	300	486.50 \pm 0.15	61.51 \pm 0.02	0.845 \pm 0.001
24	300	596.30 \pm 0.38	58.55 \pm 0.01	0.894 \pm 0.001
24	900	591.72 \pm 0.30	61.15 \pm 0.01	0.895 \pm 0.001
24	1800	584.37 \pm 0.25	61.51 \pm 0.01	0.893 \pm 0.001
24	3600	562.62 \pm 0.25	66.07 \pm 0.01	0.895 \pm 0.001
24	7200	571.61 \pm 0.25	67.50 \pm 0.03	0.897 \pm 0.001
25	300	753.15 \pm 0.76	61.84 \pm 0.01	0.919 \pm 0.001

Table 4.11: Best-fit parameters of $\text{Cr}_{0.79}\text{Fe}_{0.21}$ to the random trap model Eq.(4.18).

T (K)	t_w (sec)	M_0 ($\times 10^{-2}\text{emu/g}$)	γ	x
10	60	44.1 ± 0.2	0.012 ± 0.003	0.46 ± 0.02
12	60	44.2 ± 0.2	0.019 ± 0.003	0.55 ± 0.02
14	60	42.9 ± 0.2	0.023 ± 0.002	0.72 ± 0.02
14	300	42.9 ± 0.2	0.026 ± 0.002	0.79 ± 0.02
14	900	43.9 ± 0.2	0.027 ± 0.002	0.78 ± 0.02
14	1800	44.8 ± 0.2	0.028 ± 0.002	0.78 ± 0.02
14	3600	42.9 ± 0.2	0.029 ± 0.002	0.77 ± 0.02
16	60	43.5 ± 0.2	0.024 ± 0.002	0.82 ± 0.02
18	60	47.0 ± 0.2	0.021 ± 0.002	0.91 ± 0.01
20	60	52.1 ± 0.2	0.015 ± 0.002	0.92 ± 0.01
22	60	45.6 ± 0.2	0.018 ± 0.002	0.93 ± 0.01

Table 4.12: Best-fit parameters of $(\text{Fe}_{0.65}\text{Ni}_{0.35})_{0.882}\text{Mn}_{0.118}$ to the random trap model Eq.(4.18).

T (K)	t_w (sec)	M_0 ($\times 10^{-3}\text{emu/g}$)	γ	x
40	60	131.80 ± 0.01	0.015 ± 0.001	0.29 ± 0.01
45	60	131.70 ± 0.02	0.021 ± 0.001	0.43 ± 0.01
50	60	131.70 ± 0.04	0.029 ± 0.001	0.59 ± 0.01
52	60	133.70 ± 0.06	0.033 ± 0.001	0.69 ± 0.01
55	60	139.80 ± 0.16	0.038 ± 0.001	0.82 ± 0.01
57	60	161.70 ± 0.49	0.038 ± 0.001	0.90 ± 0.01
57	300	165.90 ± 0.36	0.049 ± 0.001	0.91 ± 0.01
57	900	164.00 ± 0.30	0.041 ± 0.001	0.91 ± 0.01
57	3600	159.80 ± 0.24	0.042 ± 0.001	0.91 ± 0.01
57	10800	155.50 ± 0.23	0.044 ± 0.001	0.91 ± 0.01
60	60	402.10 ± 5.69	0.042 ± 0.001	0.96 ± 0.01

Function (4.18) only holds in the extreme non-ergodic limit, where the parameter x is supposed to depend only on temperature and is independent of the

wait time t_w , as is the parameter γ . However, the previous fits show that both γ and x vary with t_w , and this dependence suggests some flaw in the analysis. It is possible to overlook this discrepancy and to regard the parameters as being approximately constant. If the response of a real system was purely nonergodic then, for a given temperature T , the relaxation data for different t_w should scale onto a universal curve when plotted as a function of t/t_w , since the predicted response $m(t, t_w)/m_0$ in Eq.(4.18) depends only on the reduced variable t/t_w . Figures 13(a), 14(a) and 15(a) show the measured thermoremanent decay, normalized to its value m_0 at $t = 0$, and plotted versus $\log(t/t_w)$, for three temperatures $T = 17$ K, 19 K, and 21 K, and several wait times $t_w = 1$ m, 3m, 5m, 10m, 15m, 30m, 1h and 2h. The value of m_0 was determined by using the previous fits to the superposition of a stretched exponential and a constant in Section 4.3, and extrapolating to $t = 0$.

The lack of universality and the change in the relaxation rate for the different t_w data is obvious. Furthermore, if we were to fix x and γ for a given temperature T and different wait times t_w , this nonergodic function would not fit the data very well at all, as shown in Figure 4.12(a). Here, we have used the values for the parameters x and γ , obtained from the best fits to the $t_w = 60$ s data, because the youngest set of data satisfies the nonergodic condition best. If we generate theoretical curves from function (4.18) for the same x and γ but different t_w and compare with the experimental data in Figure 4.12(a), we do not get a satisfactory result. The systematic deviations clearly get worse as t_w increases. In fact, the parameter γ in equation(2.109) is actually predicted to decrease a little bit as t_w increases. So, the situation might get even worse if we were to use the more accurate exponent γ from this model, that is, choose one by fitting a particular t_w curve, and then calculate the other γ 's.

These failures to describe the data using only the extreme nonergodic function suggest that the real system does not age as rapidly as the nonergodic function predicts it should, and that the magnetization $m(t, t_w)$ should be represented as a

superposition of independent response functions, each weighted according to a distribution $P(t_{erg})$, as we discussed in Section (2.6). If we also invoke the assumption that the crossover from nonergodic to ergodic behaviour occurs suddenly, which is equivalent to assuming that the most probable ergodic time $t_{erg} = \tau_0 S^{1/x}$ is also the only ergodic time for a subsystem which occurs with any appreciable probability for any given subsystem, and that the crossover takes place when $t_w = t_{erg}$ (rather than when $t + t_w = t_{erg}$, as it actually does (Bouchaud et al., 1994)), then each term in the superposition is either purely ergodic or purely nonergodic, and the total magnetization is given by function (2.112). Now, the t/t_w - scaling is corrected by a factor $1 - F$, i.e.,

$$m(t, t_w)/(m_0(1 - F)) = f\left(\frac{t}{t_w}\right). \quad (4.20)$$

Figures 4.13(b), 4.14(b) and 4.15(b) show the corrected scaling plots, and Figure 4.12(b) shows the corrected fits to the relaxation isotherms. Both these fits and the universal behaviour are remarkably improved, and the “best-fit” parameters are listed in Table 4.13. The correction factor $1 - F$ is numerically calculated as described in Section 2.6. The systematic deviations observed in Figure 4.12(a) are removed, although there is clearly some mismatch in slopes which may be due to our choice of a Gaussian distribution. Inspection of Table 4.13 shows that (a) the width of the distribution of ergodic times is relatively large ($\sigma_{erg} \cong 2$) and temperature independent, (b) the mean of the logarithm of the ergodic time is relatively small ($\overline{\log_{10} t_{erg}} \leq 2$) and decreases with increasing temperature, which is consistent with the observed tendency of the system to age less and thus to approach equilibrium faster as T increases, (c) the parameter x , which describes the structure of configuration space, increases with increasing temperature and approaches unity as $T \rightarrow T_g^-$, which is more consistent with Derrida’s model (Derrida, 1981) of random energy levels than with Sherrington and Kirkpatrick’s

model (Sherrington and Kirpatrick, 1975) of random exchange bonds, in agreement with the conclusions reached by Bouchaud and coworkers (Bouchaud et al., 1994).

For our particular choice of distribution, the mean ergodic time \bar{t}_{erg} can be calculated from

$$\bar{t}_{erg} = \int_0^{\infty} t_{erg} P(t_{erg}) dt_{erg} \quad (4.21)$$

$$= \exp\left(\overline{\log_{10} t_{erg}} / \log_{10} e + \sigma_{erg}^2 / (2(\log_{10} e)^2)\right) / \log_{10} e \quad (4.22)$$

which yields values of \bar{t}_{erg} ranging from $\bar{t}_{erg}(17 \text{ K}) \sim 9 \times 10^6 \text{ s}$ to $\bar{t}_{erg}(21 \text{ K}) \sim 9 \times 10^4 \text{ s}$, listed in Table 4.13, once again comparable to those deduced by Bouchaud et al. (1994).

The same scaling analysis was performed for the remaining samples and the results are collected in Appendix B. For $\text{Fe}_{0.65}\text{Ni}_{0.23}\text{Cr}_{0.12}$, $T_m = 20 \text{ K}$, 21 K , 22 K , and 24 K , and $t_w = 5\text{m}$, 15m , 30m , 1h , and 2h , the scaling analysis yielded the best fit scaling parameters listed in Table 4.14, and the scaling plots shown in Figures B.6-B.9; For $\text{Cr}_{0.79}\text{Fe}_{0.21}$, $T_m = 14 \text{ K}$ and $t_w = 1\text{m}$, 5m , 15m , 30m , and 1h , the best fit scaling parameters are listed in Table 4.15, and the scaling plots are shown in Figure B.10; For $(\text{Fe}_{0.65}\text{Ni}_{0.35})_{0.882}\text{Mn}_{0.118}$, $T_m = 48 \text{ K}$, 52 K , 56 K and 57 K , and $t_w = 1\text{m}$, 2m , 3m , 4m , 5m , 10m , 15m , 30m , 1h , and 2h , the best fit scaling parameters are listed in Table 4.16, and the scaling plots are shown in Figures B.11-B.14. A comparison of the scaling plots for these different systems, shows that the scaling analysis works a little better in the systems $\text{Fe}_{0.65}\text{Ni}_{0.24}\text{Cr}_{0.11}$ and $(\text{Fe}_{0.65}\text{Ni}_{0.35})_{0.882}\text{Mn}_{0.118}$. The relaxation isotherms in these two systems have somewhat weaker curvature which makes them more compatible with the shape of the theoretical functions.

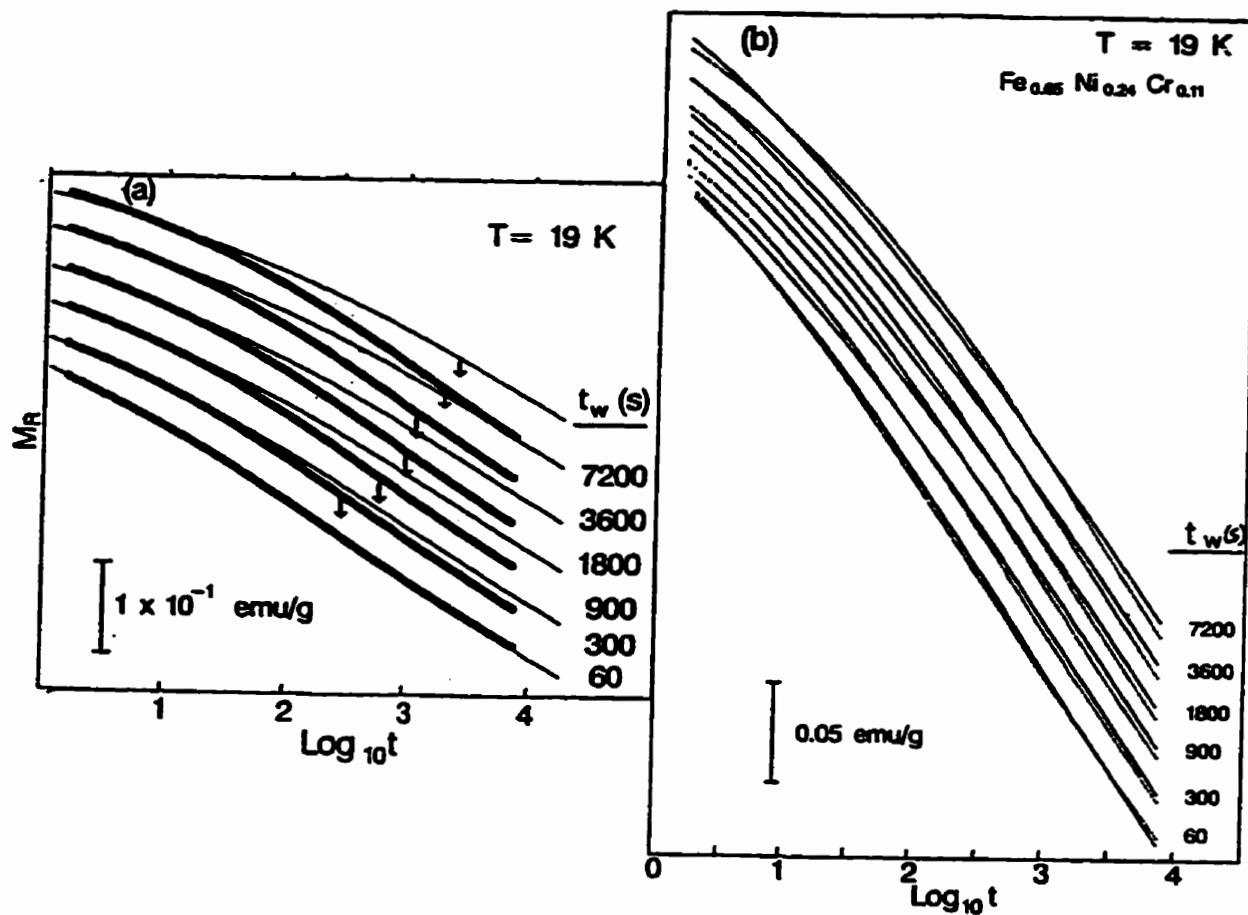


Figure 4.12: (a) Fits (solid curves) of $\text{Fe}_{0.65}\text{Ni}_{0.24}\text{Cr}_{0.11}$ for $T_m = 19 \text{ K}$ and for different wait times t_w to Eq.(4.18) with fixed $\gamma = 0.0130$ and $x = 0.882$. m_0 is chosen by extrapolating stretched exponential fits to $t = 0$. (b) Fits (solid curves) of $T_m = 19 \text{ K}$ for different wait times t_w to Eq.(2.112) with the fixed γ and x values in Table 4.13. m_0 is 3.378, 3.361, 3.376, 3.380, 3.359 and 3.369 emu/g for $t_w = 60\text{s}$, 300s, 900s, 1800s, 3600s, 7200s respectively.

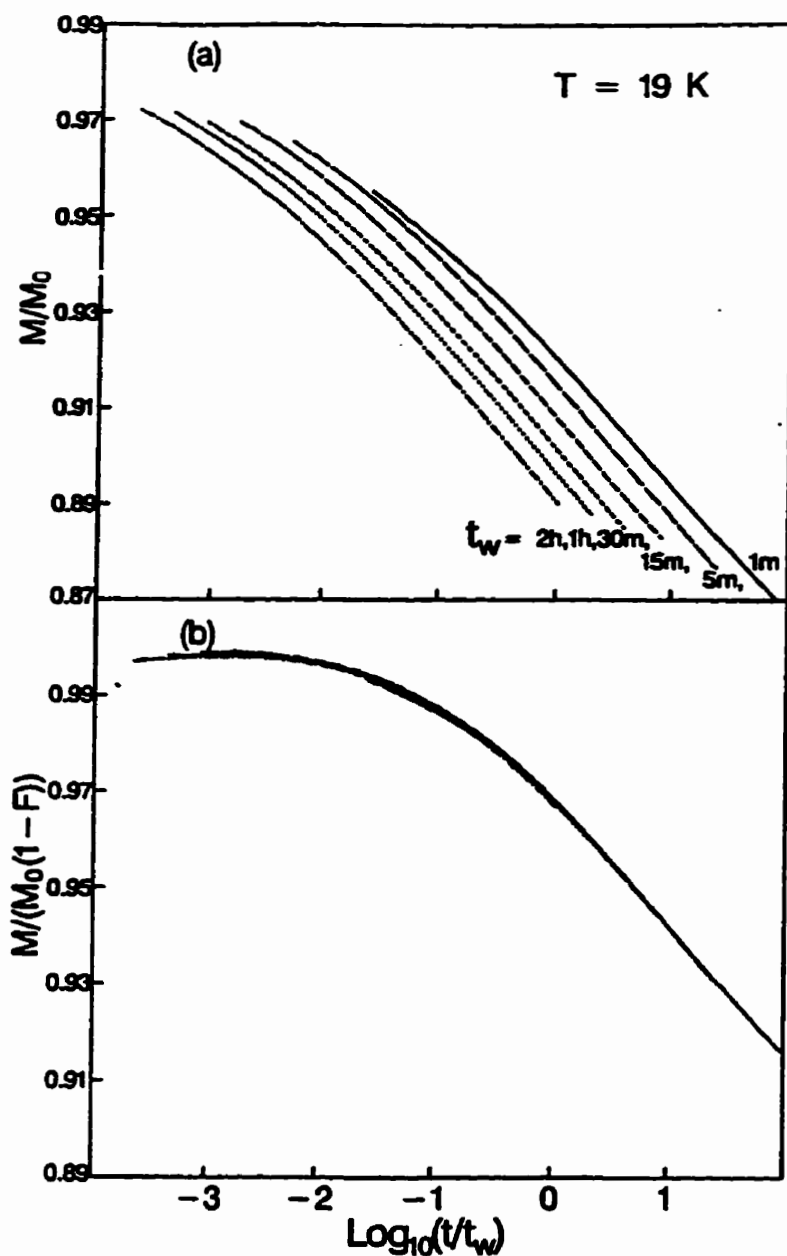


Figure 4.13: (a) Scaling of $\text{Fe}_{0.65}\text{Ni}_{0.24}\text{Cr}_{0.11}$ isotherms at $T_m = 19 \text{ K}$ for different wait times t_w , as m/m_0 versus t/t_w . m_0 is chosen by the empirical stretched exponential model. (b) Scaling of $\text{Fe}_{0.65}\text{Ni}_{0.24}\text{Cr}_{0.11}$ isotherms at $T_m = 19 \text{ K}$ for different wait times t_w by Eq.(2.112). m_0 is 3.378, 3.361, 3.376, 3.380, 3.359 and 3.369 emu/g for $t_w = 60\text{s}$, 300s, 900s, 1800s, 3600s, 7200s respectively. Other parameters are in Table 4.13.

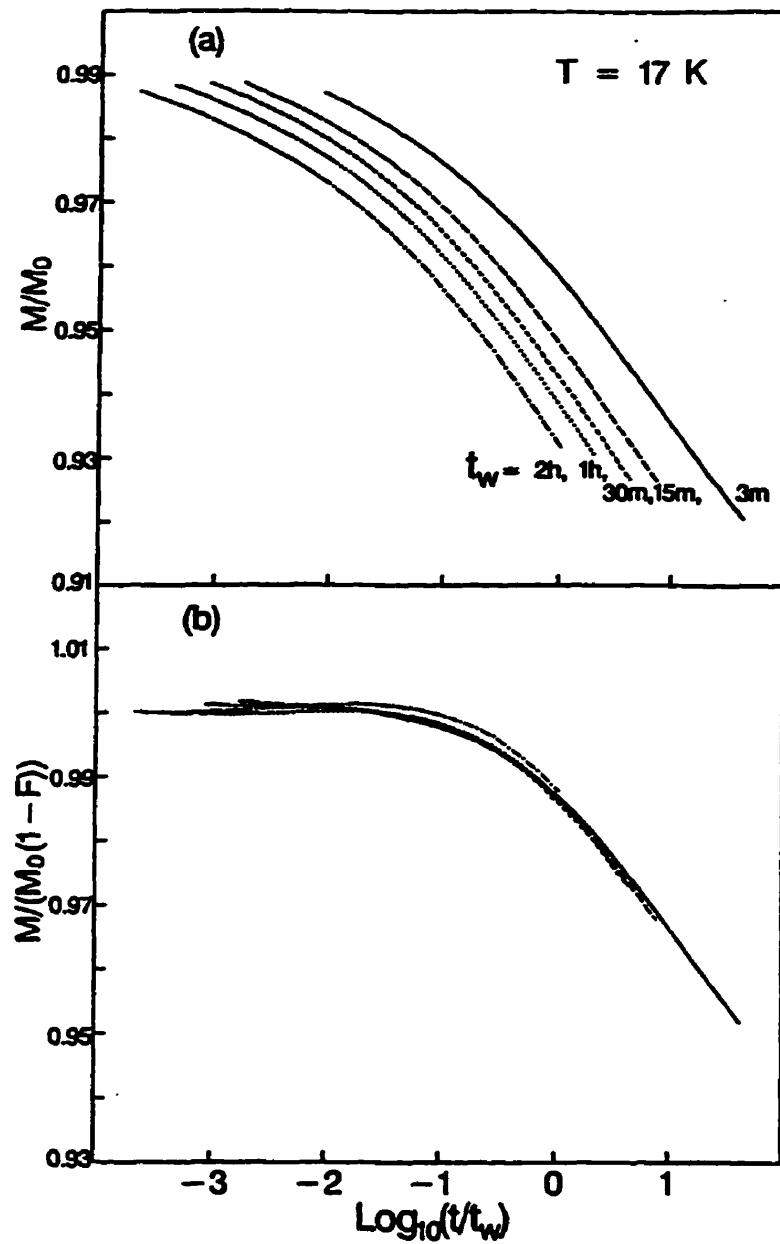


Figure 4.14: (a) Scaling of $\text{Fe}_{0.65}\text{Ni}_{0.24}\text{Cr}_{0.11}$ isotherms at $T_m = 17 \text{ K}$ for different wait times t_w , as m/m_0 versus t/t_w . m_0 is chosen by the empirical stretched exponential model. (b) Scaling of $\text{Fe}_{0.65}\text{Ni}_{0.24}\text{Cr}_{0.11}$ isotherms at $T_m = 17 \text{ K}$ for different wait times t_w by Eq.(2.112). m_0 is 3.342, 3.322, 3.306, 3.343 and 3.340 emu/g for $t_w = 60\text{s}$, 900s, 1800s, 3600s, 7200s respectively. Other parameters are listed in Table 4.13.

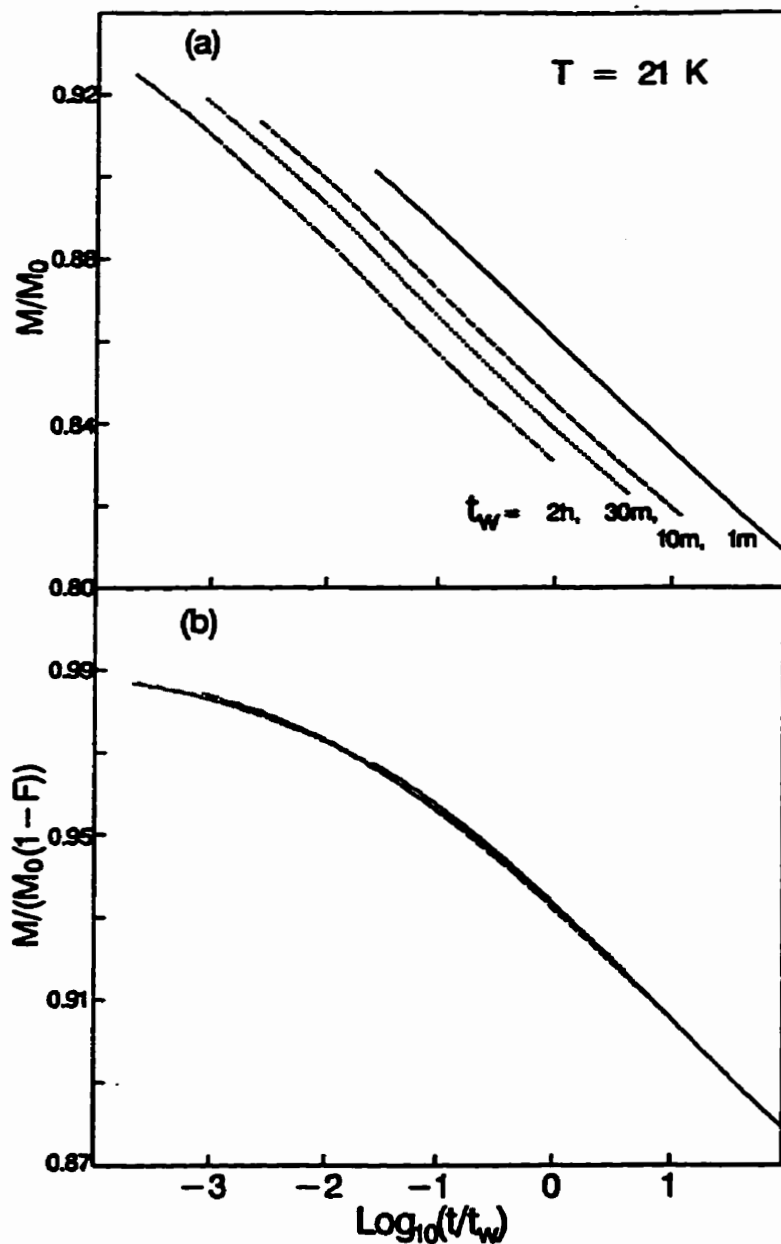


Figure 4.15: (a) Scaling of $\text{Fe}_{0.65}\text{Ni}_{0.21}\text{Cr}_{0.11}$ isotherms at $T_m = 21 \text{ K}$ for different wait times t_w , as m/m_0 versus t/t_w . m_0 is chosen by the empirical stretched exponential model. (b) Scaling of $\text{Fe}_{0.65}\text{Ni}_{0.21}\text{Cr}_{0.11}$ isotherms at $T_m = 21 \text{ K}$ for different wait times t_w by Eq.(2.112). m_0 is 3.426, 3.416, 3.426 and 3.432 emu/g for $t_w = 60\text{s}$, 600s, 1800s, 7200s respectively. Other parameters are in Table 4.13.

Table 4.13: Scaling parameters of $\text{Fe}_{0.65}\text{Ni}_{0.24}\text{Cr}_{0.11}$ to Eq.(2.112).

T(K)	$\overline{\log_{10} t_{erg}}$	σ_{erg}	\bar{t}_{erg} ($\times 10^5 s$)	x	γ
17	2.0 ± 0.2	2.0 ± 0.3	92.7	0.10 ± 0.05	0.0128 ± 0.0010
19	1.0 ± 0.3	2.0 ± 0.3	9.27	0.60 ± 0.10	0.0135 ± 0.0010
21	0.0 ± 0.3	2.0 ± 0.3	0.93	0.83 ± 0.10	0.0140 ± 0.0010

Table 4.14: Scaling parameters of $\text{Fe}_{0.65}\text{Ni}_{0.23}\text{Cr}_{0.12}$ to Eq.(2.112).

T(K)	$\overline{\log_{10} t_{erg}}$	σ_{erg}	\bar{t}_{erg} ($\times 10^{12} s$)	x	γ
20	2.2 ± 0.2	3.0 ± 0.3	8.39	0.10 ± 0.05	0.044 ± 0.001
21	1.8 ± 0.2	3.0 ± 0.3	3.34	0.20 ± 0.05	0.050 ± 0.001
22	1.6 ± 0.2	3.0 ± 0.3	2.11	0.30 ± 0.05	0.058 ± 0.001
24	0.3 ± 0.2	3.0 ± 0.3	1.06	0.40 ± 0.05	0.068 ± 0.001

Table 4.15: Scaling parameters of $\text{Cr}_{0.79}\text{Fe}_{0.21}$ to Eq.(2.112).

T(K)	$\overline{\log_{10} t_{erg}}$	σ_{erg}	\bar{t}_{erg} ($\times 10^6 s$)	x	γ
14	1.8 ± 0.2	2.0 ± 0.2	5.85	0.20 ± 0.02	0.025 ± 0.001

Table 4.16: Scaling parameters of $(\text{Fe}_{0.65}\text{Ni}_{0.35})_{0.882}\text{Mn}_{0.118}$ to Eq.(2.112).

T(K)	$\overline{\log_{10} t_{erg}}$	σ_{erg}	\bar{t}_{erg} ($\times 10^6 s$)	x	γ
48	2.5 ± 0.2	2.0 ± 0.2	29.3	0.20 ± 0.05	0.036 ± 0.001
52	1.6 ± 0.2	2.0 ± 0.2	3.69	0.40 ± 0.05	0.043 ± 0.001
56	0.9 ± 0.2	2.0 ± 0.2	0.74	0.60 ± 0.05	0.050 ± 0.001
57	2.0 ± 0.2	2.0 ± 0.2	5.85	0.80 ± 0.05	0.041 ± 0.001

4.5 Relaxation Dynamics: An Elementary Decay Model (EDM) Analysis

The EDM model predicts a 7-parameter decay function given by Eq.(2.136):

$$M(t, t_w) = M_0 \left\{ (1 - c) \frac{g_1(b_1, \tau=r_0(t+t_w+t_{in1}))}{g_1(b_1, \tau=r_0(t_w+t_{in1}))} + c \frac{g_2(b_2, \tau=r_0(t+t_{in2}))}{g_2(b_2, \tau=r_0 t_{in2})} \right\} \quad (4.23)$$

In this section we illustrate the EDM analysis by applying the model to the $\text{Cr}_{0.79}\text{Fe}_{0.21}$ TRM relaxation curves both below and above T_g . The best fitting parameters are listed in Tables 4.17 and 4.18, and the data and the fits are collected in Figures 4.16, 4.17 and 4.18. Figures 4.16(a) and 4.17(a) show the time dependence of the decay $M_R(t_d)$ and of the corresponding relaxation rate $S(t_d) = -\partial M_R(t_d)/\partial \ln t_d$, respectively, both plotted on the same logarithmic observation time scale $\log_{10} t_d$. The solid curves and the inserts are predictions of the EDM. First, a few words about the actual fitting procedure. Generally speaking, it was necessary to include both components of (4.23) when fitting the data. The first, age-dependent component g_1 alone has far too much curvature, and decays to zero far too rapidly, to provide a suitable representation of the experimental data which is a very gradual decay with quite subtle changes in curvature. The second, age-independent component g_2 has a very different value of the parameter b and provides a virtually constant baseline which improves the quality of the fits considerably. The parameter r_0 was fixed at 1 because the fits were relatively insensitive to it. The other 6 parameters then determined the fits to the experimental data with some limitations. The parameter c must be between 0 and 1. If the fits yielded $c > 1$, it was fixed at 1. If only g_2 was used to describe the data ($c = 1$), as follows:

$$M(t) = M_{base} + M_0 \left(\frac{g_2(b_2, \tau = t + t_{in2})}{g_2(b_2, \tau = t + t_{in2})} \right) \quad (4.24)$$

then it was necessary to add a baseline M_{base} to match the decay magnitude and the curvature of the data. This usually happened for the data around or above T_g ; t_{in_1} and t_{in_2} are both larger than zero. If t_{in_1} or t_{in_2} were less than zero in the fits, they were fixed at a constant positive number since a negative cooling time does not make physical sense. The ratio t_w/b_1 corresponds to the inflection point of the decay function, and the maximum in the relaxation rate, which should match that of the data. Sometimes b_1 had to be adjusted by hand for the longer wait times, in order to make t_w/b_1 match the inflection point.

The quality of the fits is excellent especially for the shorter wait times ($t_w \leq 300s$). This model generally provided the best fits of all the models we used, particularly to the structure in the relaxation rates. For longer wait times ($t_w \geq 900s$), the function crossed the data a few times and some deviations could be observed in the relaxation rate.

The inserts in Figures 4.16 and 4.17 show the final “aged” distribution of activation energies $(1 - c)f'_{0,b_1}(E, t_w) + cf_{0,b_2}(E)$ at $\tau_d = 0$ (just after the field change), with f_0 and f'_0 defined by Eq.(2.118) and Eq.(2.133) respectively, evaluated with the best fit EDM parameters in Table 4.17. The first term $(1 - c)f'_{0,b_1}(E, t_w)$ incorporates the effect of aging in a field, and contributes a relatively narrow, weak *maximum* to the final distribution, at an activation energy which increases as a function of a system age t_w . The second, age-independent term $cf_{0,b_2}(E)$, which is created by the field change, is characterized by a value of $b_2 \sim 0.01$ which is at least an order of magnitude less than b_1 , and is responsible for the very broad, comparatively flat background which dominates the distribution. This age-independent component cf_{0,b_2} contributes a quasi-logarithmic decay $cg'_{b_2, \tau_{in_2}}$ which accounts for virtually the entire *magnitude* of the remanence since $c \sim 0.9$, while the age-dependent component $(1 - c)f'_{0,b_1}$ yields a relatively small amplitude, quasi-power law decay $(1 - c)g'_{b_1, \tau_{in_1}, \tau_w}$ which accounts for most

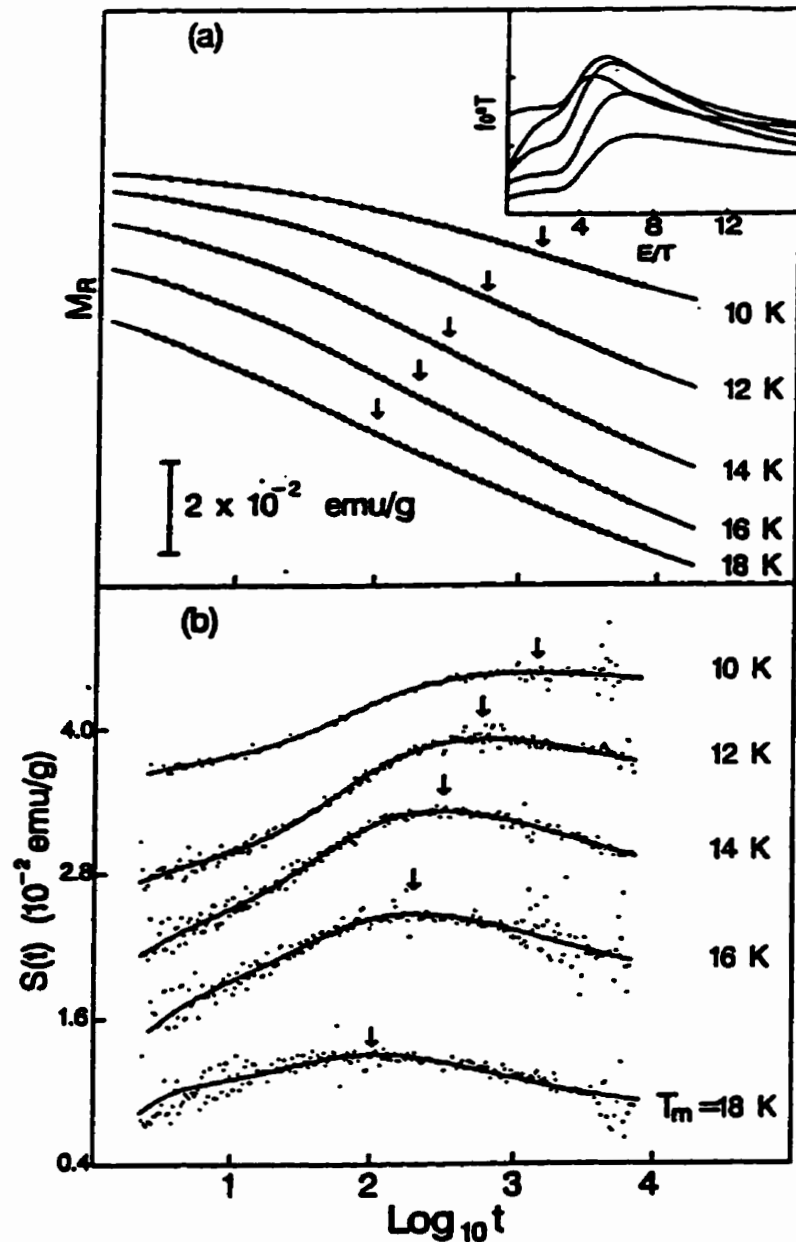


Figure 4.16: (a) EDM fits of Eq.(4.23) (solid curves) to the thermoremanent relaxation isotherms of $\text{Cr}_{0.79}\text{Fe}_{0.21}$ for $T_m = 10, 12, 14, 16$ and 18 K ($T_R = 25$ K) and for a common wait time $t_w = 60$ s. The vertical arrows mark the inflection points τ . (b) Relaxation rates for the data (dots) and the prediction of the EDM function (solid curves). The insert shows the final "aged" distribution of activation energies (just after the field change). The peaks from bottom to top corresponds to the temperatures from low to high.

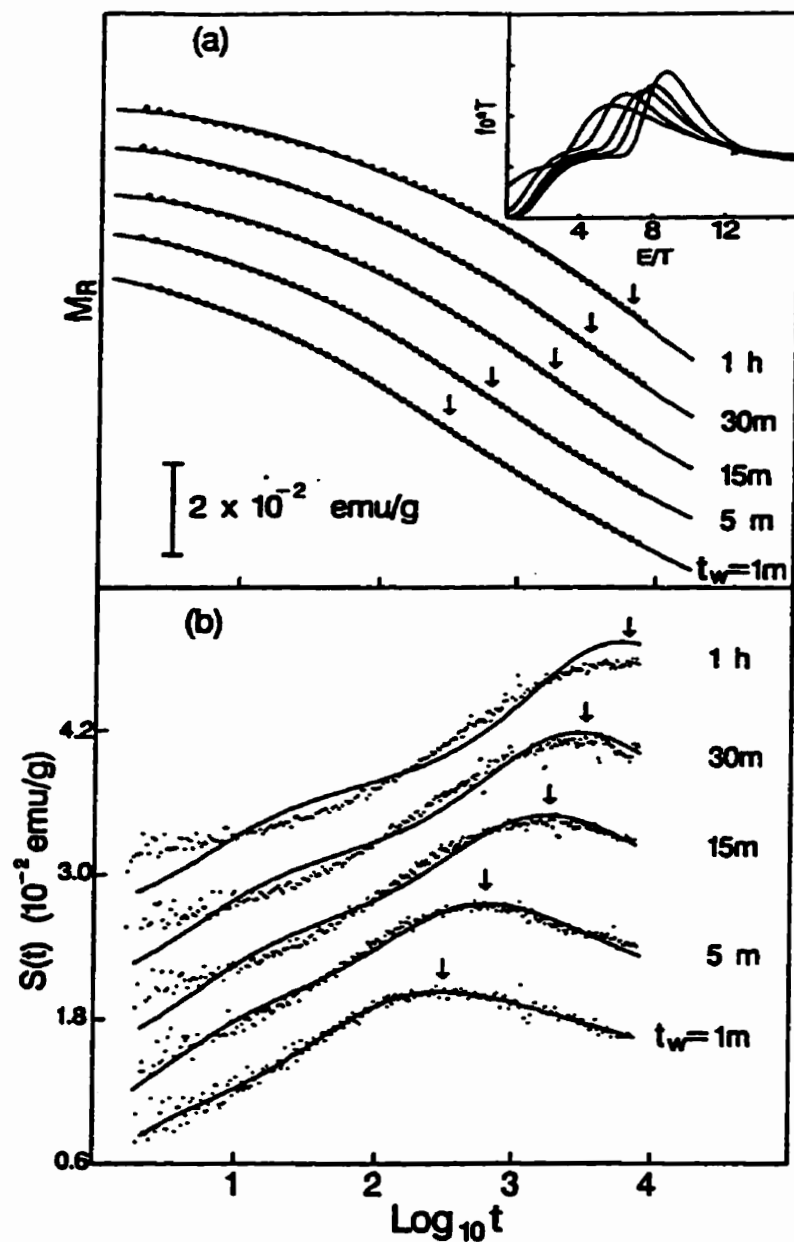


Figure 4.17: (a) EDM fits of Eq.(4.23)(solid curves) to the wait-time dependence of the thermoremanent relaxation of $\text{Cr}_{0.79}\text{Fe}_{0.21}$ at $T_m = 14$ K and for wait times $t_w = 1\text{m}, 5\text{m}, 15\text{m}, 30\text{m}$ and 1h . The vertical arrows mark the characteristic times (inflection points) τ . (b) Measured relaxation rates(dots) and the predictions of the theory (solid curves). The insert shows the final "aged" distribution of activation energies (just after the field change). The peaks from left to right corresponds to the wait times from short to long.

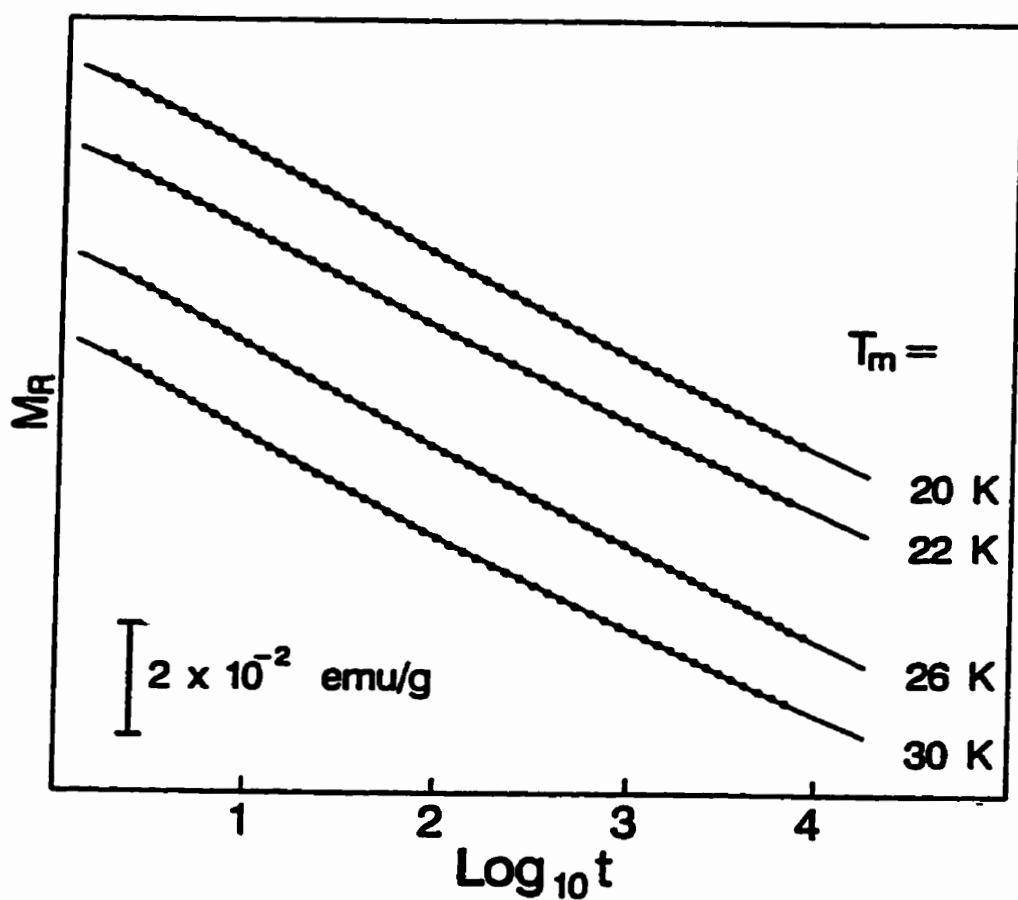


Figure 4.18: EDM fits (solid curves) of Eq.(4.23) to the thermoremanent relaxation curves of $\text{Cr}_{0.79}\text{Fe}_{0.21}$ for $T_m = 20$ K and 22 K ($< T_g$), $t_w = 60$ s, and of Eq.(4.24) to $T_m = 26$ and 30 K ($> T_g$) for $t_w = 60$ s ($T_R = 25$ K).

of the *structure* in the measured relaxation rate $S(t)$. The parameter c increases monotonically with temperature and approaches unity near 25 K, above which the age-dependent component vanishes $(1 - c) = 0$, and the measured relaxation response is described by g'_{b_2} and Eq.(4.24) alone.

The EDM is clearly capable of reproducing the principle structure features of the TRM decay very well, including both subtle variations in its curvature, as well as its overall magnitude. The success of this description rests on the following key assumptions regarding the distribution of activation energies: (a) Its initial form immediately following the quench is Poissonian; (b) The distribution is not static, but instead evolves with wait time t_w (at constant temperature and field) by losing the contribution from relaxation processes within a progressively expanding region at the lower energy end of the activation energy spectrum; (c) The effect of the field change is to modify substantially the distribution which exists at the end of the aging period, but in such a way that the new distribution, which defines the actual observed decay, nevertheless retains some memory of the aging process. This evolutionary sequence is illustrated in Figure 4.19 using the best fit parameters for one of the relaxation isotherms analyzed for the system: $\text{Fe}_{0.65}\text{Ni}_{0.23}\text{Cr}_{0.12}$, with $T_m = 20$ K, $t_w = 1800$ s. Aging converts the original Poissonian distribution (solid curve) in Fig.4.19(a), which is dominated by low energy (or short time) activation events, into a distribution (dashed curve) in Fig.4.19(a), which indicates that those relaxation process which remain active at the end of the interval (in the sense that they have not yet decayed to equilibrium) tend to be clustered around a particular characteristic activation energy E_c . (This peak is a consequence of multiplying two exponentials, $\exp(-t_w/\tau)$ and $\exp(-E/\bar{E})$). However, Fig.4.19(b) shows that, contrary to expectation, this characteristic energy does not dominate the final decay because the field change effectively “disperses” the distribution over a very wide range of activation energies, leaving only a weak

artifact in the vicinity of E_c to “echo” the effect of aging. If the EDM is to be consistent with experiment, these distributions must have one further property, which is particularly crucial to the subsequent interpretation.

According to the EDM, a relaxing physical observable derives its time dependence from the decay of an underlying distribution function:

$$g(\tau) = \int_0^\infty f(E, \tau) dE \quad (4.25)$$

where $f \sim \exp(-\tau_w \exp(-E/T))$ in the aging regime $\tau \leq \tau_w$ and $f \sim \exp(-\tau_d \exp(-E/T))$ in the post-aging regime $\tau > \tau_w$. Although the model decay in these two regimes is thus governed by the same exponential factor, it is an *experimental fact* that the field-cooled magnetization is observed to be essentially *constant* throughout the waiting period. Thus, activation events, which occur during the aging period ($\tau \leq \tau_w$) do not translate into measurable physical losses, and this can be accomplished within the EDM formalism, if aging acts to merely *redistribute* the activation events *while continuously preserving the normalization of the distribution*. This renormalization has been incorporated into the dashed curve of Fig. 4.19(a). Once the field is changed, however, these same activation processes become “operative”, in the sense that they represent real losses to the distribution, and hence to the decaying physical observable.

The EDM itself offers no particular insight into the physical origin of these effects. However, at least some of this behavior is reminiscent of Bouchaud's model of activated hopping among metastable traps, and suggests the following interpretation for the EDM. Once again we adopt the general premise that a disordered system consists of a collection of magnetically independent subsystems, each of which possesses a very rugged free energy landscape with many local minima. Each minimum represents a particular metastable spin configuration of the N-spin subsystem, and each is characterized by its own macroscopic magnetization. During the waiting time t_w , each subsystem ergodically explores a limited

region of its own configuration space by thermally driven hopping among the traps, but has the *largest probability* to be found after a time t_w in a trap with a characteristic time $\sim t_w$ (which is usual for random walks involving broad distributions, where the most significant contributions arise from the largest, but most infrequent, events). In other words, the behaviour of all physical observables is dominated by the properties of the deepest trap which the subsystems were allowed to probe during the aging period. This is precisely the trend observed in Fig.4.19(a) (both the solid and the dashed curves), where the distribution evolves from a function dominated by short time activation events to one dominated by activations near E_c , corresponding to a relaxation time $t_c = t_w/b_1 \sim t_w$ since $b_1 \sim 0.5$. Furthermore, the constancy of the field-cooled magnetization M_{FC} implies that the system is limited, in its excursions through configuration space, to a particular subgroup of traps, all of which are favoured energetically, since an extensive free energy M_{FCHC} would be required in order for the system to escape from this region of configuration space. These considerations suggest that we may interpret the EDM distribution $f'_{0,b_1}(E, t_w)$ as the fractional number of subsystems which occupy traps of depth E *within a particular "pool of traps" of fixed magnetization M_{FC}* , after a wait time t_w . Since no subsystems are lost from this pool during the aging period t_w , the distribution f'_{0,b_1} remains normalized to unity and the magnetization cannot decay.

With this identification, it is then possible to suggest a physical interpretation for the change in the distribution from $f'_{0,b_1}(E, t_w) \rightarrow (1 - \alpha)f'_{0,b_1}(E, t_w) + \alpha f_{0,b_2}(E)$ when the field is changed. Suppose that changing the field changes the *depth* of the traps by a factor ξ which depends on the typical number N of spins which must be flipped in order to escape from the bottom of a trap and on their Zeeman energy with respect to the field change (Vincent et al., 1995a). This number N , and the net uncompensated moment $m \sim \pm\sqrt{N}$, are both expected

to increase with the depth of the trap, so that the field-induced redefinition of the traps is *non-uniform*, and becomes progressively more significant as the traps become deeper. This redefinition has the effect of dispersing the energetically localized subsystems in Fig.4.19(a) (dashed curve) over a much broader range of trap depths. These redefined traps now experience “real” depopulation in the sense that subsystems activated out of these redefined M_{FC} -traps are lost from this region of configuration space to other energetically more favourable regions of configuration space, where the traps have zero magnetization.

While similar considerations by Vincent et al.(1995a) only allow for the possibility of a reduction in the trapping time by this mechanism, it is clear from Fig.4.19(b) that the EDM predicts both increases as well as decreases in the trapping times as a consequence of the field change. However, the most significant feature of the proposed redefinition is that changing the field completely “resets” many of the subsystems, since many of the shallow traps emptied during aging are refilled by changing the field, and in this regards, the EDM certainly agrees with Vincent’s picture.

The EDM analysis was also performed for the other systems both below and above the glass temperatures. The best-fit parameters are listed in Tables 4.19-4.25, and the fits are shown in Figures C.1-C.18, Appendix C. The parameter c , which describes the fractional contribution of the non-aging component, increases towards unity as the temperature approaches T_g , but decreases slightly with increasing wait time t_w . The parameter b_1 increases with temperature and wait time t_w , while b_2 increases with temperature, but decreases slightly with increasing wait time t_w . The parameter t_{in1} tends to be larger at lower temperatures and shorter wait times, which is consistent with the longer cooling times expected at the lower temperatures. The parameter t_{in2} is around 1s and increases with wait time t_w .

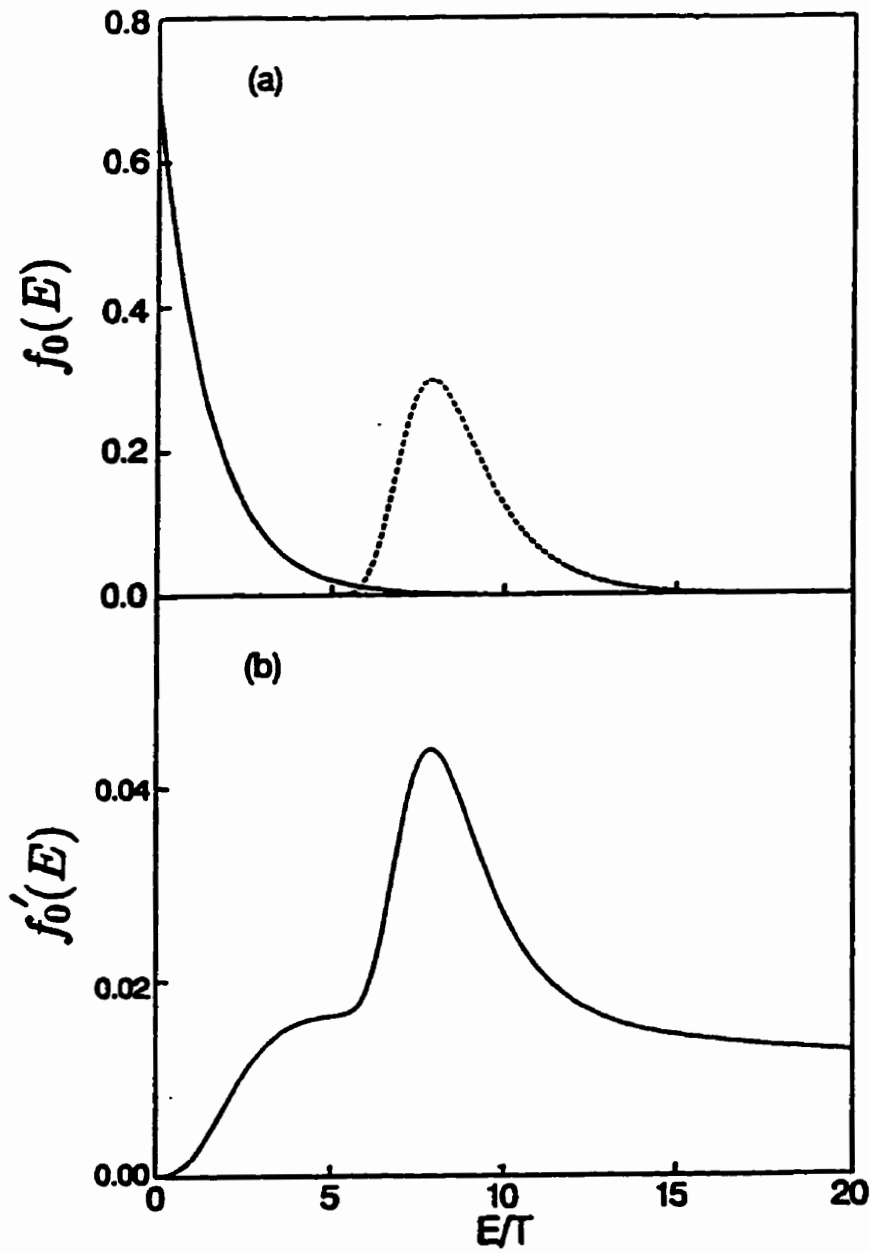


Figure 4.19: (a) The original Poissonian distribution of energy (solid curve) and the distribution of energy converted by aging after wait time t_w (dashed curve) for $\text{Fe}_{0.65}\text{Ni}_{0.23}\text{Cr}_{0.12}$, with $T_m = 20$ K and $t_w = 1800$ s. (b) The distribution of energy at the beginning of the field cut off for the same sample and same condition.

Table 4.17: Best-fit parameters of the EDM model Eq.(4.23) to $\text{Cr}_{0.79}\text{Fe}_{0.21}$.

T (K)	t_w (sec)	M_0 ($\times 10^{-1}\text{emu/g}$)	c	b_1 ($\times 10^{-1}$)	b_2 ($\times 10^{-2}$)	t_{in1} (sec)	t_{in2} (sec)
10	60	4.412 ± 0.001	0.83 ± 0.02	0.58 ± 0.05	0.43 ± 0.01	16 ± 4	0.5 ± 0.2
12	60	4.410 ± 0.001	0.86 ± 0.05	1.17 ± 0.04	0.73 ± 0.01	15 ± 2	0.3 ± 0.1
14	60	4.196 ± 0.001	0.907 ± 0.001	1.92 ± 0.01	1.23 ± 0.01	1.0	0.62 ± 0.04
14	300	4.132 ± 0.001	0.953 ± 0.001	4.5	1.55 ± 0.01	1.0	2.80 ± 0.04
14	900	4.260 ± 0.001	0.951 ± 0.001	5.0	1.50 ± 0.01	1.0	4.76 ± 0.04
14	1800	4.365 ± 0.001	0.949 ± 0.001	6.0	1.41 ± 0.01	1.0	5.01 ± 0.04
14	3600	4.195 ± 0.001	0.938 ± 0.001	6.0	1.37 ± 0.01	1.0	6.46 ± 0.05
16	60	4.082 ± 0.001	0.948 ± 0.001	2.70 ± 0.01	1.69 ± 0.01	1.0	0.94 ± 0.04
18	60	4.053 ± 0.001	0.978 ± 0.001	4.85 ± 0.04	1.72 ± 0.01	1.0	0.13 ± 0.02
20	60	4.6 ± 0.2	0.993 ± 0.001	5.7 ± 0.1	1.37 ± 0.01	1.0	0.02 ± 0.02
22	60	3.83 ± 0.09	0.996 ± 0.001	4.0 ± 0.1	1.62 ± 0.01	1.0	0.01

Table 4.18: Best-fit parameters of the EDM model Eq.(4.24) to $\text{Cr}_{0.79}\text{Fe}_{0.21}$.

T (K)	t_w (sec)	M_{base} ($\times 10^{-1}\text{emu/g}$)	M_0 ($\times 10^{-1}\text{emu/g}$)	b_2 ($\times 10^{-2}$)	t_{in2} (sec)
26	60	0.002	3.802 ± 0.075	1.791 ± 0.001	0.01
30	60	1.155	1.790 ± 0.098	4.146 ± 0.001	0.01

Table 4.19: Best-fit parameters of $\text{Fe}_{0.65}\text{Ni}_{0.24}\text{Cr}_{0.11}$ to the EDM model Eq.(4.23).

T (K)	t_w (sec)	M_0 (emu/g)	c	b_1 ($\times 10^{-1}$)	b_2 ($\times 10^{-2}$)	t_{in1} (sec)	t_{in2} (sec)
8	60	3.451 ± 0.001	0.60 ± 1.32	0.01 ± 0.04	0.06 ± 0.13	90 ± 35	0.5 ± 0.7
10	60	3.354 ± 0.002	0.57 ± 0.67	0.03 ± 0.05	0.11 ± 0.13	87 ± 9	0.3 ± 0.4
12	60	3.380 ± 0.002	0.60 ± 1.73	0.07 ± 0.03	0.20 ± 0.58	99 ± 31	1.1 ± 0.2
14	60	3.367 ± 0.001	0.65 ± 0.15	0.14 ± 0.06	0.30 ± 0.01	45 ± 5	0.7 ± 0.1
15	60	3.329 ± 0.001	0.68 ± 0.08	0.17 ± 0.04	0.42 ± 0.01	35 ± 4	1.2 ± 0.1
16	60	3.351 ± 0.001	0.73 ± 0.04	0.24 ± 0.04	0.49 ± 0.01	29 ± 3	1.0 ± 0.1
17	60	3.334 ± 0.001	0.901 ± 0.006	0.68 ± 0.04	0.58 ± 0.01	19 ± 3	1.1 ± 0.1
17	900	3.306 ± 0.001	0.973 ± 0.001	3.7	0.73 ± 0.01	1.0	5.3 ± 0.1
17	1800	3.289 ± 0.001	0.974 ± 0.001	4.7	0.75 ± 0.01	1.0	6.9 ± 0.1
17	3600	3.317 ± 0.001	0.970 ± 0.001	5.0	0.72 ± 0.01	1.0	8.4 ± 0.1
17	7200	3.316 ± 0.001	0.969 ± 0.001	8.0	0.67 ± 0.01	1.0	7.8 ± 0.1
18	60	3.300 ± 0.001	0.945 ± 0.001	1.17 ± 0.06	0.80 ± 0.01	0.2 ± 3	1.1 ± 0.1
19	60	3.307 ± 0.001	0.977 ± 0.001	2.08 ± 0.02	1.02 ± 0.01	1.0	0.37 ± 0.02
19	300	3.285 ± 0.001	0.990 ± 0.001	4.41 ± 0.06	1.14 ± 0.01	1.0	1.94 ± 0.02
19	900	3.297 ± 0.001	0.990 ± 0.001	8.0	1.13 ± 0.01	1.0	2.53 ± 0.02
19	1800	3.297 ± 0.001	0.990 ± 0.001	11.0	1.11 ± 0.01	1.0	2.82 ± 0.02
19	3600	3.270 ± 0.001	0.989 ± 0.001	18.0	1.09 ± 0.01	1.0	3.20 ± 0.02
19	7200	3.195 ± 0.001	0.988 ± 0.001	26.0	1.07 ± 0.01	1.0	3.59 ± 0.02
20	60	3.228 ± 0.001	0.986 ± 0.001	3.43 ± 0.03	1.17 ± 0.01	1.0	0.45 ± 0.02
21	60	3.196 ± 0.001	0.994 ± 0.001	7.10 ± 0.05	1.26 ± 0.01	1.0	0.01
21	600	3.197 ± 0.001	0.997 ± 0.001	33.2 ± 0.5	1.31 ± 0.01	1.0	0.20 ± 0.01
21	1800	3.198 ± 0.001	0.997 ± 0.001	65.0	1.31 ± 0.01	1.0	0.44 ± 0.01
21	7200	3.195 ± 0.001	0.998 ± 0.001	83.0	1.31 ± 0.01	1.0	0.74 ± 0.01
22	60	3.099 ± 0.001	0.996 ± 0.001	17.9 ± 0.2	1.26 ± 0.01	1.0	0.01

Table 4.20: Best-fit parameters of $\text{Fe}_{0.65}\text{Ni}_{0.24}\text{Cr}_{0.11}$ to the EDM model Eq.(4.24).

T (K)	t_w (sec)	M_{base} (emu/g)	M_0 (emu/g)	b_2 ($\times 10^{-2}$)	t_{in2} (sec)
24	60	2.109	0.880 ± 0.001	4.689 ± 0.001	0.01
25	60	2.109	0.776 ± 0.001	4.826 ± 0.001	0.01
26	60	1.922	0.929 ± 0.001	3.371 ± 0.001	0.01
28	60	1.688	1.123 ± 0.001	2.385 ± 0.001	0.01
30	60	0.469	2.293 ± 0.001	1.069 ± 0.001	0.01
33	60	0.281	2.481 ± 0.001	1.100 ± 0.001	0.01
35	60	0.937	1.805 ± 0.001	1.628 ± 0.001	0.01
40	60	1.406	1.232 ± 0.001	2.400 ± 0.001	0.01
45	60	1.688	0.905 ± 0.001	2.961 ± 0.001	0.01
50	60	1.594	0.953 ± 0.001	2.387 ± 0.001	0.01
60	60	1.406	1.003 ± 0.001	1.855 ± 0.001	0.01
70	60	1.406	0.804 ± 0.001	2.327 ± 0.001	0.01

Table 4.21: Best-fit parameters of $\text{Fe}_{0.65}\text{Ni}_{0.23}\text{Cr}_{0.12}$ to the EDM model Eq.(4.23).

T (K)	t_w (sec)	M_0 ($\times 10^{-1}\text{emu/g}$)	c	b_1 ($\times 10^{-1}$)	b_2 ($\times 10^{-2}$)	t_{in1} (sec)	t_{in2} (sec)
16	300	4.038 ± 0.001	0.863 ± 0.001	1.65 ± 0.03	0.87 ± 0.01	1.0	3.6 ± 0.1
18	300	4.099 ± 0.001	0.894 ± 0.001	3.44 ± 0.02	1.14 ± 0.01	1.0	1.8 ± 0.1
20	300	4.260 ± 0.001	0.883 ± 0.001	3.21 ± 0.02	2.10 ± 0.01	1.0	3.5 ± 0.1
20	900	4.284 ± 0.001	0.900 ± 0.001	5.0	2.02 ± 0.01	1.0	5.4 ± 0.1
20	1800	4.203 ± 0.001	0.907 ± 0.001	7.0	1.99 ± 0.01	1.0	6.3 ± 0.1
20	3600	4.155 ± 0.001	0.903 ± 0.001	8.0	1.94 ± 0.01	1.0	8.5 ± 0.1
20	7200	4.075 ± 0.001	0.910 ± 0.001	12.0	1.74 ± 0.01	1.0	8.5 ± 0.1
21	300	4.309 ± 0.001	0.908 ± 0.001	4.47 ± 0.02	2.57 ± 0.01	1.0	2.8 ± 0.1
21	900	4.162 ± 0.001	0.926 ± 0.001	8.93 ± 0.03	2.44 ± 0.01	1.0	3.6 ± 0.1
21	1800	4.221 ± 0.001	0.924 ± 0.001	10.0	2.49 ± 0.01	1.0	6.4 ± 0.1
21	3600	4.181 ± 0.001	0.921 ± 0.001	11.0	2.44 ± 0.01	1.0	7.0 ± 0.1
21	7200	4.168 ± 0.001	0.907 ± 0.001	12.0	2.39 ± 0.01	1.0	8.5 ± 0.1
22	300	4.300 ± 0.001	0.916 ± 0.001	3.87 ± 0.02	3.50 ± 0.01	1.0	3.0 ± 0.1
22	900	4.412 ± 0.001	0.931 ± 0.001	8.42 ± 0.04	3.11 ± 0.01	1.0	4.0 ± 0.1
22	1800	4.328 ± 0.001	0.933 ± 0.001	12.0	3.08 ± 0.01	1.0	4.8 ± 0.1
22	3600	4.334 ± 0.001	0.931 ± 0.001	13.0	3.07 ± 0.01	1.0	6.0 ± 0.1
22	7200	4.263 ± 0.001	0.926 ± 0.001	15.0	3.01 ± 0.01	1.0	7.4 ± 0.1
23	300	4.163 ± 0.001	0.939 ± 0.001	6.30 ± 0.03	4.42 ± 0.01	1.0	1.8 ± 0.1
24	300	4.447 ± 0.001	0.970 ± 0.001	9.24 ± 0.04	4.77 ± 0.01	1.0	1.4 ± 0.1
24	900	4.496 ± 0.001	0.972 ± 0.001	18.1 ± 0.1	4.63 ± 0.01	1.0	1.6 ± 0.1
24	1800	4.544 ± 0.001	0.972 ± 0.001	25.8 ± 0.1	4.41 ± 0.01	1.0	2.0 ± 0.1
24	3600	4.313 ± 0.001	0.969 ± 0.001	42.0 ± 0.2	4.50 ± 0.01	1.0	2.2 ± 0.1
24	7200	4.394 ± 0.001	0.963 ± 0.001	54.6 ± 0.2	4.30 ± 0.01	1.0	2.3 ± 0.1
25	300	4.846 ± 0.001	0.981 ± 0.001	8.72 ± 0.06	5.21 ± 0.01	1.0	0.1 ± 0.1

Table 4.22: Fit parameters of the EDM model Eq.(4.24) to $\text{Fe}_{0.65}\text{Ni}_{0.23}\text{Cr}_{0.12}$.

T (K)	t_w (sec)	M_{base} ($\times 10^{-1}\text{emu/g}$)	M_0 ($\times 10^{-1}\text{emu/g}$)	b_2 ($\times 10^{-2}$)	t_{in2} (sec)
26	300	0.918	9.983 ± 0.001	7.752 ± 0.001	0.01
28	300	1.837	2.918 ± 0.001	11.240 ± 0.001	0.01

Table 4.23: Best-fit parameters of the EDM model Eq.(4.23) to $(\text{Fe}_{0.65}\text{Ni}_{0.35})_{0.882}\text{Mn}_{0.118}$.

T (K)	t_w (sec)	M_0 ($\times 10^{-1}\text{emu/g}$)	c	b_1 ($\times 10^{-1}$)	b_2 ($\times 10^{-2}$)	t_{in1} (sec)	t_{in2} (sec)
40	60	1.323 ± 0.001	0.69 ± 0.19	0.36 ± 0.23	0.73 ± 0.17	104 ± 28	1.6 ± 0.5
45	60	1.324 ± 0.001	0.72 ± 0.07	0.56 ± 0.15	1.13 ± 0.08	63 ± 15	1.0 ± 0.3
50	60	1.328 ± 0.001	0.78 ± 0.03	0.77 ± 0.12	1.85 ± 0.04	33 ± 10	1.0 ± 0.2
52	60	1.317 ± 0.001	0.82 ± 0.02	1.12 ± 0.11	1.99 ± 0.04	7.1 ± 0.7	0.3 ± 0.2
55	60	1.278 ± 0.001	0.927 ± 0.008	2.43 ± 0.24	2.80 ± 0.05	17 ± 10	0.6 ± 0.1
57	60	1.283 ± 0.001	0.967 ± 0.004	4.59 ± 0.66	3.19 ± 0.04	47 ± 20	0.44 ± 0.09
57	300	1.293 ± 0.001	0.967 ± 0.006	6.37 ± 0.09	3.08 ± 0.01	1.0	0.62 ± 0.03
57	900	1.289 ± 0.001	0.971 ± 0.001	9.70 ± 0.18	3.10 ± 0.01	1.0	1.01 ± 0.03
57	3600	1.281 ± 0.001	0.972 ± 0.001	15.0	3.05 ± 0.01	1.0	1.58 ± 0.03
57	10800	1.255 ± 0.001	0.966 ± 0.001	18.0	3.04 ± 0.01	1.0	1.97 ± 0.03
60	60	1.264 ± 0.001	0.989 ± 0.001	17.96 ± 0.85	3.50 ± 0.01	1.0	0.87 ± 0.04

Table 4.24: Best-fit parameters of the EDM model Eq.(4.24) to $(\text{Fe}_{0.65}\text{Ni}_{0.35})_{0.882}\text{Mn}_{0.118}$.

T (K)	t_w (sec)	M_{base} ($\times 10^{-1}\text{emu/g}$)	M_0 ($\times 10^{-1}\text{emu/g}$)	b_2 ($\times 10^{-2}$)	t_{in2} (sec)
65	60	0.517	0.696 ± 0.001	6.645 ± 0.001	0.01
70	60	0.776	0.421 ± 0.001	10.240 ± 0.001	0.01
80	60	0.853	0.361 ± 0.001	8.027 ± 0.001	0.01
90	60	0.905	0.391 ± 0.001	5.552 ± 0.001	0.01
100	60	0.957	0.327 ± 0.001	5.091 ± 0.001	0.01
110	60	0.957	0.241 ± 0.001	7.800 ± 0.001	0.01

Table 4.25: Best-fit parameters of the EDM model Eq.(4.23) to $(\text{Fe}_{0.65}\text{Ni}_{0.35})_{0.882}\text{Mn}_{0.118}$.

T (K)	t_w (sec)	M_0 ($\times 10^{-1}\text{emu/g}$)	c	b_1 ($\times 10^{-1}$)	b_2 ($\times 10^{-2}$)	t_{in1} (sec)	t_{in2} (sec)
48	60	1.416 ± 0.001	0.63 ± 0.05	0.59 ± 0.08	1.97 ± 0.12	30 ± 7	1.3 ± 0.3
48	180	1.405 ± 0.001	0.809 ± 0.003	1.29 ± 0.04	1.69 ± 0.02	1.0	1.6 ± 0.2
48	300	1.407 ± 0.001	0.849 ± 0.002	1.77 ± 0.05	1.71 ± 0.05	1.0	3.8 ± 0.2
52	60	1.412 ± 0.001	0.83 ± 0.01	1.40 ± 0.11	2.69 ± 0.03	29 ± 7	1.6 ± 0.2
52	120	1.394 ± 0.001	0.853 ± 0.001	1.72 ± 0.03	2.70 ± 0.02	1.0	2.0 ± 0.1
52	180	1.404 ± 0.001	0.875 ± 0.001	2.18 ± 0.04	2.65 ± 0.02	1.0	2.3 ± 0.1
52	300	1.401 ± 0.001	0.900 ± 0.001	3.22 ± 0.04	2.63 ± 0.01	1.0	2.7 ± 0.1
52	900	1.396 ± 0.001	0.918 ± 0.001	6.02 ± 0.07	2.54 ± 0.01	1.0	4.0 ± 0.1
56	60	1.419 ± 0.001	0.900 ± 0.001	2.61 ± 0.04	3.51 ± 0.02	1.0	0.5 ± 0.1
56	120	1.396 ± 0.001	0.933 ± 0.001	3.39 ± 0.04	3.75 ± 0.02	1.0	1.1 ± 0.1
56	180	1.427 ± 0.001	0.942 ± 0.001	4.16 ± 0.04	3.70 ± 0.01	1.0	1.4 ± 0.1
56	240	1.386 ± 0.001	0.947 ± 0.001	5.16 ± 0.05	3.82 ± 0.01	1.0	1.6 ± 0.1
56	300	1.387 ± 0.001	0.949 ± 0.001	5.41 ± 0.06	3.86 ± 0.01	1.0	1.9 ± 0.1
56	600	1.398 ± 0.001	0.946 ± 0.001	8.12 ± 0.07	3.61 ± 0.01	1.0	1.2 ± 0.1

4.6 Relaxation Dynamics: A Percolation Analysis

The percolation model of Chamberlin and Haines, which is also a theory of activated dynamics, but for dispersive excitations within a *fixed* distribution of *finite* domains, is based on such general geometrical considerations that it is difficult to appreciate the physical origins of either the aging or temperature-cycling effects within this theoretical framework. Nevertheless, the two model relaxation functions Eq.(2.141) and (2.142) do provide a reasonable description of the relaxation isotherms, since each is reducible to one of the empirical expressions Eq.(4.1) or (4.2) in an appropriate limit (Chamberlin and Hains, 1990): for $C\omega_+t < 1$, $M_+(t)$ (Eq.(2.141)) \rightarrow a stretched exponential, while for $C\omega_-t \gg 1$, $M_-(t)$ (Eq.(2.142)) \rightarrow a simple power law. Figures 4.20-4.22 illustrate these fits for the $\text{Fe}_{0.65}\text{Ni}_{0.23}\text{Cr}_{0.12}$ sample. A six-parameter fit to a superposition of the aligned and antialigned relaxation functions yields unreliaibly high parameter un-

certainties, and thus reinforces the need to consider the contribution from only one type of domain, at least over the temporal range of this experiment. Ultimately the following representations were favoured for our analysis:

(a) In the high-temperature ferromagnetic phase, the best description was achieved by superposing the aligned function on a constant baseline, $M_- + M_0$, as shown by the solid curves for the $T_m = 26$ K and 28 K isotherms in Fig. 4.20. The quality of the fits are indistinguishable from the empirical power-law fits in section 4.3. The best-fit parameters for the high-temperature isotherms of $\text{Fe}_{0.65}\text{Ni}_{0.23}\text{Cr}_{0.12}$ are listed in Table 4.27. The characteristic relaxation times of the average-size aligned domains, $\bar{\tau}_- \equiv [\omega_\infty^- \exp(-C/\bar{x})]^{-1}$, where $\bar{x} = (19/6)^{3/2}$, were calculated and are also listed in Table 4.27.

(b) In the low-temperature reentrant phase, the most consistent results are obtained by a simple superposition of the antialigned function and a constant baseline, $M_+(t) + M_0$. However, the quality of the fits was clearly dependent on the age of the system: for relatively short wait times ($t_w \leq 900$ s), the fits were measurably inferior to the stretched exponential ($\ln \chi_+^2/\chi_e^2 \sim 1.1$), but improved systematically with increasing age until, for ($t_w \geq 900$ s), the two representations became essentially interchangeable. The solid curves through the isotherms $16\text{K} \leq T_m \leq 25\text{K}$ and for $t_w = 5\text{m}, 15\text{m}, 30\text{m}, 1\text{h},$ and 2h in Figures 4.20-4.22 show the best fits, and the vertical arrows mark the inflection points, which are systematically longer than the characteristic relaxation times of the average-size antialigned domains $\bar{\tau}_+ \equiv [\omega_\infty^+ \exp(+C/\bar{x})]^{-1}$. The corresponding fitting parameters and $\bar{\tau}_+$ are listed in Table 4.26 and they satisfy the condition $C\omega_\infty^+ t \leq 1$ for $M_+(t)$ to reduce to a stretched exponential.

Tables 4.26 and 4.27 provide a complete list of the best-fit parameters for all the reentrant isotherms. The correlation coefficient C increases with temperature, so that, with the physically reasonable assumption of a temperature-

independent average interaction between the spins Δ , the percolation correlation length $\xi \propto (\Delta/CT)^{\sigma\nu}$, where $\sigma = 0.45$ and $\nu = 0.88$ are percolation scaling exponents, decreases with increasing temperature throughout the reentrant phase, which is consistent with its behavior in pure spin glasses (Chamberlin and Haines, 1990). Thus, a Chamberlin-Haines analysis of the dynamic crossover suggests that the dynamics in the ferromagnetic phase are dominated by domains which are *aligned* with the field, presumably because the reorientation of antialigned domains on field cooling is relatively unhindered in this phase. In the reentrant phase, such aligned reorientation is inhibited, and the decay is due predominantly to slowly relaxing, higher-energy *antialigned* domains. However, the wait-time dependence of the fits in the reentrant phase may reflect the inadequacy of a single, fixed domain size distribution, due to possible domain growth in the early stages of aging, and the microscopic origins of the aging process have yet to be resolved within this formalism.

Tables 4.28–4.34 list the best-fit parameters for the remaining systems and the fits are shown in Figures D.1–D.10, Appendix D.

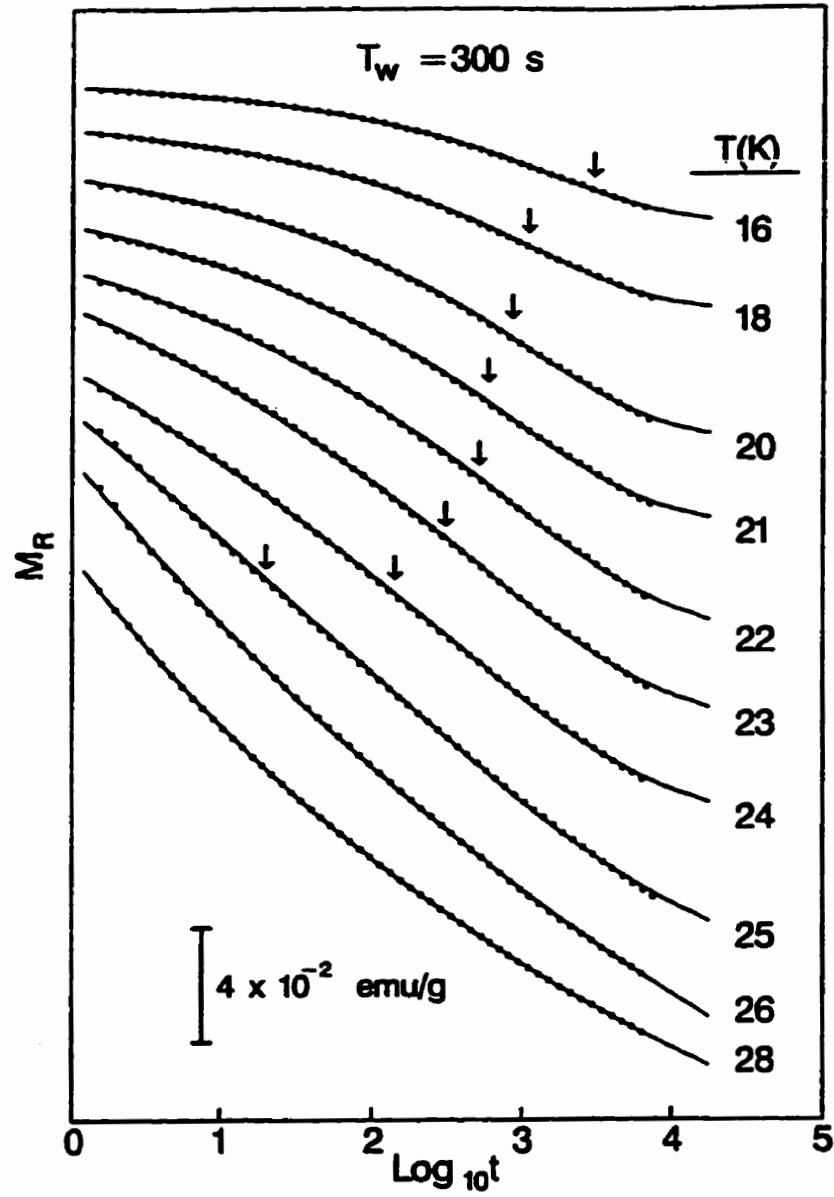


Figure 4.20: Thermoremanent relaxation isotherms of $\text{Fe}_{0.65}\text{Ni}_{0.23}\text{Cr}_{0.12}$ for a sequence of temperatures and for a common wait time $t_w = 300$ s to the percolation model. The solid curves for $T_m \leq 25$ K are fits to Eq.(2.141) and vertical arrows mark the characteristic inflection points τ . The solid curves for $T_m \geq 26$ K are fits to Eq.(2.142).

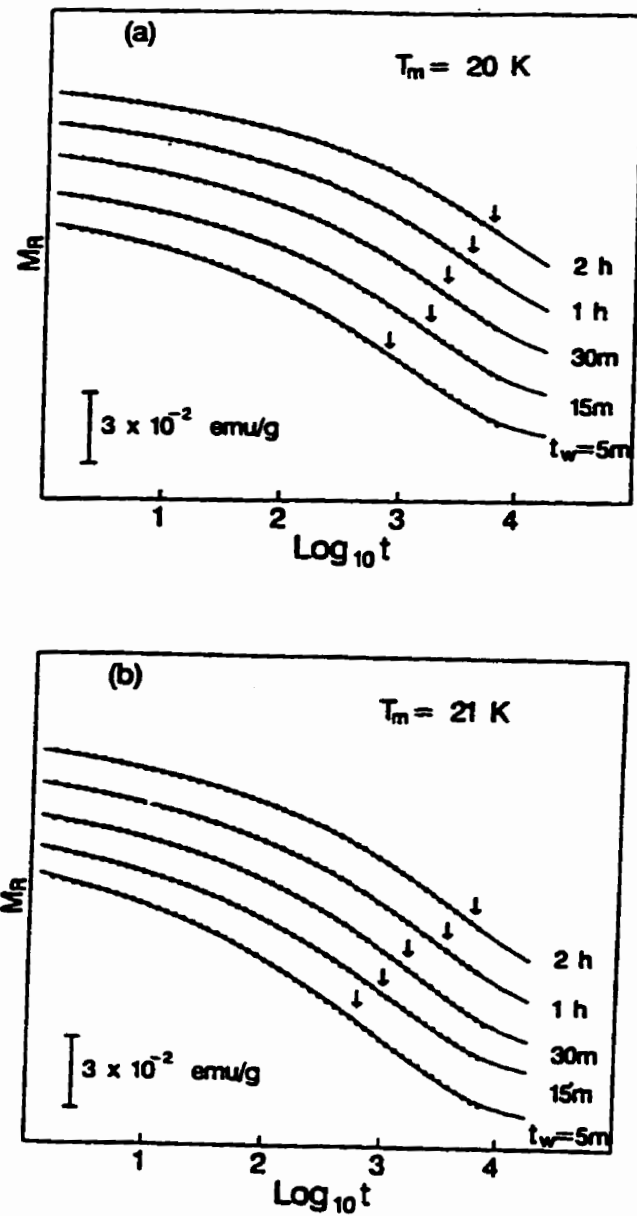


Figure 4.21: (a) Wait-time dependence of the thermoremanent relaxation of $\text{Fe}_{0.65}\text{Ni}_{0.23}\text{Cr}_{0.12}$ at $T_m = 20$ K. The solid curves are fits to the percolation model and vertical arrows mark the characteristic inflection points τ . (b) Same sample and analysis as in (a) but for $T_m = 21$ K.

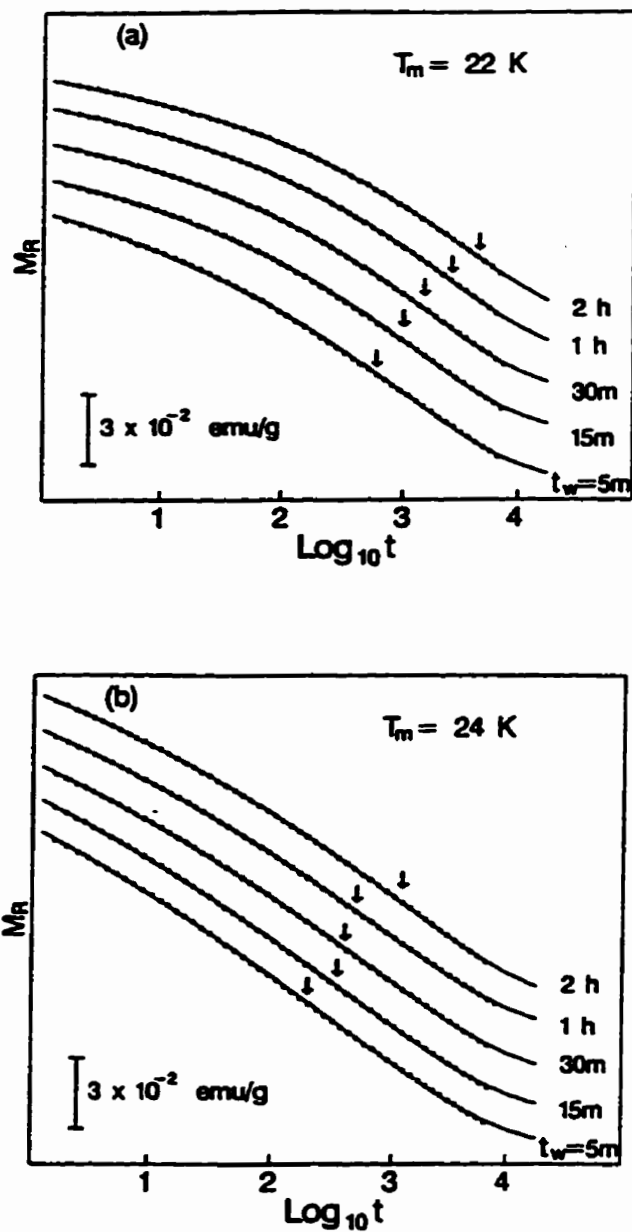


Figure 4.22: (a) Wait-time dependence of the thermoremanent relaxation of $\text{Fe}_{0.65}\text{Ni}_{0.23}\text{Cr}_{0.12}$ at $T_m = 22 \text{ K}$. The solid curves are fits to the percolation model and vertical arrows mark the characteristic inflection points τ . (b) Same sample and analysis as in (a) but for $T_m = 24 \text{ K}$.

Table 4.26: Best-fit parameters of $\text{Fe}_{0.65}\text{Ni}_{0.23}\text{Cr}_{0.12}$ to the percolation model Eq.(2.141).

T (K)	t_w (sec)	M_0 ($\times 10^{-3}\text{emu/g}$)	M_i ($\times 10^{-3}\text{emu/g}$)	ω_+ ($\times 10^{-5}\text{Hz}$)	C	τ_+ (sec)
16	300	354.8 ± 0.1	16.26 ± 0.03	4.93 ± 0.06	15.5 ± 0.1	1290 ± 28
18	300	344.0 ± 0.1	22.45 ± 0.03	5.19 ± 0.04	17.9 ± 0.1	797 ± 13
20	300	332.0 ± 0.1	34.05 ± 0.04	3.80 ± 0.03	21.3 ± 0.1	596 ± 8
20	900	338.3 ± 0.1	31.28 ± 0.04	3.25 ± 0.02	18.8 ± 0.1	1090 ± 15
20	1800	330.7 ± 0.1	30.85 ± 0.05	2.34 ± 0.02	18.7 ± 0.1	1540 ± 26
20	3600	326.1 ± 0.2	30.33 ± 0.08	1.46 ± 0.02	18.5 ± 0.1	2600 ± 54
20	7200	316.0 ± 0.4	30.89 ± 0.14	0.68 ± 0.02	19.4 ± 0.1	4700 ± 140
21	300	323.2 ± 0.1	41.42 ± 0.04	3.18 ± 0.02	25.7 ± 0.1	331 ± 5
21	900	316.4 ± 0.1	36.92 ± 0.04	3.02 ± 0.02	23.3 ± 0.1	526 ± 8
21	1800	322.1 ± 0.1	35.81 ± 0.04	2.57 ± 0.02	20.9 ± 0.1	949 ± 14
21	3600	317.8 ± 0.1	35.86 ± 0.06	1.48 ± 0.02	22.0 ± 0.1	1370 ± 26
21	7200	316.3 ± 0.2	35.30 ± 0.08	1.04 ± 0.01	21.4 ± 0.1	2160 ± 47
22	300	299.5 ± 0.1	55.29 ± 0.06	1.50 ± 0.01	33.4 ± 0.1	177 ± 3
22	900	319.0 ± 0.1	48.00 ± 0.05	2.01 ± 0.01	27.7 ± 0.1	364 ± 6
22	1800	312.4 ± 0.1	46.17 ± 0.05	1.74 ± 0.01	26.4 ± 0.1	527 ± 8
22	3600	313.1 ± 0.1	45.88 ± 0.07	1.15 ± 0.01	26.8 ± 0.1	748 ± 14
22	7200	308.8 ± 0.2	44.46 ± 0.09	0.80 ± 0.01	26.9 ± 0.1	1060 ± 24
23	300	264.4 ± 0.1	73.55 ± 0.09	0.94 ± 0.01	44.1 ± 0.1	42.5 ± 0.9
24	300	278.2 ± 0.1	94.68 ± 0.14	0.49 ± 0.01	57.3 ± 0.1	8 ± 1
24	900	284.5 ± 0.1	90.47 ± 0.08	0.51 ± 0.01	54.7 ± 0.1	12.1 ± 0.3
24	1800	292.9 ± 0.1	85.04 ± 0.12	0.46 ± 0.01	52.2 ± 0.1	20.8 ± 0.6
24	3600	274.8 ± 0.1	80.01 ± 0.11	0.47 ± 0.01	49.9 ± 0.1	29.8 ± 0.8
24	7200	279.1 ± 0.1	77.91 ± 0.11	0.38 ± 0.01	47.6 ± 0.1	56 ± 2
25	300	268.6 ± 0.1	178.6 ± 0.5	0.031 ± 0.001	103.1 ± 0.3	0.04 ± 0.01

Table 4.27: Best-fit parameters of $\text{Fe}_{0.65}\text{Ni}_{0.23}\text{Cr}_{0.12}$ to the percolation model Eq.(2.142).

T (K)	t_w (sec)	M_0 ($\times 10^{-3}\text{emu/g}$)	M_i ($\times 10^{-3}\text{emu/g}$)	ω_- (Hz)	C	τ_- (sec)
26	300	2.5 ± 1.2	177.5 ± 1.1	$(5.89 \pm 0.05) \times 10^3$	77.5 ± 0.2	161 ± 21
28	300	101.1 ± 0.7	175.3 ± 2.6	$(7.43 \pm 0.99) \times 10^3$	53.5 ± 0.1	1.81 ± 0.28

Table 4.28: Best-fit parameters of $\text{Fe}_{0.65}\text{Ni}_{0.24}\text{Cr}_{0.11}$ to the percolation model Eq.(2.141).

T (K)	t_w (sec)	M_0 ($\times 10^{-2}$ emu/g)	M_i ($\times 10^{-2}$ emu/g)	ω_+ ($\times 10^{-5}$ Hz)	C	$\bar{\tau}_+$ (sec)
8	60	343.1 \pm 0.1	0.73 \pm 0.04	0.81 \pm 0.28	29.4 \pm 1.4	658 \pm 386
10	60	331.0 \pm 0.1	1.52 \pm 0.02	1.70 \pm 0.11	22.1 \pm 0.3	1164 \pm 132
12	60	329.7 \pm 0.1	2.85 \pm 0.01	2.18 \pm 0.06	19.8 \pm 0.1	1368 \pm 74
14	60	322.8 \pm 0.1	4.78 \pm 0.01	2.81 \pm 0.04	20.2 \pm 0.1	990 \pm 30
15	60	315.5 \pm 0.1	6.23 \pm 0.01	2.40 \pm 0.03	22.4 \pm 0.1	787 \pm 20
16	60	313.5 \pm 0.1	7.84 \pm 0.01	2.12 \pm 0.02	24.1 \pm 0.1	662 \pm 14
17	60	307.4 \pm 0.1	10.31 \pm 0.02	1.47 \pm 0.02	30.2 \pm 0.1	318 \pm 8
17	900	306.3 \pm 0.1	9.04 \pm 0.02	1.92 \pm 0.02	24.2 \pm 0.1	704 \pm 16
17	1800	304.4 \pm 0.1	8.94 \pm 0.02	1.54 \pm 0.02	23.7 \pm 0.1	962 \pm 22
17	3600	307.3 \pm 0.1	8.88 \pm 0.02	1.05 \pm 0.02	23.6 \pm 0.1	1460 \pm 39
17	7200	304.8 \pm 0.1	9.65 \pm 0.04	0.45 \pm 0.01	24.9 \pm 0.1	2653 \pm 96
18	60	298.4 \pm 0.1	14.41 \pm 0.02	0.661 \pm 0.01	41.4 \pm 0.1	98 \pm 2
19	60	292.4 \pm 0.1	21.25 \pm 0.05	0.172 \pm 0.01	61.9 \pm 0.2	10 \pm 1
19	300	292.2 \pm 0.1	18.47 \pm 0.04	0.298 \pm 0.01	51.3 \pm 0.1	37 \pm 1
19	900	294.8 \pm 0.1	16.48 \pm 0.03	0.502 \pm 0.01	44.2 \pm 0.1	79 \pm 3
19	1800	295.0 \pm 0.1	15.91 \pm 0.03	0.469 \pm 0.01	42.4 \pm 0.1	116 \pm 4
19	3600	293.1 \pm 0.1	15.13 \pm 0.03	0.504 \pm 0.01	40.0 \pm 0.1	164 \pm 5
19	7200	293.0 \pm 0.1	15.02 \pm 0.03	0.385 \pm 0.01	39.6 \pm 0.1	230 \pm 8
20	60	281.5 \pm 0.1	25.79 \pm 0.07	0.078 \pm 0.01	74.0 \pm 0.2	2.5 \pm 0.1
21	60	273.9 \pm 0.1	39.13 \pm 0.02	(5.0 \pm 0.3) \times 0.01	116.6 \pm 0.6	(2.0 \pm 0.3) \times 0.01
21	600	273.7 \pm 0.1	39.9 \pm 0.2	(6.3 \pm 0.3) \times 0.001	109.4 \pm 0.6	(5.8 \pm 0.9) \times 0.01
21	1800	273.7 \pm 0.1	34.6 \pm 0.2	(6.8 \pm 0.4) \times 0.001	102.8 \pm 0.5	0.18 \pm 0.03
21	7200	273.7 \pm 0.1	32.3 \pm 0.2	(7.1 \pm 0.4) \times 0.001	96.8 \pm 0.5	0.40 \pm 0.05
22	60	266.5 \pm 0.1	43.1 \pm 0.3	(2.9 \pm 0.2) \times 0.001	133.4 \pm 0.9	(1.8 \pm 0.4) \times 0.001

Table 4.29: Best-fit parameters of $\text{Fe}_{0.65}\text{Ni}_{0.24}\text{Cr}_{0.11}$ to the percolation model Eq.(2.142).

T (K)	t_w (sec)	M_0 ($\times 10^{-2}\text{emu/g}$)	M_i ($\times 10^{-2}\text{emu/g}$)	ω_- (Hz)	C	$\bar{\tau}_-$ (sec)
24	60	216.8 ± 0.4	26.4 ± 0.2	$(1.51 \pm 0.15) \times 10^3$	89.0 ± 0.6	$(4.78 \pm 0.98) \times 10^3$
25	60	211.9 ± 0.5	25.1 ± 0.3	$(3.60 \pm 0.59) \times 10^3$	93.2 ± 0.9	$(4.26 \pm 1.34) \times 10^3$
26	60	207.4 ± 0.8	25.3 ± 0.3	$(1.08 \pm 0.24) \times 10^4$	109.0 ± 1.4	$(2.32 \pm 1.07) \times 10^4$
28	60	183.1 ± 2.2	33.5 ± 1.0	$(8.20 \pm 6.07) \times 10^6$	164.5 ± 4.4	$(5.85 \pm 8.93) \times 10^5$
30	60	153.0 ± 1.4	40.4 ± 0.5	$(9.48 \pm 3.00) \times 10^7$	213.2 ± 2.7	$(2.83 \pm 2.27) \times 10^7$
33	60	135.5 ± 1.5	44.7 ± 0.5	$(2.19 \pm 0.55) \times 10^7$	214.2 ± 2.5	$(1.47 \pm 1.02) \times 10^8$
35	60	160.3 ± 1.2	39.0 ± 0.5	$(1.28 \pm 0.42) \times 10^7$	168.5 ± 2.1	$(7.87 \pm 5.58) \times 10^5$
40	60	159.3 ± 1.1	36.5 ± 0.5	$(9.52 \pm 3.43) \times 10^6$	159.0 ± 2.0	$(1.89 \pm 1.36) \times 10^5$
45	60	167.3 ± 1.6	33.3 ± 0.9	$(3.88 \pm 2.87) \times 10^7$	158.9 ± 3.4	$(4.57 \pm 6.07) \times 10^4$
50	60	148.1 ± 1.6	34.1 ± 0.6	$(3.65 \pm 1.45) \times 10^7$	213.5 ± 3.7	$(7.81 \pm 8.30) \times 10^8$
60	60	143.3 ± 4.0	30.6 ± 1.4	$(3.20 \pm 3.10) \times 10^7$	226.7 ± 10.2	$(9.17 \pm 25.5) \times 10^9$
70	60	155.1 ± 1.0	23.4 ± 0.5	$(1.74 \pm 1.00) \times 10^7$	214.2 ± 3.0	$(9.01 \pm 9.90) \times 10^4$

Table 4.30: Best-fit parameters of $\text{Cr}_{0.79}\text{Fe}_{0.21}$ to the percolation model Eq.(2.141).

T (K)	t_w (sec)	M_0 ($\times 10^{-3}\text{emu/g}$)	M_i ($\times 10^{-3}\text{emu/g}$)	ω_+ ($\times 10^{-5}\text{Hz}$)	C	$\bar{\tau}_+$ (sec)
10	60	407.33 ± 0.05	12.46 ± 0.03	2.63 ± 0.04	23.21 ± 0.10	620 ± 20
12	60	388.81 ± 0.04	19.53 ± 0.03	3.16 ± 0.03	24.63 ± 0.06	400 ± 80
14	60	353.21 ± 0.04	28.45 ± 0.04	1.91 ± 0.02	34.05 ± 0.08	124.7 ± 0.1
14	300	349.15 ± 0.04	25.83 ± 0.03	2.27 ± 0.02	28.75 ± 0.06	268 ± 5
14	900	362.78 ± 0.06	24.05 ± 0.04	1.74 ± 0.02	25.33 ± 0.06	641 ± 14
14	1800	370.66 ± 0.10	24.61 ± 0.05	1.03 ± 0.01	25.63 ± 0.06	1030 ± 20
14	3600	351.53 ± 0.22	24.89 ± 0.08	0.46 ± 0.01	25.64 ± 0.06	2280 ± 70
16	60	335.27 ± 0.06	36.81 ± 0.08	0.78 ± 0.01	46.94 ± 0.14	3.1 ± 1.2
18	60	330.69 ± 0.09	50.47 ± 0.20	$(9.5 \pm 0.3) \times 0.01$	78.52 ± 0.36	$(9.4 \pm 0.9) \times 0.001$
20	60	386.70 ± 0.27	65.57 ± 0.61	$(1.9 \pm 0.2) \times 0.001$	125.7 ± 1.2	$(1.0 \pm 0.3) \times 0.01$
22	60	300.08 ± 1.03	93.95 ± 2.55	$(6.8 \pm 3.0) \times 10^{-6}$	195.1 ± 5.4	$(1.4 \pm 1.9) \times 10^{-5}$

Table 4.31: Best-fit parameters of $\text{Cr}_{0.79}\text{Fe}_{0.21}$ to the percolation model Eq.(2.142).

T (K)	t_w (sec)	M_0 ($\times 10^{-3}\text{emu/g}$)	M_i ($\times 10^{-3}\text{emu/g}$)	ω_- (Hz)	C	$\bar{\tau}_-$ (sec)
26	60	151.2 ± 3.0	73.6 ± 1.2	$(1.22 \pm 0.87) \times 10^{-6}$	141.4 ± 2.3	$(8.2 \pm 5.9) \times 10^5$
30	60	122.7 ± 1.7	59.4 ± 1.0	$(2.57 \pm 1.37) \times 10^{-4}$	105.2 ± 1.3	$(3.8 \pm 2.1) \times 10^3$

Table 4.32: Best-fit parameters of $(\text{Fe}_{0.65}\text{Ni}_{0.35})_{0.882}\text{Mn}_{0.118}$ to the percolation model Eq.(2.141).

T (K)	t_w (sec)	M_0 ($\times 10^{-3}\text{emu/g}$)	M_i ($\times 10^{-3}\text{emu/g}$)	ω_+ ($\times 10^{-5}\text{Hz}$)	C	$\bar{\tau}_+$ (sec)
40	60	119.80 ± 0.08	4.30 ± 0.04	2.1 ± 0.1	20.7 ± 0.3	1210 ± 120
45	60	113.40 ± 0.08	7.00 ± 0.04	1.5 ± 0.1	25.4 ± 0.2	735 ± 75
50	60	104.60 ± 0.10	11.90 ± 0.07	0.54 ± 0.02	37.2 ± 0.3	252 ± 23
52	60	100.60 ± 0.05	13.60 ± 0.06	0.69 ± 0.02	39.7 ± 0.3	126 ± 10
55	60	91.10 ± 0.08	19.90 ± 0.12	0.25 ± 0.01	57.9 ± 0.4	1.1 ± 0.1
57	60	88.60 ± 0.10	26.20 ± 0.22	$(8.0 \pm 0.6) \times 0.01$	78.1 ± 0.8	1.2 ± 0.2
60	60	85.40 ± 0.16	42.90 ± 0.67	$(4.7 \pm 0.6) \times 0.001$	130.9 ± 2.0	$(1.7 \pm 0.8) \times 0.01$

Table 4.33: Best-fit parameters of $(\text{Fe}_{0.65}\text{Ni}_{0.35})_{0.882}\text{Mn}_{0.118}$ to the percolation model Eq.(2.141).

T (K)	t_w (sec)	M_0 ($\times 10^{-3}\text{emu/g}$)	M_i ($\times 10^{-3}\text{emu/g}$)	ω_+ ($\times 10^{-6}\text{Hz}$)	C	$\bar{\tau}_+$ (sec)
48	60	113.5 ± 0.1	10.6 ± 0.1	21.6 ± 0.5	25.7 ± 0.1	484 ± 20
48	180	113.6 ± 0.1	9.8 ± 0.1	26.5 ± 0.5	22.8 ± 0.1	660 ± 24
48	300	114.2 ± 0.1	9.6 ± 0.1	24.9 ± 0.5	21.8 ± 0.1	839 ± 32
52	60	103.7 ± 0.1	16.2 ± 0.1	12.6 ± 0.3	35.4 ± 0.2	148 ± 9
52	120	102.4 ± 0.1	15.6 ± 0.1	14.5 ± 0.3	33.2 ± 0.2	190 ± 11
52	180	103.8 ± 0.1	15.0 ± 0.1	15.3 ± 0.3	31.5 ± 0.1	244 ± 9
52	300	104.0 ± 0.1	14.5 ± 0.1	16.2 ± 0.3	29.9 ± 0.1	306 ± 11
52	900	104.1 ± 0.1	13.6 ± 0.1	13.9 ± 0.3	26.9 ± 0.1	608 ± 24
56	60	93.2 ± 0.1	27.4 ± 0.1	3.09 ± 0.09	59.4 ± 0.3	8.6 ± 0.7
56	120	92.2 ± 0.1	25.4 ± 0.1	3.93 ± 0.11	54.5 ± 0.3	16.0 ± 1.3
56	180	95.3 ± 0.1	24.7 ± 0.1	4.14 ± 0.10	52.4 ± 0.2	22.1 ± 1.3
56	240	92.5 ± 0.1	23.7 ± 0.1	5.28 ± 0.14	50.1 ± 0.2	26.1 ± 1.6
56	300	92.5 ± 0.1	23.7 ± 0.1	4.71 ± 0.12	49.8 ± 0.2	30.8 ± 1.9
56	900	92.5 ± 0.1	22.6 ± 0.1	4.46 ± 0.12	47.5 ± 0.2	49.0 ± 3.1
57	60	88.6 ± 0.2	26.2 ± 0.2	0.80 ± 0.06	78.1 ± 0.8	1.2 ± 0.2
57	300	89.8 ± 0.1	23.3 ± 0.1	0.95 ± 0.06	69.1 ± 0.6	4.9 ± 9.8
57	900	88.8 ± 0.2	23.0 ± 0.2	0.57 ± 0.04	68.8 ± 0.6	8.8 ± 1.5
57	3600	85.5 ± 0.3	23.8 ± 0.2	0.13 ± 0.02	72.8 ± 0.8	18.5 ± 5.5
57	7200	78.8 ± 0.8	25.8 ± 0.4	0.02 ± 0.01	80.2 ± 0.2	33 ± 15

Table 4.34: Best-fit parameters of $(\text{Fe}_{0.65}\text{Ni}_{0.35})_{0.882}\text{Mn}_{0.118}$ to the percolation model Eq.(2.142).

T (K)	t_w (sec)	M_0 ($\times 10^{-3}$ emu/g)	M_i ($\times 10^{-3}$ emu/g)	ω_- (Hz)	C	$\bar{\tau}_-$ (sec)
65	60	49.4 ± 0.7	24.1 ± 0.5	$(7.3 \pm 0.2) \times 10^2$	71.4 ± 1.0	432 ± 88
70	60	61.8 ± 0.8	27.3 ± 4.7	$(5.9 \pm 0.1) \times 10^4$	65.1 ± 1.2	1.75 ± 0.40
80	60	75.6 ± 0.9	24.6 ± 4.3	$(7.6 \pm 1.5) \times 10^5$	69.3 ± 2.7	0.29 ± 0.19
90	60	87.2 ± 1.1	21.2 ± 3.6	$(2.4 \pm 0.6) \times 10^6$	82.6 ± 2.0	0.96 ± 0.58
100	60	89.3 ± 1.4	19.0 ± 3.7	$(5.9 \pm 1.8) \times 10^6$	89.9 ± 1.7	1.43 ± 0.89
110	60	83.1 ± 1.3	17.6 ± 3.1	$(1.9 \pm 0.5) \times 10^7$	96.9 ± 1.8	1.57 ± 0.91

4.7 Relaxation Dynamics: Temperature Fluctuation Effects

The observation of a thermally driven crossover from equilibrium to nonequilibrium relaxation dynamics certainly offers compelling preliminary support for an orientational collapse from parallel to random spin alignment. However it does not constitute conclusive evidence for genuine spin-glass freezing, since aging is also a feature of other types of systems, such as amorphous polymers (Struik, 1978), high- T_c superconductors (Rossel, 1990), and charge-density waves (Biljakovic et al., 1991). However, as mentioned earlier, the spin-glass state exhibits a unique sensitivity to temperature. According to droplet scaling theories of spin glasses, neighbouring states at temperatures T and $T + \Delta T$ share nearly identical equilibrium spin correlations $\langle \mathbf{S}_i \cdot \mathbf{S}_j \rangle_T$ only up to the overlap length $l_{\Delta T}$, beyond which the signs of the correlations at T are uncorrelated with those at $T + \Delta T$. Alternatively, according to Replica Symmetry Breaking models, there is an heirarchical structure of metastable states, and cooling causes a given state to bifurcate into "new" states.

Temperature-shifting and temperature-cycling experiments are more complicated thermal protocols which may provide direct evidence for this type of thermal fragility and which may help to decide which of these two pictures, droplet

versus hierarchical, is more appropriate as a description of frustrated systems. The corresponding experimental procedures have already been shown in Figure 4.4 and Figure 4.5.

Figures 4.23(a) and (b) show the results of a temperature-shifting experiment. The temperature-shifting is performed by (a) overcooling to $T_m - \Delta T$, waiting for t_w , heating to T_m , and removing the field, and (b) undercooling to $T_m + \Delta T$, waiting for t_w , cooling to T_m , and removing the field. The temperature increments ΔT are listed in the figures. The results show that (a) aging at a lower temperature $T_m - \Delta T$ and measuring at T_m always makes the system look younger, meaning that the inflection point shifts towards smaller values until, at a threshold increment $\Delta T_{threshold} = 2K$, the memory of aging at $T_m - \Delta T$ is completely destroyed and the relaxation response is exactly the same as that obtained by a direct quench to T_m followed by an immediate removal of the field. According to droplet theories, the state at T_m is then uncorrelated with that at $T_m - \Delta T_{threshold}$ and $l_{\Delta T_{threshold}} = 0$. (b) aging at a higher temperature $T_m + \Delta T$ and measuring at T_m makes the system look older when $\Delta T < \Delta T^* \cong 0.5 K$ and beyond that makes the system look progressively younger until the memory of aging at $T_m + \Delta T$ is once again completely destroyed when $\Delta T = \Delta T_{threshold} = 2K$. Some of these results can be interpreted as a temperature dependence of the growth rate of the domains, which is schematically illustrated in Figure 4.24. When the sample is aged at a temperature $T_m - \Delta T$, the growth of the domains is slower than at T_m . When the temperature is increased to T_m , after t_w , we move from A to B in the figure and a system that appears to be younger than it would have been at T_m is probed. The overall features of the relaxation rate curve are preserved, but the maximum in $S(t)$ is shifted towards shorter observation times. Similarly, if the system is aged at a higher temperature than T_m , the growth of domains is faster at $T_m + \Delta T$ than at T_m , and a system that appears older is probed after cooling to T_m (C to D in Figure 4.24). Figure 4.24 is only plausible over the temperature

range where a sufficient “overlap” between the equilibrium spin configurations at the two temperatures exists. The fact that the system appears to get younger in Figure 4.23(b) when $\Delta T > \Delta T^* = 0.5$ K can not be explained directly by the mechanism in Figure 4.24 because this theory predicts that the system will continue to appear older with increasing $\Delta T > 0$. However, when $T_m + \Delta T \sim T_g$, then the influence of the ordering temperature might also affect the aging and if ΔT is too large, so that $T_m + \Delta T > T_g$, the ordered state will be destroyed, and the system will behave as if it was quenched directly to T_m .

As evidence of the temperature dependence of the aging rate, we plot the inflection points at different temperatures and for a sequence of wait times in Figure 4.25(a) for $\text{Fe}_{0.65}\text{Ni}_{0.24}\text{Cr}_{0.11}$ and 4.25(b) for $\text{Fe}_{0.65}\text{Ni}_{0.23}\text{Cr}_{0.12}$. We find that in both cases the aging rate is larger at lower temperatures for the same wait time and the aging rate increases faster at lower temperatures. In Figure 4.25(a), the rate for $T_m = 17$ K increases faster than linearly, and linearly for $T_m = 19$ K, and slower than linearly for $T_m = 21$ K; in Figure 4.25(b) as the temperature decreases from 24 K to 20 K, the aging rate get faster and deviates more from linearity.

We can also interpret these temperature shifting effects from the perspective of the the heirarchical RSB theories by analyzing the evolution of the population of the metastable states.

In the first class of experiments where the sample ages at a temperature $T_m - \Delta T$, the complexity of the free-energy landscape is higher (see Figure 4.26), and the aging process is slower, relative to that at T_m . If we suppose that the system jumps over a barrier via a thermally activated process, then after a time t_w , the subregion of configuration space which has been explored is characterized by a highest barrier

$$\Delta_{\text{max}}(T_m, t_w) = T_m \ln(t_w/\tau_0), \quad (4.26)$$

where τ_0 is a microscopic attempt time. Thus, at $T_m - \Delta T$, the region of phase

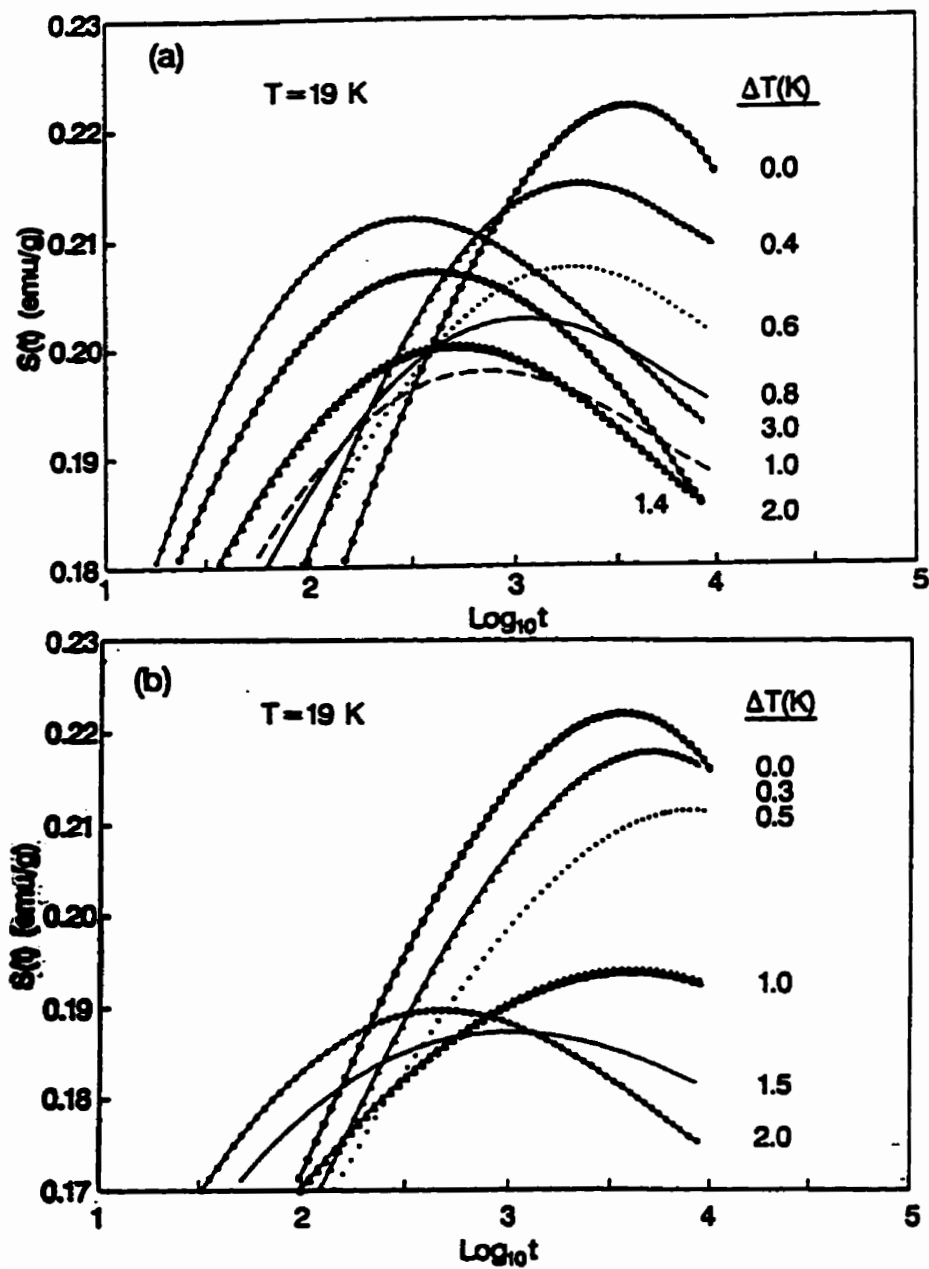


Figure 4.23: Relaxation rate $S(t) = -\partial M(t)/\partial \ln(t)$ vs. $\log(t)$ at $T_m = 19\text{ K}$ for $\text{Fe}_{0.65}\text{Ni}_{0.24}\text{Cr}_{0.11}$. (a) Temperature undercooling shifting: i.e., the sample is cooled from T_{ref} to $T_m - \Delta T$, aged for 2 hrs, then the temperature is raised to T_m , the field is cut off and the decay of the magnetization recorded. (b) Temperature overheating shifting: similar as (a). but the sample is cooled to $T_m + \Delta T$ in the beginning.

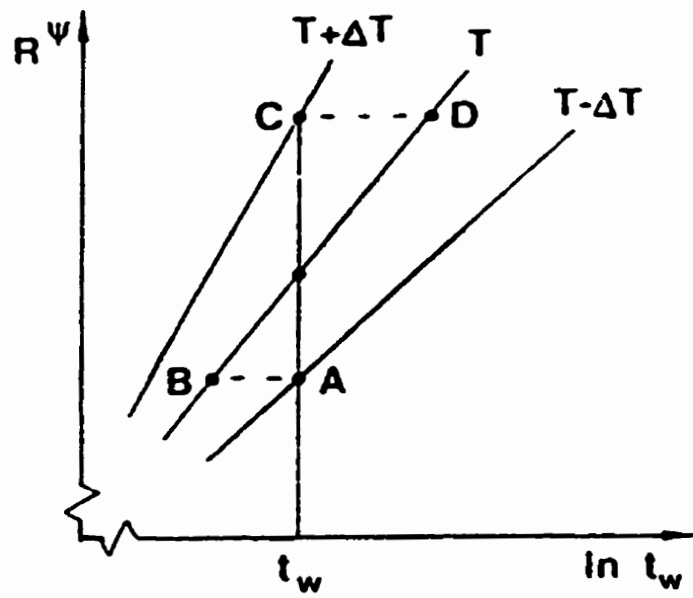


Figure 4.24: Schematic illustration of the temperature dependence of domain growth. Ψ is a barrier exponent. From Lundgren 1988.

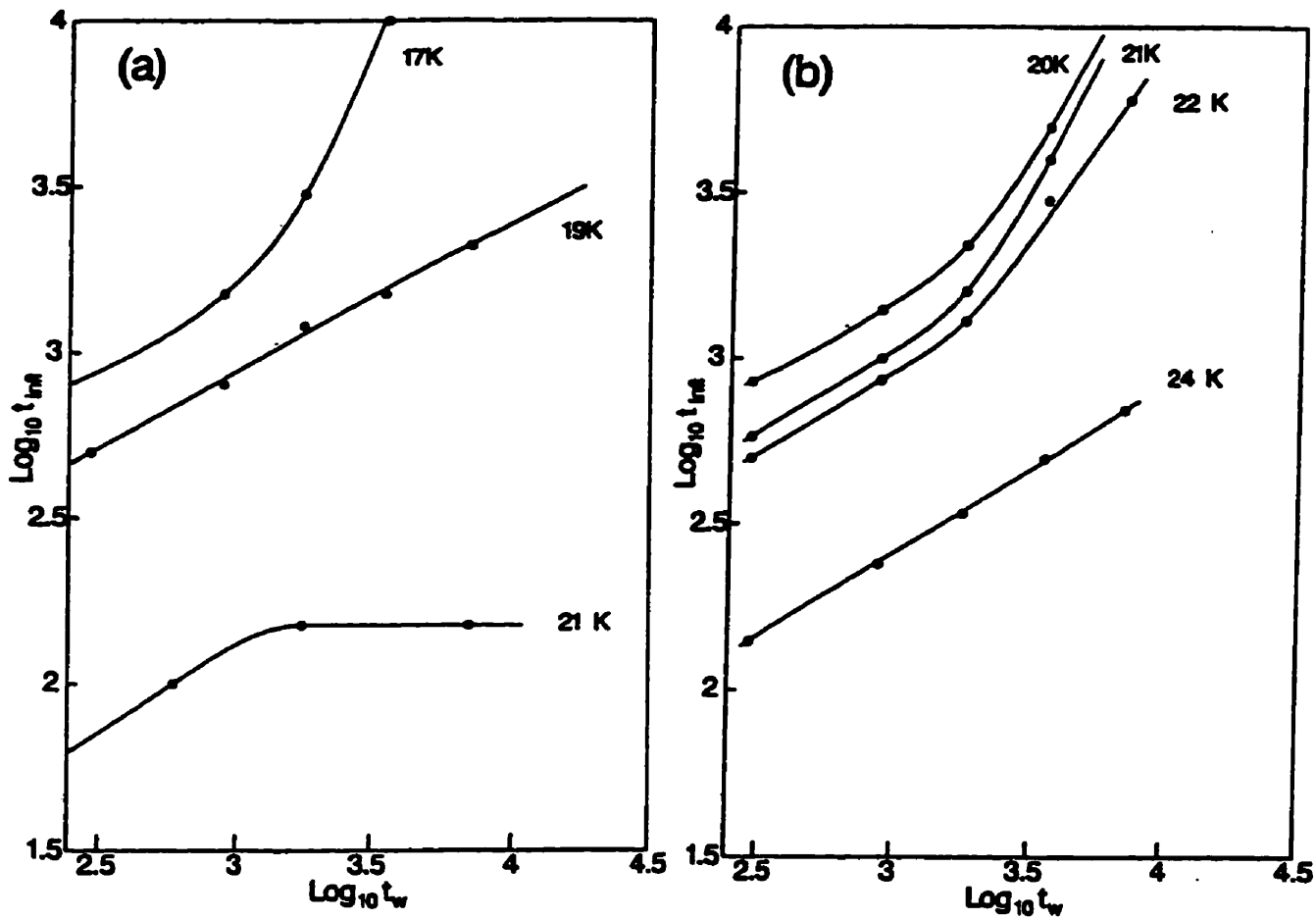


Figure 4.25: Aging rates for a series of t_w at the different temperatures. (a) for $\text{Fe}_{0.65}\text{Ni}_{0.24}\text{Cr}_{0.11}$ ($T_R = 22\text{K}$). (b) for $\text{Fe}_{0.65}\text{Ni}_{0.23}\text{Cr}_{0.12}$ ($T_R = 25\text{K}$). The solid lines are guide for the eye.

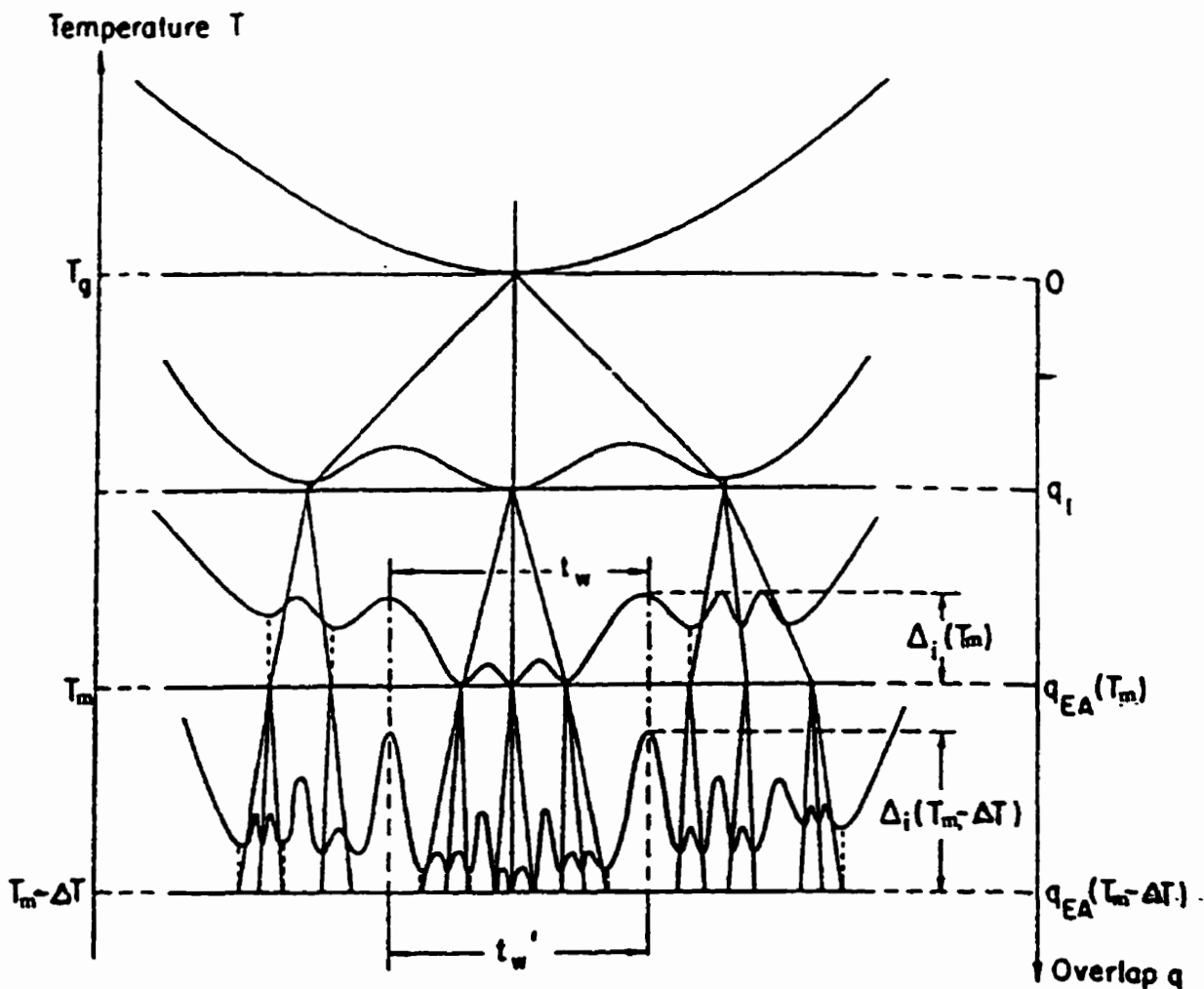


Figure 4.26: Hierarchical organization of metastable states. The coarse-gained free-energy surface is represented at each level corresponding to a given temperature. When the temperature is decreased, each valley subdivides into others. The times t_w and t_w' which are necessary to explore, at T_m and $T_m - \Delta T$, respectively, the region of phase bounded by the same barriers are indicated. The closest common ancestor to all states within the space bounded by Δ_i at T_m and $T_m - \Delta T$ is the same, and its corresponding value of the overlap function is q_1 . The sketch also shows that, as the system explores more of phase space, it encounters ever increasing barrier heights, and that the free-energy surface has a self-similar structure. From Lederman et al., (1991).

space populated during a given fixed waiting time t_w is bounded by barriers $\Delta_m(T_m - \Delta T, t_w)$ whose height is smaller than it would have been at T_m . This implies that, when the system is subsequently heated to T_m , the effective waiting time at T_m will be smaller than it should be and will decrease with increasing ΔT .

The second class of experiments can also be described following this approach. The sample is now field cooled to $T_m + \Delta T$. After a time t_w , a certain number N' of metastable states are populated at that temperature. As the temperature is lowered to T_m , each one of those states gives "birth" to new ones (see Fig. 4.26). Thus, when the field is cut to zero and the decay of TRM measured, the shape of the decay will reflect two processes. First, at short times the system populates the new states created by lowering the temperature. This is a fast process because it corresponds to populating states which are very close together in phase space (with a large overlap) or, similarly, states separated by very small barriers [compared to $\Delta_{max}(T_m, t_w)$]. Thus the decay of the TRM is faster than in a conventional experiment. Second, at long times, it populates the region of phase space not populated immediately after cooling from $T_m + \Delta T$ to T_m . Now, the higher the temperature, the faster the aging process and the quicker the system equilibrates. Therefore, for a fixed waiting time t_w at $T_m + \Delta T$, the system will explore a larger region of phase space through second-stage processes than it would have at T_m . This is the reason why, as ΔT increases, the system ages more and more at large observation times beyond its normal age t_w at temperature T_m . The TRM decay is slower at long observation times than the reference one at T_m with the same waiting time.

Figures 4.27 and 4.28 show the results of the temperature cycling experiments for $(\text{Fe}_{0.65}\text{Ni}_{0.35})_{0.882}\text{Mn}_{0.118}$ and $\text{Cr}_{0.79}\text{Fe}_{0.21}$ respectively. For $(\text{Fe}_{0.65}\text{Ni}_{0.35})_{0.882}\text{Mn}_{0.118}$, we cooled the sample in a field $H_a = 5$ Oe to the measurement temperature $T_m < T_{SG}$, and after a long wait time t_w at T_m , performed a temperature cycling $T_m \rightarrow T_m + \Delta T \rightarrow T_m$, after which the field was re-

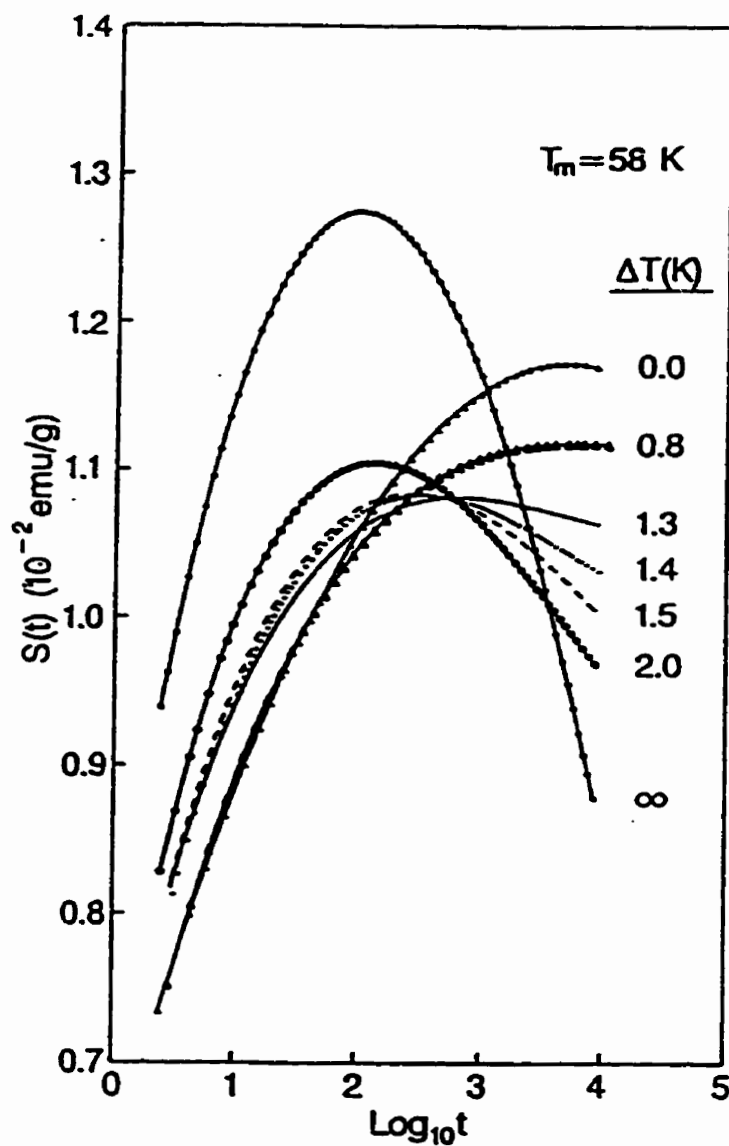


Figure 4.27: The relaxation rate S for $(\text{Fe}_{0.65}\text{Ni}_{0.35})_{0.882}\text{Mn}_{0.118}$ measured after cooling in a field $H_a = 5.0$ Oe to $T_m = 58$ K, waiting for $t_{w1} = 10^4$ s, cycling from $T_m \rightarrow T_m + \Delta T \rightarrow T_m$, with $t_{\text{cycle}} \cong 300$ s, and then removing the field (which defines $t = 0$). $\Delta T = \infty$ corresponds to warming above T_g . Note that the disappearance of one maximum is accompanied by the simultaneous growth of the other.

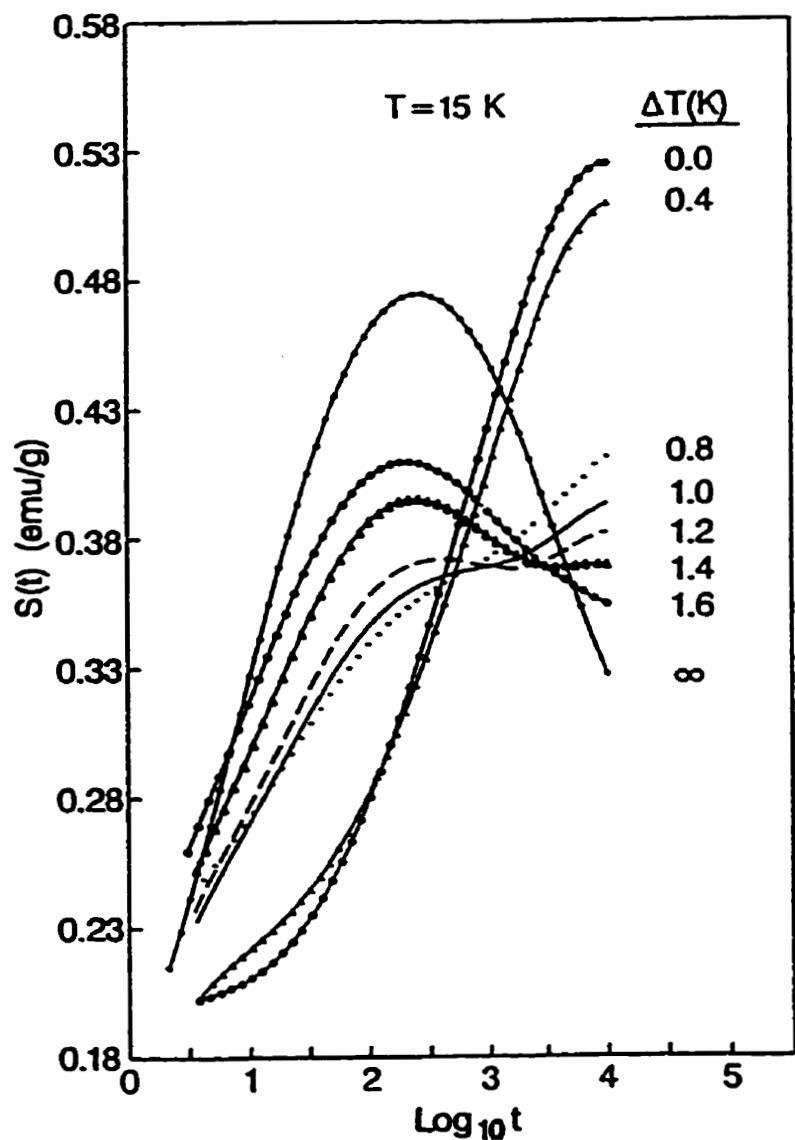


Figure 4.28: The relaxation rate S for $\text{Cr}_{0.79}\text{Fe}_{0.21}$ measured after cooling in a field $H_a = 1.0 \text{ Oe}$ to $T = 15 \text{ K}$, waiting for $t_{w1} = 10^4 \text{ s}$, cycling from $T \rightarrow T + \Delta T \rightarrow T$, with $t_{\text{cycle}} \cong 300 \text{ s}$, and then removing the field (which defines $t = 0$). $\Delta T = \infty$ corresponds to warming above T_g . Note that the disappearance of one maximum is accompanied by the simultaneous growth of the other.

moved. The wait time was $t_w = 10^4 s$, and the temperature cycling duration was $t_{cycle} = 300 s \ll t_w$. Figure 4.27 shows the result at $T_m = 58$ K for the temperature increments ΔT from 0 to 2 K as listed. The isotherm $\Delta T = \infty$ was obtained by heating the system above T_{SG} , then cooling and aging at T_m for $t_w \cong t_{cycle}$.

As shown in the figure, for small values of $\Delta T (< 1 K)$, there is a single maximum at $t_m \cong t_w = 10^4 s$, which is gradually suppressed with increasing ΔT . However, for values of ΔT larger than 1 K, not only is this maximum at longer wait times suppressed, but a second maximum begins to grow at shorter observation times, in the vicinity of $t'_m \cong t_{cycle}$. As the maximum at longer times weakens, the maximum at shorter times strengthens.

The droplet model of Fisher and Huse provides a possible explanation of this phenomenon. According to this model, the spin-glass state exhibits a unique sensitivity to temperature, so that neighbouring states at temperature T_m and $T_m + \Delta T$ share nearly identical equilibrium spin correlations $\langle \mathbf{S}_i \cdot \mathbf{S}_j \rangle_T$ only up to the overlap length $l_{\Delta T}$, beyond which the signs of the correlations at T_m are uncorrelated with those at $T_m + \Delta T$. If a spin glass is field cooled to a temperature T_m and, after a wait time t_w has elapsed, is subjected to a brief temperature cycle $T_m \rightarrow T_m + \Delta T \rightarrow T_m$, of duration $t_{cycle} \ll t_w$, immediately prior to field removal, then the subsequent behaviour depends on the magnitude of ΔT as follows: (a) If $\Delta T < \Delta T_{threshold}$, then $l_{\Delta T} > R_T(t_w)$ (the overlap length is larger than the typical domain size at T_m), and there is only one type of domain and hence one maximum in the relaxation rate $S(t)$ at $t \sim t_w$. (b) If $\Delta T > \Delta T_{threshold}$, then $l_{\Delta T} < R_T(t_w)$ and some of the T_m domains will fracture into smaller ($T_m + \Delta T$) domains of dimension $l_{\Delta T}$, so $S(t)$ will exhibit two maxima at $t \sim t_{cycle}$ and $t \sim t_w$, corresponding to the two distinct domain sizes. (c) If $\Delta T \gg \Delta T_{threshold}$, virtually all the T_m domains will be annihilated, and there will be one maximum in $S(t)$ at $t \sim t_{cycle}$ due to the ($T_m + \Delta T$) domains alone.

There is alternative explanation for this phenomenon, based on the existence of an heirarchical organization of states in phase space, as predicted by Parisi's solution of the SK model. Suppose we return to the heirarchy of metastable states and its evolution with temperature shown in Figure 4.29. As we stated previously, cooling cause the valleys to continuously split into multiple subvalleys, while, on warming, the process is reversed and the subvalleys coalesce. Further suppose that the energy barriers between states α , β , γ , are such that the characteristic time to overcome them is of the order of or slightly larger than the experimental time t_{exp} , and make the same assumption for the barriers inside the sets $\{\alpha_i\}$, $\{\beta_i\}$, and $\{\gamma_i\}$ ($i = 1, 2, 3$) at $T_m - \Delta T$. When the system is quenched from above T_{SG} to $T_m - \Delta T$, it falls somewhere in the complicated landscape defined at $T_m - \Delta T$ (suppose that it is in one of the states $\{\alpha_i\}$). As the system ages, it approaches equilibrium by first sampling the various *subvalleys* in $\{\alpha_i\}$, but has difficulty in equilibrating among the valleys α, β, γ due to the higher energy barriers. When the temperature is raised to T_m , the set $\{\alpha_i\}$ collapses into a single valley α , so that when the temperature is again lowered to $T_m - \Delta T$, memory of the previous equilibrium is lost and the system essentially must begin to equilibrate all over again, and thus appears to be younger.

We also performed a temperature cycling experiment on $\text{Cr}_{0.79}\text{Fe}_{0.21}$ as follows. The sample was cooled in a field $H_c = 0.5$ Oe to the measurement temperature $T_m = 15$ K, and after a long wait time $t_w = 10^4$ s at $T = 15$ K, a temperature cycling $T_m \rightarrow T_m + \Delta T \rightarrow T_m$ was performed for $t_{cycle} \cong 300$ s, after which the field was removed. Figure 4.28 shows the results for the temperature increments ΔT from 0 to 1.6 K as listed. As before, the isotherm $\Delta T = \infty$ was obtained by heating the system above T_{SG} , then cooling and aging at T_m for $t_w \cong t_{cycle}$.

As shown in the figure, for small values of ΔT (< 0.8 K), there is a single maximum at $t_m \cong t_w = 10^4$ s, which is gradually suppressed with increasing

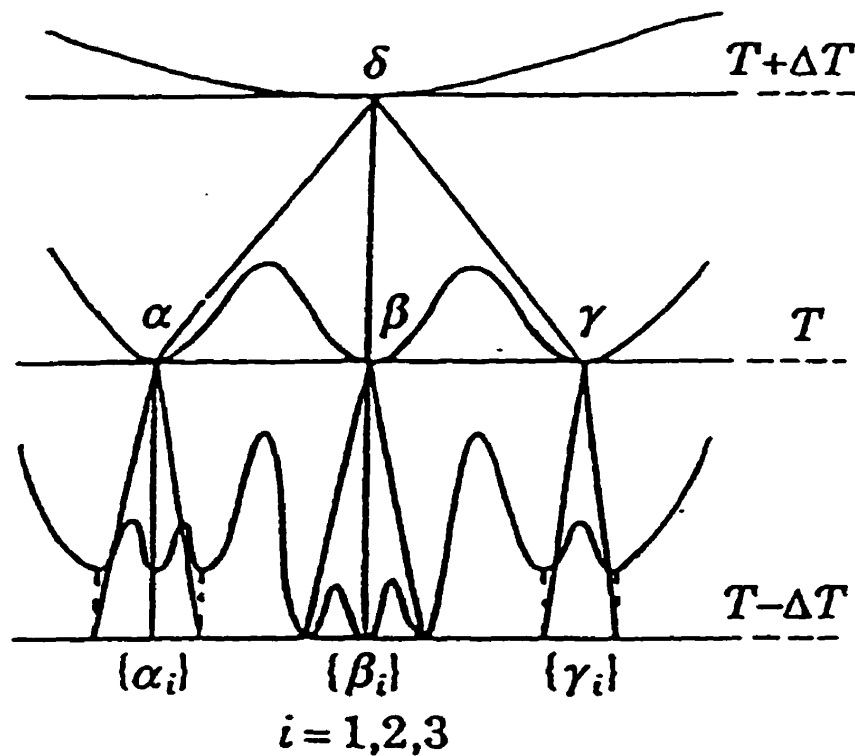


Figure 4.29: Sketch of the coarse-grained free-energy surface at different temperatures around T . When the temperature decreases from T to $T - \Delta T$, state α , β and γ <<give birth>> to set of states $\{\alpha_i\}$, $\{\beta_i\}$ and $\{\gamma_i\}$, respectively. Conversely when the temperature is raised from T to $T + \Delta T$, state α , β , γ merge into a single state δ . From Lefloch et al., (1992).

ΔT . However, for values of ΔT larger than 0.8 K, not only is this maximum at longer wait times suppressed, but a second maximum begins to grow at shorter observation times, in the vicinity of $t'_m \cong t_{cycle}$. As the maximum at longer times weakens, the maximum at shorter times strengthens. A comparison of Figures 4.27 and 4.28 shows that the structure induced by temperature cycling is much more clearly defined in $\text{Cr}_{0.79}\text{Fe}_{0.21}$ than it is in $(\text{Fe}_{0.65}\text{Ni}_{0.35})_{0.882}\text{Mn}_{0.118}$. This is probably because the shorter cooling times in the former system lead to stronger curvature in the original relaxation isotherms, and this in turn permits multiple inflection points to be resolved more easily.

While the droplet and heirarchical approaches both offer apparently reasonable, although very different, explanations for this phenomenon, recent reports in the literature (Lefloch, et al. 1992) of *negative* temperature cycling experiments appear to support the heirarchical picture. According to these reports, lengthy aging at T_m , followed by a cycling from $T_m \rightarrow T_m - \Delta T \rightarrow T_m$, does not appear to influence the *age* of the system, and when the temperature is returned to T_m , the system simply continues to age from the state reached *before* the cycling was performed. Thus there is a clear asymmetry in the experiments which contradicts the droplet model, according to which large domains will fracture into small domains whenever the *modulus* $|\Delta T|$ is large enough for the overlap length $l_{\Delta T}$ to fall below the domain size at T .

Can this asymmetry be accounted for within the heirarchical picture? Referring back to Figure 4.29, suppose the system is cooled to T_m and falls into valley β , for example. As aging proceeds at T_m , the system attempts to explore the other valleys α and γ and establish an equilibrium population distribution. If the system is now cooled to $T_m - \Delta T$, it will equilibrate quickly within the sets (subvalleys) β_i , but the relative populations of the different sets α_i, β_i and γ_i will not change because the barriers between the sets are too high. Thus cooling does not bring the system any closer to equilibrium with regard to the α, β, γ

populations, and when $T_m - \Delta T \rightarrow T_m$, the additional equilibration within the subvalleys is lost by coalescence, and the system simply picks up where it left off after the original aging at T_m .

4.8 Relaxation Dynamics: Field Effects

In an ordinary TRM experiment, a sample is cooled from above T_c in a field, to a measurement temperature T_m , and kept at constant field and temperature for a time t_w , before the field is cut off and the decay of the magnetization is measured. In the last section, we showed that the relaxation isotherms are sensitive to temperature fluctuations during the waiting period. Here we will show that the relaxation curve is also sensitive to the field amplitude before the field is removed. The magnetization will relax faster after a larger field step.

Figures 4.30(a) and 4.31(a) show the $m(t)/m_0$ versus $\log_{10}(t/t_w)$ plots for experiments performed at $T_m = 17$ K and 19 K for $\text{Fe}_{0.65}\text{Ni}_{0.24}\text{Cr}_{0.11}$, for a series of different cooling fields. In these two figures, all of the wait times are $t_w = 1$ hour; m_0 is the normalization factor for the individual curves, which is obtained by fitting the curve to an empirical stretched exponential function plus a constant, and extrapolating to $t = 0$. Within the accuracy of our measurement, m_0 is approximately the same as the field-cooled (FC) magnetization.

On a plot of $m(t)/m_0$ versus $\log_{10}(t/t_w)$, not only does the shape of the curve change with field but also the magnitude of $m(t)/m_0$ changes as well. For fields $H_a \leq 2$ Oe, the inflection point of the curve essentially does not move; but for larger fields, the inflection point of the curves experiences a significant shift. So, for the system $\text{Fe}_{0.65}\text{Ni}_{0.24}\text{Cr}_{0.11}$, we could say that the range of linear field response is less than 2 Oe. This value is very different from the field threshold for the system $\text{Cd}_{1.7}\text{In}_{0.3}\text{S}_4$ which is an insulating spin glass (Vincent et al., 1995)

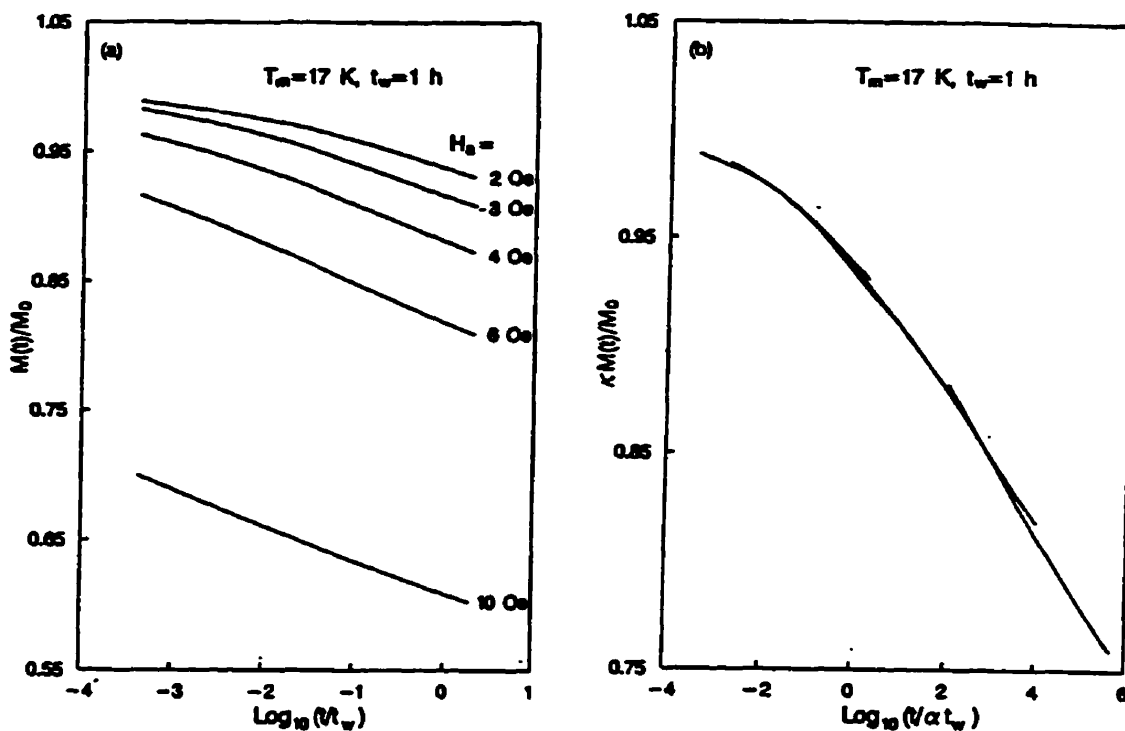


Figure 4.30: TRM relaxation at $T_m = 17\text{ K}$ for $t_w = 1\text{ h}$ for $\text{Fe}_{0.65}\text{Ni}_{0.21}\text{Cr}_{0.11}$ with the values of the applied field ranging from 2 to 10 Oe. (a) A plot of $M(t)/M_0$ vs. $\log(t/t_w)$, where $M_0 = 2.848, 3.521, 4.091, 4.958$ and 7.754 are the normalized factors obtained from fitting the curves for a stretched exponential and extrapolating to $t = 0$. (b) Scaling plot of (a) corrected by both parameters α and κ .

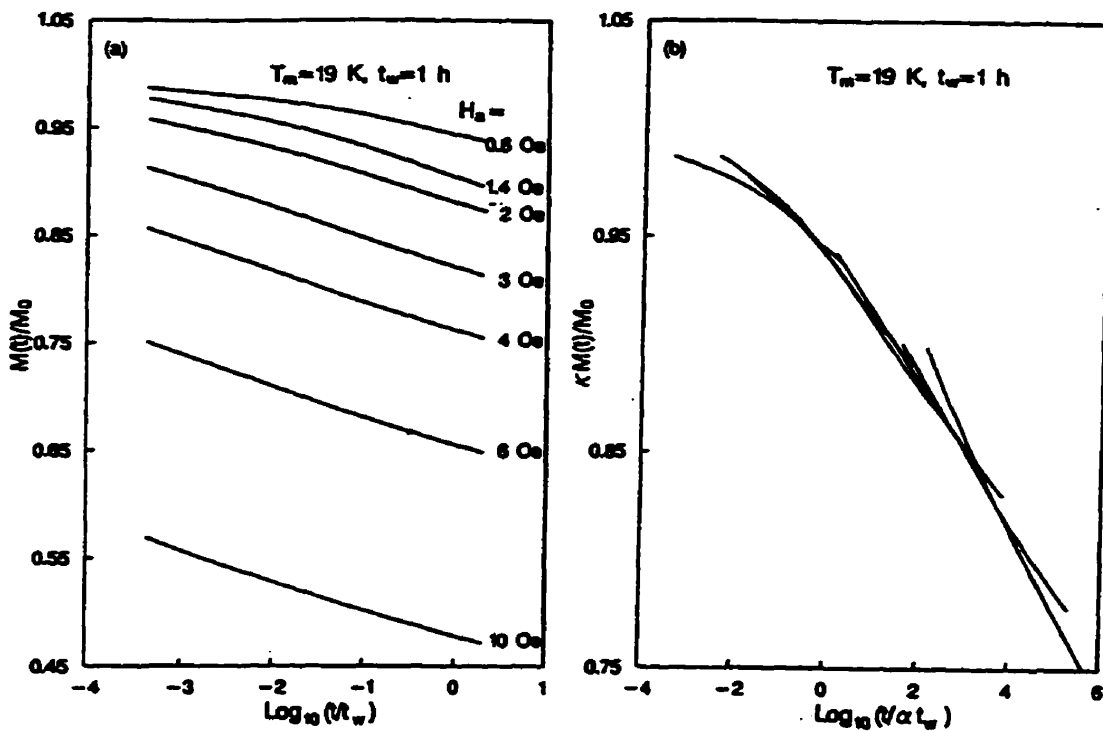


Figure 4.31: TRM relaxation at $T_m = 19 \text{ K}$ for $t_m = 1 \text{ h}$ for $\text{Fe}_{0.65}\text{Ni}_{0.21}\text{Cr}_{0.11}$ with the values of the applied field ranging from 0.8 to 10 Oe. (a) A plot of $M(t)/M_0$ vs. $\log(t/t_w)$, where $M_0 = 1.510, 2.020, 2.783, 3.470, 4.408, 5.858$ and 8.996 are the normalized factors obtained from fitting the curves for a stretched exponential and extrapolating to $t = 0$. (b) Scaling plot of (a) corrected by both parameters α and κ .

and the system Cu–6%Mn, which is a metallic spin glass (Chu et al., 1995), for which the field thresholds are 20 Oe and 30 Oe, respectively, but similar to that of $(\text{Fe}_{0.15}\text{Ni}_{0.85})_{75}\text{P}_{16}\text{B}_6\text{Al}_3$ which is an amorphous spin glass (Djurberg et al., 1995). So, the sensitivity of the relaxation function to the magnitude of the field is very different from system to system.

Based on Bouchaud's model of random traps, the relaxation function $m(t)/m_0$ essentially depends only on the ratio t/t_w . In the extreme limit of nonergodic behaviour, the plot should yield a "master curve" in which data for different t_w all lie on the same curve. The plots in Figures. 4.30(a) and 4.31(a) clearly indicate that the data do not scale with t/t_w .

As already stated previously, while aging, the system evolves among states with same magnetization (M_{FC} states) as inferred from the time independence of the field-cooled magnetization. When the field is changed by ΔH , a new Zeeman term is added which increases the free energy of the M_{FC} states by $M_{FC}\Delta H$ and tends to bring the system into a set of $M_{FC} + \Delta M$ states. If we assume that this results in a decrease in the barriers by the same amount $M_{FC}\Delta H$, then, the escape times $\{\tau\}$ of the whole set of M_{FC} states are lowered to $\{\tau'\}$ by the factor $\alpha = \exp(-b\Delta H)$, where $\tau' = \alpha\tau$ and $\alpha < 1$. Thus at the instant t^* the field is changed, the τ distribution is shifted and the measurement now probes states for which the most probable depth is αt^* instead of t^* . The system thus appears to be younger, as if it had only aged for a time αt^* .

In order to interpret and improve the scaling plots in Figures 4.30(a) and 4.31(a), it is necessary to extend Bouchaud's picture of random traps beyond the phase-space description and include more details of how the traps couple to a field. Following Vincent et. al (1995), the trapping time τ is assumed to be related to the number N of spins which must be flipped to escape from a trap by

$$\tau = \tau_0 \exp(B(N)/(k_B T)) \quad (4.27)$$

where the depth $B(N)$ of the trap increases with N . Due to the random couplings between the spins, the net uncompensated moment for this trap is $\sqrt{N}\mu_B m$ where $\mu_B m$ is the spin moment, so the Zeeman energy is

$$E(\Delta H) = \sqrt{N}m\mu_B\Delta H \quad (4.28)$$

and the lifetime of the τ traps is reduced to

$$\tau'(N) = \alpha\tau(N) = \tau_0 \exp\left[\frac{B(N) - E(\Delta H, N)}{k_B T}\right] \quad (4.29)$$

Figure 4.32 shows two sets of traps corresponding to two different values of the magnetization. The field perturbation tilts the free energy landscape, and favours one set of traps over the other.

Experiments on the out of phase susceptibility χ'' (Vincent et al 1995) support some of this picture. In these experiments, the sample is cooled from the paramagnetic phase to the glass phase, and the ac susceptibility is observed to decrease as the system ages at a constant temperature. If a static field is subsequently applied, then the relaxation is restarted, just as if the age of the system was reduced by the field perturbation. This effect is illustrated in Figure 4.33(a) for a $\text{CdCr}_{1.7}\text{In}_{0.3}\text{S}_4$ insulating spin glass, which shows measurements of χ'' at $\omega = 1$ Hz for a sequence of field changes of different amplitude. If measurements at different frequencies are compared, such as those in Figure 4.33(b) for $\omega = 0.1$ and 1 Hz, where the time t_1 of the field change is chosen so as to keep ωt_1 constant, then it is clear that the effect of the field perturbation is stronger for deeper traps (that is, for larger t_1). However, a close inspection of these data shows that the measured relaxation restarts more abruptly after a field change than can be accounted for by a simple reduction in age, as if some of the subsystems experience a new quench from above T_G . In order to account for this effect, it is assumed that $B(N)$ grows less rapidly than $E(\Delta H, N) \sim \sqrt{N}$, so that $\tau'(N)$ initially increases

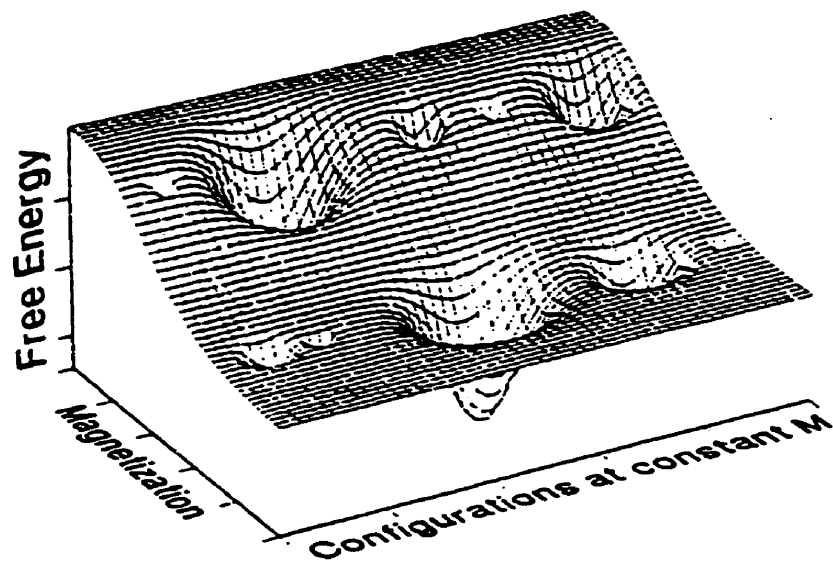


Figure 4.32: Schematic picture of the free-energy landscape after a field variation. The magnetically unfavorable metastable states have been tilted, and their depth has diminished; the deeper the trap, the larger its extension, and the stronger the effect of the field perturbation. From Vincent et al. (1995).

but then eventually decreases for values of N in excess of a critical size N^* defined by

$$\tau'(N^*) = \alpha\tau(N^*) = \alpha\tau^* = \frac{1}{\omega} \quad (4.30)$$

This is illustrated in Figure 4.34.

This effectively divides the set of traps into two families, “hard” traps with $\tau < \tau^*$ which experience a reduced age described by α , and “fragile” traps with $\tau > \tau^*$ which are completely destabilized and wiped out by the field change. Vincent et al. defined p as the proportion of subsystems which are fragile at the time t_1 of the perturbation, and wrote χ'' as the sum of two terms

$$\chi''(w, t > t_1) = p\chi''(w, t - t_1) + (1 - p)\chi''(w, \alpha t_1 + t - t_1) \quad (4.31)$$

Our TRM measurements are also sensitive to these effects. In order to scale the relaxation isotherms on to a universal curve, it is necessary to use two correction factors, one α for the t/t_w axis and another κ for the vertical M/M_{FC} axis, so that the scaling function for the TRM is

$$\frac{M}{M_{FC}} = \kappa F\left(\frac{t}{\alpha(t_w)t_w}\right) \quad (4.32)$$

where $\alpha(t_w) = \exp[-\chi_0(t_w)H^2]$. This H^2 dependence of $\alpha(t_w)$ is an integrated form of $b\Delta H$ assuming that $b\Delta H \propto \chi_0 H\Delta H$. The factor κ allows for a field and/or a t_w dependence of the initial fast response.

The scaling procedure described above has been applied to the data in Figures 4.30(a) and 4.31(a) and the resulting plots are shown in Figs.4.30(b) and 4.31(b). The various TRM decay curves have been shifted horizontally and vertically in order to make them coincide as much as possible. The best fit scaling

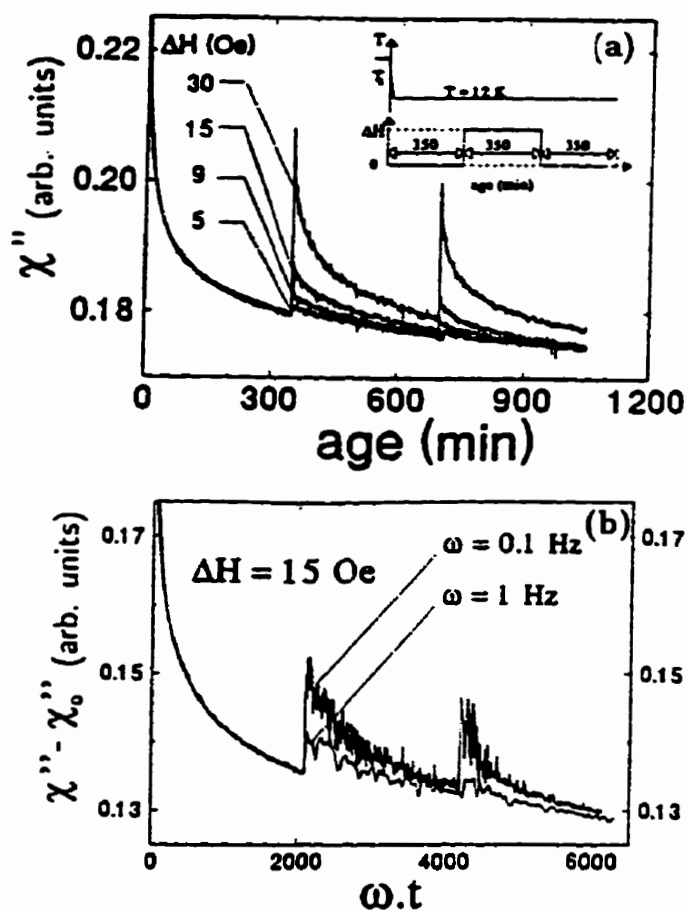


Figure 4.33: a). Relaxation of the out-of-phase susceptibility χ'' (in arb. units) at frequency $\omega = 1$ Hz and constant temperature 12 K, as a function of the time (age) following a quench from above $T_g = 16.7$ K. The sample is $\text{CdCr}_{1.7}\text{In}_{0.3}\text{S}_4$ insulating spin glass. After 350 min, a static field ΔH ($=5, 9, 15,$ or 30 Oe) is applied, producing a renewed χ'' relaxation. After another 350 min, the field is removed. The inset sketches the procedure. b). Comparison of the effect on χ'' of a dc field variation in two experiments at frequencies $\omega = 0.1$ and 1 Hz. The field variation is applied at a time t_1 ($=350$ and 35 min, respectively) such that the product $\omega \cdot t_1$ is kept constant. The curves are plotted as a function of $\omega \cdot t$, and have been vertically shifted in order to superpose both relaxations before the field variation. At constant $\omega \cdot t$, the effect of the perturbation is seen to be stronger for the lowest frequency (longest t_1). From Vincent et al. (1995).

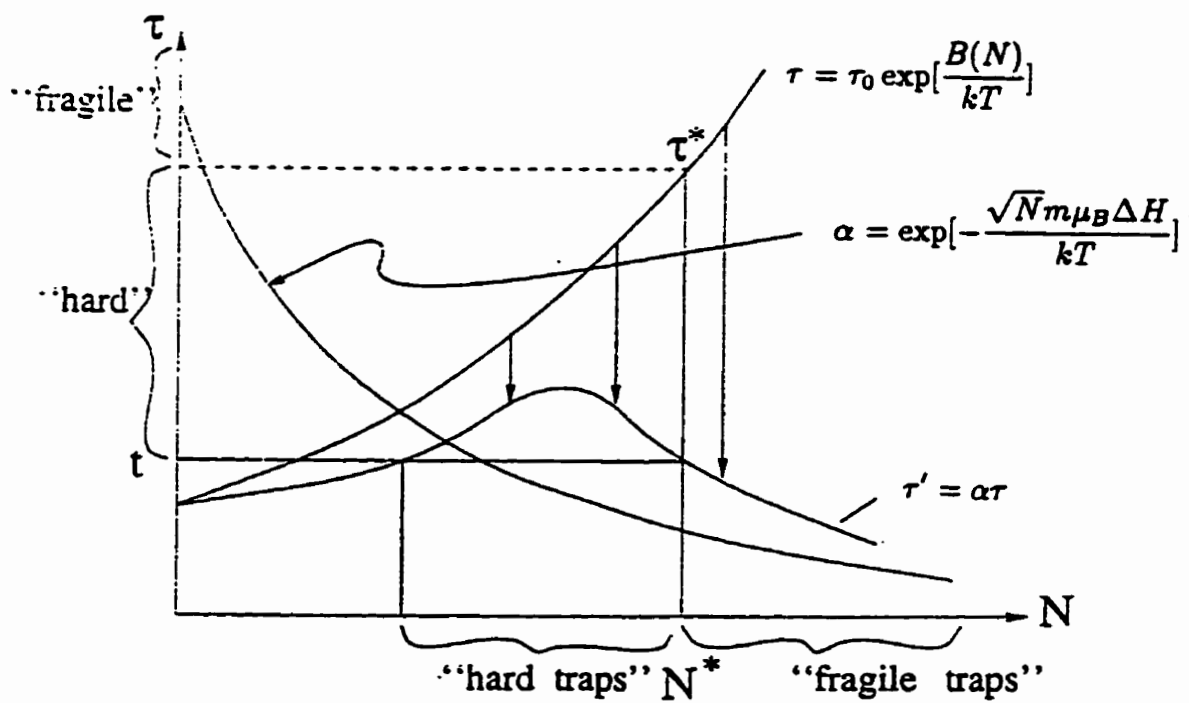


Figure 4.34: Escaping times in "hard" and "fragile" traps. The "hard" traps only reduce their age, but the "fragile" traps will be completely wiped out in the field perturbation.

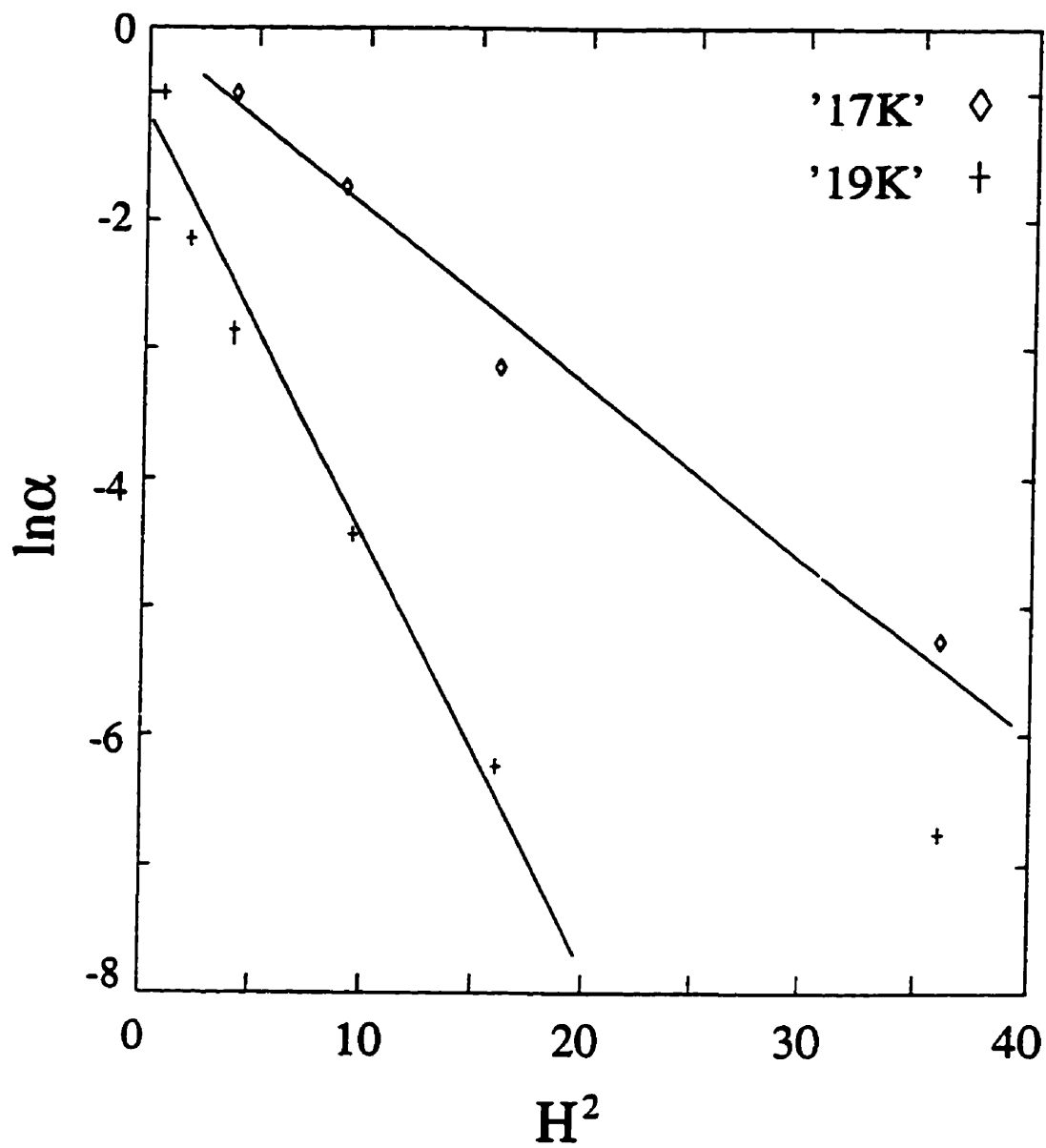


Figure 4.35: The relation of parameter α to the magnetic field for $T = 17K$ and $T = 19K$.

parameters α and κ for the different fields are listed in Tables 4.35 and 4.36. The scaled curves lie reasonably well on a “master relaxation curve”. With increasing field, the various isotherms describe progressively longer-time portions of this master curve than it is possible to observe in the usual experiments; the reduction of the effective age of the system allows us to measure the relaxation function for very large values of $t/(\alpha t_w)$. Obviously the curves fall together nicely and universal behaviour is obtained. The horizontal and vertical shifts determine the factors α and κ .

Table 4.35: Scaling parameters for $\text{Fe}_{0.65}\text{Ni}_{0.24}\text{Cr}_{0.11}$ for $T_m = 17$ K.

H (Oe)	2	3	4	6	10
α	1.0	0.23 ± 0.01	0.014 ± 0.001	$(2.0 \pm 0.1) \times 10^{-4}$	$(4 \pm 1) \times 10^{-6}$
κ	1.0	1.002 ± 0.001	1.004 ± 0.001	1.011 ± 0.001	1.26 ± 0.01

Table 4.36: Scaling parameters for $\text{Fe}_{0.65}\text{Ni}_{0.24}\text{Cr}_{0.11}$ for $T_m = 19$ K.

H (Oe)	0.8	1.4	2	3	4	6	10
α	1.0	0.10 ± 0.01	0.025 ± 0.001	$(2.0 \pm 0.1) \times 10^{-4}$	$(2.8 \pm 0.1) \times 10^{-5}$	$(1.0 \pm 0.1) \times 10^{-5}$	$(3 \pm 1) \times 10^{-6}$
κ	1.0	1.010 ± 0.001	1.020 ± 0.001	1.05 ± 0.01	1.10 ± 0.01	1.20 ± 0.01	1.58 ± 0.01

The parameter α describes the reduction in the depth of hard traps, which renormalizes the time axis t/t_w to $t/(\alpha t_w)$ as expected. The parameter κ accounts for the partial quench effect. It describes the proportion of subsystems which are located in the region of fragile traps and which are completely washed out by the field variation. These subsystems are directly responsible for the initial fast decay of the magnetization which precedes the much slower TRM decay, and are

therefore expected to affect the initial value of M/M_{FC} through κ . From Tables 4.35 and 4.36, it is seen that α decreases as H increases.

A plot of $\ln \alpha$ *v.s.* H^2 is shown in Figure 4.35, (a) for $T_m = 17K$ and (b) for $T_m = 19K$. The curves are approximately straight lines, in agreement with the expression $\alpha = \exp(-\chi_0 H^2)$.

We finally wish to point out that the proposed field scaling of the TRM relaxations is in agreement with a more general scaling form suggested by Paris(1995).

Chapter 5

Summary and Conclusions

The purpose of this thesis was to study the relaxation of the thermoremanent magnetization in several different magnetic systems which exhibit ferromagnetic ordering with low temperature reentrant collapse, to establish its principal characteristics as a function of observation time t , waiting (or aging) time t_w , temperature T , and magnetic field H , and to compare these measurements with the predictions of several of the most prominent theories of relaxation in systems with quenched disorder. The experimental systems were chosen from among those for which the existence of sequential ferromagnetic to spin glass transitions has been reasonably well established, primarily through the observation of certain structure in the *ac* magnetic susceptibility, but for which no data was available concerning the relaxation response to abrupt changes in magnetic field in either of the two ordered phases.

In a nutshell, if one of these systems is cooled in a magnetic field H from above its Curie temperature to a temperature T_m below the temperature T_R where the ferromagnetic state appears to collapse into a glassy spin state, and held for a curing time t_w at fixed (T_m, H) before abruptly removing the field at $t = 0$, then the relaxation isotherm exhibits an inflection point t_{infl} when plotted on a logarithmic time scale $\log_{10}t$, and the entire experimental response function shifts

towards longer observation times with increasing age t_w . The latter characteristic is striking evidence that the system does not reach equilibrium immediately following the "quench" to T_m , but continues to evolve during the curing period. Unlike the behaviour reported by Lundgren et al in pure spin glasses (Lundgren et al, 1983), this age-induced shift is not equal to t_w and has a very significant temperature dependence. The relaxation isotherms are not unique functions of (T_m, H) , but are sensitive to the past history of the temperature and field so that, for example, small fluctuations in temperature or field during the curing period can have a dramatic effect on both the location of the inflection point and on the amplitude of the decay. This means that the correlations established as the state grows with time are extremely fragile functions of temperature and field, and growth can be interrupted and even "restarted" for increments of ΔT or ΔH which exceed certain threshold values. None of these appear to be characteristics of the ferromagnetic phase. When the measurement temperature T_m is above T_R , the relaxation response behaves like a simple unique transient connecting two equilibrium states, with no age dependence, no fragility to temperature and field fluctuations, and no inflection point.

There are a number of prominent theories in the literature which purport to explain slow nonexponential decay of a physical observable in response to a step function excitation in systems with disorder, and one of the motivations of this thesis was to provide a critical evaluation and comparison of these various theories, using reentrant ferromagnets, with their two thermally distinct relaxation regimes, as "test subjects". In fact, one of the features which distinguishes the current study from most others in this area is the use of detailed fits of the experimental data to specific functional forms as one of the criteria for establishing the validity of a theory.

Probably the best empirical descriptions of the data are provided by the Kohlraush stretched exponential $\exp[(-t/\tau)^\beta]$ for the age-dependent reentrant

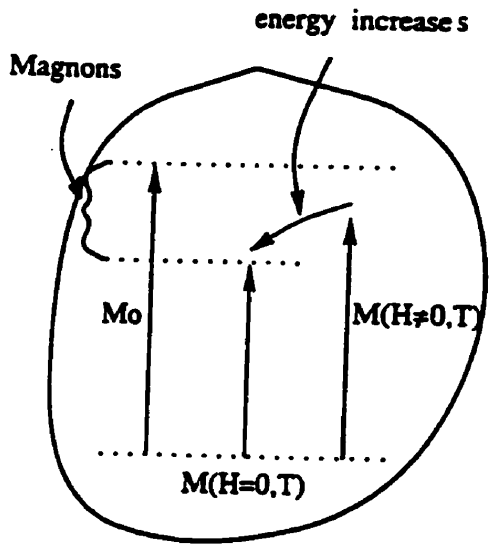
(spin glass) data, and (somewhat less satisfactory) a power law $t^{-\alpha}$ for the stationary ferromagnetic relaxation isotherms. However, both functions must be supplemented by a substantial constant baseline, which is difficult to justify theoretically, and furthermore none of the models which yield stretched exponential behaviour offer any explicit mechanism for aging, so that the physical significance of the various fitting parameters is difficult to appreciate.

The percolation model of Chamberlin is based on the assumption that magnetic systems segregate into mesoscopic dynamically correlated domains (DCD) within each of which the spins share a common relaxation rate. The DCD's are either "aligned" with the field, in which case their magnon density is reduced by the field so that their energy increases after H is removed, or "antialigned", in which case they have a higher level of magnon excitation in a field and must consequently lose energy when the field is removed. The characteristics of both types of domains are summarized in Figure 5.1. The most important feature of the model is that the magnon energy level spacing δE is finite-size quantized, and thus varies inversely as the number s of spins in the domain, $\delta E = \Delta/s$. Thus the relaxation times for the aligned domains vary from $\tau_- = \infty$ for $s = 0$ to $\tau_- = \tau_{\infty}^-$ for the largest domain $s = \infty$, while for antialigned domains τ_+ varies from $\tau_+ = 0$ for $s = 0$ to $\tau_+ = \tau_{\infty}^+$ for the largest domain $s = \infty$, as shown in Figure 5.1. Percolation theory gives the distribution of domain sizes to be $n_s \sim s^{1/9} \exp[-(c's)^{2/3}]$ and the total relaxation is a parallel combination of activated relaxation from all the domains. Our analysis shows that the reentrant phase dynamics are dominated by antialigned domains, while the ferromagnetic dynamics are dominated by aligned domains. Thus the behaviour in the reentrant phase is different from that of the pure spin glasses studied by Chamberlin, which are characterized by a mixture of both aligned and antialigned domains, but appears to bear a much closer resemblance to the ordered phase of pure ferromagnets like EuS, which also shows a crossover from antialigned to aligned domination as the tempera-

ture increases through the Curie temperature T_c . It is interesting to compare the behaviour of the two $\text{Fe}_{0.65}\text{Ni}_{0.23}\text{Cr}_{0.12}$ and $\text{Fe}_{0.65}\text{Ni}_{0.24}\text{Cr}_{0.11}$ alloys. Figure 5.2 shows the behaviour of the average characteristic times $\bar{\tau}_+$ and $\bar{\tau}_-$ as a function of temperature T at a fixed wait time $t_w = 60\text{s}$, and Figure 5.3 shows the wait time dependence of $\bar{\tau}_+$ in the reentrant phase of the two alloys. Assuming, like Chamberlin, that the magnon bandwidth Δ is constant, then Figure 5.1 tells us that the average domain size \bar{s} in the reentrant phase decreases with increasing temperature T but increases with increasing wait time t_w . As far as we are aware, the current investigation is the first to apply the Chamberlin formalism explicitly to variable wait time data, so we have no points of comparison here. Nevertheless, there is one very interesting similarity with Chamberlin's analysis: the $\text{Fe}_{0.65}\text{Ni}_{0.24}\text{Cr}_{0.11}$ alloy shows a large jump in $\bar{\tau}$ at $T = T_R$ which is very reminiscent of the behaviour observed by Chamberlin in EuS and attributed by him to a critical divergence of the correlation length. The current data seems to imply a corresponding divergence at T_R . Since the 11at% alloy is a good ferromagnet while the 12at% alloy is on the borderline between the ferromagnetic and the spin glass phases, it is tempting to interpret this jump as evidence of a critical change of phase at T_R , which of course requires the existence of a well-defined ferromagnetic state, so that it is present at 11at% and absent at 12at%. However this is quite speculative at this stage. In spite of its apparent generality and power, it should be noted that the Chamberlin function must still be supplemented by a constant baseline (this was true of Chamberlin's original studies as well), and this once again suggests a weakness in the formalism.

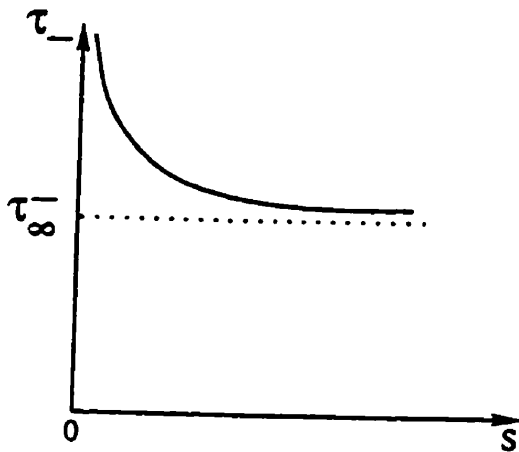
We now turn to the two remaining models, the Elementary Decay Model (EDM) and Bouchaud's model of random traps. Both are remarkable in that they incorporate explicit mechanisms which replicate many of the essential features of aging observed in disordered systems. The EDM is noteworthy for its ability to reproduce all of the standard functional forms quoted in the various

ALIGNED DOMAINS

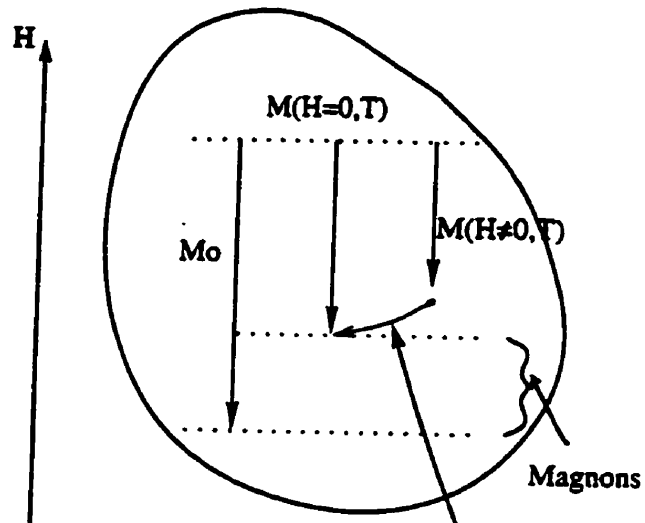


$$\delta E = \frac{\Delta}{s} > 0$$

$$\tau_- = \tau_\infty^- \exp(+\Delta/(Ts))$$



ANTI-ALIGNED DOMAINS



$$\delta E = -\frac{\Delta}{s} < 0$$

$$\tau_+ = \tau_\infty^+ \exp(-\Delta/(Ts))$$

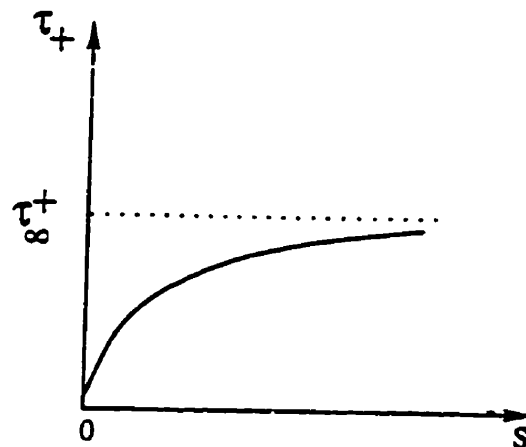


Figure 5.1: Aligned and antialigned domains and a comparison of their characteristics.

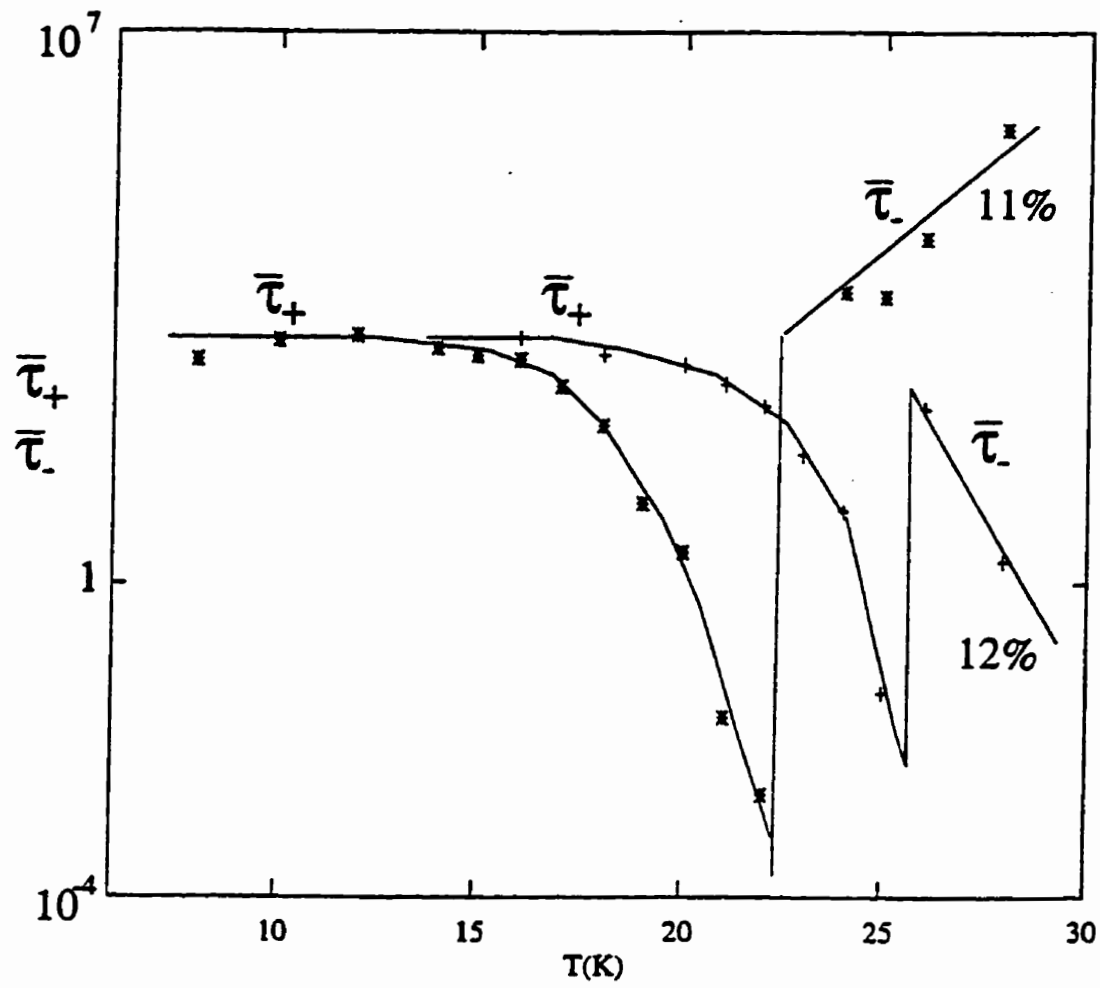


Figure 5.2 Average characteristic time versus temperature in $\text{Fe}_{0.65}\text{Ni}_{0.24}\text{Cr}_{0.11}$ and $\text{Fe}_{0.65}\text{Ni}_{0.23}\text{Cr}_{0.12}$.

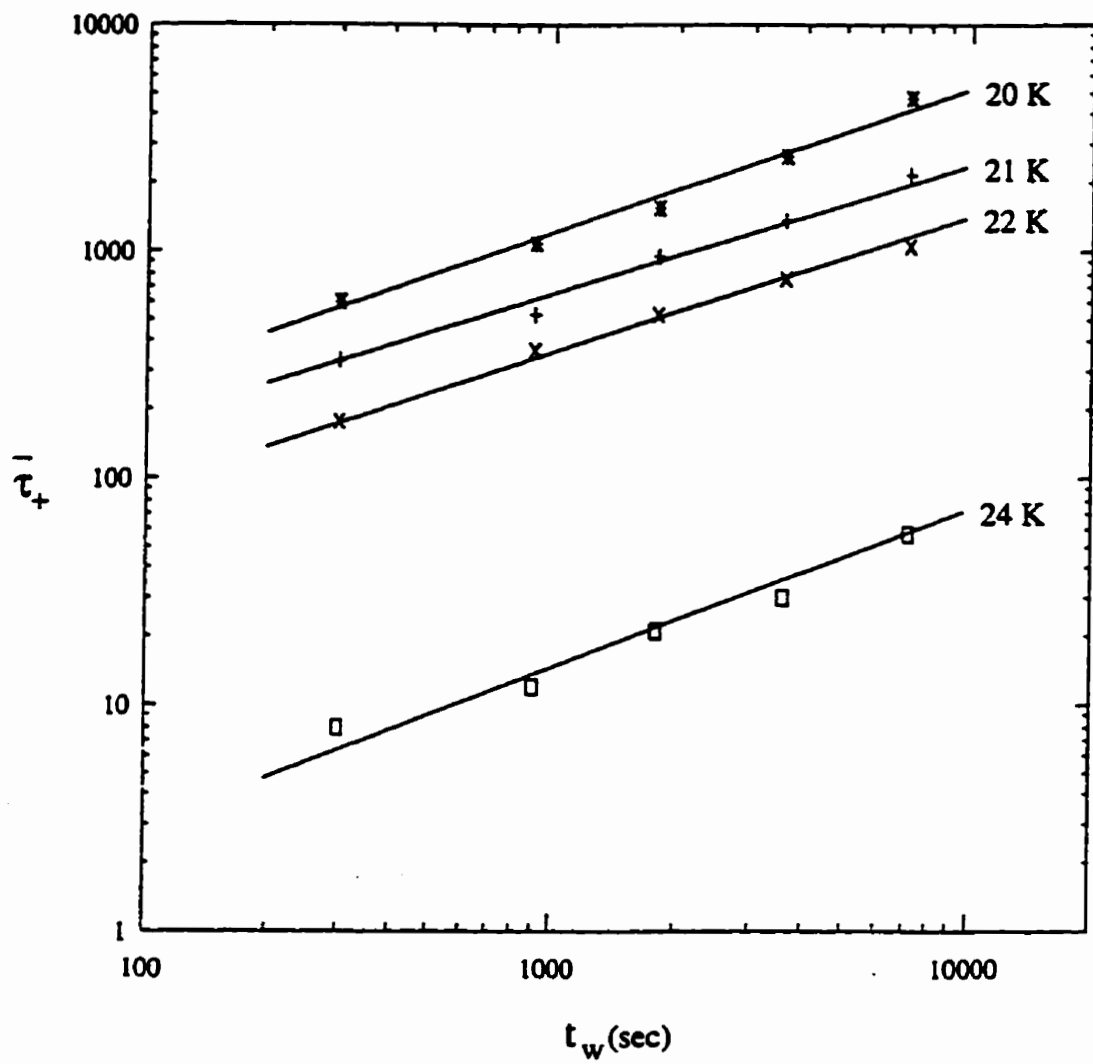


Figure 5.3: Average characteristic time versus wait time in $\text{Fe}_{0.65}\text{Ni}_{0.23}\text{Cr}_{0.12}$.

analyses of slow relaxation data which appear in the literature, in a closed form which is valid for all experimental times $0 \leq t < \infty$, and with only one parameter $b = T/\bar{E}$ determining the complete shape of the decay. The random traps model is noteworthy because it offers a very appealing physical picture of how a disordered system evolves towards equilibrium by randomly exploring a progressively larger number of metastable states in its configuration space, and it also yields an explicit functional form for the decay whose shape is also determined by only one parameter x , with $0 \leq x \leq 1$. Both models are also capable of describing nonexponential decay in a variety of physical systems including high T_c superconductors, type II superconductors, spin glasses, polymers, and charge density wave systems.

The EDM assumes that the decay originates from a sequence of thermally activated Arrhenius relaxations over a Poissonian distribution of energy barriers, and that the decay begins at the moment that the system is quenched below the ordering temperature. Thus aging corresponds to those activation events which are “lost” during the waiting period prior to the field removal, and the relaxation function, measured from the instant $\tau = 0$ that the field is reduced to zero is

$$g_{b,\tau_w}(\tau) = \int_0^\infty f_0(E') \exp[-\tau_w \exp(-E')] \cdot \exp[-\tau \exp(-E')] dE'$$

where $f_0(E') = b \exp(-bE')$, $E' = E/T$, and $b = T/\bar{E}$. When the EDM formalism is applied to our reentrant ferromagnets, it is immediately apparent that a single relaxation function is completely inadequate to describe the the total measured response, and that a superposition of two such functions with very different values of the shape parameter b is necessary in order to account for the large amplitude of the remanence which remains even after several hours of relaxing. The first contribution is wait time dependent and is characterized by a value of $b_1 \sim 0.1 - 0.5$ (typically) which increases with temperature, but much faster than linearly, particularly in the vicinity of T_R , as shown in Figure 5.4. This means that the

average activation trap \bar{E} is also strongly temperature dependent, and decreases rapidly with increasing temperature. Our analysis also shows that this wait time dependent term becomes progressively weaker as T approaches T_R from below (that is, the parameter $c \rightarrow 1$), and the decay is represented exclusively by the second age-independent contribution above T_R . This latter term is characterized by a shape parameter b_2 which is roughly an order of magnitude of smaller than b_1 . In spite of its impressive ability to replicate quite subtle variations in curvature, particularly in the relaxation rate $S = -\partial m / \partial \ln t$, the EDM offers no insight into the physical origin of the activation barriers or the nature of the “entities” which are relaxing or the genesis of the second distribution, which appears to be induced by the field change. One of the more significant contributions of this thesis has been to provide a physical interpretation for the EDM, but for this we had to rely to a large extent on the random traps model of Bouchaud.

Bouchaud’s model assumes that the configuration space of any disordered system consists of many local energy minima which represent all the metastable configurations which the system passes through in its search for the equilibrium configuration, which is the deepest (or global) minimum. This process is a thermally activated random walk among a set of “traps” with a distribution of trapping times τ :

$$\psi(\tau) = \frac{\tau_0^x}{\tau^{(1+x)}},$$

and if $x < 1$, the search is essentially never completed, at least within a finite wait time t_w . We believe that it is no coincidence that the single most important parameter x of this model, which controls the “extent” of the trapping distribution $\psi(\tau)$, exhibits the same temperature dependent systematics as the parameter b in the EDM, which similarly defines the “width” of the activation barrier distribution. Both increase with temperature, indicating that the distribution is dominated by shallow traps (or low barriers) as the temperature approaches the

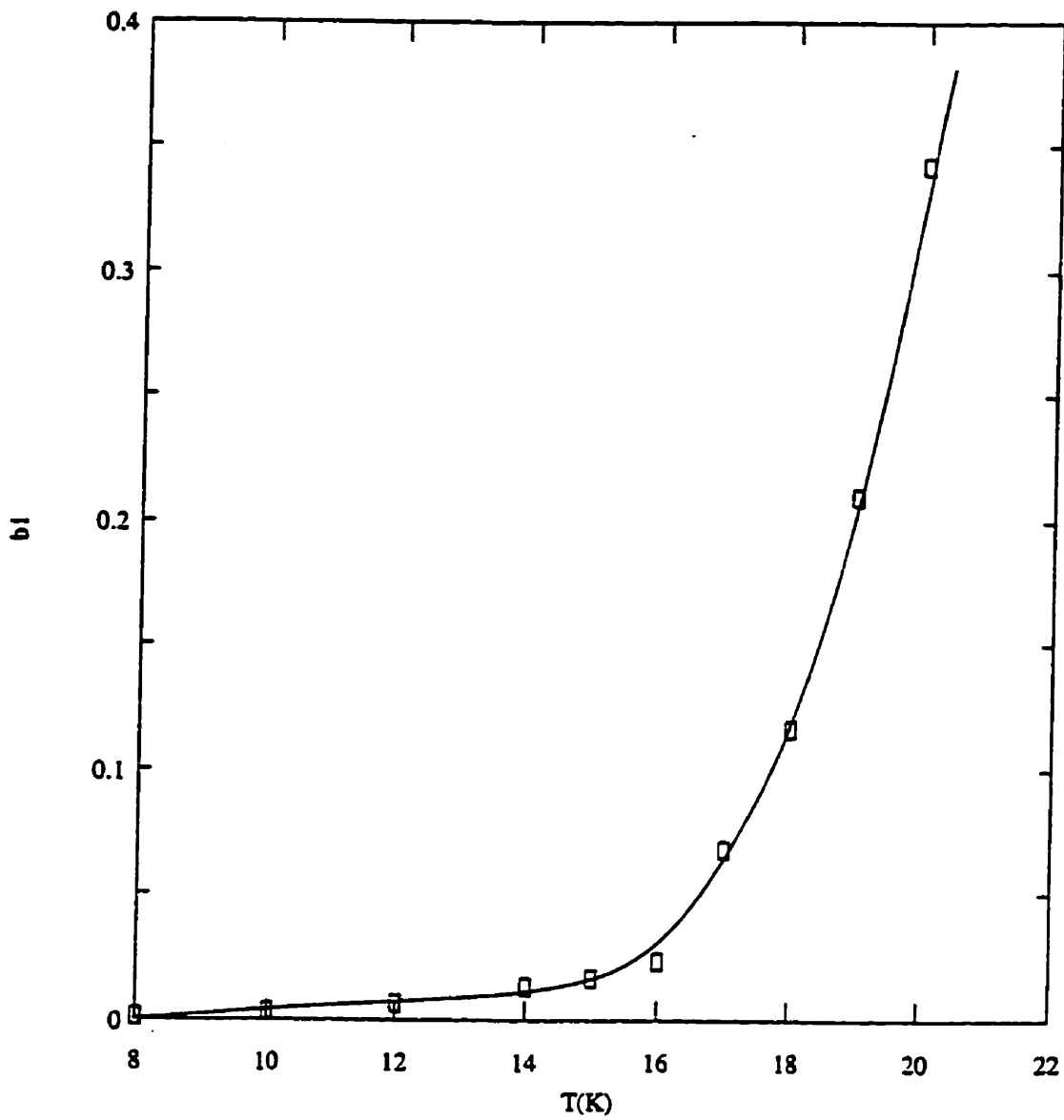


Figure 5.4: Shape parameter b_1 versus temperature in $\text{Fe}_{0.65}\text{Ni}_{0.24}\text{Cr}_{0.11}$.

glass temperature from below. In order to explain the behaviour of our reentrant ferromagnets, particularly the failure of the experimental data to scale with t/t_w as predicted by the purely nonergodic expression derived by Bouchaud, it became necessary to regard a disordered system as a collection of independent subsystems, and this also formed the basis for our interpretation of the Poissonian distribution of the EDM and its transformation into a single-peaked structure during the wait time t_w . Furthermore, we postulate that it is the renormalization of the depths of these traps caused by the Zeeman energy shift, as proposed by Vincent et. al (1995), that is described by the second, non-age-dependent EDM distribution; in other words, the field-induced component of the EDM energy distribution represents the way the subsystems which compose the entire system are effectively redispersed among the original set of traps by the field change. Our investigations suggest that the most promising approach will ultimately be a compromise which exploits the analytical power of the EDM and the simplicity and transparency of the random trap physics. However, at the current stage neither of these models have evolved sufficiently to replicate subtle (higher order) effects like those related to temperature cycling during the curing period, and future work must focus on incorporating these subtleties into the formalism.

Chapter 6

References

- Acet, M., Stamm, W., Wassermann, E.F. and Zahres, H., 1987 *J. Magn. Magn. Mat.* **70** 427.
- Acet, M., Zahres, H., Stamm, W. and Wassermann, E.F., 1988 *J. Appl. Phys.* **63**(8) 3921.
- Adachi, K., Sato, K., Matsui, M. and Fujio, Y., 1971 *J. Phys. Soc. Japan* **30** 1201.
- Adachi, K., Sato, K., Matsui, M. and Mitani, S., 1973 *J. Phys. Soc. Japan* **35** 426.
- Aharoni, A., 1985 *J. Appl. Phys.* **57** (10) 4702.
- Aharoni, A., 1992 *Phys. Rev. B* **46** 5434.
- Alba, M., Ocio, M. and Hammann, J., 1986 *Europhys. Lett.* **2**(1) 45.
- Alba, M., Hammann, J., Ocio, M. and Refregier, Ph., 1987 *J. Appl. Phys.* **61**(8) 3683.
- Andersson, J.O., Mattsson, J. and Svedlindh, P., 1992 *Phys. Rev. B* **46** 8297.
- Antropov, V.P., Dorofeev, Yu.A., Kazantsev, V.A., Men'shikov, A.Z. and Teplykh, A.E., 1988 *Sov. Phys. JETP* **67**(2) 336.
- Banerjee, S. and Raychaudhuri, A.K., 1993 *J. Phys.: Condens. Matter* **5** L295.
- Beck, P.A., 1981 *Phys. Rev. B* **24** 2867.
- Biljakovic, K., Lasjaunias, J.C., Monceau, P. and Lery, F., 1991 *Phys. Rev. Lett.*

67 1902.

Binder, K. and Schroder, K., 1976 *Phys. Rev. B* **14** 2142.

Binder, K. and Young, A.P., 1986 *Rev. Mod. Phys.* **58** 801.

Bohner, R. and Angell, C.A., 1992 *Phys. Rev. B* **45** 10091.

Bouchaud, J.P., 1992 *J. Phys. I France* **2** 1705.

Bouchaud, J.P., Vincent, E. and Hammann, J., 1994 *J. Phys. I France* **4** 139.

Bray, A.J. and Moore, M.A., 1987 *Phys. Rev. Lett.* **58** 57.

Brodale, G.E., Fisher, R.A., Fogle, W.E., Phillips, N.E. and van Curen, J., 1983 *J. Magn. Magn. Mat.* **31-34** 1331.

Burke, S.K. and Rainford, B.D., 1983 *J. Phys. F: Met. Phys.* **13** 441.

Burke, S.K., Cywinski, R., Davis, J.R. and Rainford, B.D., 1983 *J. Phys. F: Met. Phys.* **13** 451.

Cannella, V. and Mydosh, J.A., 1972 *Phys. Rev. B* **6** 4220.

Chamberlin, R.V., 1991 *Phys. Rev. Lett.* **66** 959.

Chamberlin, R.V., 1993 *Phys. Rev. B* **48** 15638.

Chamberlin, R.V., G. Mozurkewich, and R. Orbach, 1984 *Phys. Rev. Lett.* **52** 867.

Chamberlin, R.V. and Haines, D.N., 1990 *Phys. Rev. Lett.* **65** 2197.

Chamberlin, R.V. and Holtzberg, F., 1991a *Phys. Rev. Lett.* **67** 1606.

Chamberlin, R.V., Haines, D.N. and Kingsbury, D.W., 1991b *J. Non-cryst Solids* **131-133** 192.

Chu, D., Kenning, G.G. and Orbach, R., 1995 *Philos. Mag. B* **71** 479.

Crane, S., Carnegie, D.W., Jr. and Claus, H., 1982 *J. Appl. Phys.* **53**(3) 2179.

De Almeida, J.R.L. and Thouless, D.J., 1978 *J. Phys. A: Math. Gen.* **11** 983.

De Dominicis, C., Orland, H. and Laine, F., 1985 *J. Phys. Lett.* **46** L-463.

Derrida, B., 1980 *Phys. Rev. Lett.* **45** 79.

Derrida, B., 1981 *Phys. Rev. B* **24** 2613.

Deryabin, A.V., Chirkov, Y.A. and T'kov, A.V., 1984 *Sov. Phys. JETP* **59**(2) 355.

- Deryabin, A.V., T'kov, A.V., Shvetsov, B.N., Larionov, A.P. and Zakharov, I.V., 1985 *Sov. Phys. Solid State* **27**(3) 511.
- Deryabin, A.V., Kazantsev, V.K., T'kov, A.V. and Zakharov, I.V., 1987 *Sov. Phys. JETP* **65**(5) 987.
- Dixon, P.K., Wu, L., Nagel, S.R., Williams, B.D. and Carini, J.P., 1990 *Phys. Rev. Lett.* **65** 1108.
- Djurberg, C., Mattsson, J. and Nordblad, P., 1995 *Europhys. Lett.* **29**(2) 163.
- Edwards, S.F. and Anderson, P.W., 1975 *J. Phys. F: Metal Phys.* **5** 965.
- Erhart, P., Portis, A.M., Senning, B. and Waldner, F., 1994a *J. Phys.: Condens. Mat.* **6** 2881.
- Erhart, P., Senning, B. and Waldner, F., 1994b *J. Phys.: Condens. Mat.* **6** 2893.
- Ferry, J.D., 1980 *Viscoelastic properties of polymers* (New York: Wiley).
- Fisher, K.H., 1975 *Phys. Rev. Lett.* **34** 1438.
- Fisher, K.H. and Hertz, J.A., *Spin Glasses*, Edited by D. Edwards and D. Melville, (Cambridge University Press, 1991).
- Fisher, D.S. and Sompolinsky, H., 1985 *Phys. Rev. Lett.* **54** 1063.
- Fisher, D.S. and Huse, D.A., 1986 *Phys. Rev. Lett.* **56** 1601.
- Fisher, D.S., 1986 *Phys. Rev. Lett.* **56** 416.
- Fisher, D.S. and Huse, D.A., 1987 *J. Phys. A: Math. Gen.* **20** L1005.
- Fisher, D.S. and Huse, D.A., 1988a *Phys. Rev. B* **38** 373.
- Fisher, D.S. and Huse, D.A., 1988b *Phys. Rev. B* **38** 386.
- Fisher, M.E., *Lecture Notes in Physics*(186), 1982 (Springer-Verlag, Berlin) p17
- Franz, S. and Hertz, J. , 1995, *Phys. Rev. Lett.* **74** 2114.
- Furusaka, M., Ishikawa, Y., Yamaguchi, S. and Fujino, Y., 1986 *J. Phys. Soc. Japan* **55** 2253.
- Gabay, M. and Toulouse G., 1981 *Phys. Rev. Lett.* **47** 201.
- Gibbs, M.R.J., Evetts, J.E. and Leake, J.A., 1983 *J. Mat. Sci.* **18** 278.
- Goldfarb, R.B., Rao, K.V. and Chen, H.S., 1985 *Solid State Communications* **54** 799.

- Granberg, P., Sandlund, L., Nordbl , P., Svedlinth, P. and Lundgren, L., 1988 *Phys. Rev. B* **38** 7097.
- Griffiths, R.B., Weng, C.Y. and Langer, J.S., 1966 *Phys. Rev.* **149** 301.
- Hagen, C.W. Griessen, R., 1989 *Phys. Rev. Lett.* **62** 2857.
- Hammann, J., Lederman, M., Ocio, M., Orbach, R. and Vincent, E., 1992 *Physica A* **185** 278.
- Harris, A.B. and Lubensky, T.C., 1981 *Phys. Rev. B* **24** 2656.
- Hoogerbeets, R., Luo, W.L. and Orbach, R., 1986 *Phys. Rev. B* **34** 1719.
- Huck, B. and Hesse, J., 1987 *J. Magn. Magn. Mat.* **70** 425.
- Huck, B., Landes, J., Stasch, R. and Hesse, J., 1988 *J. Phys.(France)* **C8** 1141.
- Hygate, G. and Gibbs, M.R.J., 1990 *J. Phys.:Condens. Matter* **2** 1425.
- Jackle, J., 1986 *Rep. Prog. Phys.* **49** 171.
- Koper, G.J.M. and Hilhorst, H.J., 1988 *J. Phys. France* **49** 429.
- Kovacs, A.J., R.A. Stratton and J.D. Ferry, 1963 *J. Phys. Chem.* **67** 552.
- Kunkel, H., Roshko, R.M., Ruan, W. and Williams, G., 1991 *Philos. Mag. B* **63** 1213.
- Kunkel, H., Roshko, R.M., Ruan, W. and Williams, G., 1991 *Philos. Mag. B* **64** 153.
- Kunkel, H., Roshko, R.M., Ruan, W. and Williams, G., 1991 *J. Appl. Phys.* **69** 5060.
- Lederman, M., Orbach, R., Hammann, J.M., Ocio, M. and Vincent, E., 1991 *Phys. Rev. B* **44** 7403.
- Lefloch, F., Hammann, J., Ocio, M. and Vincent, E., 1992 *Europhys. Lett.* **18**(7) 647.
- Lottis, D.K., White, R.M. and Dahlberg, E.D., 1991 *Phys. Rev. Lett.* **67** 362.
- Lubensky, T.C. and A.J.Mckane, 1981 *J. Phys.* **A** **14** L157.
- Lundgren, L., 1988 *J. Phys.(France)* **C8** 1001.
- Lundgren, L., Nordblad, P. and Svedlinth, P., 1986 *Phys. Rev. B* **34** 8164.
- Lundgren, L., Svedlinth, P. and Beckman, O., 1981 *J. Magn. Magn. Mat.* **33-38**

33.

Lundgren, L., Svedlindh, P., Nordblad, P. and Beckman, O., 1983 *Phys. Rev. Lett.* **51** 911.

Lundgren, L., Svedlindh, P. and Beckman, O., 1983 *J. Magn. Magn. Mat.* **31-34** 1349.

Majumdar, A.K. and Blanckenhagen, P. V., 1984 *Phys. Rev. B* **29** 4079.

Manheimer, M.A., Bhagat, S.M. and Chen, H.S., 1982 *Phys. Rev. B* **26** 456.

Matsui, M., Sato, K. and Adachi, K., 1973 *J. Phys. Soc. Japan* **35** 419.

Matson, M.E., Lottis, D.K. and Dahlberg, E.D., 1994 *J. Appl. Phys.* **75**(10) 5475.

Mezard, M., Parisi, G., Sourlas, N., Toulouse, G. and Virasoro, M., 1984 *J. Phys.* **45** 843.

Mezard, M. and Parisi, G., 1985 *J. Phys. Lett.* **46** L-771.

Mezard, M., Parisi, G. and M.A. Virasoro, 1985 *J. Phys. Lett.* **46** L-217.

Mezard, M. and Parisi, G., 1986 *J. Phys.* **47** 1285.

Mitchler, P.D., Roshko, R.M. and Ruan, W., 1993 *Philos. Mag. B* **68** 539.

Mina, E., Bohorquez, A., Zamora, L.E and Alcazar, G.A.P., 1993 *Phys. Rev. B* **47** 7925.

Miyazaki, T., Ando, Y. and Takahashi, M., 1985 *J. Appl. Phys.* **57**(1) 3456.

Monod, P. and Bouchiat, H., 1982 *J. Phys. Lett.* **43** L-45.

Muller, J.B. and Hesse, J., 1983 *Z. Phys. B-Condensed Matter.* **54** 35.

Mydosh, J.A., *Spin Glasses: An Experimental Introduction*, (Taylor & Francis, London - Washington, D.C., 1993).

Nagata, S., Keesom, P.H. and Harrison, H.R., 1979 *Phys. Rev. B* **19** 1633

Nakamura, Y. and Miyata, N., 1967 *J. Phys. Soc. Japan* **23** 223.

Nemoto, K., 1988 *J. Phys. A: Math. Gen.* **21** L287.

Ngai, K.L., 1979 *Comments Solid State Phys.* **9** 127 and 1980 **9** 141.

Ngai, K.L., Rajagopal, A.K., Huang, C.Y., 1984 *J. Appl. Phys.* **55**(6) 1714.

Ngai, K.L. and Wright, G.B.(Editors), 1991 *J. Non-Cryst. Solids.* **131-133**.

Nicolaidis, G.K., Hadjipanayis, G.C. And Rao, K.V., 1993 *Phys. Rev. B* **48**

12759.

Nicolaides, G.K. And Rao, K.V., 1993, *J. Magn. Magn. Matter.* **125** 195.

Nieuwenhuizen, Th. M., 1995 *Phys. Rev. Lett.* **74** 4289.

Nieuwenhuys, G.J., Verbeek, B.H. and Mydosh, J.A., 1979 *J. Appl. Phys.* **50**(3) 1685.

Ocio, M., Alba, M. and Hammann, J., 1985 *J. Phys. Lett.* **46** 1101.

Orland, H., 1985 *J. Phys. Lett.* **46** L-763.

Palmer, R.G., 1982 *Adv. Phys.* **31** 669.

Palmer, R.G., Stein, D.L., Abrahams, E. and Anderson, P.W., 1984 *Phys. Rev. Lett.* **53** 958.

Palmer, R.G., *Lecture Notes in Physics (275)*, 1986, (Springer-Verlag, Berlin).

Parisi, G., 1979 *Phys. Rev. Lett.* **43** 1754.

Parisi, G., 1980 *J. Phys. A* **13** 1101.

Parisi, G., 1983 *Phys. Rev. Lett.* **50** 1946.

Parisi, G., 1992 *Physica A* **185** 316.

Parisi, G., 1995 *Phil. Mag. B*, **71** 471.

Paul, A., *Chemistry of glasses* (Chapman and Hall, 1982).

Press, W.H., Teukolsky, S.A., Vetterling, W.T., and Flannery, B.P., *Numerical Recipes in FORTRAN: the Arts of Scientific Computing*, 1992.

Rammal, R., Toulouse, G. and Virasoro, M.A., 1986 *Rev. Mod. Phys.* **58** 765.

Refregier, Ph., Vincent, E., Hammann, J. and Ocio, M. 1987 *J. Physique* **48** 1533.

Roshko, R.M. and Ruan, W., 1991 *J. Phys. I France* **1** 1809.

Roshko, R.M. and Williams, G., 1984 *J. Magn. Magn. Mat.* **50**.

Rossel, C., Maeno, Y. and Morgenstern, I., 1989 *Phys. Rev. Lett.* **62** 681.

Rossel, C., *Relaxation in Complex Systems and Related Topics*, edited by Campell, I.A. and Giovannella, C., (Plenum, New York, 1990).

Schins, A.G., Dons, E.M., Arts, A.F.M. de Wijn, H.W., Vincent, E., Leylekian, L. and Hammann, J., 1993 *Phys. Rev. Lett.* **70** 2340.

Ruan, W., 1993 Ph.D. thesis (University of Manitoba).

- Schins, A.G., Arts, A.F.M. and de Wijn, H.W., 1993 *Phys. Rev. B* **48** 16524.
- Sherrington, D. and Kirkpatrick, S., 1975, *Phys. Rev. Lett.* **35** 1792.
- Sherrington, D. and Kirkpatrick, S., 1978, *Phys. Rev. B* **17** 4384.
- Shiga, M. and Nakamura, Y., 1984 *J. Magn. Magn. Mat.* **40** 319.
- Shiga, M., Satake, T., Wada, Y. and Nakamura, Y., 1985 *J. Magn. Magn. Mat.* **51** 123.
- Sibani, P. and Hoffmann, K.H., 1989, *Phys. Rev. Lett.* **63** 2853.
- Stein, D.L. (Editor), *Spin glasses and Biology* (World Scientific, 1992).
- Struik, L.C.E., *Physical aging in amorphous polymers and other materials*(Elsevier North-Holland Inc., 1978).
- Struik, L.C.E., 1991 *J. Non-Cryst Solids* **131-133** 395.
- Svedlinth, P., Granberg, P., Nordblad, P., Lundgren, L. and Chen, H.S., 1987 *Phys. Rev. B* **35** 268.
- Takzei, G.A., 1987 *Sov. Phys. Solid State* **31**(9) 1507.
- Takzei, G.A., Kostyshin, A.M. and Grebenyuk, Yu.P., 1984 *Sov. Phys. Solid State* **26**(9) 1648.
- Takzei, G.A., Kostyshin, A.M., Grebenyuk, Yu.P. and Sych, I.I., 1986 *Sov. Phys. JETP* **63**(5) 1081.
- Takzei, G.A., Kostyshin, A.M. and Sych, I.I., 1987 *Sov. Phys. Solid State* **29**(8) 1401.
- Vertechi, D. and Virasoro, M.A., 1989 *J. Phys. France* **50** 2325.
- Vincent, E, Hammann, J. and Ocio, M., Published as a chapter in *Recent Progress in Random Magnets*, D. H. Ryan (editor), (World Scientific Publishing Co. Pte. Ltd., Singapore 1992).
- Vincent, E., Bouchaud, J.P., Dean, D.S. and Hammann, J., 1995a *Phys. Rev. B* **52** 1050.
- Vincent, E., Bouchaud, J.P., Hammann, J. and Lefloch, F., 1995b *Philos. Mag. B* **71** 489.
- Vincent, E., Yuan, Y., Hammann, J., Hurdequint, H. and Guevara, F., 1996 *J.*

Magn. Magn. Mat.

Wassermann, E.F., 1989 *Physica Scripta* **T25** 209.

Wassermann, E.F., *Handbook of Magnetic materials Vol. V*, (North-Holland, 1980).

Watson, G.N., *A treatise on the theory of Bessel functions*, (Cambridge University Press 1962).

Weissman, M.B., 1993 *Rev. Mod. Phys.* **65** 831.

Westerholt, K., 1987 *Phys. Rev. B* **36** 2410.

Williams, G., 1991 *Magnetic susceptibility of superconductors and other spin systems*, (Plenum Press, New York).

Williams, M.L., Landel, R.F. and Ferry, J.D., 1955 *J. Am. Chem. Soc.* **77** 4701.

Wulfes, A., Bottger, Ch., Hesse, J., Sievert, J. and Ahlers, H., 1992 *J. Magn. Magn. Mat.* **104-107** 2069.

Yang, G., 1994 M.Sc. thesis (University of Manitoba).

Yi, L., Buttner, G., Usadel, K.D. and Yao, K.L., 1993 *Phys. Rev. B* **47** 254.

Appendix A

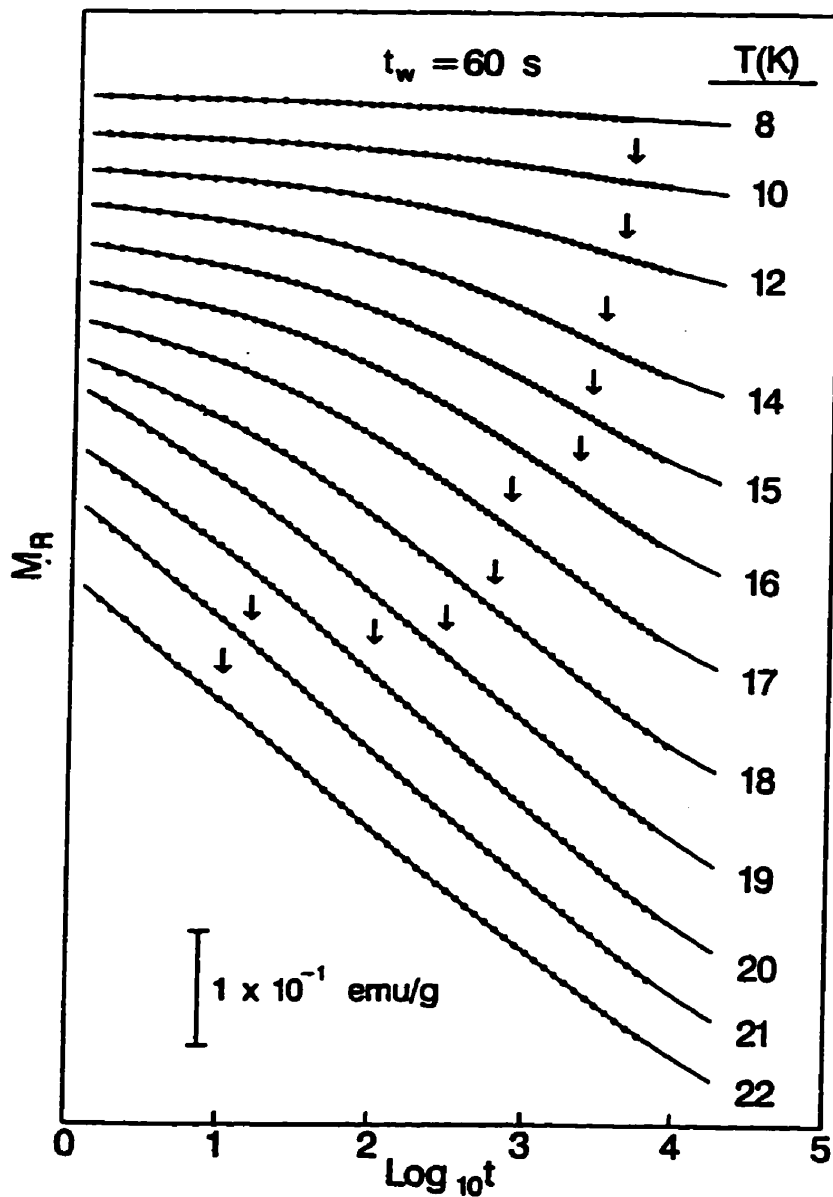


Figure A.1: Thermoremanent relaxation isotherms of $\text{Fe}_{0.65}\text{Ni}_{0.24}\text{Cr}_{0.11}$ for a sequence of temperatures $T_m \leq 22$ K and for a common wait time $t_w = 60$ s. The solid curves are fits to Eq.(4.1) and vertical arrows mark the characteristic times (inflection points) τ .

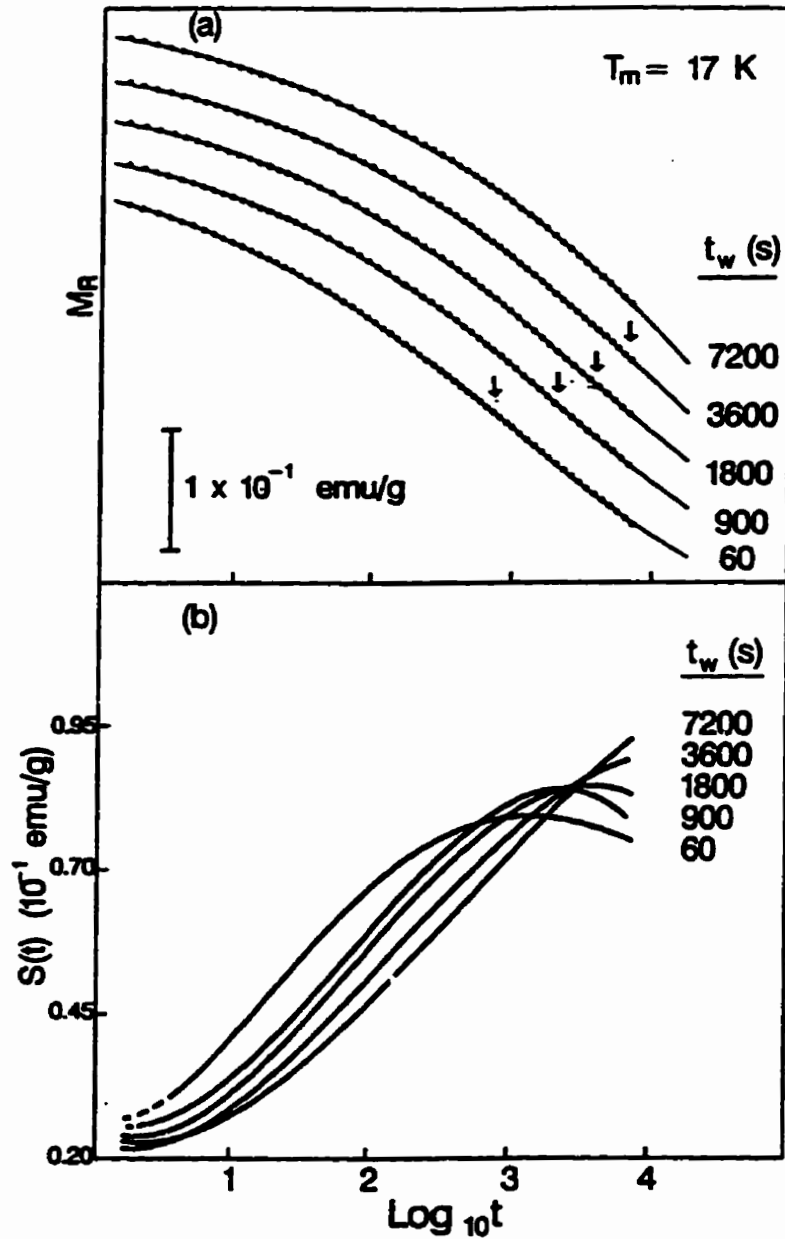


Figure A.2: (a) Wait-time dependence of the thermoremanent relaxation of $\text{Fe}_{0.65}\text{Ni}_{0.24}\text{Cr}_{0.11}$ at $T_m = 17 \text{ K}$. The solid curves are fits to Eq.(4.1) and vertical arrows mark the characteristic times (inflection points) τ . (b) The relaxation rates $S(t)$ for the isotherms in (a).

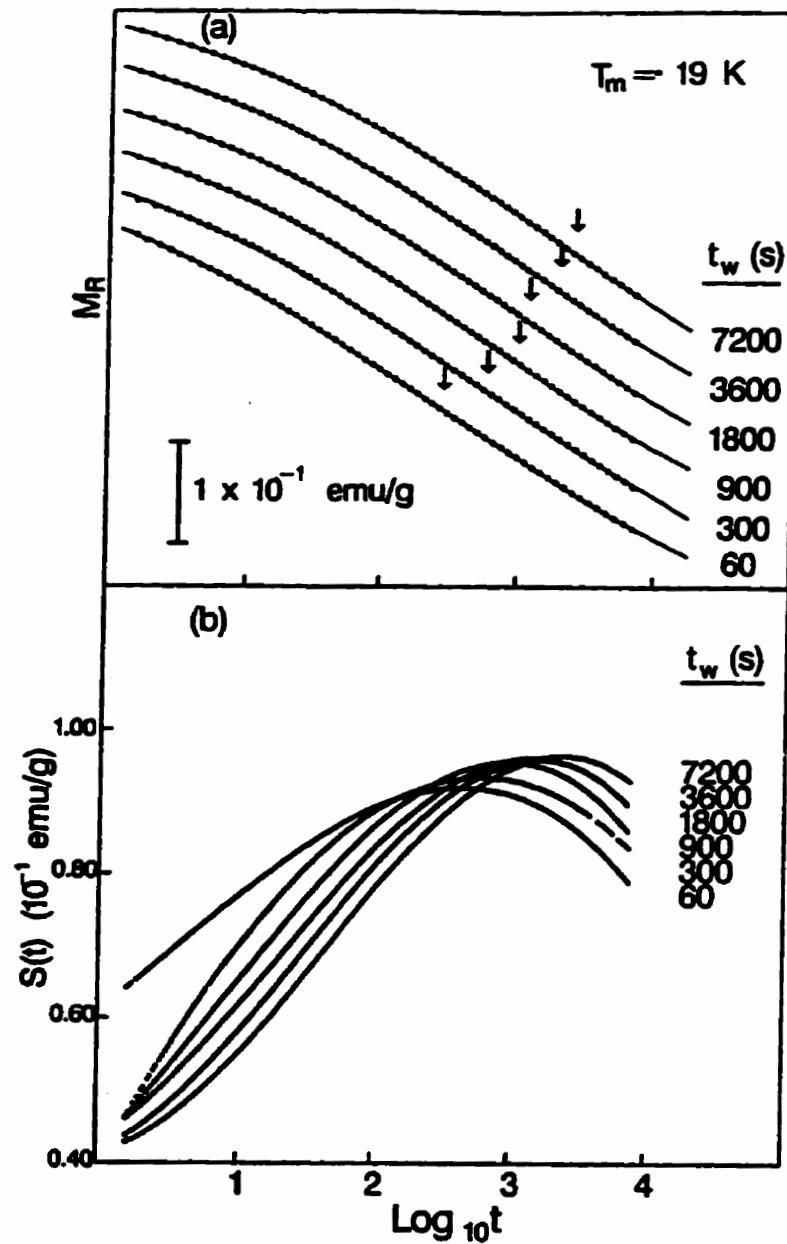


Figure A.3: (a) Wait-time dependence of the thermoremanent relaxation of $\text{Fe}_{0.65}\text{Ni}_{0.24}\text{Cr}_{0.11}$ at $T_m = 19 \text{ K}$. The solid curves are fits to Eq.(4.1) and vertical arrows mark the characteristic times (inflection points) τ . (b) The relaxation rates $S(t)$ for the isotherms in (a).

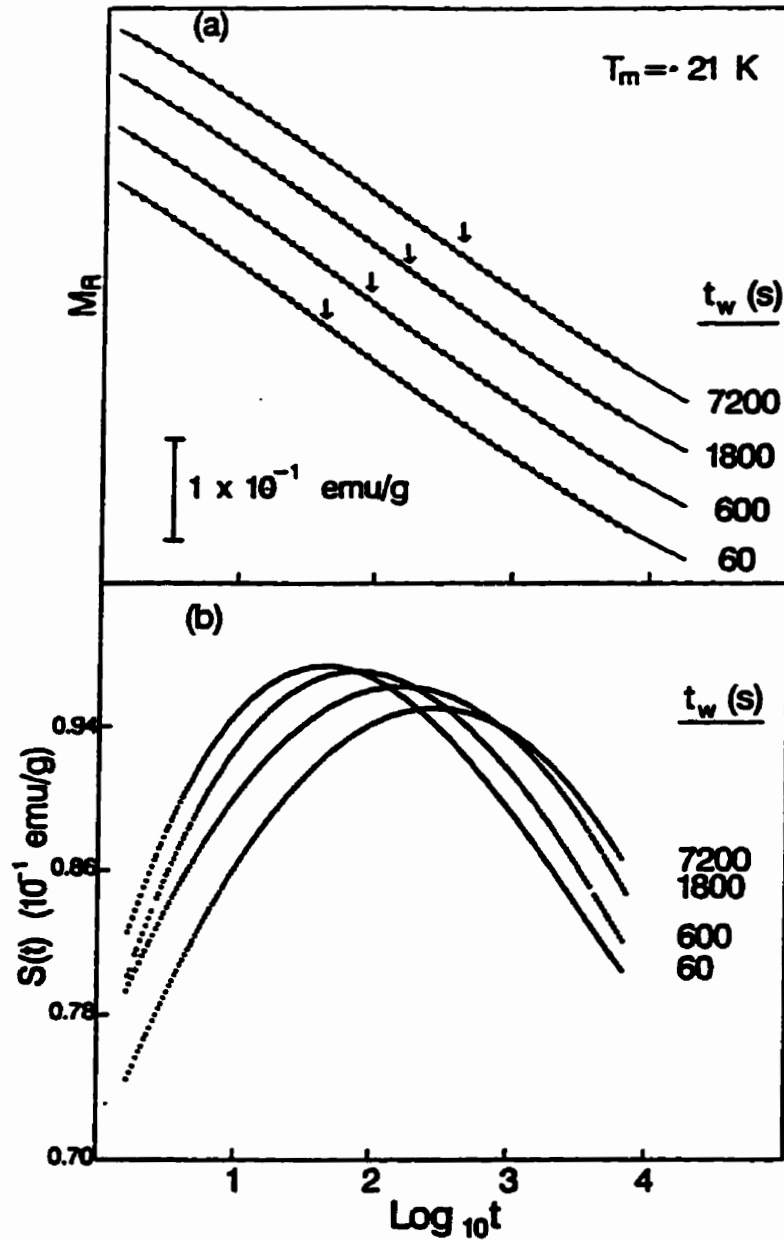


Figure A.4: (a) Wait-time dependence of the thermoremanent relaxation of $\text{Fe}_{0.65}\text{Ni}_{0.24}\text{Cr}_{0.11}$ at $T_m = 21 \text{ K}$. The solid curves are fits to Eq.(4.1) and vertical arrows mark the characteristic times (inflection points) τ . (b) The relaxation rates $S(t)$ for the isotherms in (a).

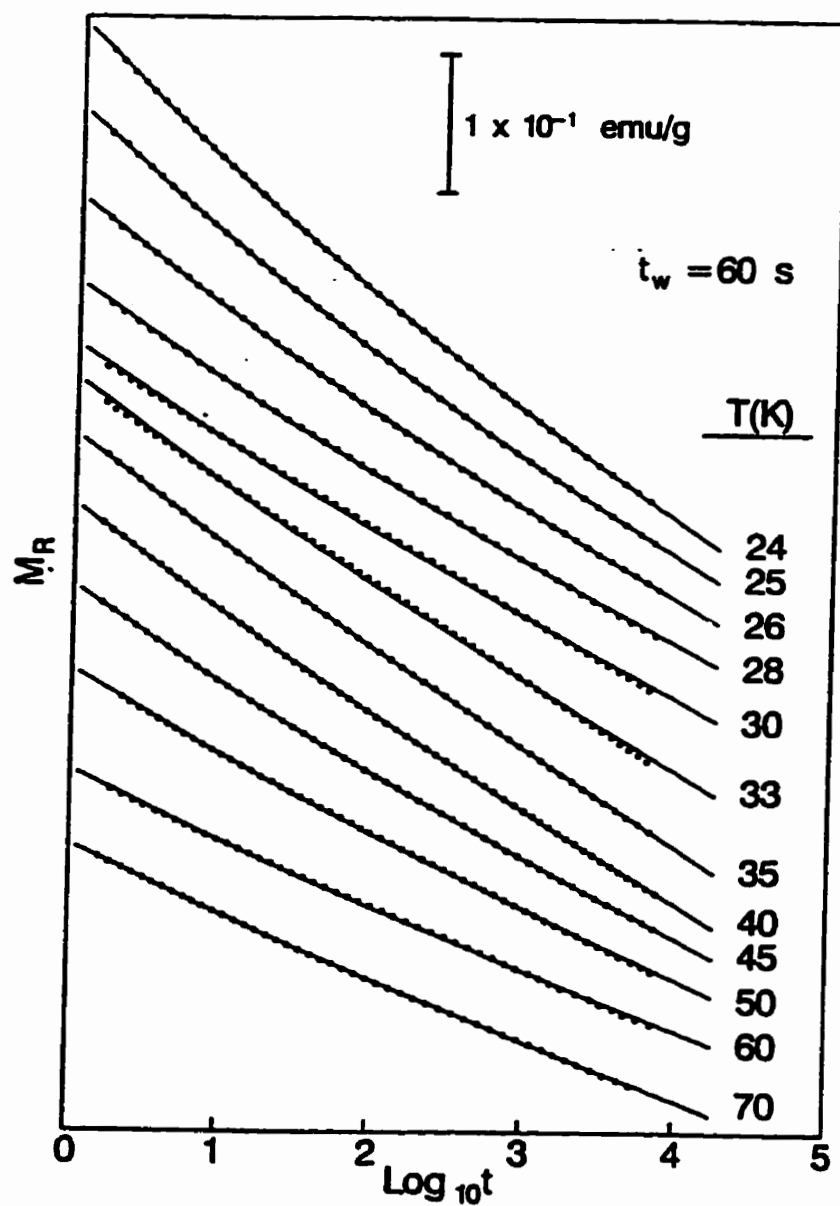


Figure A.5: Thermoremanent relaxation isotherms of $\text{Fe}_{0.65}\text{Ni}_{0.24}\text{Cr}_{0.11}$ for a sequence of temperatures $T_m \geq 24$ K and for a common wait time $t_w = 60$ s. The solid curves are fits to Eq.(4.2).

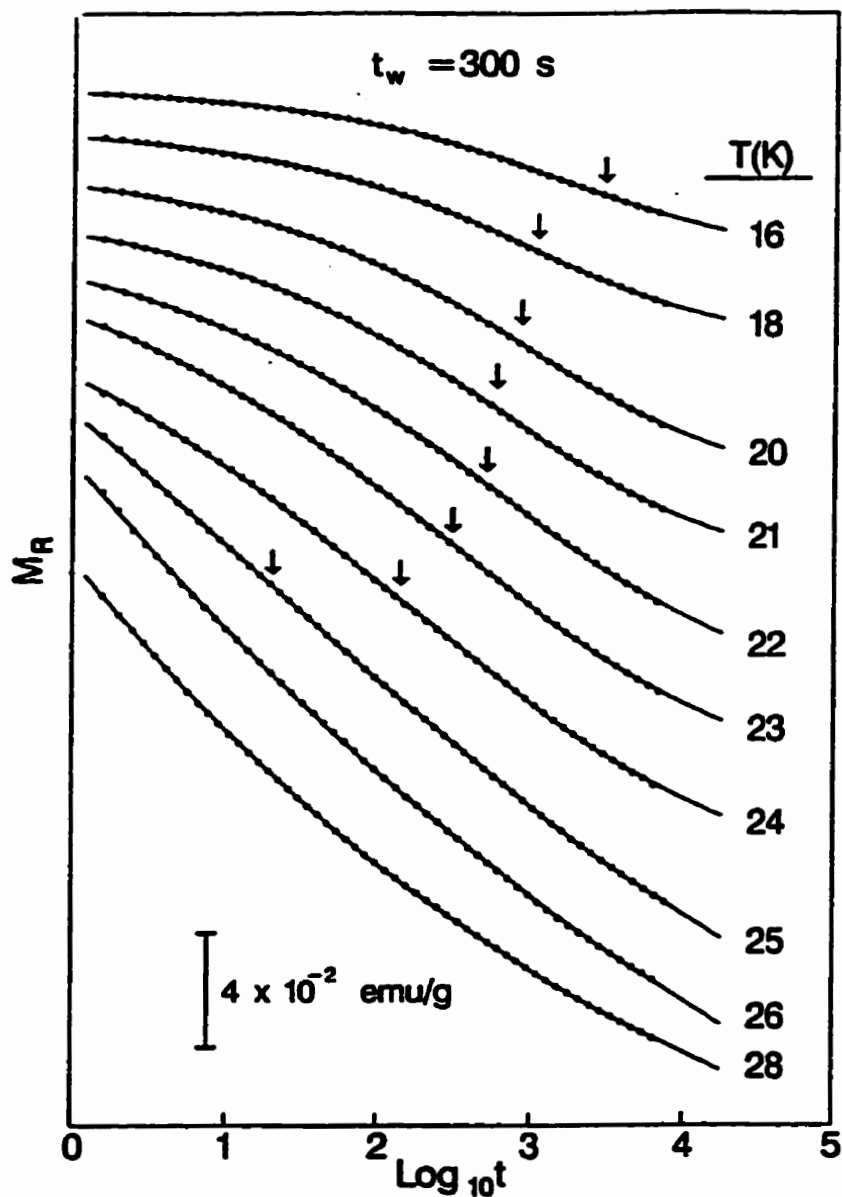


Figure A.6: Thermoremanent relaxation isotherms of $\text{Fe}_{0.65}\text{Ni}_{0.23}\text{Cr}_{0.12}$ for a sequence of temperatures T_m and for a common wait time $t_w = 300$ s. The solid curves are fits to Eq.(4.1) for $T_m \leq 25$ K and to Eq.(4.2) for $T_m \geq 26$ K. The vertical arrows mark the characteristic times (inflection points) τ .

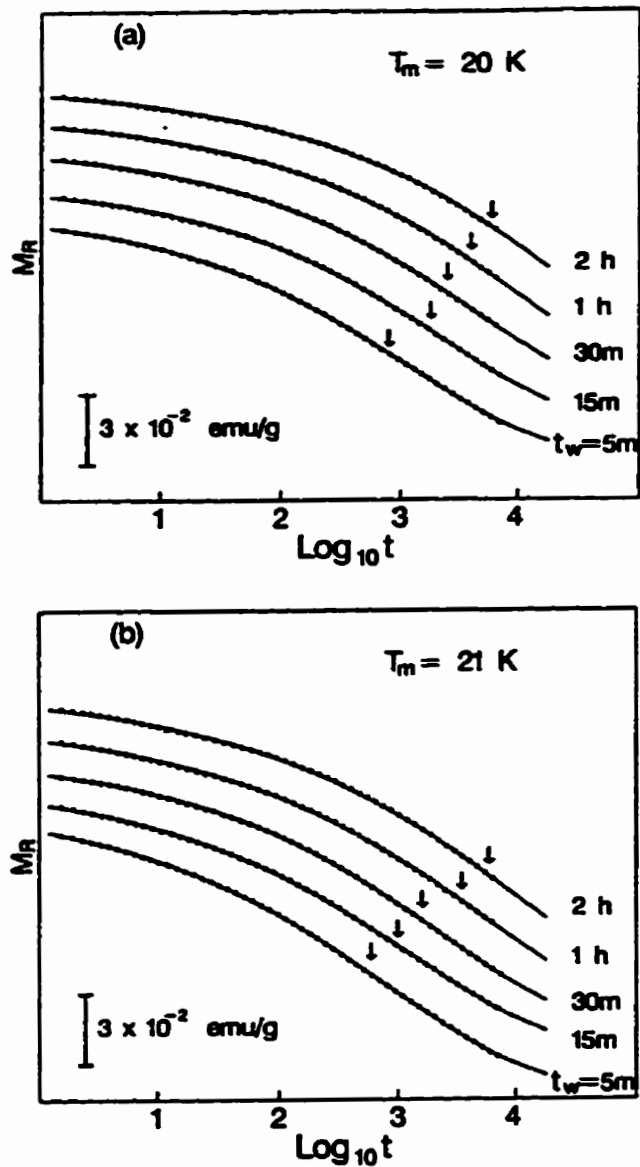


Figure A.7: (a) Wait-time dependence of the thermoremanent relaxation of $\text{Fe}_{0.65}\text{Ni}_{0.23}\text{Cr}_{0.12}$ at $T_m = 20 \text{ K}$. The solid curves are fits to Eq.(4.1) and vertical arrows mark the characteristic times (inflection points) τ . (b) Same as (a) but for temperature $T_m = 21 \text{ K}$.

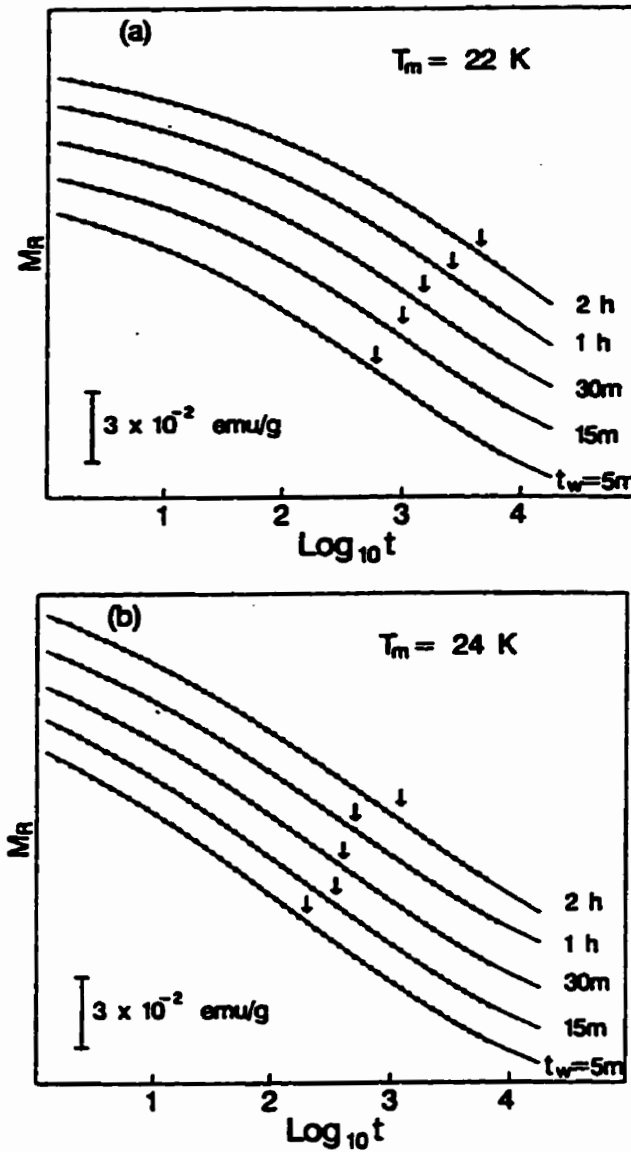


Figure A.8: (a) Wait-time dependence of the thermoremanent relaxation of $\text{Fe}_{0.65}\text{Ni}_{0.23}\text{Cr}_{0.12}$ at $T_m = 22$ K. The solid curves are fits to Eq.(4.1) and vertical arrows mark the characteristic times (inflection points) τ . (b) Same as (a) but for measurement temperature $T_m = 24$ K.

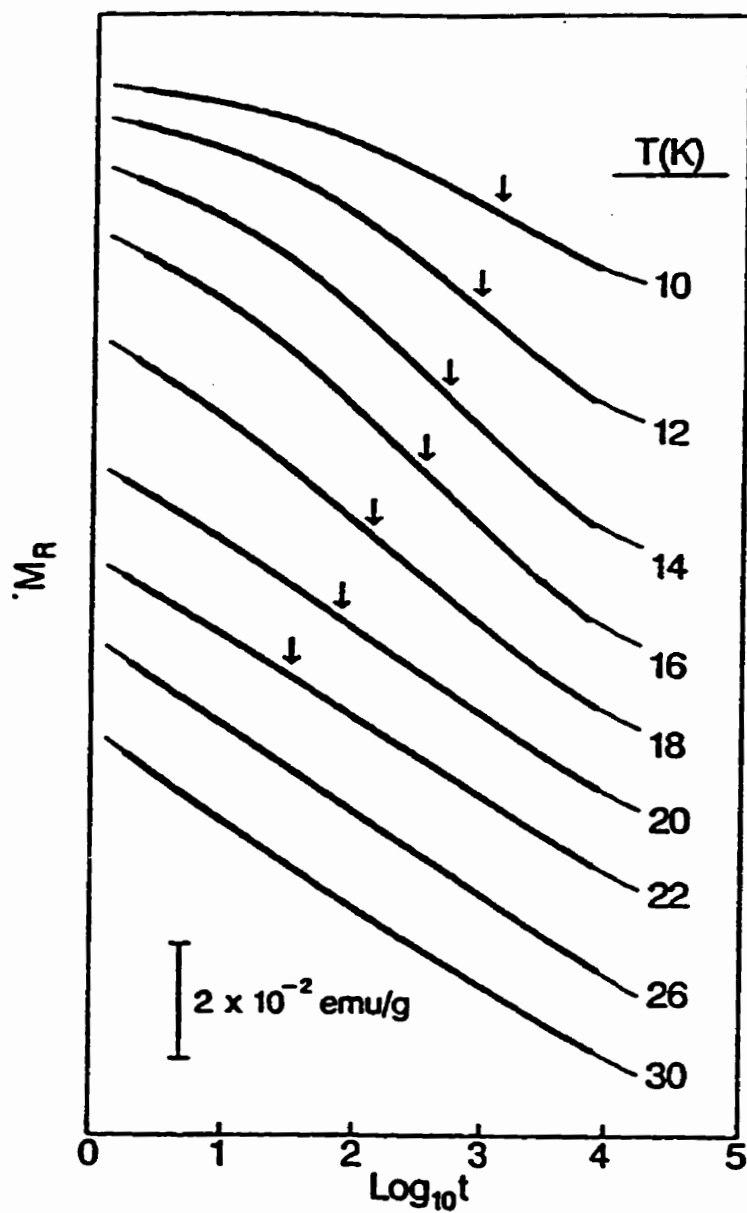


Figure A.9: Thermoremanent relaxation isotherms of $\text{Cr}_{0.79}\text{Fe}_{0.21}$ for a sequence of temperatures T_m and for a common wait time $t_w = 60\text{s}$. The solid curves are fits to Eq.(4.1) for $T_m \leq 22\text{ K}$ and to Eq.(4.2) for $T_m \geq 26\text{ K}$. The vertical arrows mark the characteristic times (inflection points) τ .

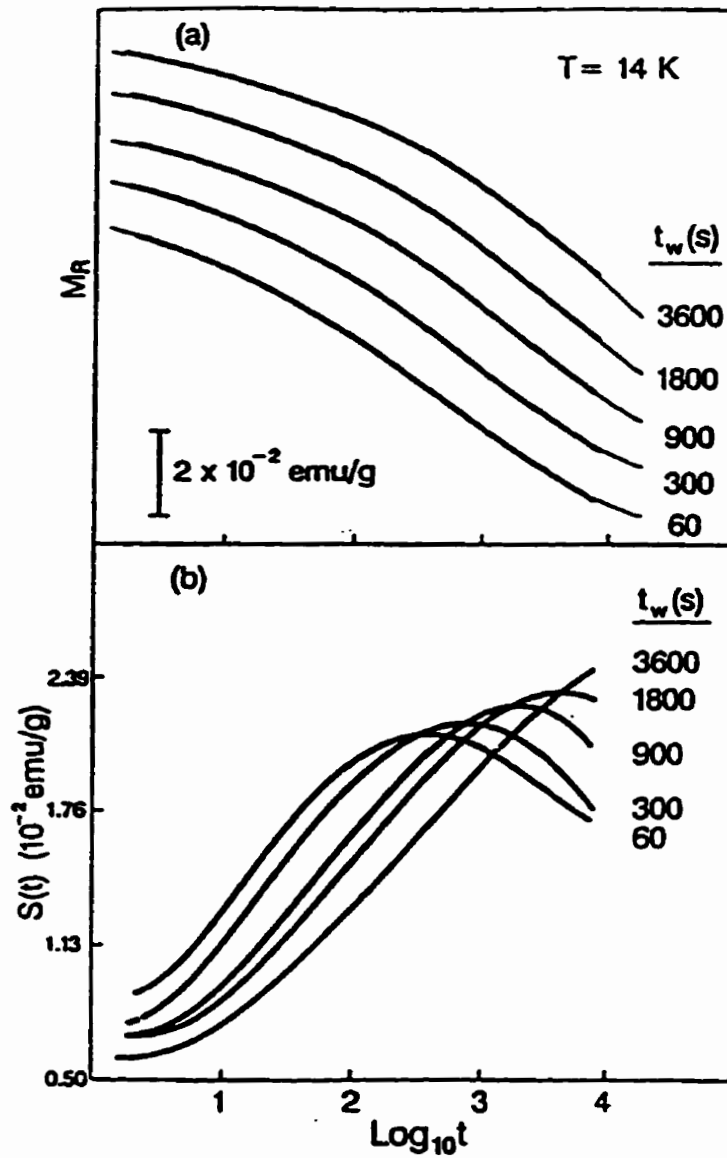


Figure A.10: (a) Wait-time dependence of the thermoremanent relaxation of $\text{Cr}_{0.79}\text{Fe}_{0.21}$ at $T_m = 14 \text{ K}$. The solid curves are fits to Eq.(4.1) and vertical arrows mark the characteristic times (inflection points) τ . (b) The relaxation rates $S(t)$ for the isotherms in (a).

Appendix B

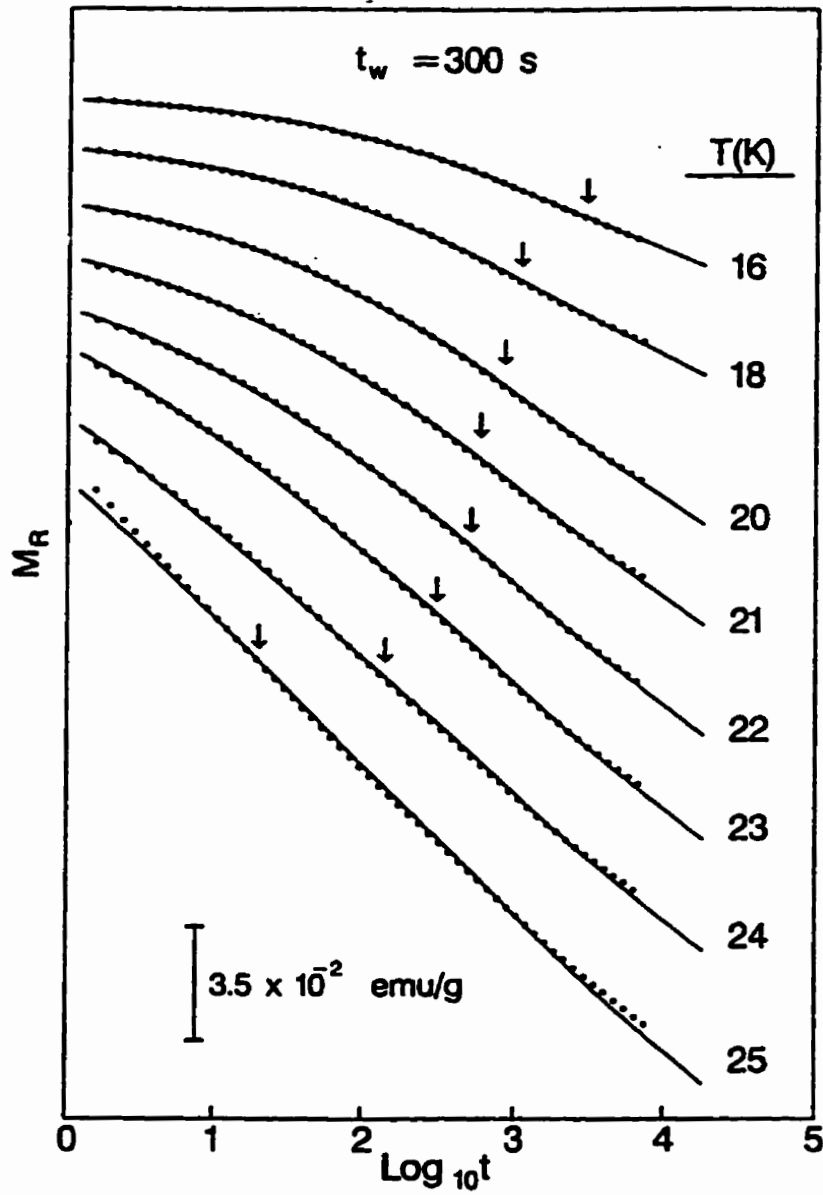


Figure B.1: Random Trap Model fits of Eq.(4.18)(solid curves) to thermoremanent relaxation isotherms of $\text{Fe}_{0.65}\text{Ni}_{0.23}\text{Cr}_{0.12}$ for a sequence of temperatures $T_m \leq 25 \text{ K}$ and for a common wait time $t_w = 300 \text{ s}$. The vertical arrows mark the characteristic times (inflection points) τ .

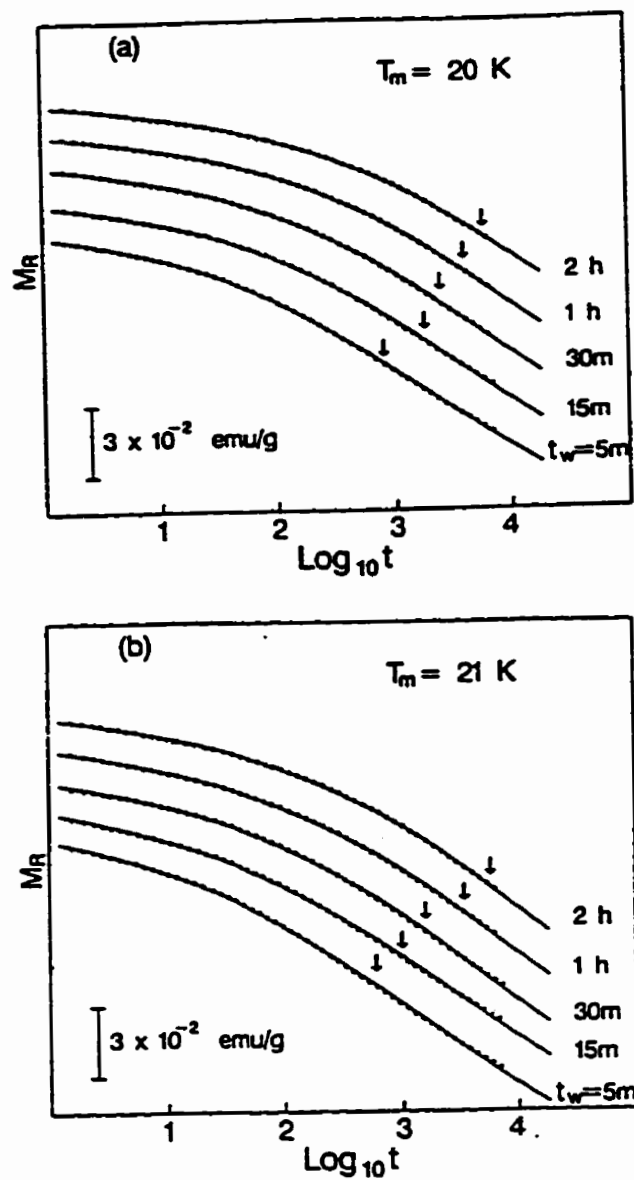


Figure B.2: (a) Random Trap Model fits of Eq.(4.18) (solid curves) to the wait-time dependence of the thermoremanent relaxation of $\text{Fe}_{0.65}\text{Ni}_{0.23}\text{Cr}_{0.12}$ at $T_m = 20$ K. The vertical arrows mark the characteristic times (inflection points) τ . (b) Same sample and analysis as in (a) but for $T_m = 21$ K.

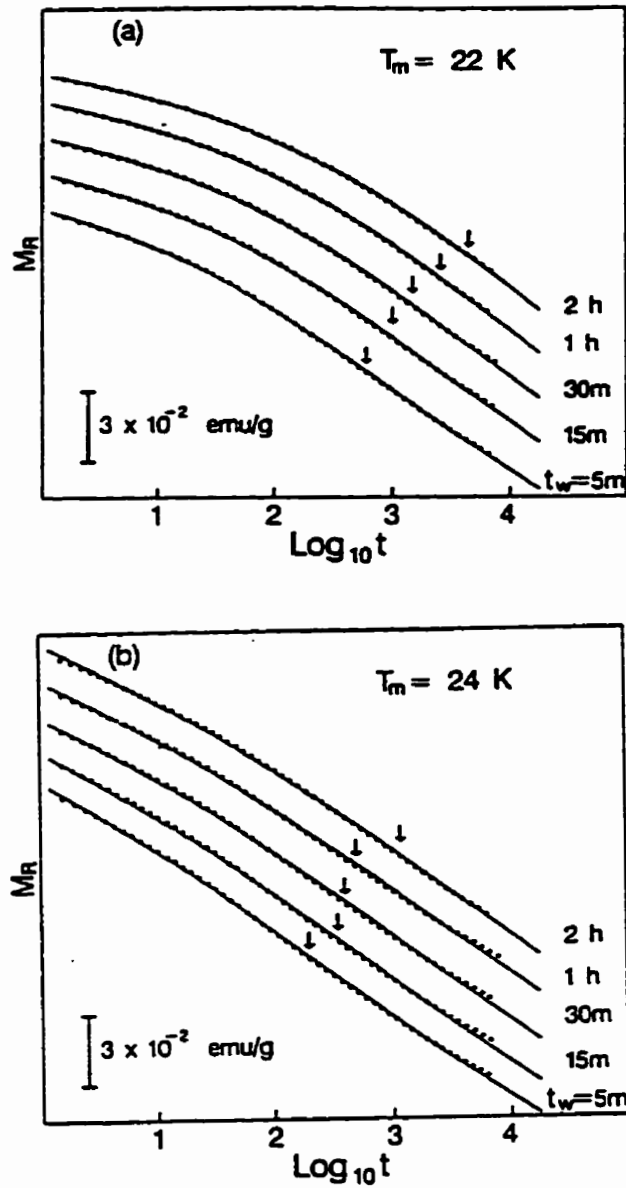


Figure B.3: (a) Random Trap Model fits of Eq.(4.18) (solid curves) to the wait-time-dependence of the thermoremanent relaxation of $\text{Fe}_{0.65}\text{Ni}_{0.23}\text{Cr}_{0.12}$ at $T_m = 22 \text{ K}$. The vertical arrows mark the characteristic times (inflection points) τ . (b) Same sample and analysis as in (a) but for $T_m = 24 \text{ K}$.

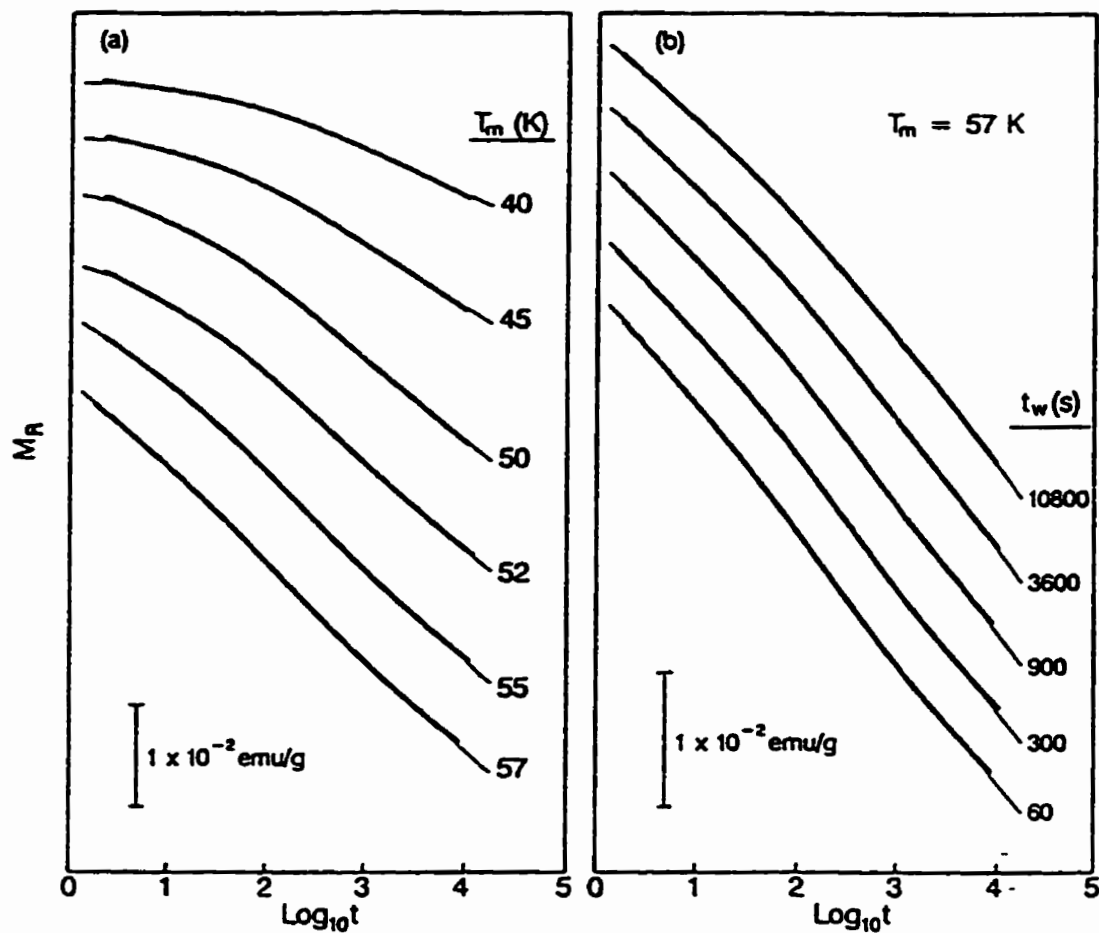


Figure B.4: (a) Random Trap Model fits of Eq.(4.18)(solid curves) to thermoremanent relaxation isotherms of $(\text{Fe}_{0.65}\text{Ni}_{0.35})_{0.882}\text{Mn}_{0.118}$ for a sequence of temperatures $T_m \leq 60$ K and for a common wait time $t_w = 60$ s. (b) Random Trap Model fits of Eq.(4.18)(solid curves) to the wait-time dependence of the thermoremanent relaxation of $(\text{Fe}_{0.65}\text{Ni}_{0.35})_{0.882}\text{Mn}_{0.118}$ at $T_m = 57$ K.

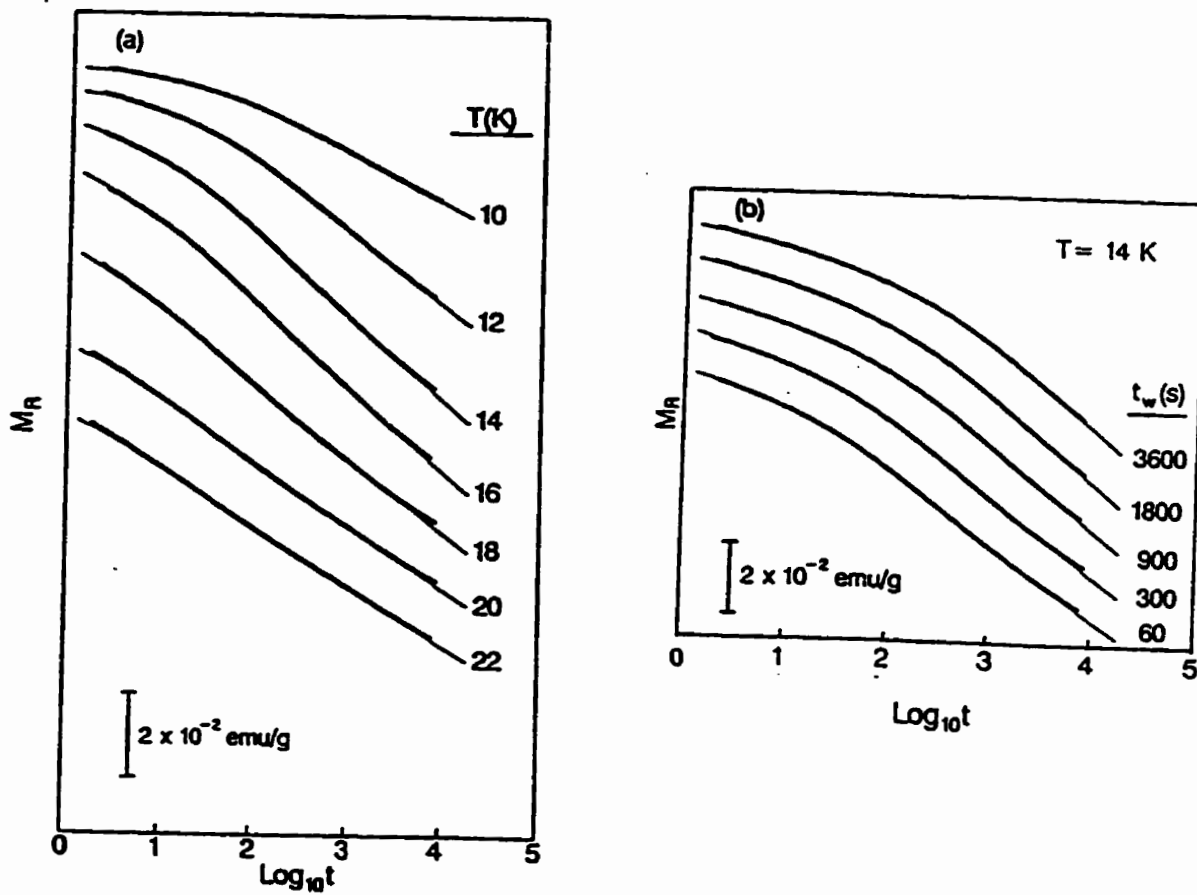


Figure B.5: (a) Random Trap Model fits of Eq.(4.18)(solid curves) to thermoremanent relaxation isotherms of $\text{Cr}_{0.79}\text{Fe}_{0.21}$ for a sequence of temperatures $T_m \leq 22$ K and for a common wait time $t_w = 60$ s. (b) Random Trap Model fits of Eq.(4.18) (solid curves) to the wait-time dependence of the thermoremanent relaxation of $\text{Cr}_{0.79}\text{Fe}_{0.21}$ at $T_m = 14$ K.

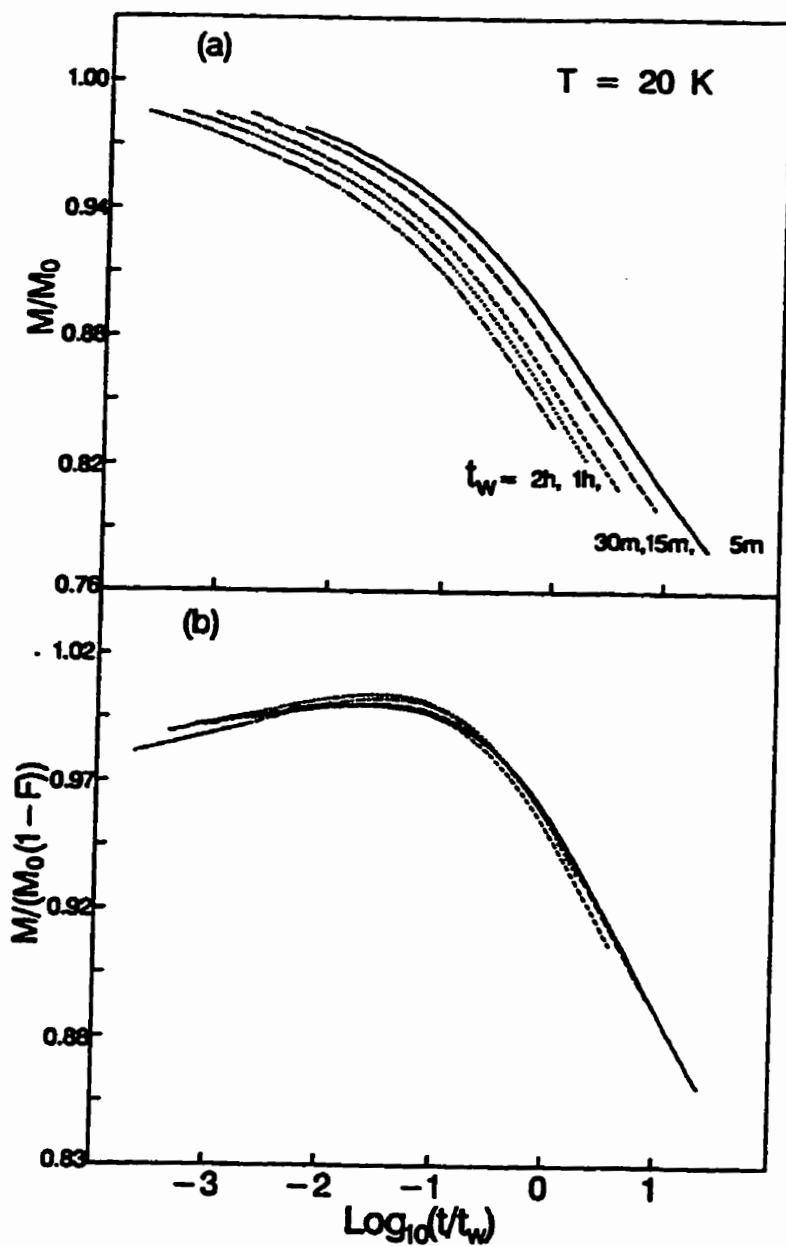


Figure B.6: (a) Scaling of $\text{Fe}_{0.65}\text{Ni}_{0.23}\text{Cr}_{0.12}$ at $T_m = 20 \text{ K}$ for different wait times using only m_0 . m_0 is chosen by the empirical stretched exponential model. (b) Scaling of $\text{Fe}_{0.65}\text{Ni}_{0.23}\text{Cr}_{0.12}$ at $T_m = 20 \text{ K}$ for different wait times using Eq.(2.112). $m_0 = 0.443, 0.448, 0.441, 0.438$ and 0.433 emu/g for $t_w = 300\text{s}, 900\text{s}, 1800\text{s}, 3600\text{s}, 7200\text{s}$ respectively.

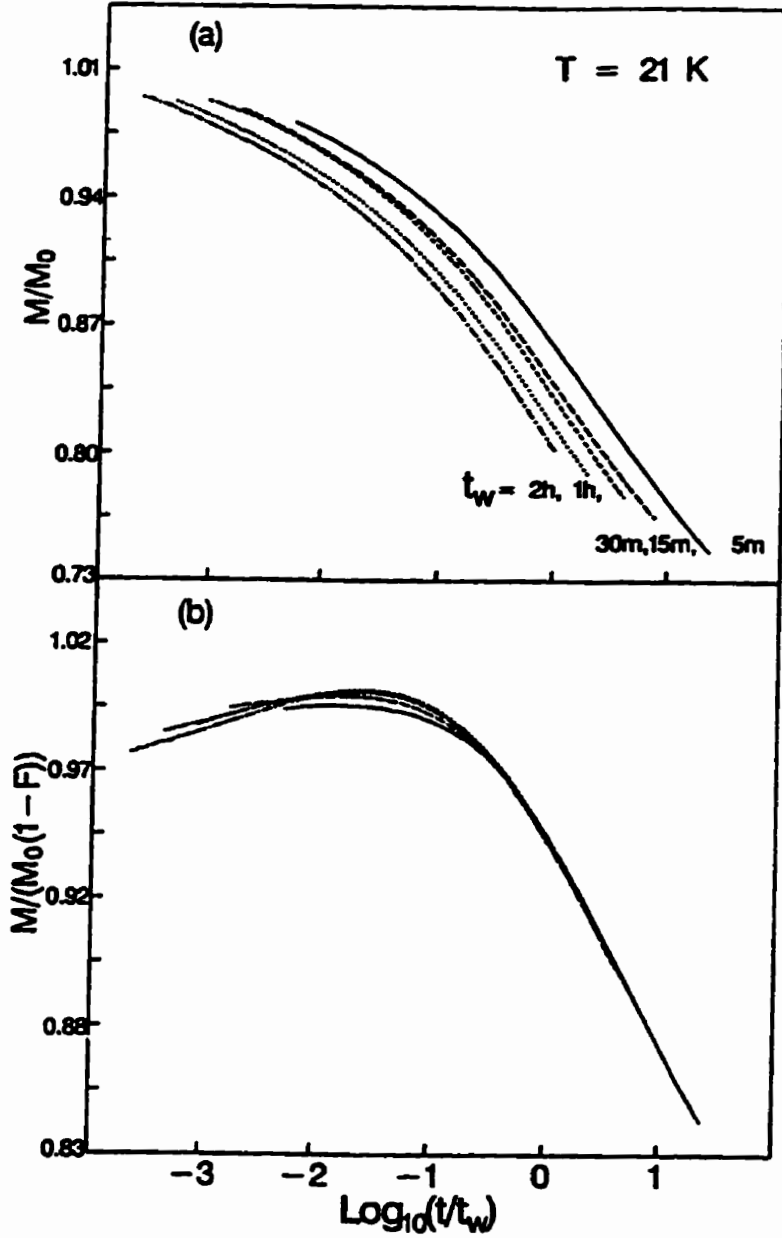


Figure B.7: (a) Scaling of $\text{Fe}_{0.65}\text{Ni}_{0.23}\text{Cr}_{0.12}$ at $T_m = 21 \text{ K}$ for different wait times using only m_0 . m_0 is chosen by the empirical stretched exponential model. (b) Scaling of $\text{Fe}_{0.65}\text{Ni}_{0.23}\text{Cr}_{0.12}$ at $T_m = 21 \text{ K}$ for different wait times using Eq.(2.112). $m_0 = 0.458, 0.443, 0.454, 0.452$ and 0.455 emu/g for $t_w = 300\text{s}, 900\text{s}, 1800\text{s}, 3600\text{s}, 7200\text{s}$ respectively.

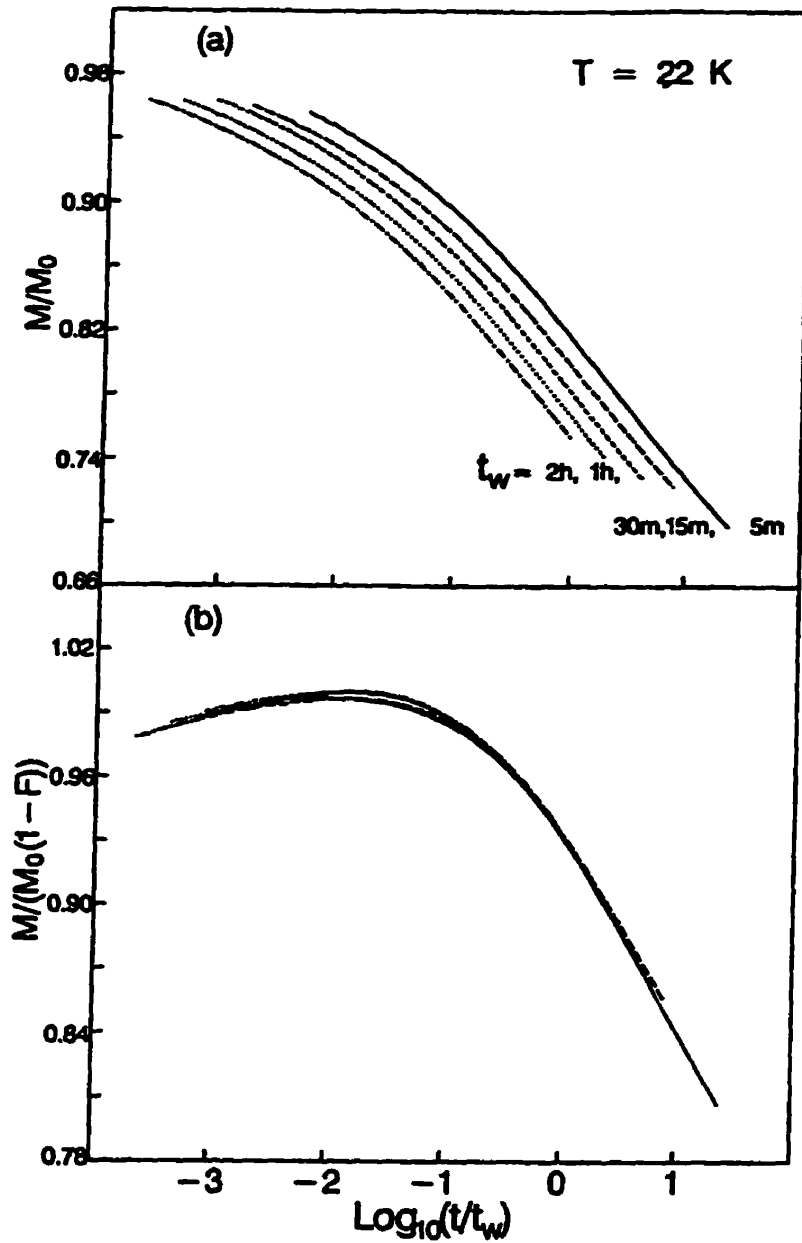


Figure B.8: (a) Scaling of $\text{Fe}_{0.65}\text{Ni}_{0.23}\text{Cr}_{0.12}$ at $T_m = 22 \text{ K}$ for different wait times using only m_0 . m_0 is chosen by the empirical stretched exponential model. (b) Scaling of $\text{Fe}_{0.65}\text{Ni}_{0.23}\text{Cr}_{0.12}$ at $T_m = 22 \text{ K}$ for different wait times using Eq.(2.112). $m_0 = 0.465, 0.482, 0.474, 0.479$ and 0.475 emu/g for $t_w = 300\text{s}, 900\text{s}, 1800\text{s}, 3600\text{s}, 7200\text{s}$ respectively.

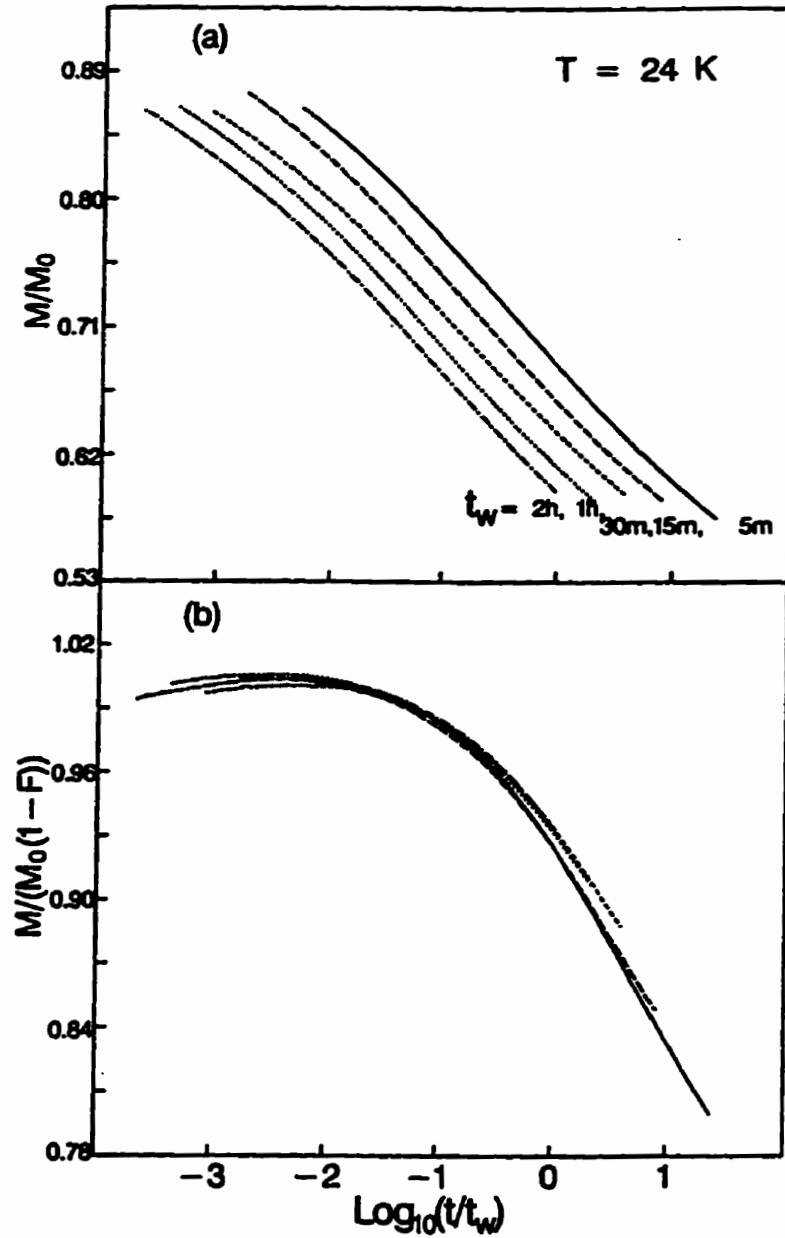


Figure B.9: (a) Scaling of $\text{Fe}_{0.65}\text{Ni}_{0.23}\text{Cr}_{0.12}$ at $T_m = 24 \text{ K}$ for different wait times using only m_0 . m_0 is chosen by the empirical stretched exponential model. (b) Scaling of $\text{Fe}_{0.65}\text{Ni}_{0.23}\text{Cr}_{0.12}$ at $T_m = 24 \text{ K}$ for different wait times using Eq.(2.112). m_0 0.509, 0.516, 0.528, 0.500 and 0.514 emu/g for $t_w = 300\text{s}$, 900s, 1800s, 3600s, and 7200s respectively.

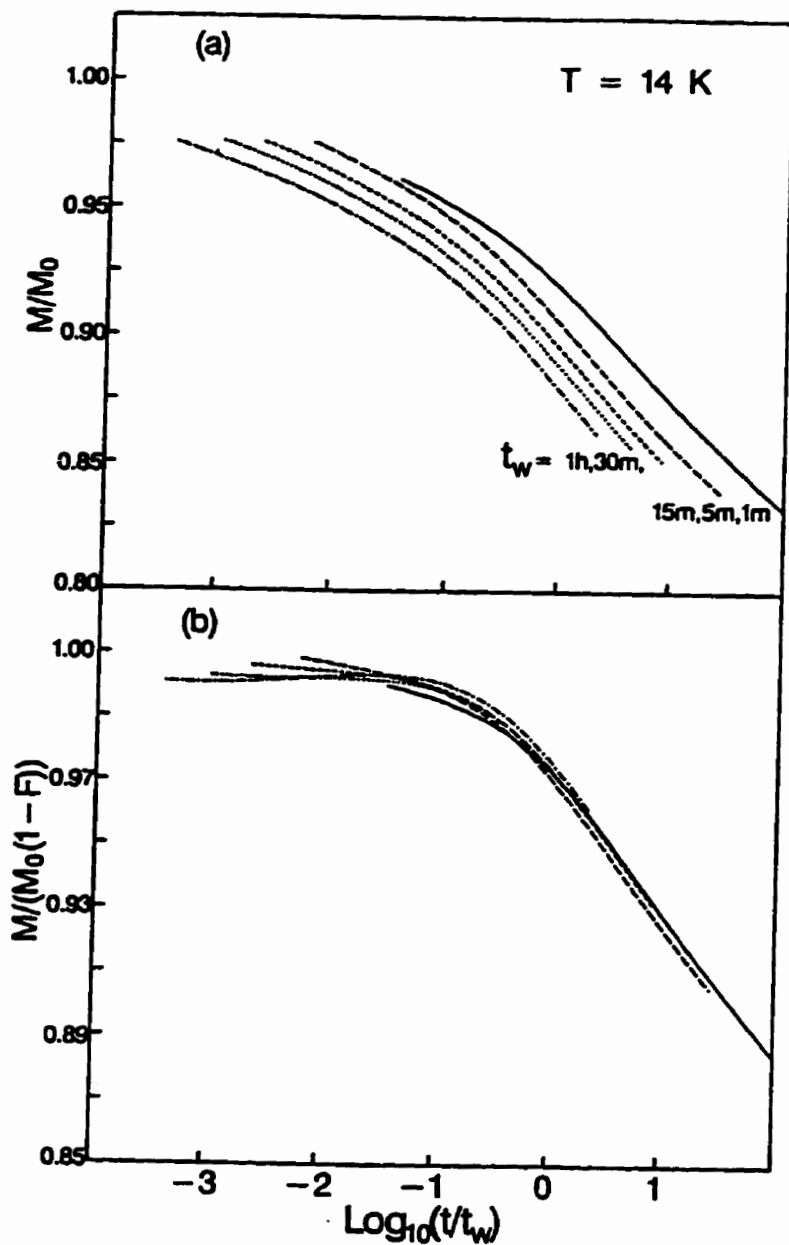


Figure B.10: (a) Scaling of $\text{Cr}_{0.79}\text{Fe}_{0.21}$ at $T_m = 14 \text{ K}$ for different wait times using only m_0 . m_0 is chosen by the empirical stretched exponential model. (b) Scaling of $\text{Cr}_{0.79}\text{Fe}_{0.21}$ at $T_m = 14 \text{ K}$ for different wait times using Eq.(2.112). m_0 0.422, 0.415, 0.430, 0.445 and 0.429 emu/g for $t_w = 60\text{s}$, 300s, 900s, 1800s, and 3600s respectively.

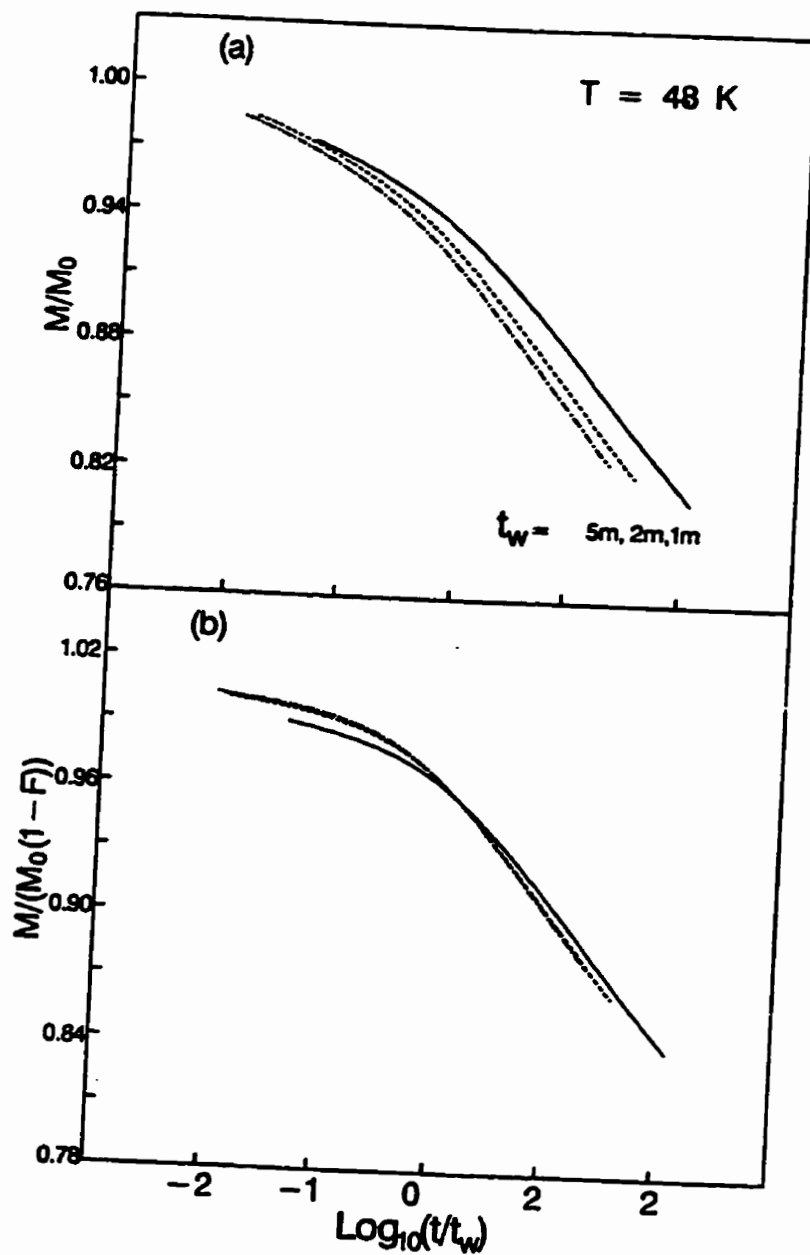


Figure B.11: (a) Scaling of $(\text{Fe}_{0.65}\text{Ni}_{0.35})_{0.882}\text{Mn}_{0.118}$ at $T_m = 48 \text{ K}$ for different wait times using only m_0 . m_0 is chosen by the empirical stretched exponential model. (b) Scaling of $(\text{Fe}_{0.65}\text{Ni}_{0.35})_{0.882}\text{Mn}_{0.118}$ at $T_m = 48 \text{ K}$ for different wait times using Eq.(2.112) $m_0 = 0.143, 0.142,$ and 0.142 emu/g for $t_w = 60\text{s}, 180\text{s},$ and 300s respectively.

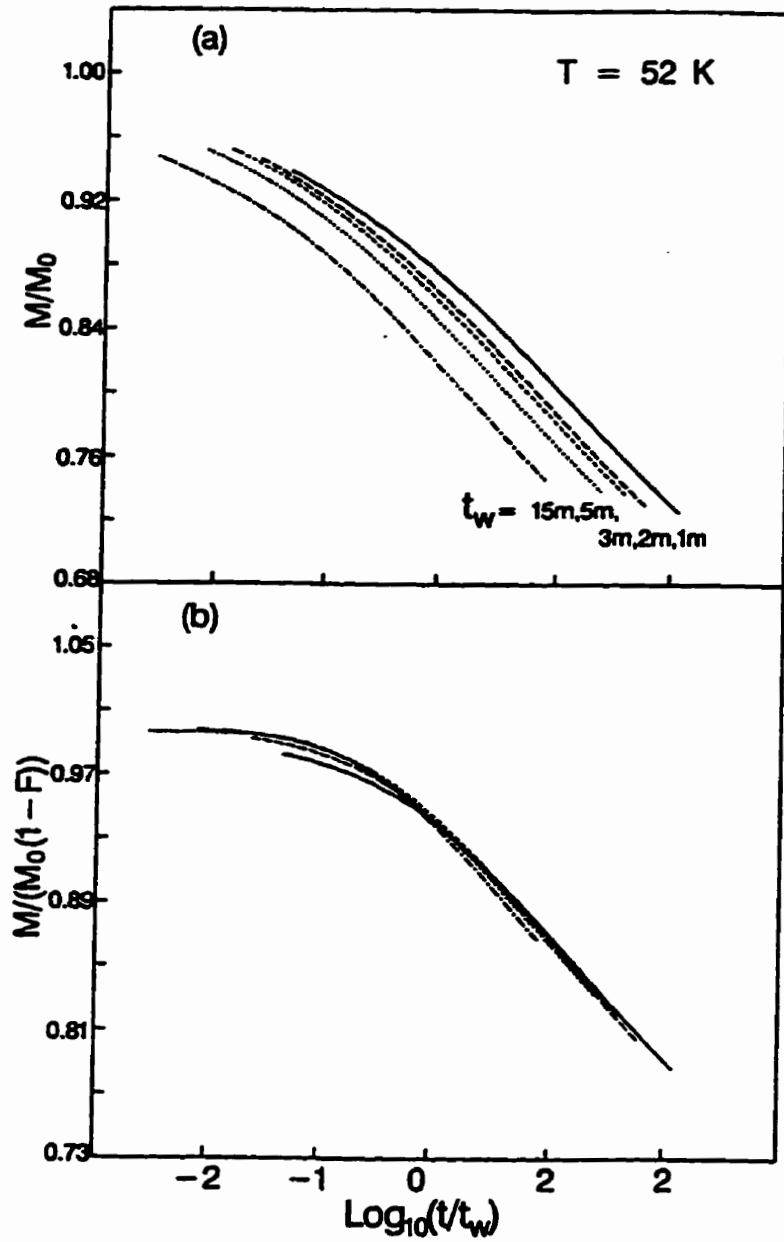


Figure B.12: (a) Scaling of $(\text{Fe}_{0.65}\text{Ni}_{0.35})_{0.882}\text{Mn}_{0.118}$ at $T_m = 52 \text{ K}$ for different wait times using only m_0 . m_0 is chosen by the empirical stretched exponential model. (b) Scaling of $(\text{Fe}_{0.65}\text{Ni}_{0.35})_{0.882}\text{Mn}_{0.118}$ at $T_m = 52 \text{ K}$ for different wait times using Eq.(2.112). $m_0 = 0.147, 0.145, 0.145, 0.145$ and 0.146 emu/g for $t_w = 60\text{s}, 120\text{s}, 180\text{s}, 300\text{s}$ and 900s respectively.

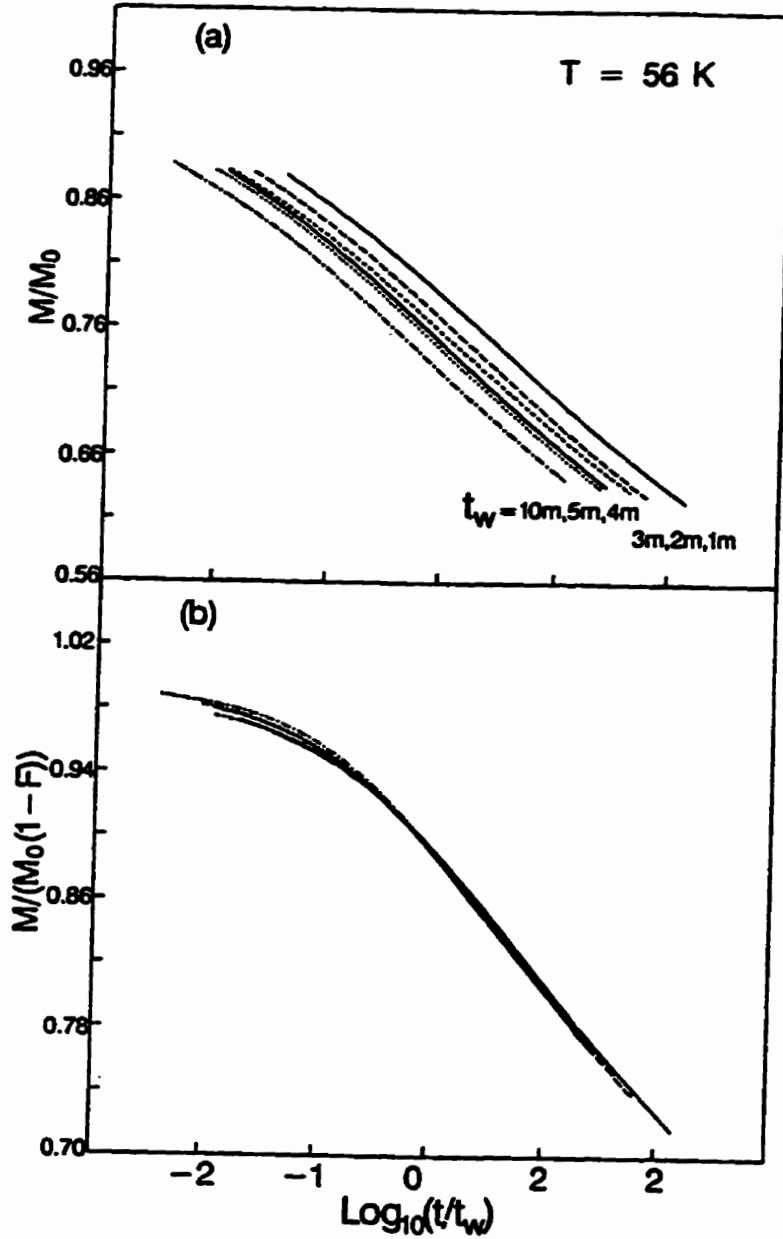


Figure B.13: (a) Scaling of $(\text{Fe}_{0.65}\text{Ni}_{0.35})_{0.882}\text{Mn}_{0.118}$ at $T_m = 56 \text{ K}$ for different wait times using only m_0 . m_0 is chosen by the empirical stretched exponential model. (b) Scaling of $(\text{Fe}_{0.65}\text{Ni}_{0.35})_{0.882}\text{Mn}_{0.118}$ at $T_m = 56 \text{ K}$ for different wait times only Eq.(2.112). m_0 0.155, 0.153, 0.156, 0.152, 0.152 and 0.152 emu/g for $t_w = 60\text{s}, 120\text{s}, 180\text{s}, 240\text{s}, 300\text{s}$ and 600s respectively.

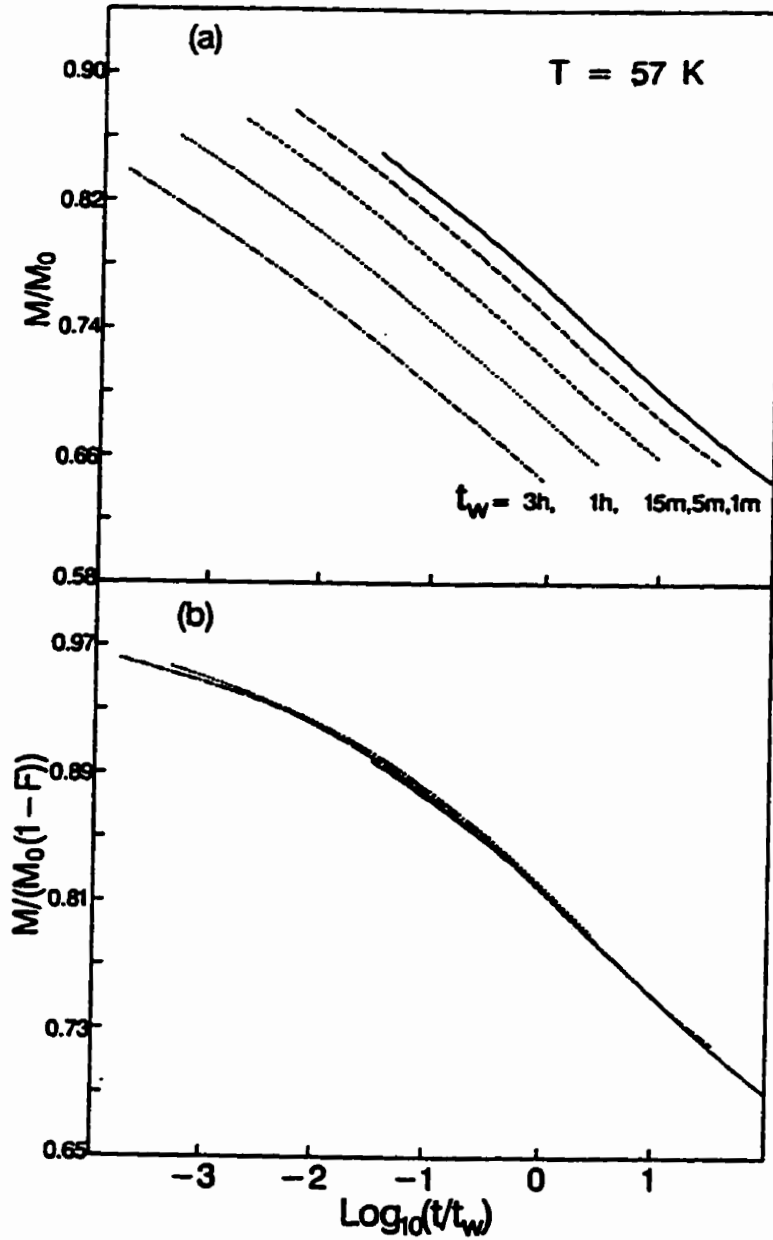


Figure B.14: (a) Scaling of $(\text{Fe}_{0.65}\text{Ni}_{0.35})_{0.882}\text{Mn}_{0.118}$ at $T_m = 57 \text{ K}$ for different wait times using only m_0 . m_0 is chosen by the empirical stretched exponential model. (b) Scaling of $(\text{Fe}_{0.65}\text{Ni}_{0.35})_{0.882}\text{Mn}_{0.118}$ at $T_m = 57 \text{ K}$ for different wait times using Eq.(2.112). $m_0 = 0.145, 0.144, 0.143, 0.142,$ and 0.140 emu/g for $t_w = 60\text{s}, 300\text{s}, 900\text{s}, 3600\text{s},$ and 10800s respectively.

Appendix C

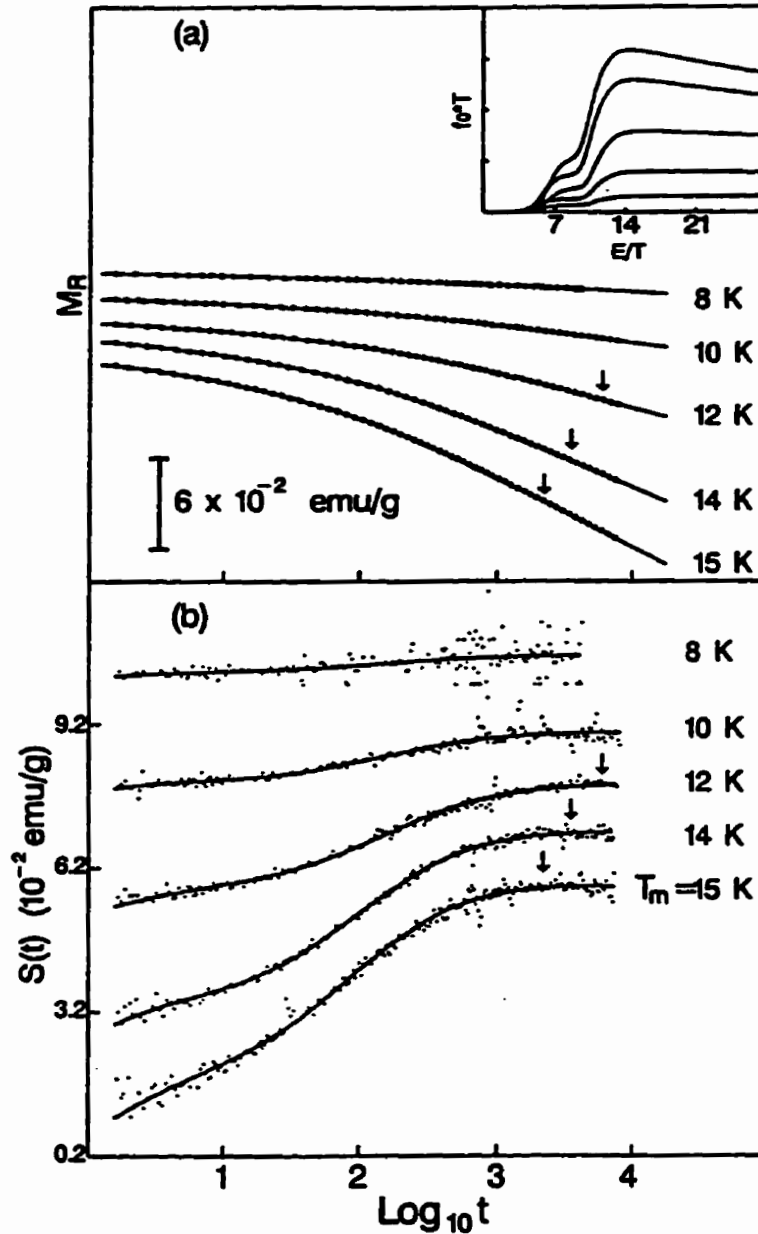


Figure C.1: (a) EDM fits of Eq.(4.23)(solid curves) to thermoremanent relaxation isotherms of $\text{Fe}_{0.65}\text{Ni}_{0.21}\text{Cr}_{0.11}$ for a sequence of temperatures $T_m = 8, 10, 12, 14,$ and 15 K and for a common wait time $t_w = 60s$. The vertical arrows mark the characteristic times (inflection points) τ . (b) Relaxation rates for the data (dots) and the theoretical function (solid curves). The insert shows the final "aged" distribution of activation energies (just after the field change). The peaks from bottom to top correspond to increasing temperature.

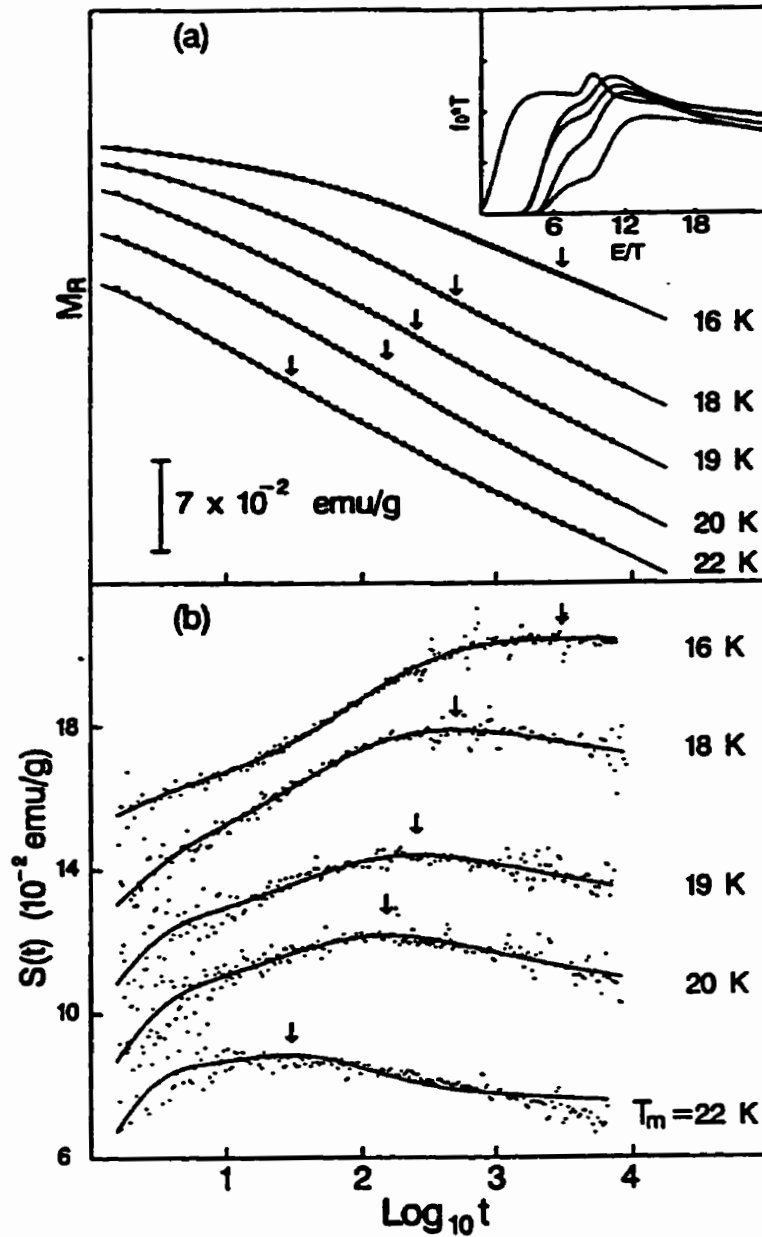


Figure C.2: (a) EDM fits of Eq.(4.23)(solid curves) to thermoremanent relaxation isotherms of $\text{Fe}_{0.65}\text{Ni}_{0.24}\text{Cr}_{0.11}$ for a sequence of temperatures $T_m = 16, 18, 19, 20,$ and 22 K and for a common wait time $t_w = 60\text{s}$. The vertical arrows mark the characteristic times (inflection points) τ . (b) Relaxation rates for the data (dots) and the theoretical function (solid curves). The insert shows the final "aged" distribution of activation energies (just after the field change). The peaks from bottom to top correspond to increasing temperature.

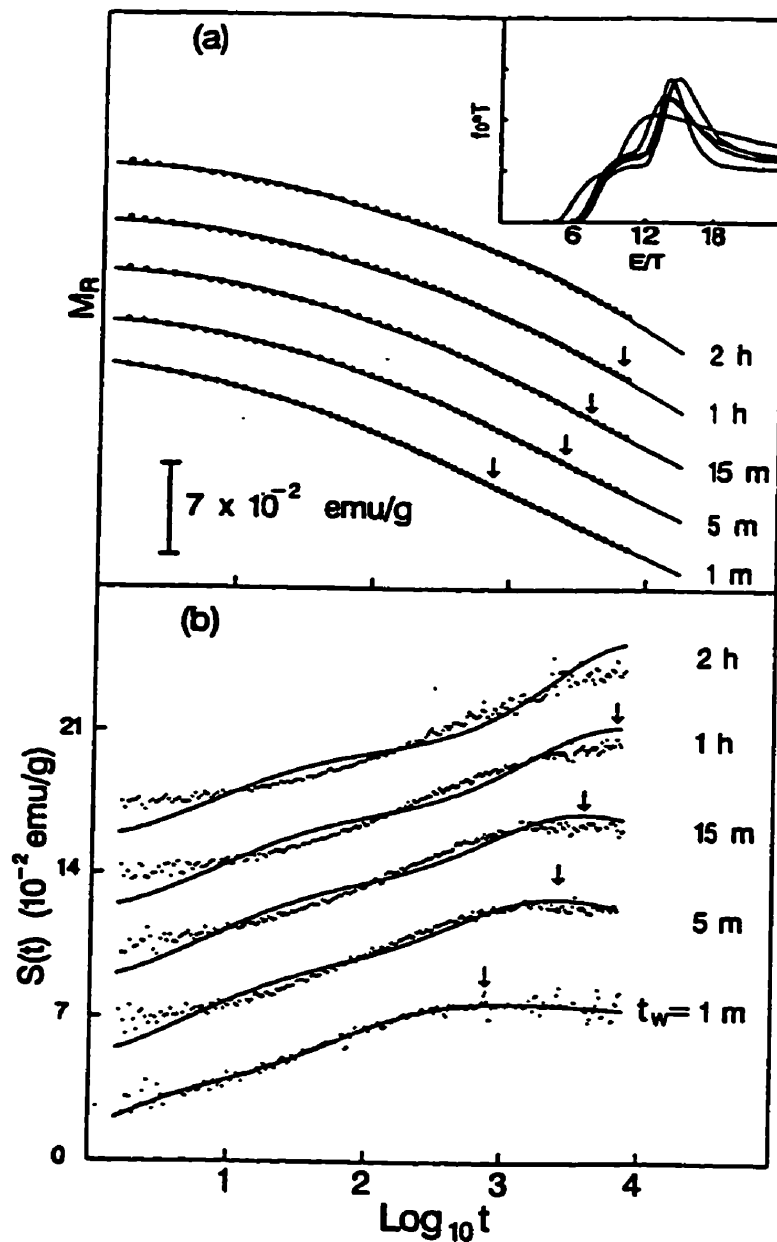


Figure C.3: (a) EDM fits of Eq.(4.23)(solid curves) to the wait-time dependence of the thermoremanent relaxation of $\text{Fe}_{0.65}\text{Ni}_{0.24}\text{Cr}_{0.11}$ at $T_m = 17$ K. The vertical arrows mark the characteristic times (inflection points) τ . (b) Relaxation rates for the data (dots) and the theoretical function (solid curves). The insert shows the final "aged" distribution of activation energies (just after the field change). The peaks from left to right correspond to increasing wait time.

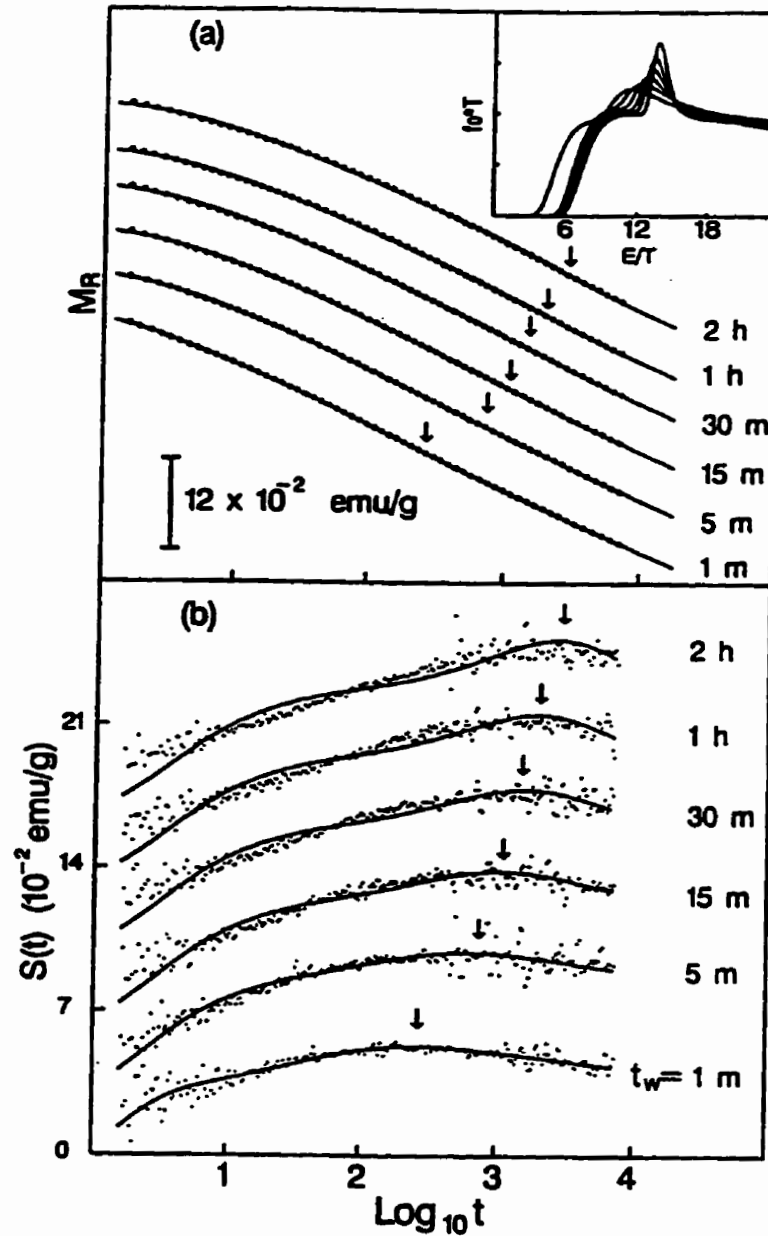


Figure C.4: (a) EDM fits of Eq.(4.23)(solid curves) to the wait-time dependence of the thermoremanent relaxation of $\text{Fe}_{0.65}\text{Ni}_{0.24}\text{Cr}_{0.11}$ at $T_m = 19$ K. The vertical arrows mark the characteristic times (inflection points) τ . (b) Relaxation rates for the data (dots) and the theoretical function (solid curves). The insert shows the final "aged" distribution of activation energies (just after the field change). The peaks from left to right correspond to increasing wait time.

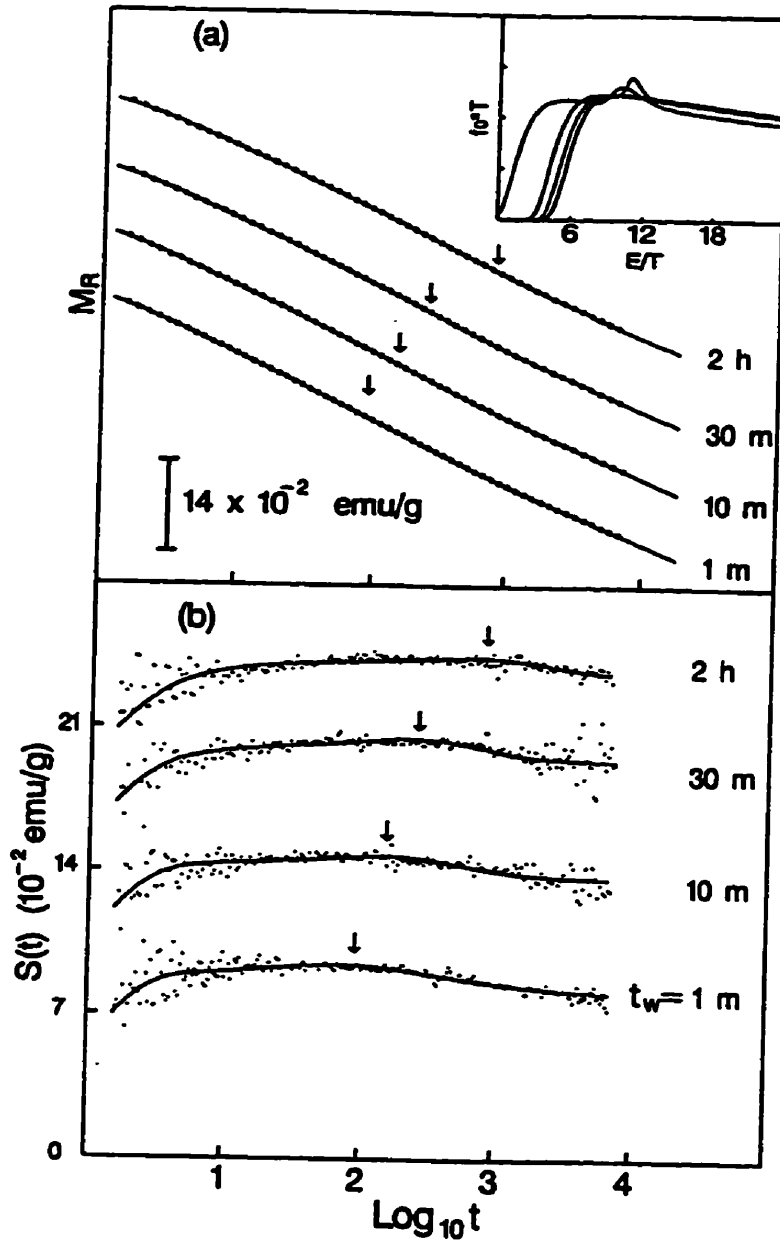


Figure C.5: (a) EDM fits of Eq.(4.23)(solid curves) to the wait-time dependence of the thermoremanent relaxation of $\text{Fe}_{0.65}\text{Ni}_{0.24}\text{Cr}_{0.11}$ at $T_m = 21$ K. The vertical arrows mark the characteristic times (inflection points) τ . (b) Relaxation rates for the data (dots) and the theoretical function (solid curves). The insert shows the final "aged" distribution of activation energies (just after the field change). The peaks from left to right correspond to increasing wait time.

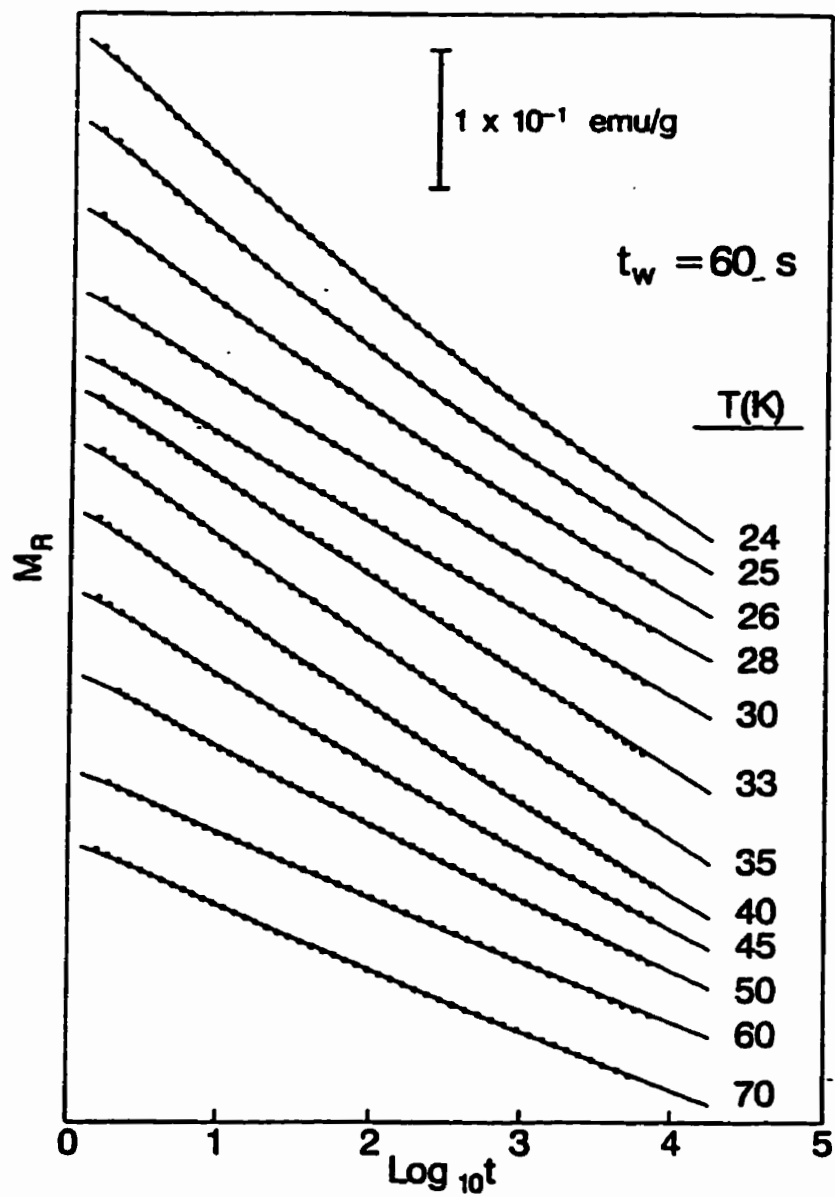


Figure C.6: EDM fits of Eq.(4.24) (solid curves) to thermoremanent relaxation isotherms of $\text{Fe}_{0.65}\text{Ni}_{0.21}\text{Cr}_{0.11}$ for a sequence of temperatures $T_m \geq 24 \text{ K}$ and for a common wait time $t_w = 60 \text{ s}$.

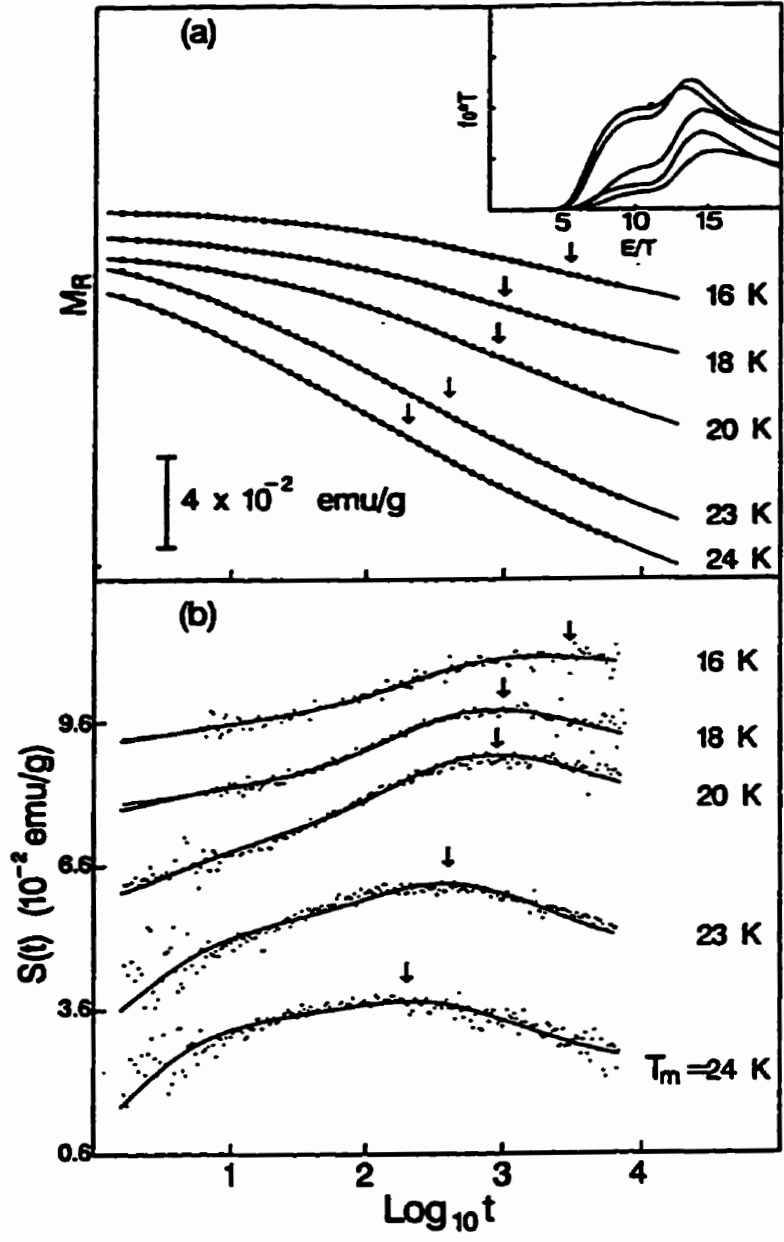


Figure C.7: (a) EDM fits of Eq.(4.23)(solid curves) to thermoremanent relaxation isotherms of $Fe_{0.65}Ni_{0.23}Cr_{0.12}$ for a sequence of temperatures $T_m \leq 24$ K and for a common wait time $t_w = 60s$. The vertical arrows mark the characteristic times (inflection points) τ . (b) Relaxation rates for the data (dots) and by the theoretical function (solid curves). The insert shows the final "aged" distribution of activation energies (just after the field change). The peaks from bottom to top correspond to increasing temperature.

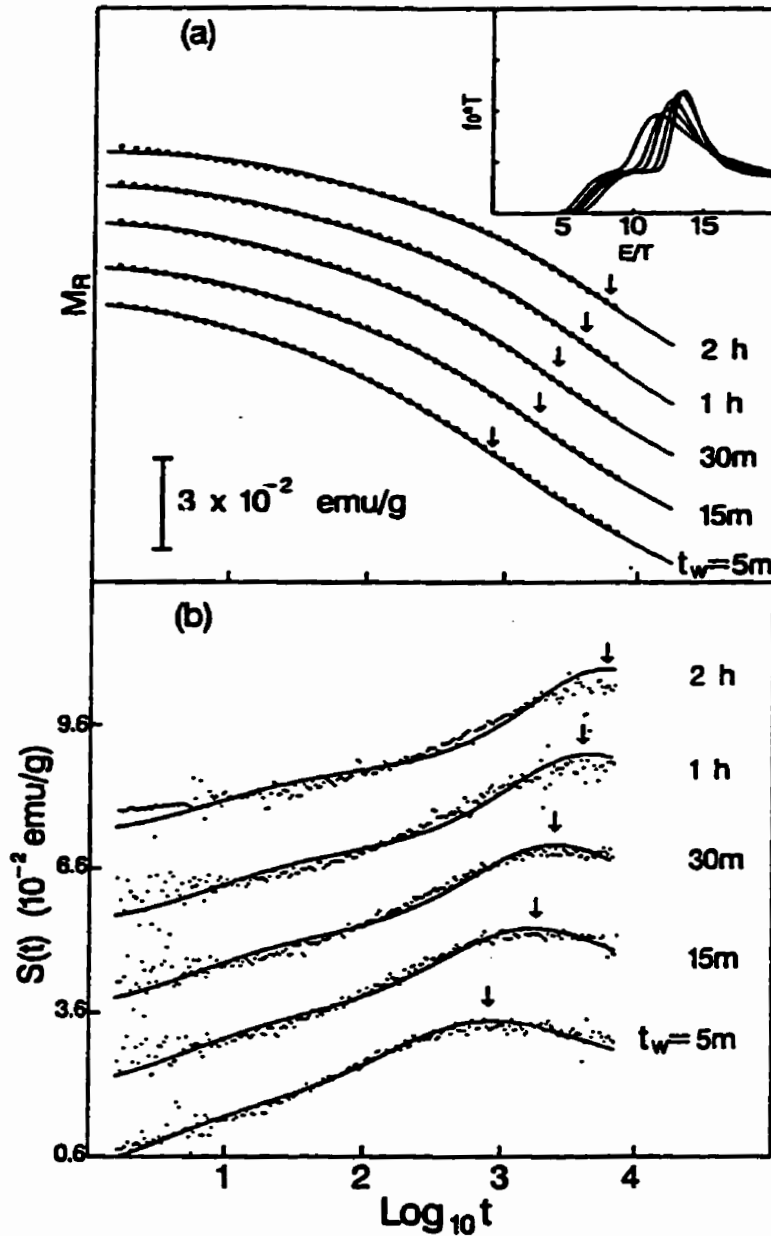


Figure C.8: (a) EDM fits of Eq.(4.23)(solid curves) to the wait-time dependence of the thermoremanent relaxation of $\text{Fe}_{0.65}\text{Ni}_{0.23}\text{Cr}_{0.12}$ at $T_m = 20$ K. The vertical arrows mark the characteristic times (inflection points) τ . (b) Relaxation rates for the data (dots) and by the theoretical function (solid curves). The insert shows the final "aged" distribution of activation energies (just after the field change). The peaks from left to right correspond to increasing wait time.

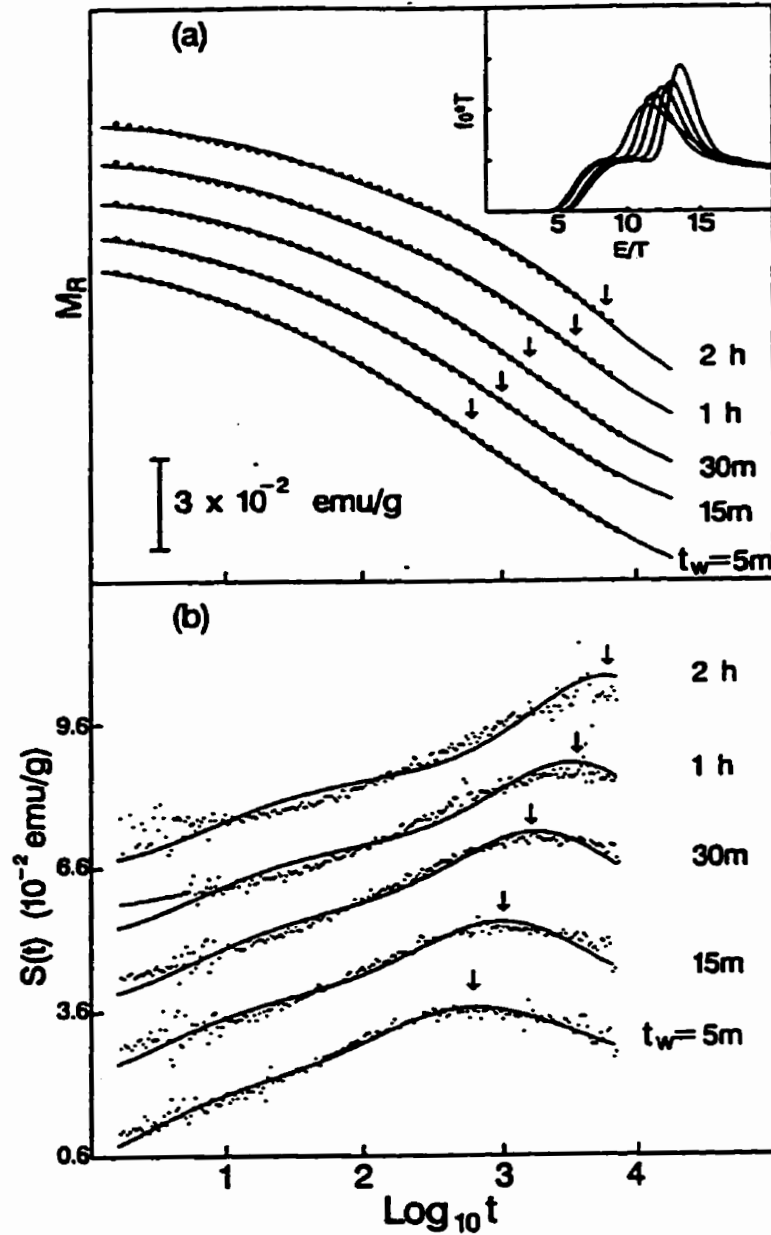


Figure C.9: (a) EDM fits of Eq.(4.23)(solid curves) to the wait-time dependence of the thermoremanent relaxation of $\text{Fe}_{0.65}\text{Ni}_{0.23}\text{Cr}_{0.12}$ at $T_m = 21$ K. The vertical arrows mark the characteristic times (inflection points) τ . (b) Relaxation rates for the data (dots) and by the theoretical function (solid curves). The insert shows the final "aged" distribution of activation energies (just after the field change). The peaks from left to right correspond to increasing wait time.

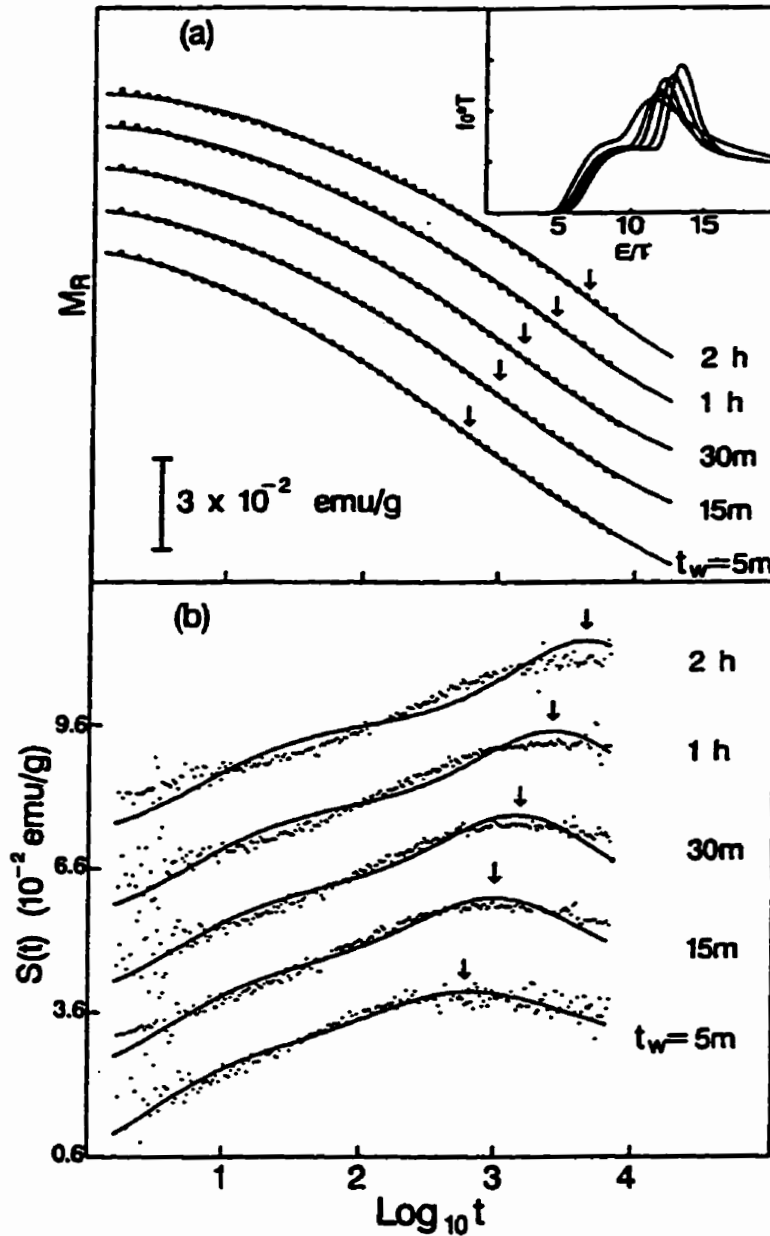


Figure C.10: (a) EDM fits of Eq.(4.23)(solid curves) to the wait-time dependence of the thermoremanent relaxation of $\text{Fe}_{0.65}\text{Ni}_{0.23}\text{Cr}_{0.12}$ at $T_m = 22$ K. The vertical arrows mark the characteristic times (inflection points) τ . (b) Relaxation rates for the data (dots) and by the theoretical function (solid curves). The insert shows the final "aged" distribution of activation energies (just after the field change). The peaks from left to right correspond to increasing wait time.

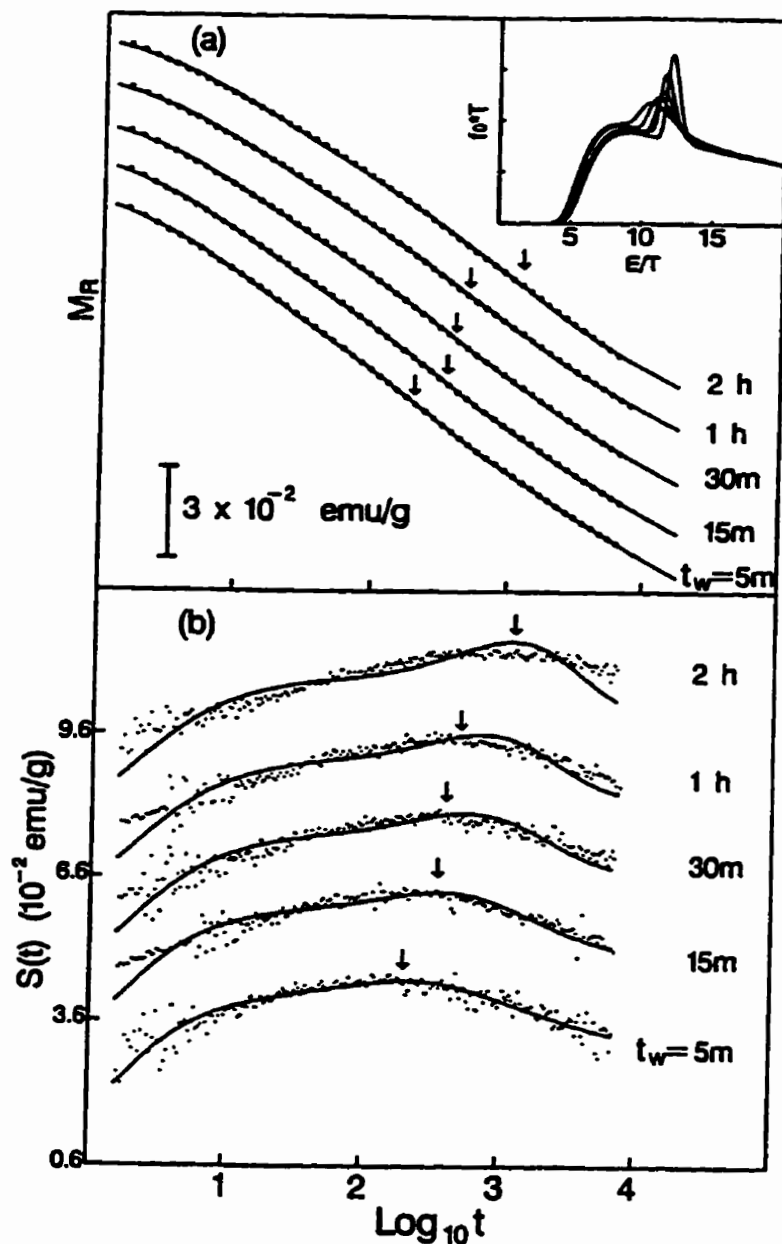


Figure C.11: (a) EDM fits of Eq.(4.23)(solid curves) to the wait-time dependence of the thermoremanent relaxation of $\text{Fe}_{0.65}\text{Ni}_{0.23}\text{Cr}_{0.12}$ at $T_m = 24$ K. The vertical arrows mark the characteristic times (inflection points) τ . (b) Relaxation rates for the data (dots) and by the theoretical function (solid curves). The insert shows the final "aged" distribution of activation energies (just after the field change). The peaks from left to right correspond to increasing wait time.

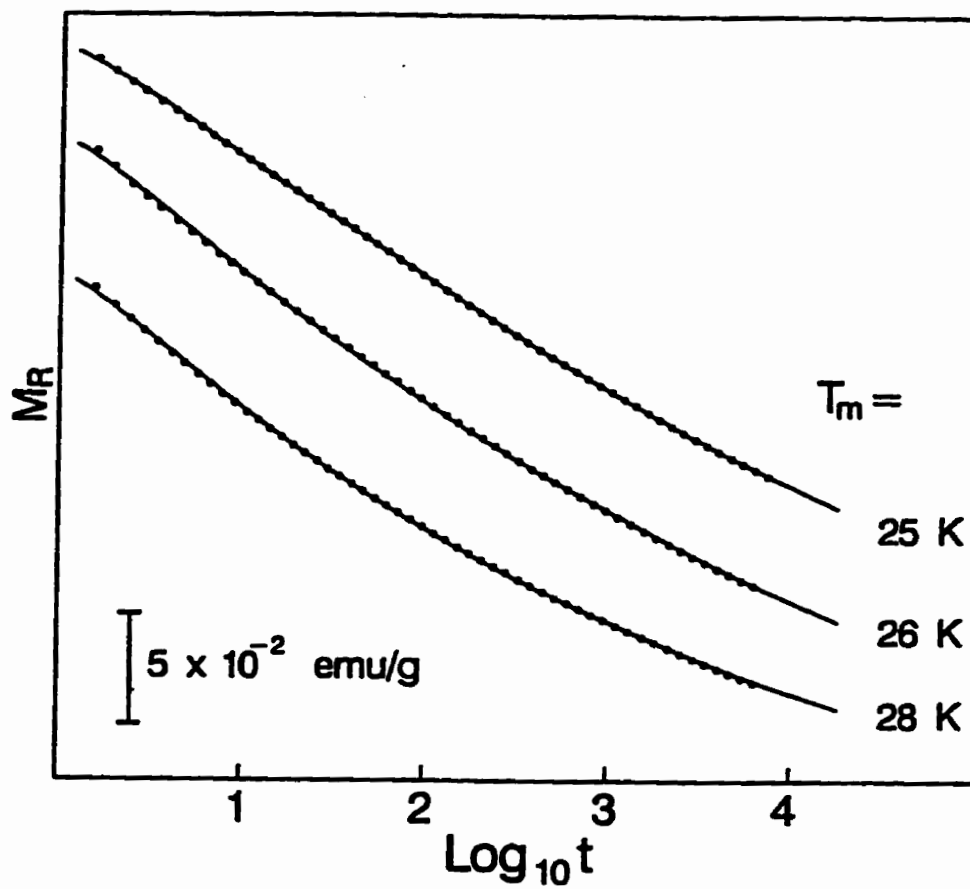


Figure C.12: EDM fits (solid curves) of the thermoremanent relaxation of $\text{Fe}_{0.65}\text{Ni}_{0.23}\text{Cr}_{0.12}$ at $T_m = 25$ K to Eq.(4.23) and $T_m = 26$ K, and 28 K to Eq.(4.24)

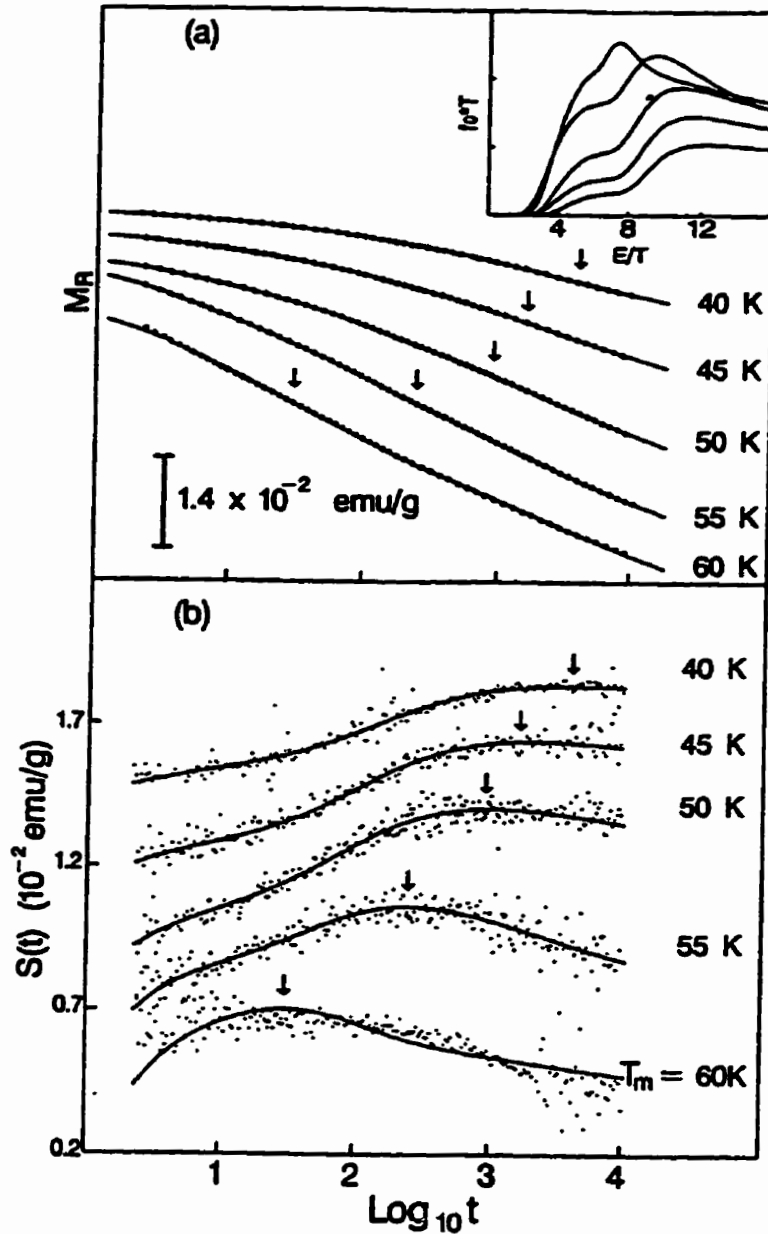


Figure C.13: (a) EDM fits of Eq. (4.23) (solid curves) to thermoremanent relaxation isotherms of $(\text{Fe}_{0.65}\text{Ni}_{0.35})_{0.882}\text{Mn}_{0.118}$ for a sequence of temperatures $T_m \leq 60$ K and for a common wait time $t_w = 60$ s. The vertical arrows mark the characteristic times (inflection points) τ . (b) Relaxation rates for the data (dots) and the theoretical function (solid curves). The insert shows the final "aged" distribution of activation energies (just after the field change). The peaks from bottom to top correspond to increasing temperature.

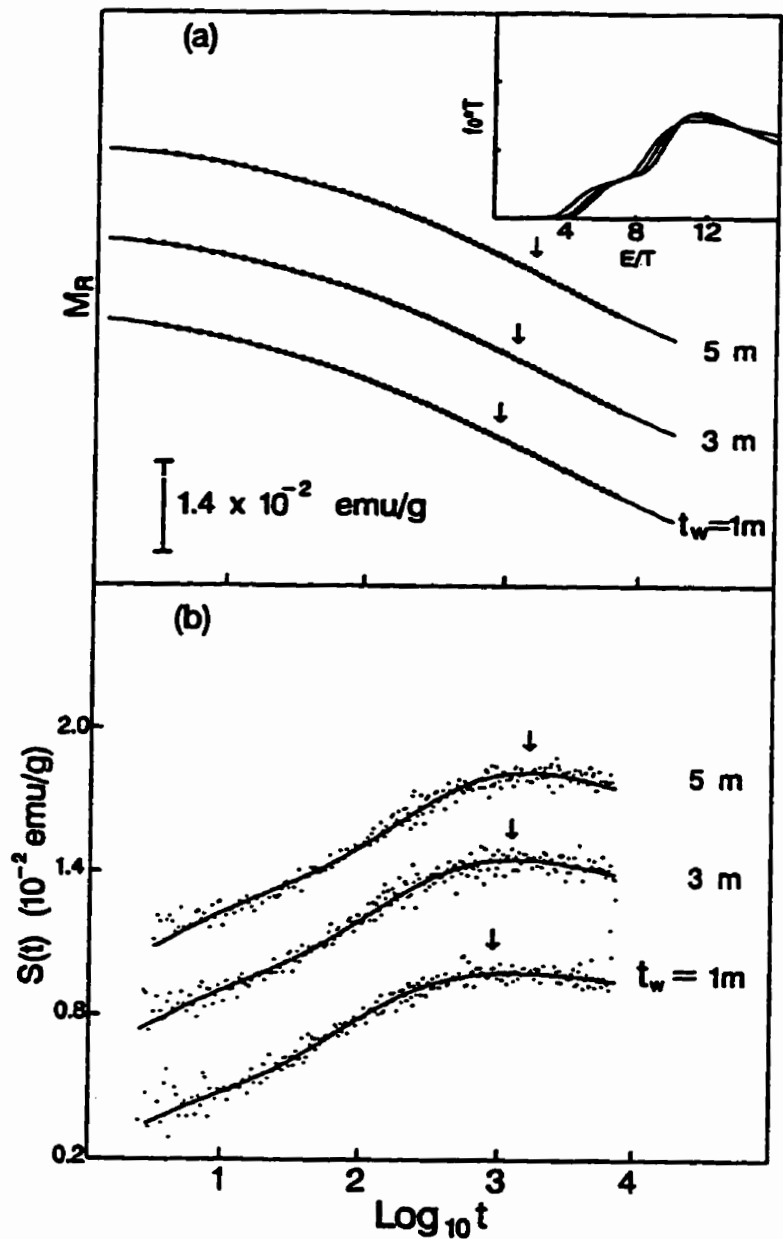


Figure C.14: (a) EDM fits of Eq.(4.23)(solid curves) to the wait-time dependence of the thermoremanent relaxation of $(\text{Fe}_{0.65}\text{Ni}_{0.35})_{0.882}\text{Mn}_{0.118}$ at $T_m = 48 \text{ K}$. The vertical arrows mark the characteristic times (inflection points) τ . (b) Relaxation rates for the data (dots) and the theoretical function (solid curves). The inset shows the final “aged” distribution of activation energies (just after the field change). The peaks from left to right correspond to increasing wait time.

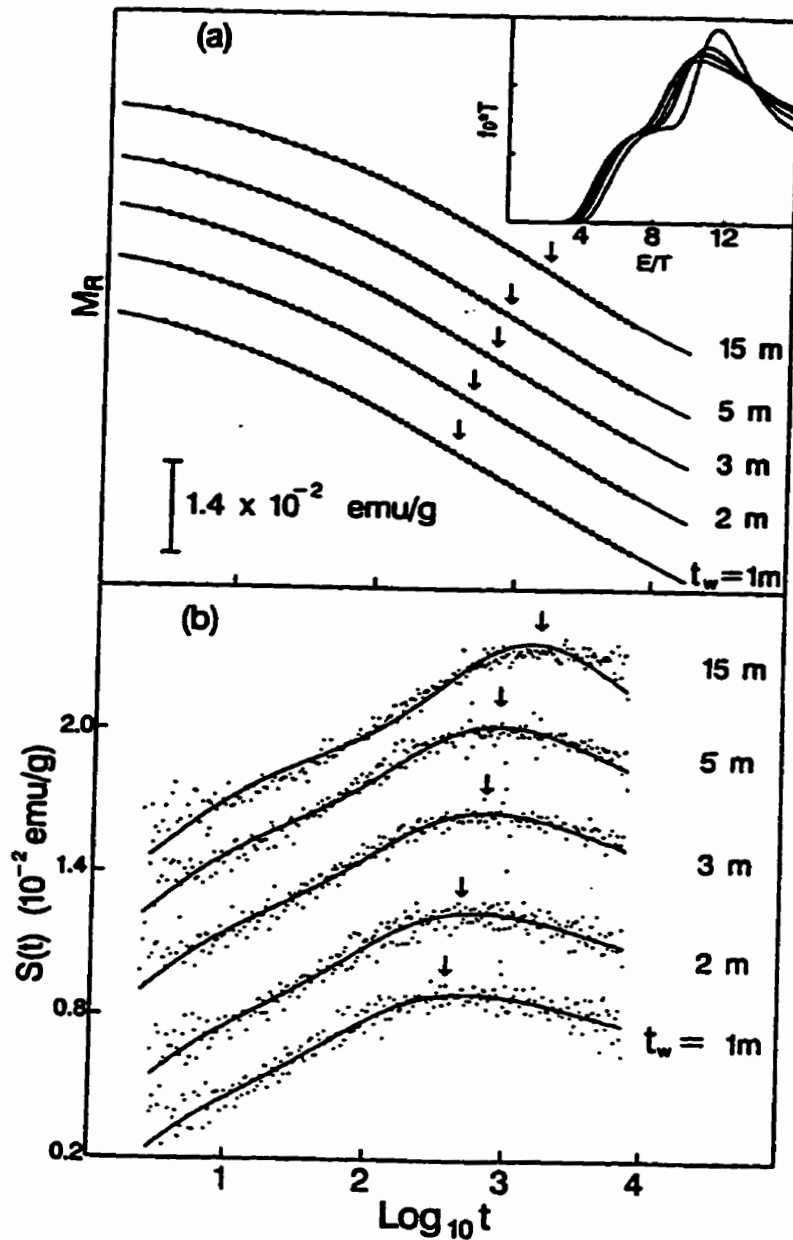


Figure C.15: (a) EDM fits of Eq.(4.23)(solid curves) to the wait-time dependence of the thermomagnetic relaxation of $(\text{Fe}_{0.65}\text{Ni}_{0.35})_{0.882}\text{Mn}_{0.118}$ at $T_m = 52$ K. The vertical arrows mark the characteristic times (inflection points) τ . (b) Relaxation rates for the data (dots) and the theoretical function (solid curves). The insert shows the final "aged" distribution of activation energies (just after the field change). The peaks from left to right correspond to increasing wait time.

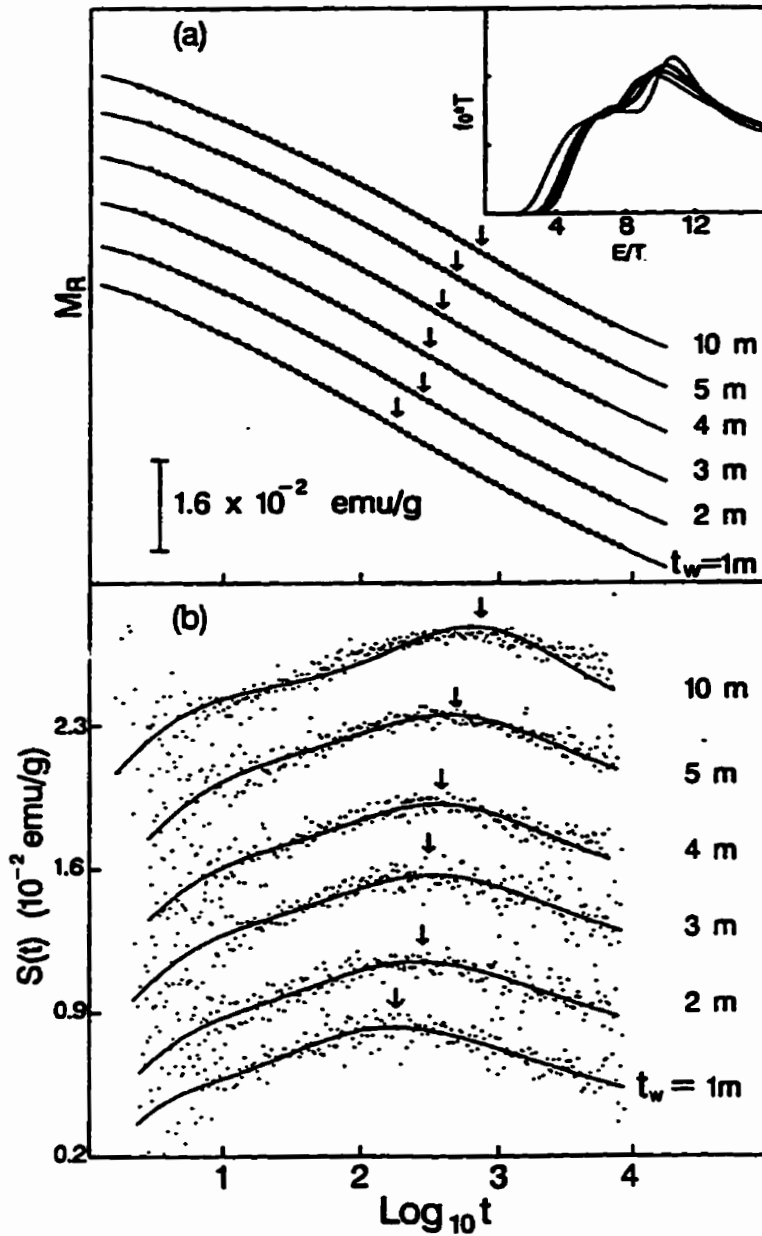


Figure C.16: (a) EDM fits of Eq.(4.23) (solid curves) to the wait-time dependence of the thermoremanent relaxation of $(\text{Fc}_{0.65}\text{Ni}_{0.35})_{0.882}\text{Mn}_{0.118}$ at $T_m = 56$ K. The vertical arrows mark the characteristic times (inflection points) τ . (b) Relaxation rates for the data (dots) and the theoretical function (solid curves). The insert shows the final "aged" distribution of activation energies (just after the field change). The peaks from left to right correspond to increasing wait time.

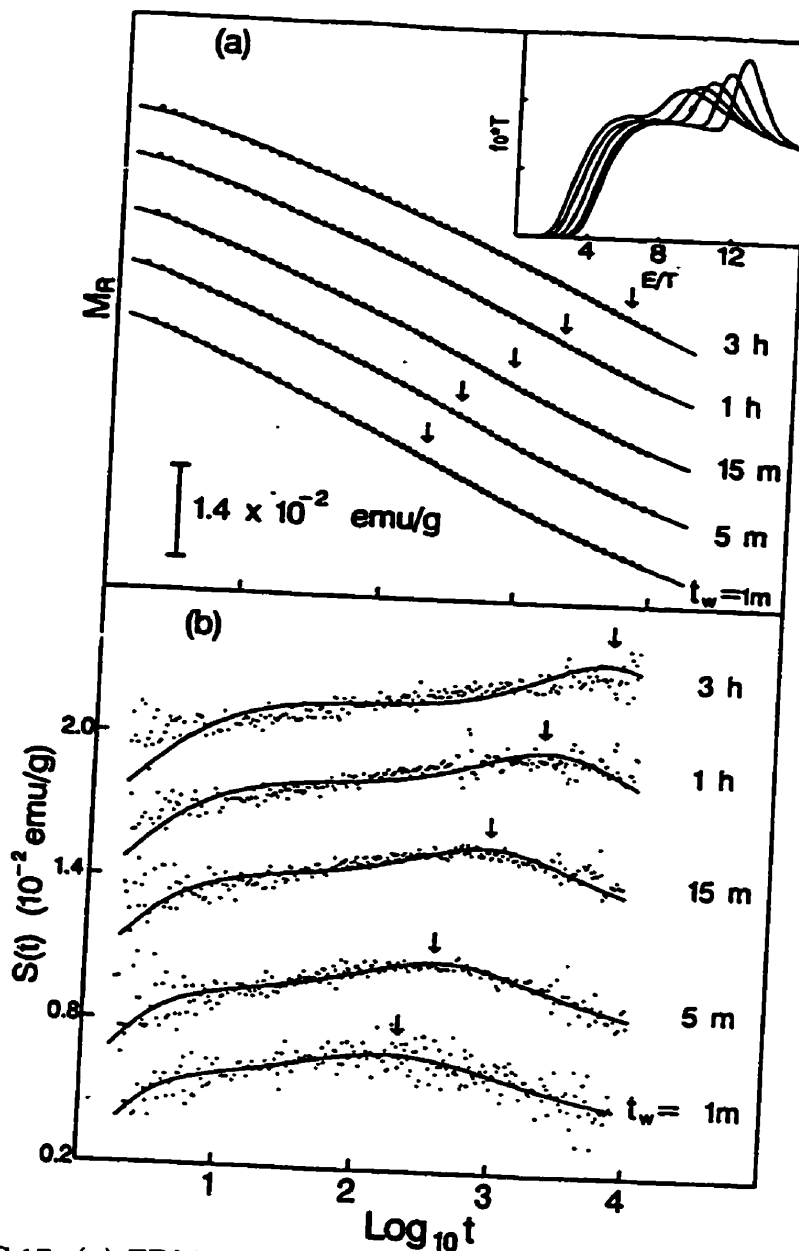


Figure C.17: (a) EDM fits of Eq.(4.23)(solid curves) to the wait-time dependence of the thermoremanent relaxation of $(\text{Fe}_{0.65}\text{Ni}_{0.35})_{0.882}\text{Mn}_{0.118}$ at $T_m = 57$ K. The vertical arrows mark the characteristic times (inflection points) τ . (b) Relaxation rates for the data (dots) and the theoretical function (solid curves). The insert shows the final "aged" distribution of activation energies (just after the field change). The peaks from left to right correspond to increasing wait time.

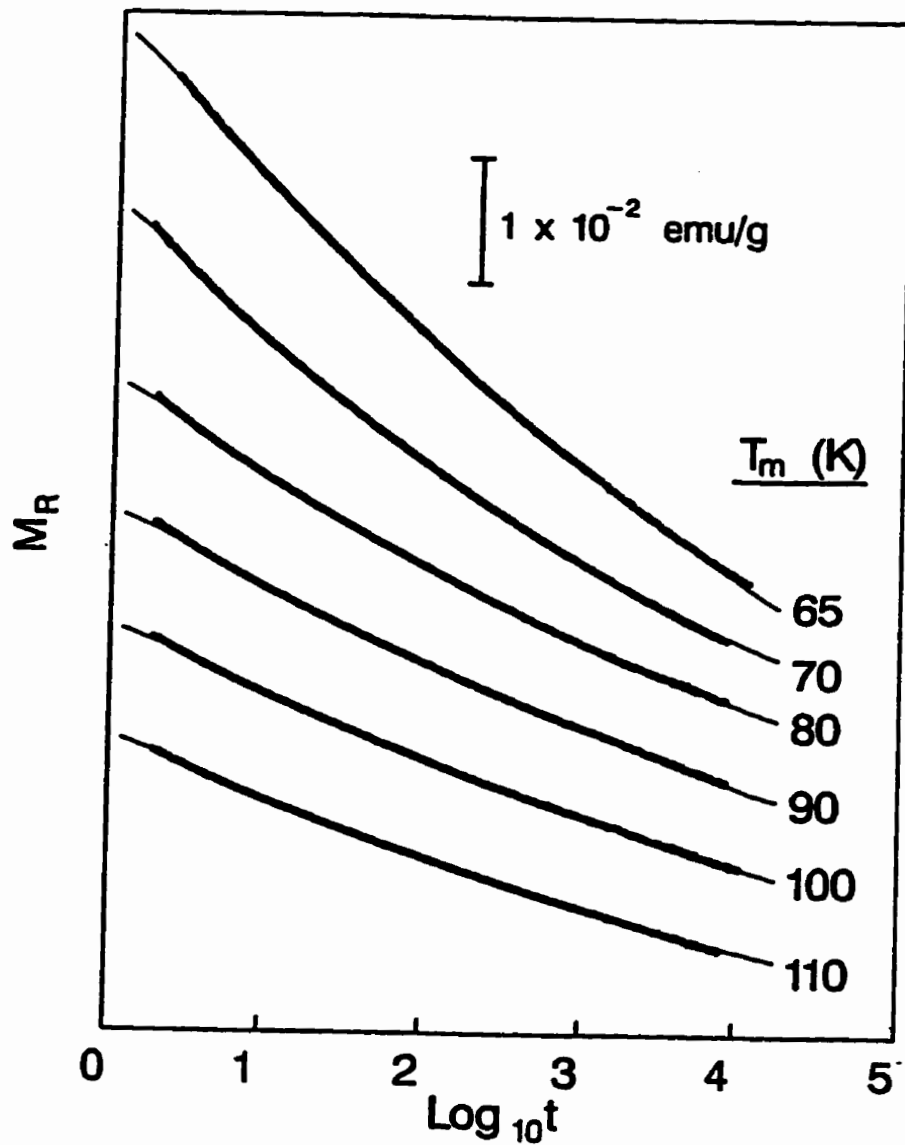


Figure C.18: EDM fits of Eq.(4.24) (solid curves) to thermoremanent relaxation isotherms of $(\text{Fe}_{0.65}\text{Ni}_{0.35})_{0.882}\text{Mn}_{0.118}$ for a sequence of temperatures $T_m \geq 65$ K and for a common wait time $t_w = 60$ s.

Appendix D

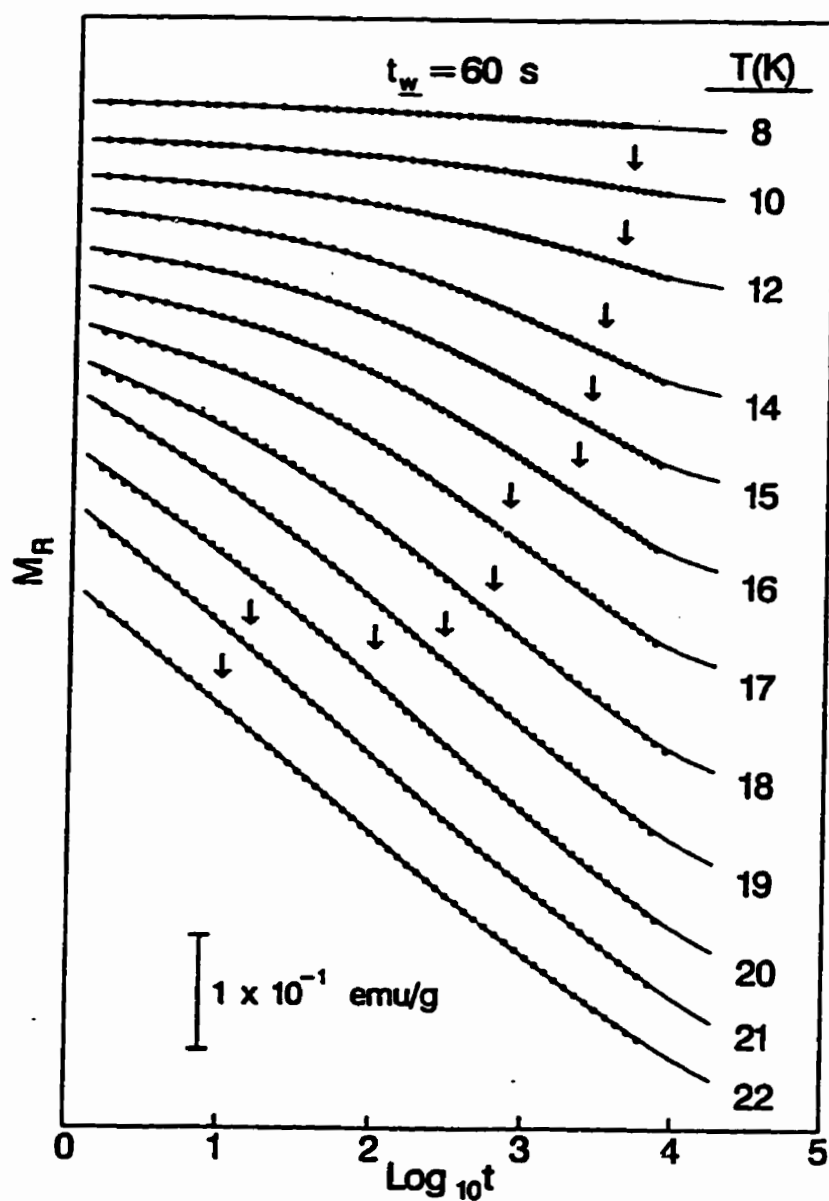


Figure D.1: Thermoremanent relaxation isotherms of $\text{Fe}_{0.65}\text{Ni}_{0.24}\text{Cr}_{0.11}$ for a sequence of temperatures $T_m \leq 22$ K and for a common wait time $t_w = 60$ s. The solid curves are fits to Eq.(2.141) and vertical arrows mark the characteristic inflection points τ .

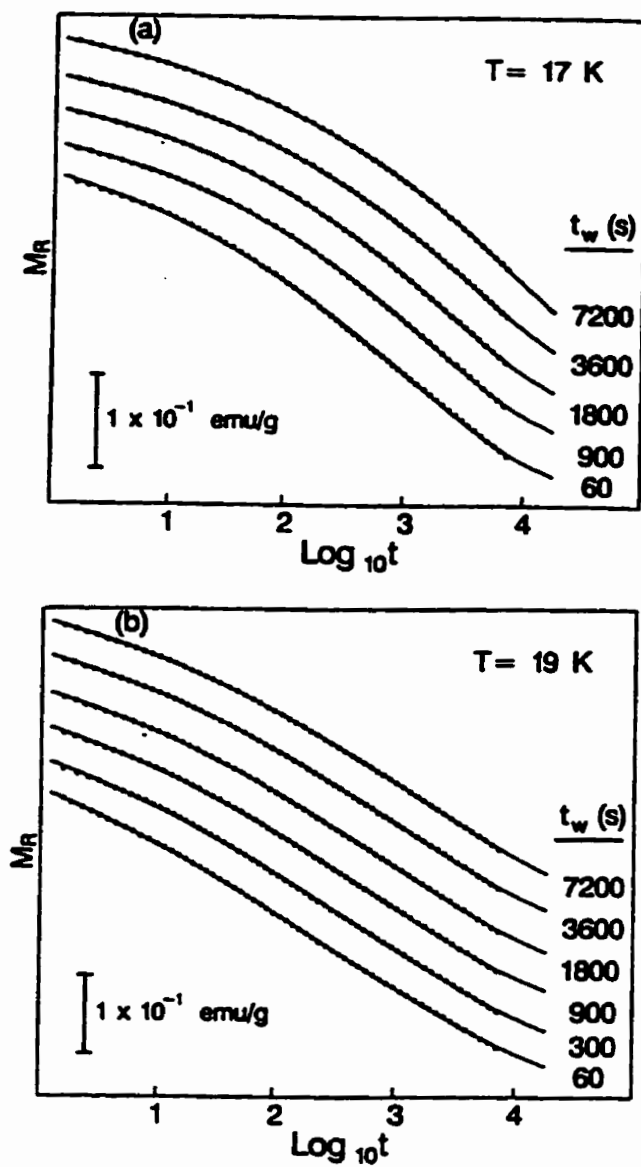


Figure D.2: (a) Wait-time dependence of the thermoremanent relaxation of $\text{Fe}_{0.65}\text{Ni}_{0.24}\text{Cr}_{0.11}$ at $T_m = 17 \text{ K}$. The solid curves are fits to Eq.(2.141). (b) Same sample and analysis as in (a) but for $T_m = 19 \text{ K}$.

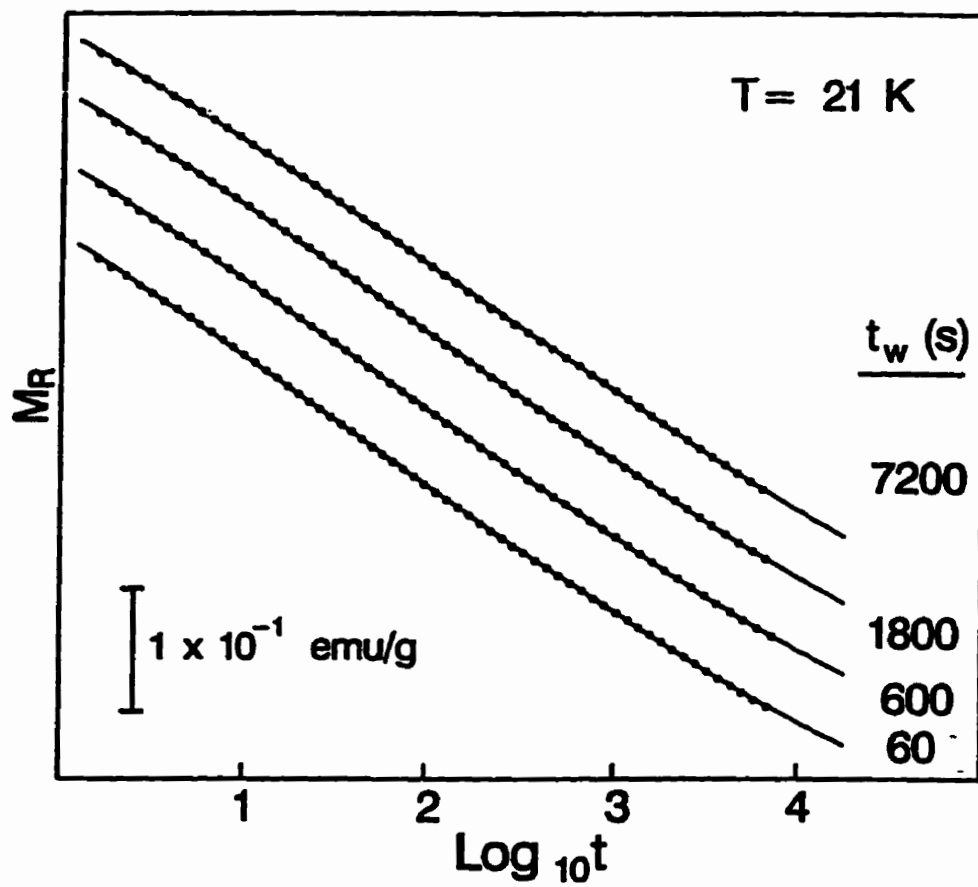


Figure D.3: Wait-time dependence of the thermoremanent relaxation of $\text{Fe}_{0.65}\text{Ni}_{0.24}\text{Cr}_{0.11}$ at $T_m = 21 \text{ K}$. The solid curves are fits to Eq.(2.141).

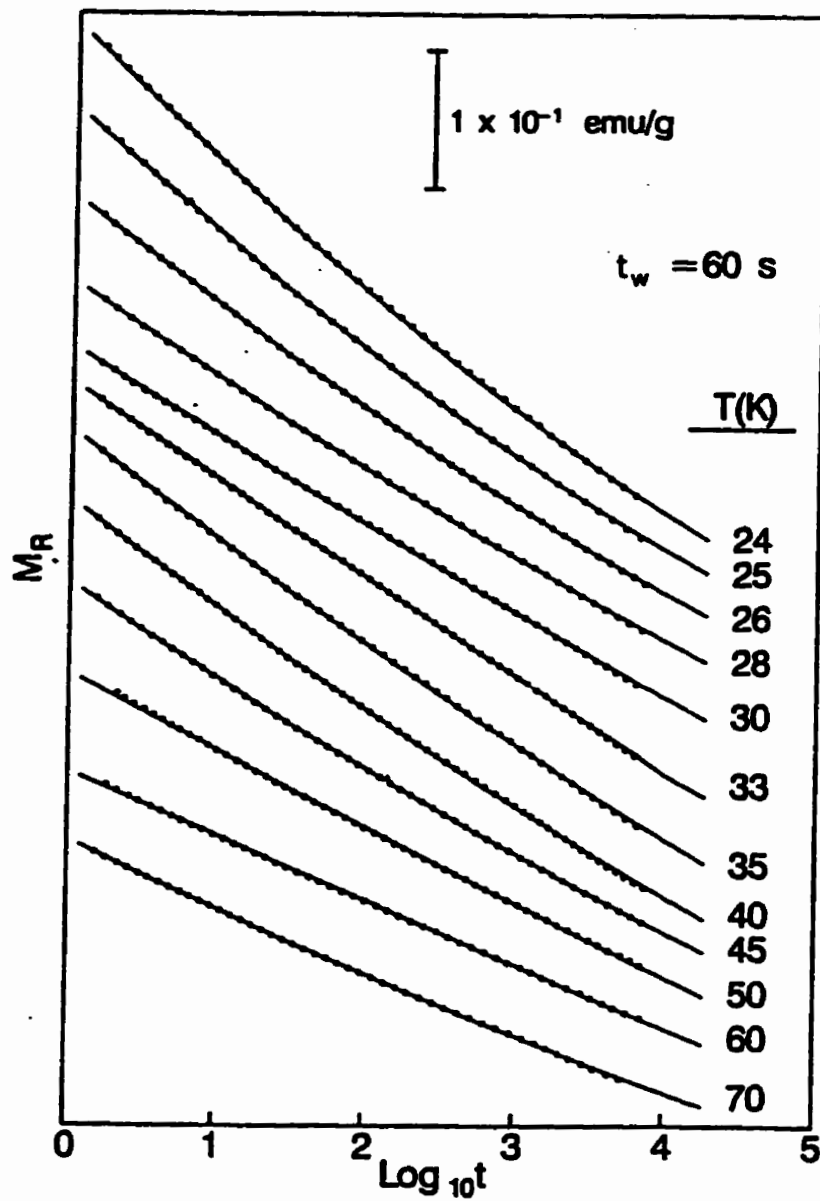


Figure D.4: Thermoremanent relaxation isotherms of $\text{Fe}_{0.65}\text{Ni}_{0.24}\text{Cr}_{0.11}$ for a sequence of temperatures $T_m \geq 24 \text{ K}$ and for a common wait time $t_w = 60 \text{ s}$. The solid curves are fits to Eq.(2.142).

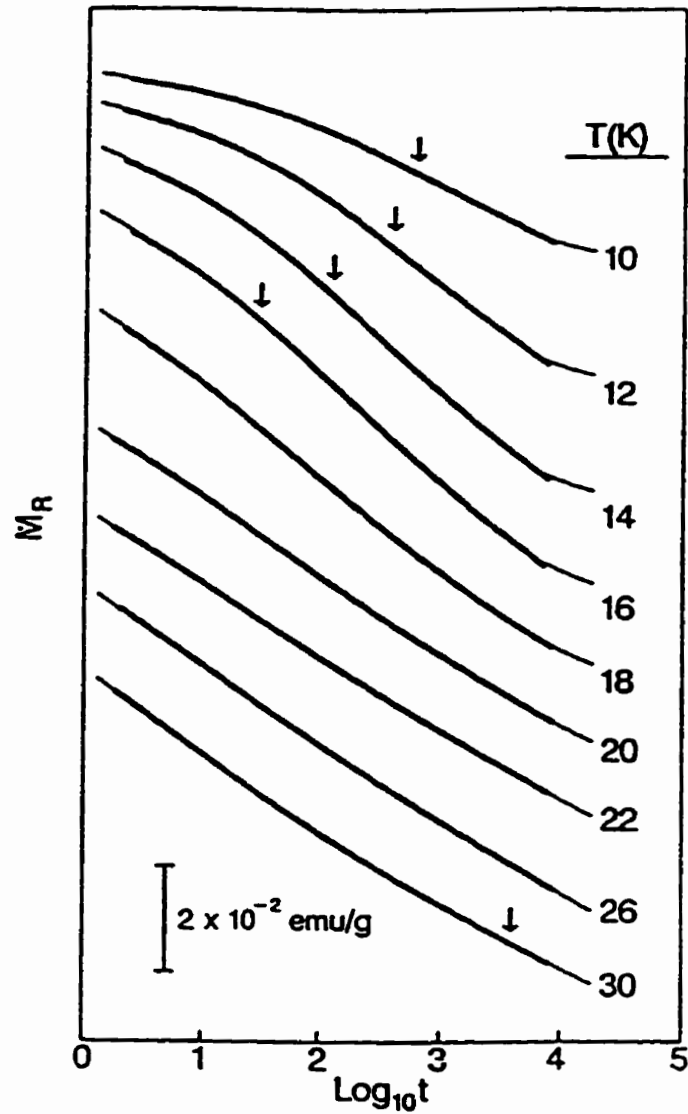


Figure D.5: Thermoremanent relaxation isotherms of $\text{Cr}_{0.79}\text{Fe}_{0.21}$ for a sequence of temperatures and for a common wait time $t_w = 60\text{s}$. The solid curves are fits to Eq.(2.141) for $T_m \leq 22\text{ K}$ and to Eq.(2.142) for $T_m \geq 26\text{ K}$. The vertical arrows mark the location of the relaxation time $\bar{\tau}_+/\bar{\tau}_-$ for average-sized antialigned/aligned domains.

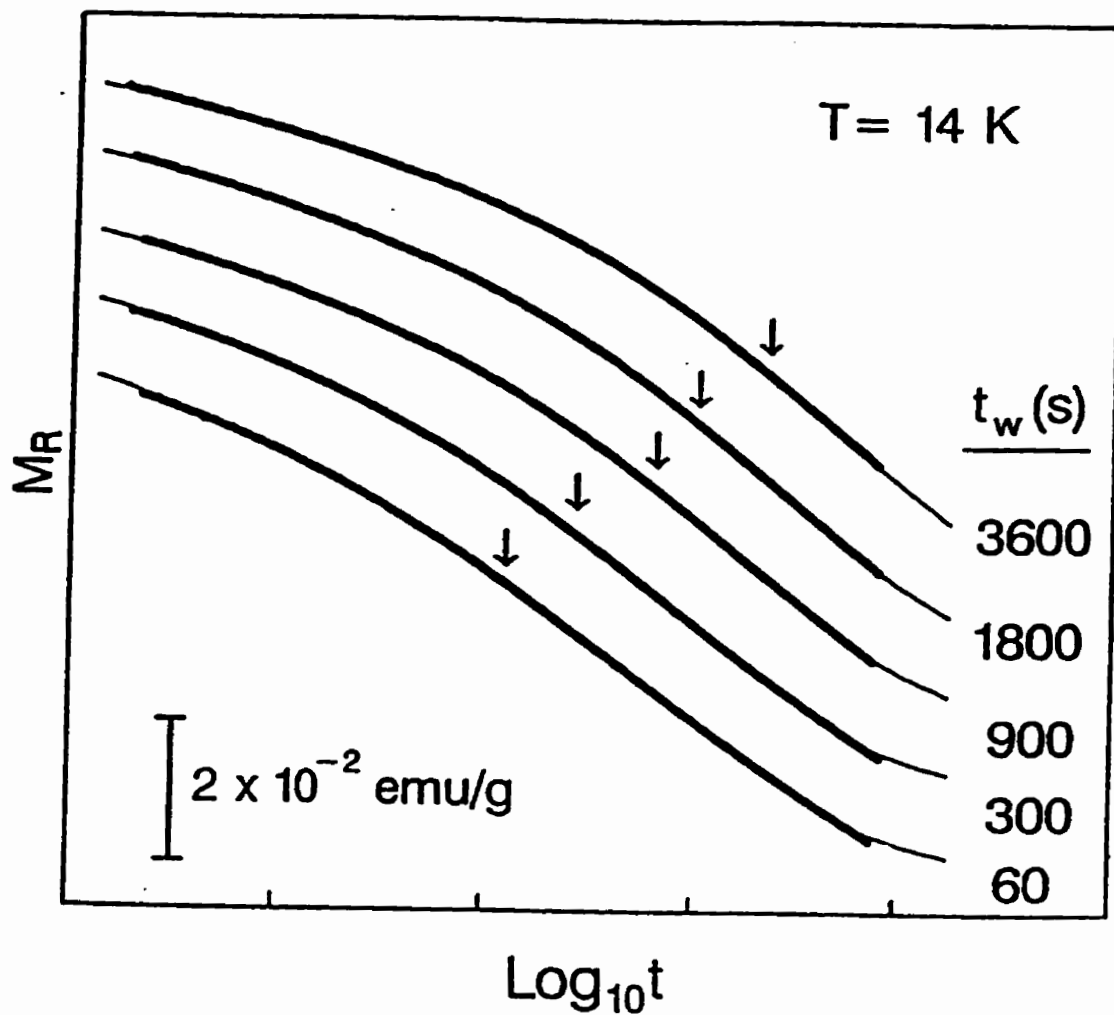


Figure D.6: Wait-time dependence of the thermoremanent relaxation of $\text{Cr}_{0.79}\text{Fe}_{0.21}$ at $T_m = 14$ K. The solid curves are fits to Eq.(2.141) and the vertical arrows mark the location of the relaxation time $\bar{\tau}_+$ for average-sized antialigned domains.

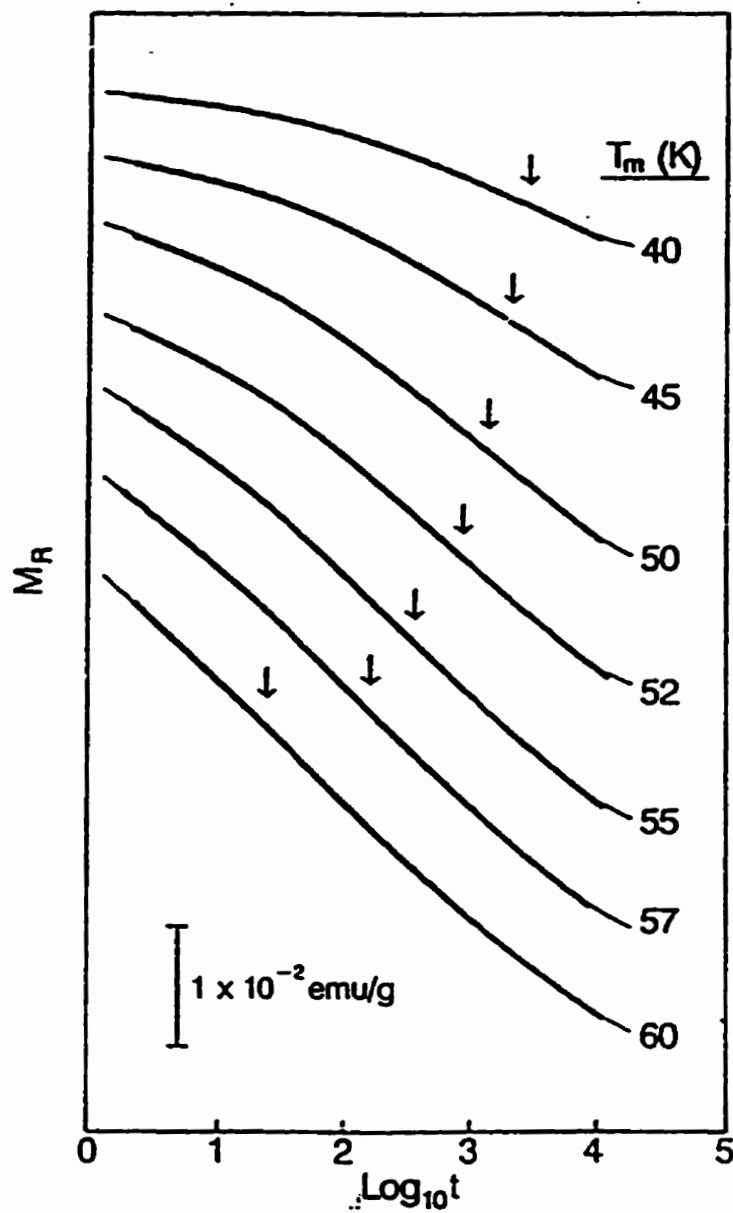


Figure D.7: Thermoremanent relaxation isotherms of $(\text{Fe}_{0.65}\text{Ni}_{0.35})_{0.882}\text{Mn}_{0.118}$ for a sequence of temperatures $T_m \leq 60$ K and for a common wait time $t_w = 60$ s. The solid curves are fits to Eq.(2.141) and vertical arrows mark the location of the relaxation time τ_+ for average-sized antialigned domains.

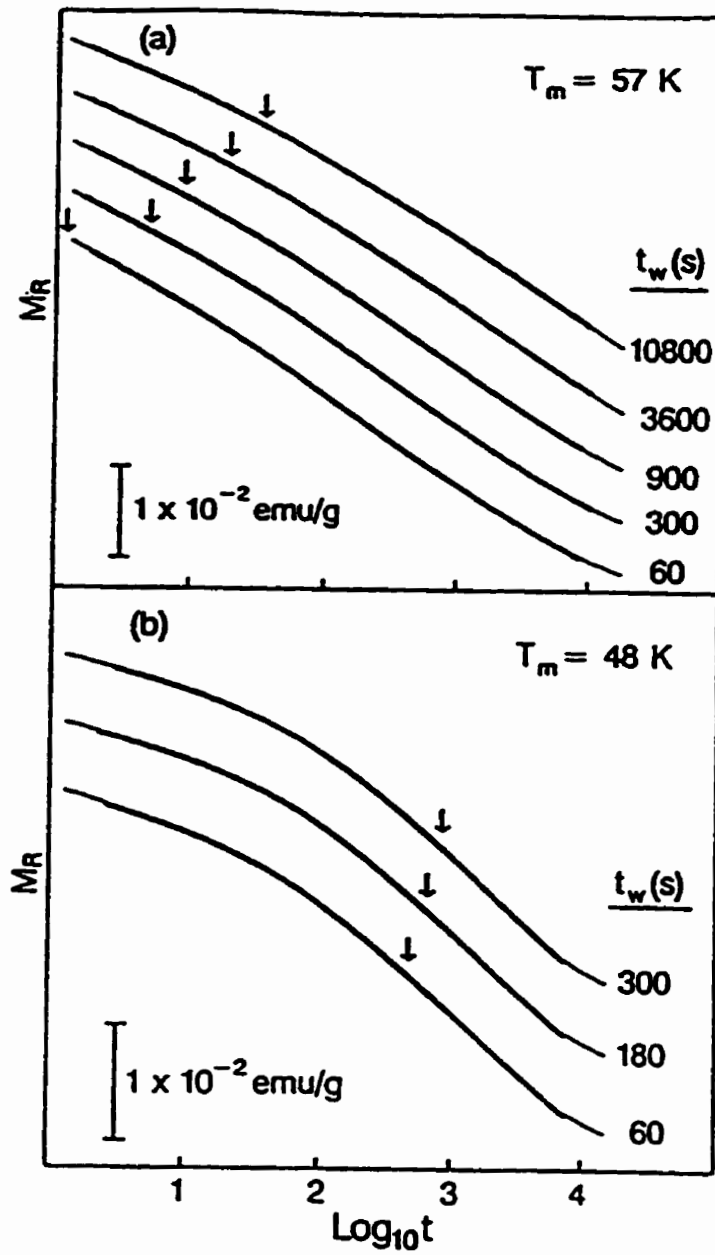


Figure D.8: Wait-time dependence of the thermoremanent relaxation of $(\text{Fe}_{0.65}\text{Ni}_{0.35})_{0.882}\text{Mn}_{0.118}$ at $T_m = 57 \text{ K}$ (a) and $T_m = 48 \text{ K}$ (b). The solid curves are fits to Eq.(2.141) and vertical arrows mark the location of the relaxation time $\bar{\tau}_+$ for average-sized antialigned domains.

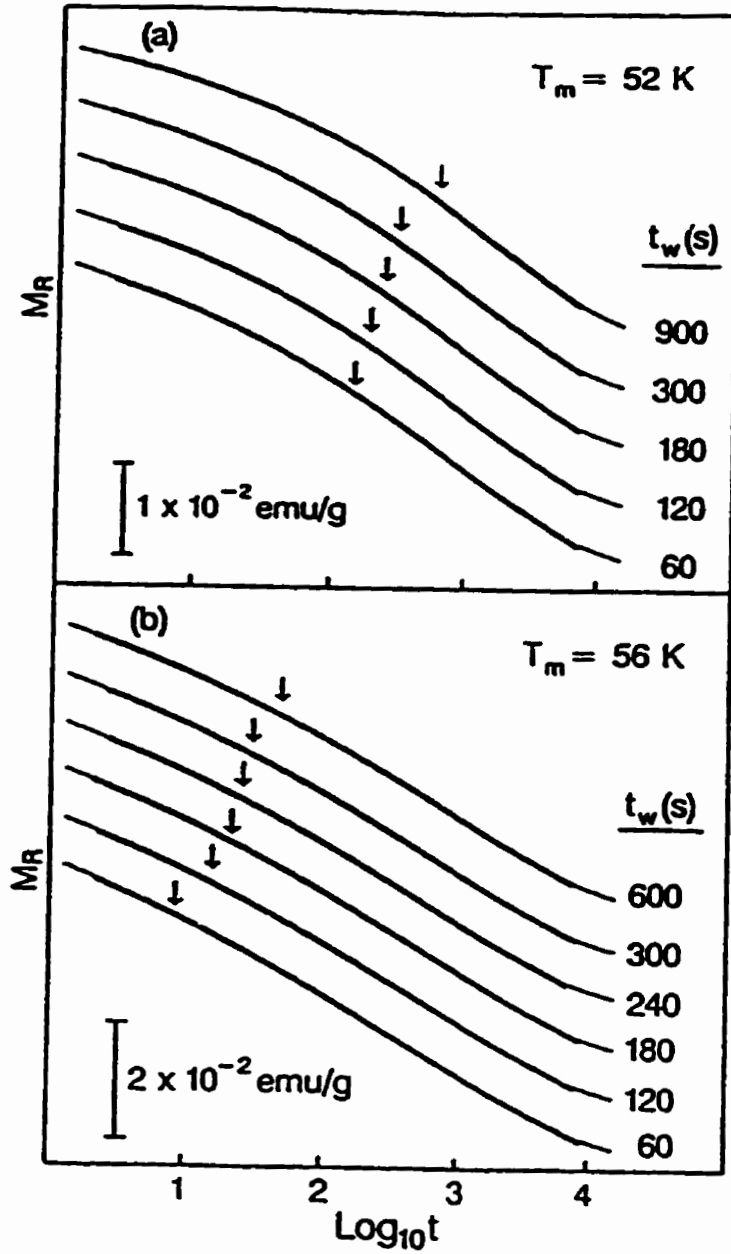


Figure D.9: Wait-time dependence of the thermoremanent relaxation of $(\text{Fe}_{0.65}\text{Ni}_{0.35})_{0.982}\text{Mn}_{0.118}$ at $T_m = 52 \text{ K}$ (a) and $T_m = 56 \text{ K}$ (b). The solid curves are fits to Eq. (2.141) and vertical arrows mark the location of the relaxation time $\bar{\tau}_+$ for average-sized antialigned domains.

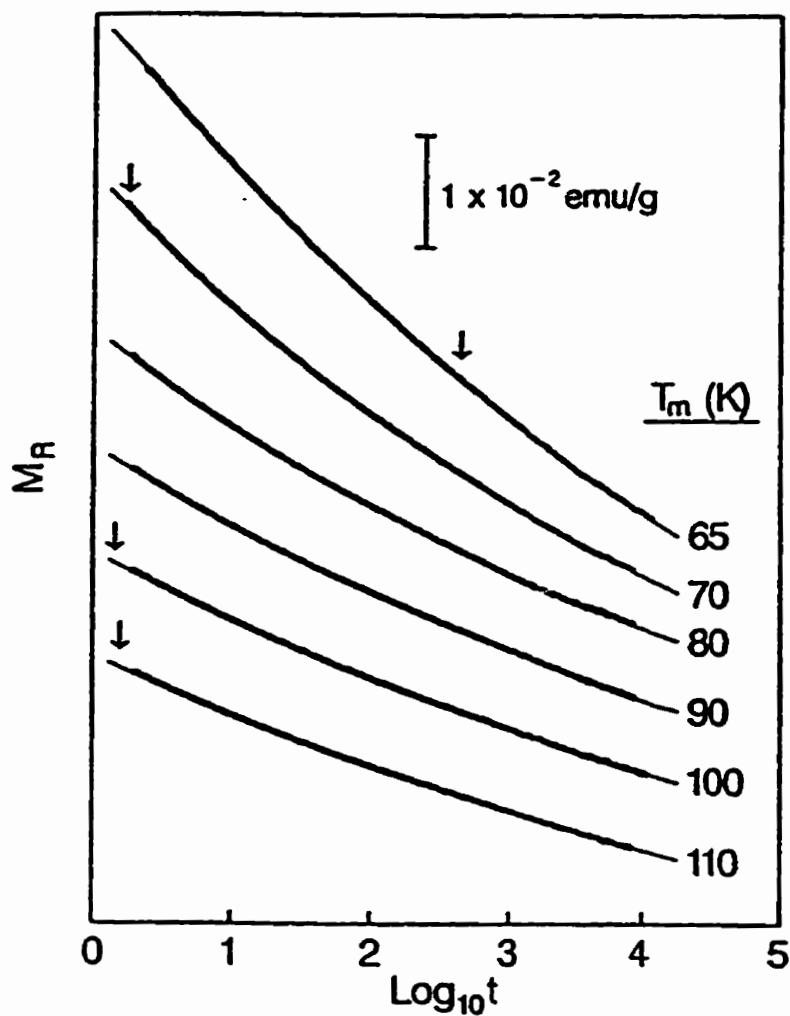


Figure D.10: Thermoremanent relaxation isotherms of $(\text{Fe}_{0.65}\text{Ni}_{0.35})_{0.882}\text{Mn}_{0.118}$ for a sequence of temperatures $T_m \geq 65 \text{ K}$ and for a common wait time $t_w = 60 \text{ s}$. The solid curves are fits to Eq.(2.142) and vertical arrows mark the location of the relaxation time $\bar{\tau}$ for average-sized aligned domains.